Universitat Autònoma de Barcelona

Departament de Física, Facultat de Ciències
Programa de Ciència de Materials
Universitat Autònoma de Barcelona

Elisa Carenza

Engineering Iron Oxide Nanoparticles For Angiogenic Therapies

DOCTORAL THESIS

Supervised by Dr. Anna Roig Serra and Dr. Anna Rosell Novel

Tutor Prof. Javier Rodriguez Viejo

to obtain the title of
PhD in Science
11th July 2014

at "Institut de Ciència de Materials de Barcelona"
and "Institut de Recerca de Vall d'Hebron"

ICMAB CSIC

Vall d'Hebron Institut de Recerca

Dra. Anna Roig Serra, Investigadora Científica del CSIC, la **Dra. Anna Rosell Novel** Investigadora del programa Miguel Servet del ISCIII i **el Prof. Javier Rodríguez Viejo**, Catedràtic d' Universitat, UAB

CERTIFIQUEN:

Que l'Elisa Carenza, Llicenciada en Química-Farmacèutica per la "Universitá degli Studi di Bari", Itàlia ha dut a terme aquesta tesis doctoral sota la seva direcció i que porta per títol **"Engineering iron oxide nanoparticles for angiogenic therapies",** la qual queda recollida en aquesta memòria per optar al grau de Doctor en Ciència en el Programa de Ciència de Materials.

I perquè així consti, signen el present certificat

Dr. Anna Roig Serra Dr. Anna Rosell Novel Prof. Javier Rodríguez Viejo

Elisa Carenza

Bellaterra, 14 de maig 2014

To my family and Ivan

“La colpa di Eva è stata quella di voler conoscere, sperimentare, indagare con le proprie forze le leggi che regolano l'universo, la terra, il proprio corpo e di rifiutare l'insegnamento calato dall'alto.”

“The guilt of Eve was she wanted to learn, to experiment, to explore the laws that govern the universe, the earth, the body and to refuse a precept.”

Margherita Hack, Italian astrophysicist.

Acknowledgements

I arrived in Barcelona for the first time four years ago and I did not know how interesting the experience would turn out to be, for many reasons.

Indeed, I was not aware of what was expecting me during the PhD work on Nanomedicine. Before, I had heard about Nanomedicine during the Master's Degree in Italy and I was soon fascinated by the subject. During these years I have become not only fascinated but also passionate! Definitely, this period has been very important for my professional and personal growth: it has changed my way to face problems and to explore the "unknown". I am very grateful to my supervisors Dr. Anna Roig and Dr. Anna Rosell for accepting me as PhD candidate. They always encouraged me to do my best. It was very interesting to work side by side: they engaged me in a fruitful and constant dialog, very useful for the progress of the thesis, offering both the material science and the medical point of view.

I am grateful to the Consolider-Nanoselect project "CSD2007-00041" that was the financial support throughout the PhD period.

I would like to express my sincere gratitude to the people who helped me in achieving such good results:

Anna Roig, thank you for your guidance and for being always available for discussions. You have been a great support to me, not only at work.

Anna Rosell, thank you for transmitting me your passion (and incredible energy) for research. You taught me many things on cell cultures, on being rigorous and patient with the outcomes.

Olivier Jordan, thank you a lot for the time you spent with me during my stage at Ecole de Pharmacie Genève–Lausanne (EPGL) in Geneva. Your help was essential for the work on magnetic nanoparticles and protein co-encapsulation.

Gerrit Borchard, thank you very much for accepting me in your group during the stage at EPGL in Geneva. I appreciated your advice on drug delivery and protein encapsulation.

People of the "Nanoparticles and Nanocomposites group" at ICMAB-CSIC: Martí, Anna Laromaine, Elena, Oana, Nerea, Muling, Maria, Laura, Pengfei, Siming: thank you for your suggestions. I really enjoyed the time spent with you inside and outside the lab. I will always remember your talent for cooking delicious cakes!

People of "Neurovascular Research group" at Vall d'Hebron Research Institute: Mar, Anna Morancho, Veronica, Anna Penalba, Cristina Boada, Cristina Merino and Joan Montaner: thank you for the many explanations you provided me during the training with cell cultures. It was a great pleasure to learn from you.

People of EPGL in Geneva: Christian, Nathalie Boulens, Brigitte, Yanna, Viktorija, Katrin, Floriane, Nathalie: thank you for helping me on the characterization of magnetic nanocapsules and for showing me some important Swiss traditions: Christmas parties and very good cheese fondues.

Pietro, Aurelia, Antonio, Ivana: thank you for being always close and supporting me, even geographically distant.

Montse, Ramon thank you for taking care of me and making me feel always at home.

Rosanna, David, Pilar thank you for your friendship! I enjoyed very much the time spent with you in Barcelona, for the innumerable conversations at Plaza d'Osca!
Ivan, I came for the first time to Barcelona four years ago and as I already said, I did not know how interesting the experience would turn out to be: I am happy to have had you at my side from that moment on…

Foreword and aim of the thesis

Research in Nanomedicine started few decades ago and encompasses multidisciplinary subjects: Chemistry, Biology, Material engineering, Medicine and Nanotechnology. Some Nanomedicine-based formulations are already commercially available as liposomes for treatment of cancers (Caelyx®, Doxil®), or serious fungal infections (Ambisome®). These products have a series of advantages compared with traditional drug formulations (capsules, tablets, etc.) as the reduction of side-effects in healthy tissues and the simplification of administration protocols. For instance, a drug into a suitable carrier can reside at the therapeutic dosage in the blood without doing repeated intravenous injections.

In 2003 the Human Genome Project was completed with a final mapping of the human genome. Among many expected and unexpected implications, it shaped a new healthcare perspective: the personalized medicine, which is a customized treatment to be administered to patients. Often drugs prescribed for lifelong treatments of cancer or cardiovascular diseases can originate unpredictable effects, thus not constituting the best therapy for a specific individual's condition. Advances in Nanotechnology are expected to help directing appropriate treatments and to design better drugs.

Iron oxide nanoparticles are magnetic particles, accepted by Food and Drug Administration (FDA) due to their biocompatibility and *in vivo* biodegradation. So far, clinical use of iron oxide nanoparticles has been restricted to negative and positive contrast agents in tumor diagnosis. A myriad of other applications are currently under investigation due to iron oxide nanoparticle "versatility": they can be regarded as multifunctional material, because they allow *in vivo* imaging by magnetic resonance imaging (MRI) as well as drugs/cells retention in a zone of interest under an applied magnetic field.

The work showed in this thesis has been realized at the Nanoparticles and Nanocomposites group, ICMAB-CSIC in close collaboration with the Neurovascular Research Group at the Vall d'Hebron Research Institute. **The thesis aims to develop new non-invasive treatments to induce angiogenesis after an ischemic event in the brain using iron oxide superparamagnetic nanoparticles (SPIONs) as imaging and guiding tool**. For that, we have worked using two different strategies. The first one, aimed to load SPIONs into endothelial progenitor cells (EPCs) which are cells with stemness characteristics with great potential in cellular-based therapy for tissue revascularization. The second one intended to load SPIONs into biodegradable and biocompatible polymeric carriers in presence of a vascular growth factor, $VEGF_{165}$, a potent mitogenic growth factor. In both cases the final goal would be to enhance angiogenesis in peri-lesional ischemic areas.

The main objectives of the thesis were the following:

1- Synthesis of monodisperse SPIONs with good magnetic properties and their stabilization in water and cell culture media;

2- Efficiently and safe labeling of EPCs to obtain still functional magnetized cells with good contrast magnetic resonance imaging (MRI) effects and high responsiveness to external magnetic fields;
3- Co-encapsulation of $VEGF_{165}$ and SPIONs into bio-compatible nanocapsules suitable for systemic administration, showing good MRI contrast effects and responsiveness to external magnetic fields. Moreover, the encapsulation method should ensure protein bioactivity after the release process in a mimicked physiological environment.

The manuscript is organized in 6 chapters.

- **Chapter 1** includes some basic concepts on Nanotechnology and a brief explanation of magnetic properties of the materials. It also includes a description of iron oxide magnetic nanoparticles summarizing the most commonly used synthetic approaches found in literature. Finally, current SPION applications in Nanomedicine are mentioned. Annex of chapter 1 reported on MRI basic concepts.
- **Chapter 2** describes SPION synthesis by thermal decomposition and microwave assisted routes. The chapter also shows SPION characterization, stabilization in water at pH=7.4 and in cell culture media before their use for *in vitro* and *in vivo* experiments. Annex of chapter 2 contains protocols for particle characterizations.
- **Chapter 3** begins with the introduction on basic concepts of angiogenesis, ischemia and targeted cellular therapy. It focuses on *in vitro* and *in vivo* experiments performed to obtain magnetically labeled and still functional EPCs. Successfully labeled EPCs were tracked by MRI and opportunely retained in the cortical area of the brain in mouse animal models through an external magnetic field. The annex of chapter 3 contains the protocols used for *in vitro* and *in vivo* experiments, namely cellular labeling, SPIONs cytotoxicity evaluation, cellular functionality regarding the formation of tubular connections and migration ability of labeled EPCs compared to non-treated cells.
- **Chapter 4** starts with an introduction on basic concepts of drug delivery, on methods of synthesis of micro-nanocarriers, and protein/SPION encapsulation. The chapter focuses on the synthesis of poly(D,L-lactic-co-glycolic acid) (PLGA) nanocapsules loaded with SPIONs and human $VEGF_{165}$ by double emulsion-solvent evaporation process. Annex of chapter 4 contains the protocols used for nanocapsule characterization, protocols for protein release study and *in vitro* bioactivity assay.
- **Chapter 5** reports on general conclusions of the thesis and some suggestions for the future work.
- **Chapter 6** contains information about the author and the publications realized during the PhD work.

Table of contents

pag.

CHAPTER 3

MAGNETICALLY LABELED ENDOTHELIAL PROGENITOR CELLS FOR TARGETED THERAPEUTIC ANGIOGENESIS IN THE BRAIN

CHAPTER 4

CO-ENCAPSULATION OF SPIONs AND RECOMBINANT HUMAN VASCULAR GROWTH FACTOR (rhVEGF$_{165}$) INTO PLGA (poly(D,L-lactic-co-glycolic acid) NANOPARTICLES FOR TARGETED THERAPEUTIC ANGIOGENESIS

Attributions

I would like to thank you the people who contributed to this thesis.

- **Anna Rosell** (Neurovascular Reaserch group, Vall d'Hebron Institute) who is co-supervisor of this thesis. She started working at magnetically labeled endothelial progenitor cells in 2009. She performed many *in vitro* and *in vivo* experiments and she helped me during my training with cell cultures and with interpretation of statistical data.
- **Dr. Olivier Jordan** (EPGL, Genève-Lausanne) who helped me in the optimization of the protocol for the co-encapsulation of iron oxide nanoparticles with vascular endothelial growth factor;
- **People of Neurovascular Reaserch group at Vall d'Hebron Institute**: Veronica Barceló, Anna Morancho, Pablo Martínez, Anna Penalba who did *in vitro* experiments and biological assays using aqueous dispersions of magnetic nanoparticles and polymeric nanocapsules. They also taught me the basics for the manipulation of cell cultures and immunological assays.
- **Ignasi Villarroya** (Servei de Anàlisi Quìmica, UAB) who performed chemical analysis for the determination of the iron content into samples.
- **Pablo Castro** (Servei de Microscopia, UAB) who did cryo-TEM analysis of aqueous colloidal dispersions of iron oxide nanoparticles and trained me in TEM use.
- **Emma Rossinyol** (Servei de Microscopia, UAB) who did SEM analysis of polymeric nanocapsules;
- **Alejandro Sánchez** (Servei de Microscopia, UAB) who helped me in the TEM analyses of cells;
- **Judit Oró** (ICMAB-CSIC) who performed TEM analysis of iron oxide nanoparticles.
- **Bernat Bozzo** (ICMAB-CSIC) who performed magnetic measurements for the characterization of iron oxide nanoparticles and magnetically labeled cells.
- **Silvia Lope Pedrafita** (Servei de Ressonància Magnètica Nuclear, UAB) who ran magnetic resonance imaging measurements on magnetic nanoparticles during *in vitro* and *in vivo* experiments.

List of symbols, abbreviations and acronyms

α-Fe_2O_3	Hematite
γ- Fe_2O_3	Maghemite
Fe_3O_4	Magnetite
χ	Magnetic susceptibility
ω_0	Larmor frequency
B_0	External magnetic field
CSIC	Consejo Superior de Investigación Científica
DLS	Dynamic Light Scattering
EBM	Endothelial basal medium
EGM-2	Endothelial growth medium
EPCs	Endothelial progenitor cells
EPGL	Ecole de Pharmacie Genève-Lausanne
FBS	Fetal bovine serum
$Fe(CO)_5$	Iron pentacarbonyl
$Fe(acac)_3$	Iron acetylacetonate
FGFs	Fibroblast growth factors
H_C	Coercitive field
ICMAB	Institut de Ciència de Materials de Barcelona
M_R	Magnetic remanence
MRI	Magnetic Resonance Imaging
MTT assay	3-(4,5-dimethylthiazol-2-yl)-2,5-diphenyltetrazolium bromide viability assay
MW-SPIONs	SPIONs synthesized by microwave-assisted non-sol gel route
OECs	Outgrowth endothelial cells
OH^-	Hydroxyl anion
PDGFs	Platelet-derived growth factors
pKa	Acidity constant dissociation
PLGA	poly(D,L-lactic-co-glycolic acid)
PVA	polyvinyl alcohol
RF	Radiofrequency pulse
$rhVEGF_{165}$	Recombinant human vascular growth factor-165
ROS	Reactive oxygen species
$r_{1/2}$	Longitudinal or transverse relaxivity
SPIONs	Superparamagnetic iron oxide nanoparticles
T_1	Longitudinal relaxation time
T_2	Transverse relaxation time
T_B	Blocking temperature
TD-SPIONs	SPIONs synthesized by thermal decomposition route
TMAOH	Tetramethylammonium hydroxide
UAB	Universitat Autònoma de Barcelona
VEGFs	Vascular endothelial growth factors

CHAPTER 1

SUPERPARAMAGNETIC IRON OXIDE NANOPARTICLES: A BRIEF INTRODUCTION

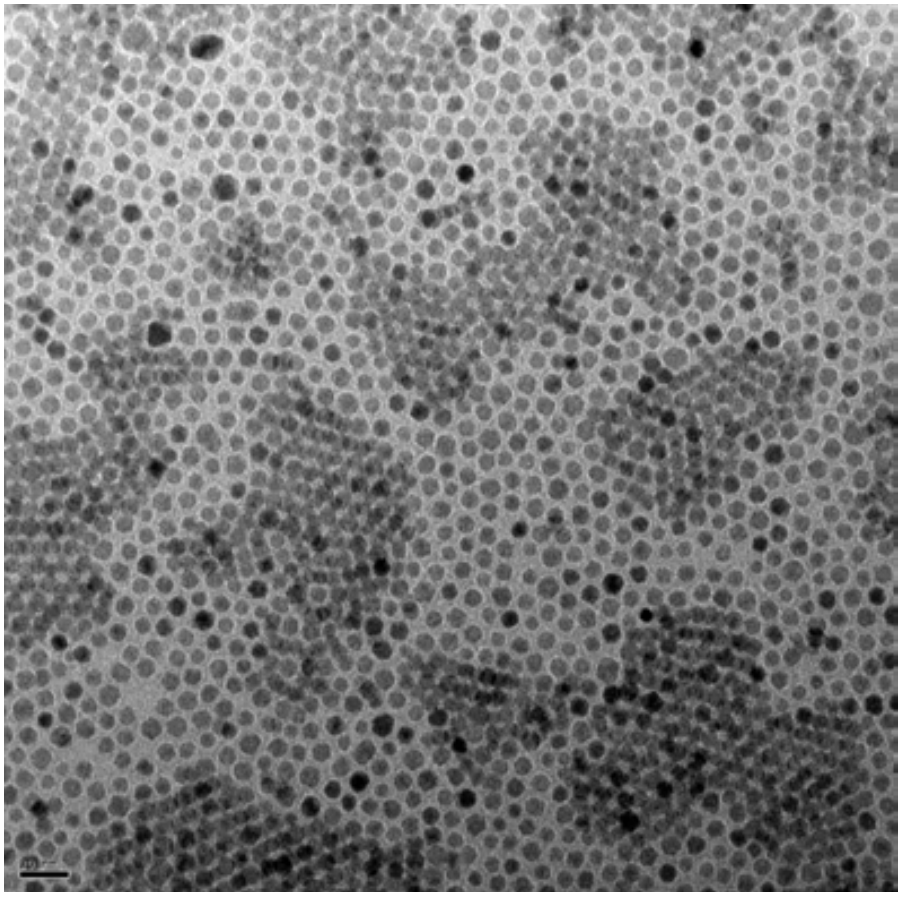

CHAPTER SUMMARY

This chapter includes some basic concepts on Nanotechnology and a brief explanation of magnetism and superparamagnetism. It also contains the description of iron oxide magnetic nanoparticles and the most common synthetic approaches found in literature. Finally, current SPION applications in biomedicine are mentioned.

CHAPTER INDEX

1.1. NANOTECHNOLOGY: GENERAL CONCEPTS

What is Nanotechnology?

Within the past few decades, the evolution of a number of new science disciplines and technologies has revolutionized many industrial sectors. Most notable among these are Biotechnology and more recently Nanotechnology. Several areas of Nanoscience including opto-electronics[1], sensing[2], medicine[3] and catalysis[4] are involved in the production of nanomaterials (nanoparticles, vesicles, surfactants, aerogels, nanotubes, etc.).

Nanotechnology has been defined as the "intentional design, characterization, production, and application of materials, structures, devices, and systems by controlling their size and shape in the nanoscale range (1 nm= 10^{-9} m)[5]."

What makes Nanotechnology and nanomaterials interesting for academies and industries? Intrinsic physical and chemical properties of materials at the nanoscale level change compared to their bulk form: nanomaterials have a much higher surface-volume ratio compared to their bulk and can show quantization effects due to the confinement of electrons in few nanometers. Specifically, this effect occurs in semiconductors when electrons and electron holes are squeezed into a dimension that approaches a critical quantum measurement, called the Bohr radius. A quantum dot is a sphere which confines in three dimensions, while a quantum wire confines in two dimensions. The control over dimensions at the nano-scale makes possible to tailor physical properties of the material as in semiconductor quantum dots[6]. Their electronic characteristics are closely related to their size and shape, in fact the band gap which determines the frequency range of the emitted light is inversely related to the size of a quantum dot. Therefore, the color of the emitted light can be shifted from red to blue by decreasing its size. Many applications for such nanostructured materials are currently under investigation as new transistors[7] and solar cells[8]. They are also studied as diagnostic agents for medical imaging[9].

Nanomaterials are similar in scale to biologic molecules and systems (Fig. 1), therefore Nanotechnology is potentially useful for medical applications. Nanoparticles can cross biological barriers and potentially distribute in all tissues.

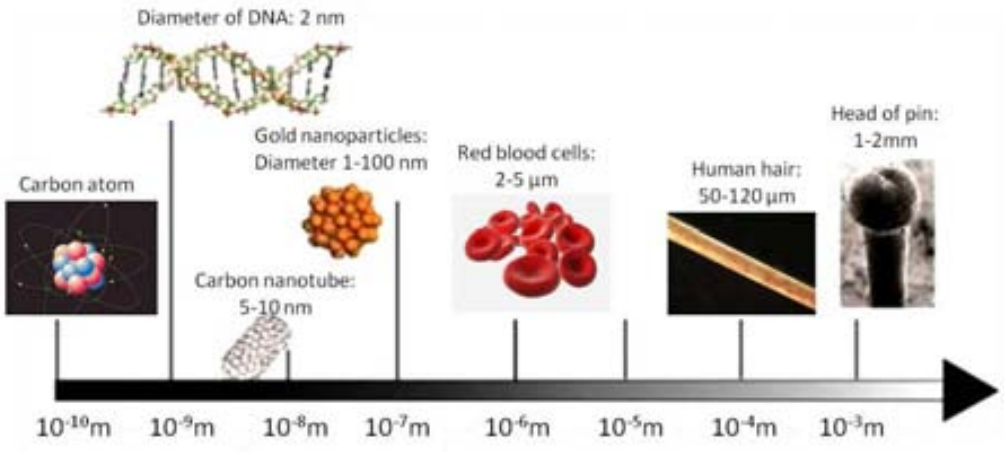

Figure 1. Image of dimensions in the range between 1 Å and 1 mm. Nano-objects and nano-devices are in the size range between 10 and 10^2 nm. Modified picture from website http://www.nanoscience.com/applications/education/.

The use of Nanotechnology for medical purposes (Nanomedicine) has grown exponentially over the past few decades. Nanomedicine aims to use properties and physical characteristics of nanomaterials for the diagnosis and treatment of diseases at the molecular level. Applications range from targeted therapy, *in vivo* imaging and *in vitro* diagnostics to biomaterials and active implants[10]. In the field of targeted therapy there are examples of nanoproducts already commercialized for anti-cancer treatments. In 1995 the first liposomal formulation of doxorubicin (Doxil®, USA) was launched: it demonstrates a more favorable pharmacokinetic profile compared to the free drug showing longer circulation time in the blood and less cardiotoxicity[11]. Another example, in the field of *in vitro* diagnostics, is colloidal gold which is used to test pregnancy and HIV by immunoassay (antibodies conjugated to nanoparticles and dyes)[12,13].

Magnetic nanoparticles are also used for cell sorting in clinical diagnosis (for instance Dynabeads®[14] for selecting and removing rare tumor cells or cell counting techniques), hyperthermia[15] and contrast agents[16]. The first product in this field with broad distribution in the market was Resovist® (an aqueous suspension containing iron oxide magnetic nanoparticles coated by carboxydextran), a specific contrast agent for Magnetic Resonance Imaging (MRI) of benign and malignant lesions as well as for proving or excluding multifocal liver lesions[17].

1.2. MAGNETIC MATERIALS

1.2.1. DEFINITIONS OF DIAMAGNETISM, PARAMAGNETISM AND FERROMAGNETISM

Some atoms have associated a magnetic moment because of the orbital and spin motions of electrons. Transition elements (principally iron-bearing) are the common materials possessing atoms with a magnetic moment, because of unfilled 3d electron orbitals.

When electrons occur in pairs they move in opposite directions behaving as dipoles and the resulting net magnetization is zero (diamagnetic materials). Alternatively, materials with some unpaired electrons have a net magnetization (paramagnetic and ferromagnetic materials). Paramagnetic materials have only a small net magnetization and are slightly attracted by an external magnetic field. When the field is removed they do not retain any magnetization.

Ferromagnetic materials have a large net magnetization and are strongly attracted by an external magnetic field. They get their strong magnetic properties due to the presence of magnetic domains. In these small regions, large numbers of atomic moments (atoms with unpaired electrons) (10^{12} to 10^{15}) are coupled together in a preferential direction (magnetic anisotropy). This alignment develops as the material develops its crystalline structure during solidification from the molten state. When the ferromagnetic material is placed in a strong magnetic field the material becomes magnetized: the magnetic domains are aligned with the magnetic field. When all of the domains are aligned, the material is said to be magnetically saturated (M_s) (Fig. 2).

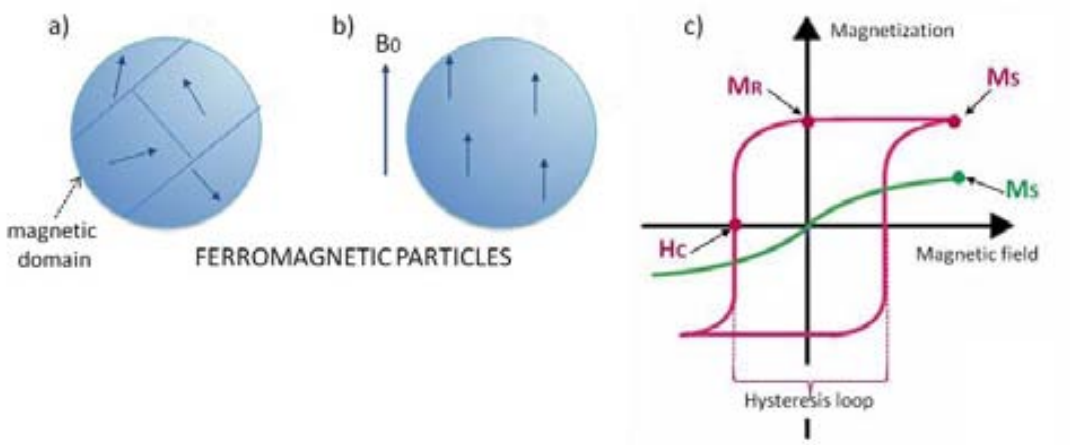

Figure 2. Scheme of magnetic domains in a ferromagnetic material: a) in absence of an applied magnetic field (B_0) magnetic domains of a ferromagnetic material are randomly aligned yielding a zero net magnetization; b) B_0 is applied and magnetic domains align themselves in the field direction and yield a net magnetization in the field direction; c) curves of magnetization versus applied magnetic field of a paramagnetic (green line) and a ferromagnetic (purple line) material. For the ferromagnetic material are highlighted the coercivity of the hysteresis loop (H_C) and the remnant magnetization (M_R). Paramagnetic material does not show nor H_C or M_R and its saturation magnetization (M_S) is lower than the M_S value of the ferromagnetic material.

Ferromagnets will tend to stay magnetized after the removal of the magnetic field. The fraction of the saturation magnetization which is retained when the field is removed is called the remnant magnetization of the material (M_R). Another important feature of the ferromagnetic materials is the tendency to "remember their magnetic history" which is called hysteresis (indicated by coercivity H_C). All ferromagnets have a maximum temperature where the ferromagnetic property disappears as a result of thermal agitation. This temperature is called the Curie temperature[18]. Iron, nickel, and cobalt are examples of ferromagnetic materials[19].

Coupling of adjacent atomic moments in a ferromagnetic material is the result of energy "exchange" of quantum mechanical nature. The Pauli Principle states that only one electron per atom tends to occupy a particular state defined by a set of four quantum numbers: the principal quantum number (n), the orbital angular momentum quantum number (l), the magnetic quantum number (m_l), and the electron spin quantum number (m_s). For an isolated atom of a transition element, the states occupied by electrons can be predicted. However, for a group of atoms within a crystal lattice, the situation becomes more complex.

Electron orbitals are "probability distributions" of electrons around a nucleus. Partial overlaps of electron "probability distributions" occur when atoms are packed together in a crystalline solid. These overlaps can develop so that electrons of adjacent atoms attempt to satisfy the Pauli Principle of both atoms simultaneously. The result is that electron states and magnetic moments of the adjacent atoms become strongly coupled. Thus, crystal structure and density of packing determine whether a solid containing transition elements is paramagnetic (no overlapping orbitals and no exchange coupling) or ferromagnetic (significant orbital overlap and resulting exchange coupling). In particular in ferromagnetic materials, energy exchange may produce either parallel or antiparallel exchange coupling. The sense of coupling depends on the transition element involved and on the solid crystal structure. Strictly speaking,

ferromagnetism refers to solids with parallel coupling of adjacent atomic magnetic moments (Fig. 3a). The situations depicted in Figure 3b and 3c involve antiparallel coupling between adjacent magnetic moments. If the atoms have equal magnetic moment, the resulting net magnetization is zero (Fig. 3b). This type of material is an antiferromagnet. If atoms of unequal magnetic moment are antiparallel, the resulting net magnetization points in the direction of the larger moment (Fig. 3c) and the material is called ferrimagnetic. Many of common iron oxides are ferrimagnetic[20].

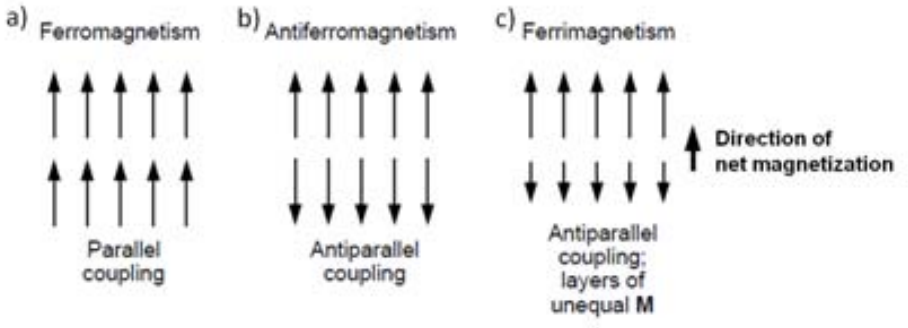

Figure 3. Possible couplings of atomic magnetic moments in a crystal structure: a) Parallel coupling generates ferromagnetic properties; b) antiparallel coupling of magnetic moments with same strength generates antiferromagnetic properties; c) antiparallel coupling of magnetic moments with different strength generates ferrimagnetic properties, with a resulting non-zero net magnetization[20].

1.2.2. DEFINITION OF SUPERPARAMAGNETISM

Superparamagnetism is a type of magnetism that occurs in small ferromagnetic nanoparticles (size less than 20 nm). These nanoparticles are single magnetic domains, because their small size renders the creation of domain walls and magnetic domains not thermodynamically preferred. In a simple approximation, the total magnetic moment of the nanoparticle can be regarded as one huge magnetic moment, composed by all the individual magnetic moments of the atoms which form the nanoparticle (Fig. 4).

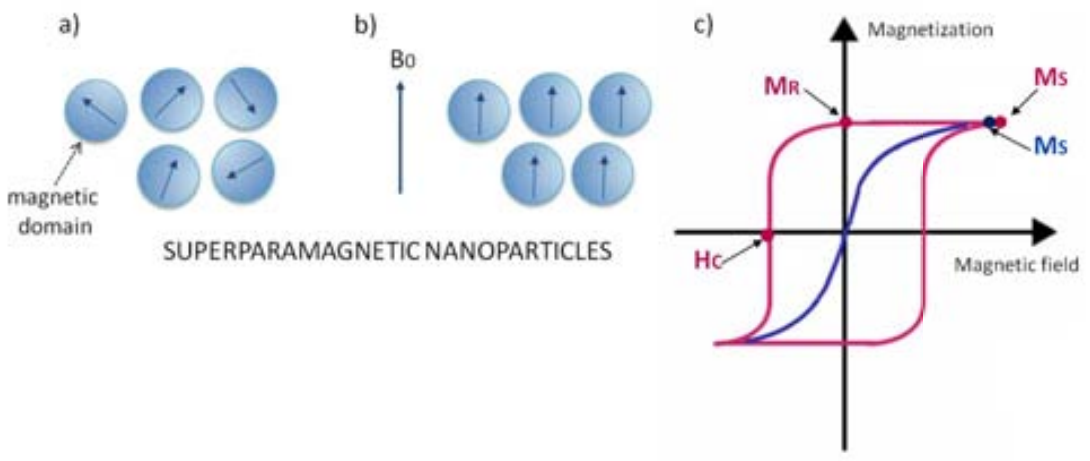

Figure 4. Scheme of magnetic domains for superparamagnetic nanoparticles: a) Superparamagnetic nanoparticles are single-domains, randomly oriented in the absence of a magnetic field; b) B_0 is applied and magnetic domains align themselves in the same direction of the field; c) curves of magnetization versus applied magnetic field of a superparamagnetic (blue line) and a ferromagnetic (purple line) material. For the ferromagnetic material are evidenced the coercivity and the remnant magnetization (M_R). Superparamagnetic material does not show nor H_C or M_R and its saturation magnetization (M_S) is as high as the ferromagnetic material.

For a superparamagnetic material the meantime between two flips of a magnetic moment (in the field direction and opposite to it) is called Néel relaxation time. The blocking temperature is the temperature above which the material is superparamagnetic because the spins have enough thermal energy to pass the energetic barrier of the Néel relaxation[21] (Fig. 5).

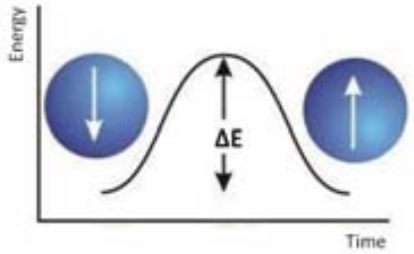

Figure 5. Graph of potential energy versus time. ΔE is the energetic barrier that spins (white arrows) have to surpass to flip between two antiparallel states.

The value of the blocking temperature of a superparamagnetic material can be known through zero-field-cooling (ZFC) and field-cooling (FC) measurements of magnetization versus temperature. During a FC measurement (in presence of a magnetic field) the magnetization decreases as temperature increases; while during a ZFC measurement (in absence of a magnetic field) the magnetization increases with the temperature until reaching the energetic barrier of the Néel relaxation at which starts decreasing. The temperature at the peak point of ZFC curve is the blocking temperature (Fig. 6)

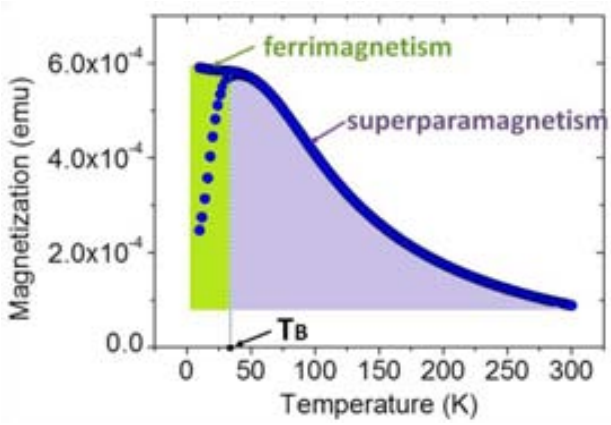

Figure 6. Zero field cooling-field cooling measurement of superparamagnetic iron oxide nanoparticles (SPIONs) in water at pH=7.4 (batch EC10-2). When the temperature decreases magnetic moments are blocked until the blocking temperature (T_B) is reached and the material behaves as ferrimagnet. When temperature increases over the blocking temperature magnetic moments are free again to move in the two states (parallel, antiparallel) and in presence or in absence of a magnetic field the net magnetization of the material goes to zero (superparamagnetism).

1.2.3. IRON OXIDE CRYSTALLINE PHASES

Iron oxides are ubiquitous in nature. Primary minerals containing iron ions are largely diffuse in Earth. Water dissolves primary minerals in soils with formation of hydroxide and oxide precipitates. Iron 3d electrons determine the electronic, magnetic and some spectroscopy properties for the iron oxides. In particular, the set of the five d orbitals is split by the electrostatic field of the surrounding ligands (negatively charged O^{2-}/OH^- ions), as a result iron d orbitals do not have the same energy. This fact influences thermodynamic and other

properties of the iron compounds, for instance Fe^{2+} occupies octahedral sites while Fe^{3+} has no preference for tetrahedral or octahedral coordination.

Iron oxides in natural settings are present in a variety of minerals in soils and rocks that range from well crystalline (hematite, goethite, lepidocrocite and maghemite/magnetite) to poorly crystalline (2-line and 6-line ferrihydrite, schwertmannite, feroxyhyte, and "green rust")[22] (Fig. 7). Among the well crystalline iron oxide phases, hematite (α-Fe_2O_3) and goethite (α-FeOOH) define the energetic and thermodynamic minimum of the system Fe_2O_3-H_2O, while magnetite is the most favorable phase in Fe^{2+} rich environments.

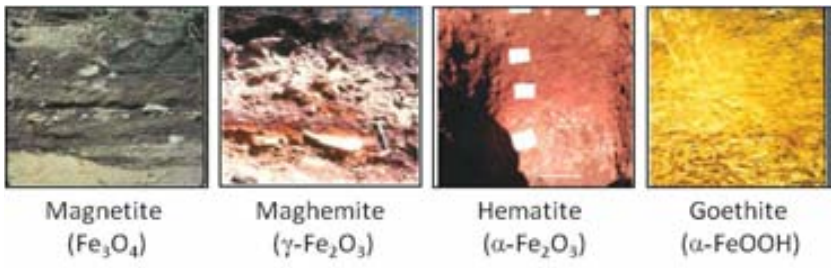

Figure 7. Soils containing different iron oxides. They are commonly used as pigments giving black, brown, red and yellow colors, respectively. Modified picture from Tartaj P. *Adv. Mater.* (2011) 23, 5243–5249.

Iron oxides with defined shape and size can be easily synthesized in laboratory. Moreover, Fe_2O_3 can be obtained as different polymorphs (materials which show same chemical composition but different crystalline structures, with different thermodynamic stabilities). It makes possible to convert an unstable phase to a more stable form by increasing the temperature, for instance, pure maghemite can be transformed to hematite by calcining at 500ºC during 3 hours[23].

Magnetite (Fe_3O_4) is the most magnetic of all minerals on Earth. It is a member of the spinel group (minerals which crystallize in cubic crystal systems) with standard formula $A(B)_2O_4$. The A and B represent different metal ions that occupy specific sites in the crystal structure. Magnetite Fe_3O_4 has a cubic inverse spinel structure (Fig. 8a) which consists of a cubic close packed array of ions where the Fe^{2+} occupy half of the octahedral sites and the Fe^{3+} are present in the remaining octahedral sites and the tetrahedral sites (Fig. 8b,c). In addition, magnetic moments of iron cations in A and B sublattices are antiparallel, therefore the magnetic contributions of both sets are not balanced and there is permanent magnetism.

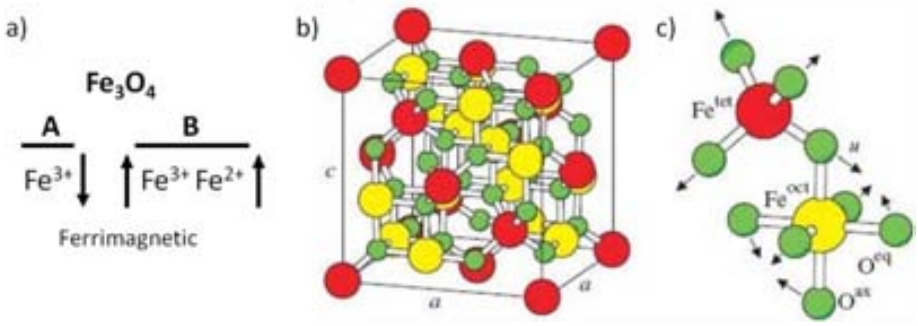

Figure 8. Magnetite crystal structure: a) scheme of inverse spinel structure of magnetite with A sublattice and B sublattice cations; b) Face-centred cubic spinel structure of magnetite; c) Magnification of one tetrahedron and one adjacent octahedron sharing an oxygen atom (green spheres). Large spheres labeled by Fe^{tet} (red spheres) and Fe^{oct} (yellow spheres) represent iron atoms in tetrahedrally and

octahedrally coordinated sublattices respectively. Modified picture from Friák M. et al. *New J. Phys*. (2007),5.

Maghemite (γ-Fe_2O_3) is an iron oxide that has the same structure as magnetite and can be obtained by controlled oxidation of magnetite at low temperatures (<200ºC). Maghemite is also a spinel ferrite, ferrimagnetic at room temperature. Iron ions are distributed in the octahedral and tetrahedral sites of the spinel structure, but maghemite differs from magnetite in that all iron ions are in the trivalent state. Cation vacancies compensate for the oxidation of Fe^{2+} cations. The vacancies ordering scheme can be closely related to the sample preparation method[24]. Grau-Crespo et al.[25] demonstrated that Fe^{3+} cations and vacancies tend to be ordered in the octahedral sites in a way that maximizes the homogeneity of the distribution and therefore minimizes the electrostatic energy of the crystal.

Nanocrystals of maghemite (and magnetite) are superparamagnetic at room temperature. So far, iron oxide especially in the trivalent oxidation state has shown relatively low biotoxicity[22]. These characteristics have significantly expanded the exploitation of iron oxides (maghemite/magnetite) in the emerging field of nanomedicine.

1.3. SYNTHESIS OF IRON OXIDE NANOPARTICLES

1.3.1. MECHANISMS OF NANOPARTICLE FORMATION

LaMer et al.[26] proposed that the formation of nanocrystals consists in a precipitation process which can be divided into two steps: nucleation followed by particle growth. First, it has to be considered that for a particular solvent, there is a given solubility for each type of solute. The addition of any excess of solute will result in precipitation and formation of nanocrystals. Similarly, in the case of nanoparticle formation, the solution must be supersaturated to start nucleation (formation of nuclei, or small crystals). During nanoparticle formation two kinds of nucleation processes may occur: homogeneous nucleation or heterogeneous nucleation. Homogenous nucleation takes place in the absence of a solid interface by combining solute molecules to produce nuclei. The heterogeneous nucleation occurs when nuclei collide and interact with a solid surface[27].

Ideally, uniformity in particle size distribution could be achieved through a unique and short nucleation period that generates all particles together, without further nucleation[28]. The induction of a single nucleation event, the so-called, burst nucleation, can be obtained by quickly increasing concentration of metal precursors to the critical saturation point (Fig. 9). Subsequently to the formation of nuclei, they grow via molecular addition, which relives the supersaturated step. When the concentration drops below the critical level, nucleation stops and particles continue to grow by molecular addition until the equilibrium concentration of the precipitated species is reached[27,28]. In the case of heterogeneous nucleation, nuclei continue to form after the first nucleation event and during particle growth, yielding a less uniform nanoparticle size distribution. Particle growth may happen via molecular addition (nuclei collision and combination), or through Ostwald ripening process[29], where at increasing temperatures small crystals dissolve and deposit on the surface of larger particles (Fig. 10).

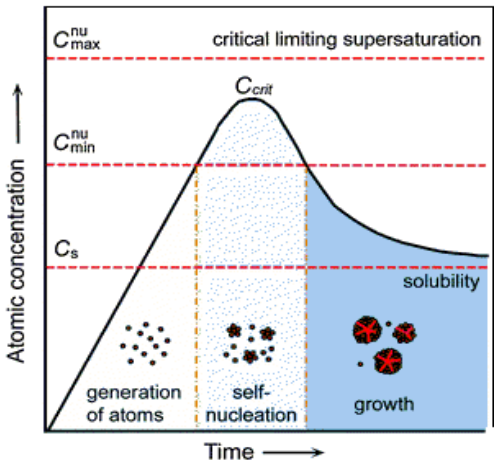

Figure 9. LaMer model describing nucleation and growth of nanocrystals as a function of reaction time and concentration of precursor atoms. Saturation concentration (C_s); critical concentration (C_{crit}) for the formation of nuclei. Picture from Sun Y. *Chem. Soc. Rev.* (2013), 42, 2497-2511.

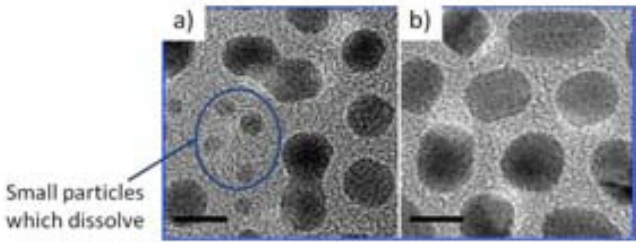

Figure 10. Particle growth by Ostwald ripening visualized by TEM images: a) FePt nanoparticles with two size populations, a smaller and a bigger one; b) small particle dissolve after heating up the sample and deposit on the surface of larger particles. Scale bar 5 nm.
Images from website http://english.nimte.cas.cn/rh/rp/201303/t20130311_99526.html.

1.3.2. METHODS OF SYNTHESIS: STATE OF THE ART

SPIONs can be obtained by chemical[30], physical[31] or biological methods[32]. In most cases SPION synthesis is performed by chemical routes as for instance co-precipitation[33,34], microemulsion[35,36], hydrothermal[37,38] and thermal decomposition[39,40]. Currently, commercialized SPIONs for clinical application as MRI contrast agents are predominately synthesized by an aqueous co-precipitation process in the presence of a coating material. In this hydrolytic process, the control of pH and the type of coating material are critical for particle formation and properties[41]. The most common co-precipitation method was developed by Massart[33] in which the addition of base to an aqueous solution of ferrous (Fe^{2+}) and ferric (Fe^{3+}) ions in a 1:2 stoichiometry produced a black precipitate of spherical magnetite (in absence of oxygen). Magnetization and crystallinity can vary vastly among synthesis methods, even within particles of similar size due to incorporation of impurities disrupting the crystal structure[42]. Typically, saturation magnetization values of magnetite nanoparticles obtained by these methods are in the range of 30–50 emu/g, which is much lower than the 90 emu/g reported for their bulk form[43,44]. The control over the crystal growth step during co-precipitation is the key step for producing monodisperse SPIONs. However, a precise control of particle size and shape is difficult to be achieved[24].

The microemulsion (water in oil: W/O) method, uses water droplets as nanoreactors in a continuous phase (oil) in the presence of surfactant molecules (e.g. Triton)[16,45]. In water-in-oil microemulsions, the aqueous phase is dispersed as microdroplets (typically 1–50 nm in diameter) surrounded by a monolayer of surfactant molecules in the continuous organic phase. The size of the nanoparticles can be controlled by controlling the size of water droplets[46]. By mixing two identical water-in-oil microemulsions containing the desired reactants, the microdroplets will continuously collide, coalesce, and break again, and finally give a precipitate[43]. The precipitate is separated by extraction with polar solvents (typically ethanol, acetone). The main drawback of this methods concerns the inefficiently scale-up, in fact microemulsion gives lower yields of SPIONs compared to other techniques and large volume of solvents are necessary for the synthesis of significant amounts of magnetic material.
Hydrothermal process exploits the solubility of inorganic materials in water at elevated temperatures (200ºC) and pressures that plays an essential role in the transformation of the precursor[27]. A typical system consists of metal precursor ($FeCl_3$), in water-ethanol solution[47]. During the synthesis of nanocrystals, parameters such as water pressure, water/polar solvent ratio and reaction time can be tuned to maintain a high simultaneous nucleation rate and good size distribution[48]. Via hydrothermal synthesis monodisperse SPIONs can be obtained with core diameter of 10 nm[49]. Recently, magnetite nanoparticle in the size range of 150-200 nm have been synthesized by hydrothermal synthesis using microwave heating[50].
Thermal decomposition in terms of size, morphology control and magnetic properties of nanoparticles seems the best method to date[43]. The developed approaches[39,51,52] consist in warming up (> 300ºC) the mixture made of metal organic precursor ($Fe(CO)_5$, $Fe(acac)_3$, Fe-oleate complex, etc.) in organic solvents with high boiling points in presence of organic surfactants (fatty acids) to induce precursor decomposition and subsequently burst nucleation. Sizes can be tuned by using different concentrations of precursor, reaction times and temperatures[53] or by a seed-mediated growth process (Fig. 11) which yields larger particles starting from smaller ones[54,55].

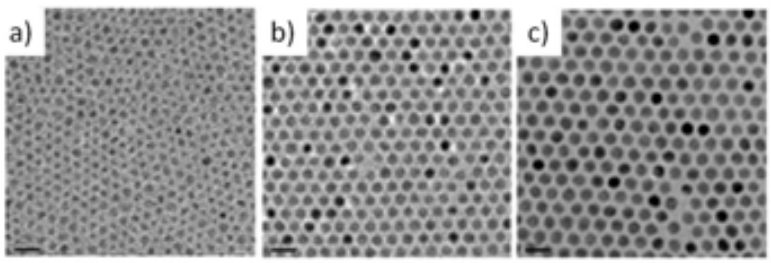

Figure 11. TEM images of SPIONs synthesized by thermal decomposition process, with seed-mediated growth. Monodisperse SPIONs with core size of a) 6; b) 8; c) 10 nm. Scale bar of 20 nm. Picture from Park J. *Angew. Chem. Int. Ed.* (2005), 44, 2872 –2877.

Particle surface reactivity is tuned by changing the chain length and concentration of the fatty acids: generally, the shorter the chain length, the faster the reaction rate is[43]. The main drawback of this approach is the use of hydrophobic surfactants (oleic acid and oleylamine) which make a hydrophobic coating on particle surface. Therefore particles synthesized by

thermal decomposition cannot be directly dispersed in water and they require additional steps before being used for biomedical purposes[51, 56,57].

Recently microwave-assisted reactions have been used for the synthesis of SPIONs at high temperatures (>200ºC) by dissolving metal precursors ($FeCl_3$, $Fe(acac)_3$, etc.) in high absorbing polar solvents (benzyl alcohol, diethylene glycol)[58]. Differently from traditional heating methods, the synthesis takes place in a short period of time (minutes) in a protect environment (microwave reactor). Particles with different shapes and narrow size distributions can be obtained[59]. The mechanism involved in particle formation is still not fully understood. An example of mechanism for monomer's formation has been proposed in the case of reaction between solvent (benzyl alcohol) and organometallic precursor[60]. The main advantages of this technique are short reaction time, easy scale-up and low environmental impact.

1.4. BIOMEDICAL APPLICATIONS OF SPIONs

SPIONs are of great interest in biomedical research and in the health sector industry because they can be visualized by means of Magnetic Resonance Imaging (MRI), acting as contrast agents. SPIONs increment the relaxation rate of opportunely excited proton nuclei, providing excellent contrast in soft tissues (see further details in annex of chapter 1, paragraph 1.5.1). During the last 20 years SPIONs have been extensively studied as contrast agents for diagnosis of cancer or cardiovascular diseases through MRI[61,62]. Due to multiple MRI methods (pulse sequences) to generate contrast in the images, several anatomical, physiological and metabolic parameters can be measured almost simultaneously and under physiological conditions[63].

In general, to achieve long time circulation *in vivo,* contrast agents should have hydrophilic coating and particle size less than 100 nm, so that they can evade the reticuloendothelial system[64,65] (particle uptake by monocytes and macrophages in liver, spleen, lymph nodes and bone marrow). Nanoparticles with large surface area/volume ratios tend to agglomerate, adsorb plasma proteins and are quickly cleared by macrophages in the reticuloendothelial system before they can reach the target zone[34] (Table 1).

Table 1. Particle removal from human cardiovascular system in function of their sizes. Data taken from Arruebo M. *Nanotoday* (2007), 2 (3).

		Size	System/Organ
Particle removal	Tight-junction capillaries	< 1 nm	Central nervous system, blood-brain barrier
	Continuous capillaries	- 6 nm	Tissues such as muscle, skin, and lung
	Fenestrated capillaries	- 50-60 nm	Kidney, intestine, and some endocrine and exocrine glands
	Sinusoidal capillaries	- 100-1000 nm	Liver, spleen, and bone marrow

In cancer diagnosis it has been found that SPIONs passively accumulate at the tumor site due to the presence of leaky vasculature (blood vessels with high permeability) as well as macrophage uptake[16,65]. The efficiency of SPION uptake by macrophage and imaging contrast is highly dependent on both circulation time and surface charge. It has been demonstrated that larger nanoparticles (150 nm hydrodynamic diameter) such as the dextran coated SPIONs

(Endorem®) are removed from blood circulation through the reticuloendothelial system and non-specifically taken up by Kupffer cells in the healthy liver, allowing for hepatic imaging[66]. Furthermore, the absence of Kupffer cells in malignancies has been exploited to allow for enhanced accuracy in distinguishing between healthy and diseased tissue through SPION endowed contrast[67]. Dextran coated SPIONs of hydrodynamic size less than 30 nm (Sinerem®) can be uptaken by macrophages in lymph-nodes, allowing for their non-invasive imaging[68]. Moreover, macrophage uptake of SPIONs at sites of atherosclerosis could indicate the diseased area, leading to earlier diagnosis and treatment [69,70]. SPIONs can be used for tracking the biodistribution of cells *in vivo*[71]. These studies typically involve the transplantation of SPION-loaded cells into living subjects and tracking cell migration[72,73] by MRI. Additionally, stem cells loaded with SPIONs can be guided toward a zone of interest through an external magnetic field for non-invasive cellular therapies and tissue regeneration purposes[74,75,76].

SPIONs can also be used to direct drugs or biological molecules (DNA, genes, proteins, etc.) toward specific tissues (targeted drug delivery)[77,78]. For this purpose SPIONs can be attached at the surface, homogenously or heterogeneously dispersed within the matrix of nano/microspheres[79,80], nano/microcapsules[81,82] or liposomes. Such magnetic carriers are studied for the targeted delivery of chemotherapeutic agents[83,84,85] and anti-inflammatory[86] molecules among others.

Finally, another important biomedical application of SPIONs is their use in hyperthermia treatments. Magnetic particles can be heated by application of a high frequency magnetic field (around 500 kHertz) because of their magnetic hysteresis loss. In particular, magnetic particles in a tumor site and placed within an oscillating magnetic field, will heat up to a temperature dependent on the magnetic properties of the material, the strength of the magnetic field, the frequency of oscillation and the cooling capacity of the blood flow in the tumor site. Cancer cells are destroyed at temperature close to 43°C, whereas normal cells can survive. There are numerous *in vitro*[87,88,89] and *in vivo* studies[90,91,92] which demonstrate SPION efficacy in cancer treatment by hyperthermia.

Currently, most of SPION formulations available in the market are used for cell separation, targeting, sensing, enzyme immobilization, immunoassays and detection systems[16]. Some examples of companies that commercialize SPIONs are listed in the Table 2.

Table 2. Examples of commercialized SPIONs. Table from Mahmoudi M. *Adv Drug Del Rev* (2011), 24-26.

Company	Reference	Applications
TurboBeads	www.turbobeads.com	Efficient magnetic separation
European Institute of Science	www.biotechniques.com	Hyperthermia
Magnabeat Inc.	www.magnabeat.com	Separation of many different bio-substances
nanoTherics Ltd.	www.nanotherics.com	Magnetic gene transfection
SEPMAG technologies.	www.sepmag.eu	Large volume magnetic separation systems
Magforce	www.magforce.de	Hyperthermia
AMAG Pharmaceuticals (Advanced Magnetics)	www.amagpharma.com	MRI contrast agents; Diagnosis of cardiovascular disease and cancer
Estapor	www.estapor.com	Application of magnetic microspheres in immunoassays
Miltenyi Biotec	www.miltenyibiotec.com	Reagents and instruments development for use in immunology, cell and molecular biology, bioinformatics, and stem cell technologies
Invitrogen and Dynal Biotech (bought by Invitrogen in 2005)	www.invitrogen.com	In vitro diagnostics, protein, cell and biomolecular purification and separation

1.5. ANNEX OF CHAPTER 1

In this annex are described the main principles of the magnetic resonance imaging (MRI) and contrast agent properties.

1.5.1. PRINCIPLES OF MAGNETIC RESONANCE IMAGING (MRI) AND DEFINITIONS OF T_1, T_2,T_2*

Magnetic resonance imaging (MRI) applied to medical diagnosis is based on the difference in nuclear magnetic relaxations of the water protons in tissues.

Considering the structure of the atom, protons and neutrons make up the nucleus. Protons and neutrons have associated intrinsic quantum properties (spins), which can results in a non-zero magnetic moment (it happens for atoms like ^{1}H, ^{13}C). In an applied magnetic field (B_0) all nuclei are forced to align themselves with B_0 resulting in a net magnetization M. Nuclei are in processing movement around the applied magnetic field with a frequency equal to Larmor ω_0 (Fig. 12).

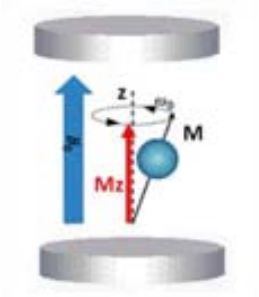

Figure 12. Precession orbit of a nucleus in the applied magnetic field B_0 with Larmor frequency ω_0. The net magnetization resulting is M which is aligned with B_0. Mz is the component of M along z axis.

When a suitable "resonance frequency" (RF pulse) in the radiofrequency range ($\omega = \omega_0$) is applied, nuclei pass from the initial lower energy state to an excited one at higher energy and the component of net magnetization M along z axis (M_z) is reduced because nuclei move in the xy plane (see Fig. 13). When the radiofrequency pulse is switched off, the relaxation of the spins, back to the lower state, produces an amount of radiofrequency (RF emitted) proportional to the received RF pulse. This emission can be measured after suitable amplification and converted to an electrical signal used to build up anatomical tomographies. The process is called Nuclear Magnetic Resonance (NMR) and lasts up to completed recovery of net magnetization along z axis (Fig. 13).

The total relaxation of the magnetic moments is mainly composed by two relaxation processes: T_1 the longitudinal relaxation time and T_2 the transversal relaxation time (Fig. 13).

- T_1 (spin-lattice relaxation time) is the characteristic time of spins, forced to move in the xy plane by the RF pulse, to align themselves around the z-axis. A variety of relaxation mechanisms allow nuclear spins to exchange energy with their surroundings (the lattice) allowing the spin populations to equilibrate. T_1 relaxation is the recovery of the signal in the z axis.
- T_2 (spin-spin relaxation time) is the characteristic time for loss of phase coherence of the spins in the x, y plane. It arises from interactions between the spins which depend on

temperature, mobility of spins, presence of large molecules, magnetic field inhomogeneities or other outside interferences.

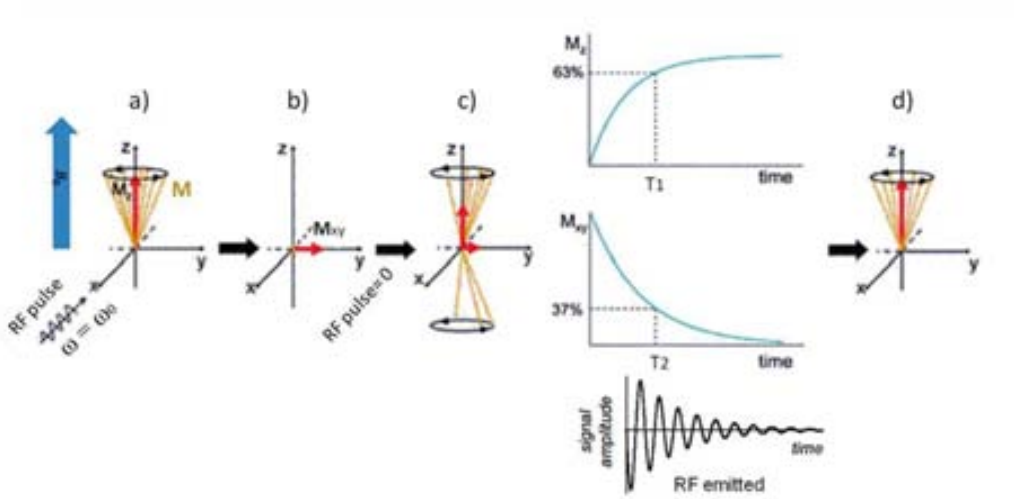

Figure 13. Nuclear magnetic resonance of a nucleus in the applied magnetic field B_0. a) The net magnetization (M) is aligned with B_0. A radiofrequency pulse (RF pulse) is switched on; b) the component along the z axis of net magnetization (M_z) is reduced while it is increasing in the x,y plane (M_{xy}); c) the RF pulse is switched off and net magnetization in the x,y plane (M_{xy}) is reducing while is recovering its orientation along z axis. This process is known as nuclear spin relaxation and occurs when the excited spins return in the equilibrium state by emitting a radiofrequency (RF emitted). This emission can be tracked by measuring signal amplitude variations in time; d) final state: the net magnetization has recovered its orientation along z axis. Modified picture from Lee N. et al. *Chem. Soc. Rev.* (2012) 41, 2575-2589.

As before mentioned, in an idealized system, all nuclei in a given chemical environment move in a precession orbit with the same frequency (Larmor ω_0) in presence of a magnetic field B_0. However, in real systems, there are minor differences in chemical environment which can lead to a distribution of resonance frequencies around the ideal. Over time, it can lead to a dispersed distribution of magnetic spin vectors, and loss of signal. Spin vectors "dephase" due to magnetic field inhomogeneity which is not a true "relaxation" process. The corresponding transverse relaxation time is thus T_2^* and is described by: $\frac{1}{T2*} = \frac{1}{T2} + \gamma Bs$ where γBs represents the relaxation by the field inhomogeneities and is called susceptibility effect[61].

In a T_1 or T_2 weighted MRI image the presence of bright or dark areas are depending on the proton density which is the concentration of protons in the tissue in the form of water and macromolecules (proteins, fat, etc) (Fig. 14). Moreover the contrast of the MR images can be manipulated by changing the pulse sequence parameters: number, strength, and timing of the RF and gradient pulses.

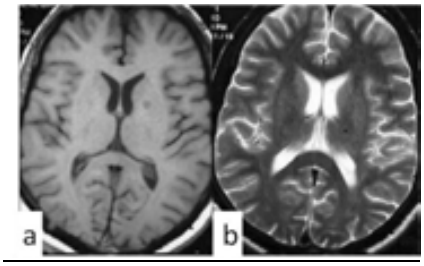

Figure 14. Magnetic resonance imaging (human brain), showing T_1-weighted (a), T_2-weighted (b) images. Picture from Malhotra H. S. *Ann Indian Acad Neurol.* (2012), 15(2):151-7.

How do contrast agents act? Magnetic resonance contrast agents act by selectively reducing T_1/T_2 relaxation times of tissue water through interactions between electron spins of the metal-containing contrast agent and water protons in tissue[93,94]. **A contrast agent increases the nuclear magnetic relaxation rate of its surrounding protons and improves the signal contrast (Fig. 15)**.

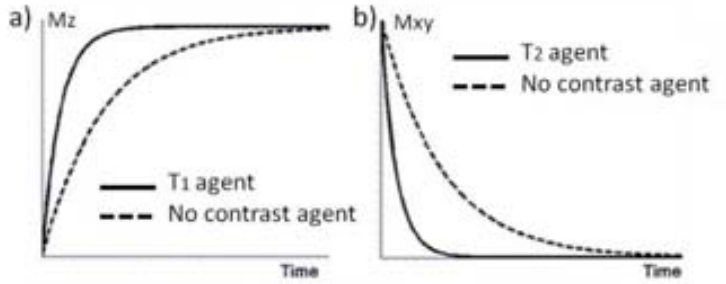

Figure 15. Effects of contrast agents on T_1, T_2 relaxation times. a) Relaxation time of the nuclear magnetization along z axis (Mz) is shortened by the presence of T_1 contrast agent; b) relaxation time of the nuclear magnetization in plane x,y (Mxy) is shortened by the presence of T_2 contrast agent.

Contrast enhancement effect is measured by the relaxation rate, $R = 1/T$ (s^{-1}) and the relaxivity, r = R versus iron concentration ($mM^{-1}\ s^{-1}$). The higher relaxivity corresponds to a more efficient contrast effect. Complexes of paramagnetic metal ions (such as Gd^{3+}) serve as a T_1 contrast agent, while magnetic nanoparticles are generally used as a T_2 contrast agent. The application of iron oxide nanoparticles as T_1 or T_2 contrast agents is strictly related to their size and colloidal stability in aqueous media. It has been demonstrated that iron oxide magnetic nanoparticles of 6 nm in size, in dispersed state can act as T_1 contrast agent[56].

1.5.2. DEFINITION OF MAGNETIC SUSCEPTIBILITY

Magnetic susceptibility is an intrinsic property of a magnetic material which indicates the sensitivity to a magnetic field. It depends on the number of spins per atoms or ions of the crystal structure and the more are the magnetic moments the more sensitive is the material to the magnetic field. For that susceptibility increases with both particle and aggregate size. When a material is placed in a magnetic field B_0, a magnetization (magnetic moment per unit volume) M is induced in the material which is related to B_0 by $M = \kappa B_0$, where κ is called the volume susceptibility. Since B_0 and M have the same dimensions, κ is dimensionless. A more useful parameter is the molar susceptibility χ_m, defined by

$$\chi_m = \kappa V_m = \kappa\ M/\rho$$

where: V_m is the molar volume of the substance, M the molar mass, and ρ the mass density. When the cgs system is used, the customary units for χ_m are $cm^3\ mol^{-1}$; the corresponding SI units are $m^3\ mol^{-1}$.

Substances that have no unpaired electron orbital or spin angular momentum generally have negative values of χ_m and are called diamagnetic. Their molar susceptibility varies only slightly with temperature. Substances with unpaired electrons, which are termed paramagnetic, have positive χ_m and show much stronger temperature dependence.

1.6. CHAPTER REFERENCES

1. Grätzel, M., Mesoporous oxide junctions and nanostructured solar cells. *Current Opinion in Colloid & Interface Science* **1999,** *4* (4), 314-321.
2. Motornov, M.; Roiter, Y.; Tokarev, I.; Minko, S., Stimuli-responsive nanoparticles, nanogels and capsules for integrated multifunctional intelligent systems. *Progress in Polymer Science* **2010,** *35* (1–2), 174-211.
3. Veiseh, O.; Gunn, J. W.; Zhang, M., Design and fabrication of magnetic nanoparticles for targeted drug delivery and imaging. *Advanced drug delivery reviews* **2010,** *62* (3), 284-304.
4. Shylesh, S.; Schünemann, V.; Thiel, W. R., Magnetically Separable Nanocatalysts: Bridges between Homogeneous and Heterogeneous Catalysis. *Angewandte Chemie International Edition* **2010,** *49* (20), 3428-3459.
5. Kim, B. Y. S.; Rutka, J. T.; Chan, W. C. W., Nanomedicine. *New England Journal of Medicine* **2010,** *363* (25), 2434-2443.
6. Klimov, V. I.; Mikhailovsky, A. A.; Xu, S.; Malko, A.; Hollingsworth, J. A.; Leatherdale, C. A.; Eisler, H.; Bawendi, M. G., Optical gain and stimulated emission in nanocrystal quantum dots. *Science* **2000,** *290* (5490), 314-7.
7. Liu, Y.; Tolentino, J.; Gibbs, M.; Ihly, R.; Perkins, C. L.; Liu, Y.; Crawford, N.; Hemminger, J. C.; Law, M., PbSe quantum dot field-effect transistors with air-stable electron mobilities above 7 cm2 V(-1) s(-1). *Nano letters* **2013,** *13* (4), 1578-87.
8. Plass, R.; Pelet, S.; Krueger, J.; Grätzel, M.; Bach, U., Quantum Dot Sensitization of Organic−Inorganic Hybrid Solar Cells. *The Journal of Physical Chemistry B* **2002,** *106* (31), 7578-7580.
9. Michalet, X.; Pinaud, F. F.; Bentolila, L. A.; Tsay, J. M.; Doose, S.; Li, J. J.; Sundaresan, G.; Wu, A. M.; Gambhir, S. S.; Weiss, S., Quantum dots for live cells, in vivo imaging, and diagnostics. *Science* **2005,** *307* (5709), 538-44.
10. Lobatto, M. E.; Fuster, V.; Fayad, Z. A.; Mulder, W. J., Perspectives and opportunities for nanomedicine in the management of atherosclerosis. *Nature reviews. Drug discovery* **2011,** *10* (11), 835-52.
11. https://www.doxil.com/.
12. Wagner, V.; Dullaart, A.; Bock, A. K.; Zweck, A., The emerging nanomedicine landscape. *Nature biotechnology* **2006,** *24* (10), 1211-7.
13. www.nanopartz.com/.
14. http://www.lifetechnologies.com/ch/en/home/brands/product-brand/dynal.html?cid=fl-dynal.
15. Petrovich, Z.; Langholz, B.; Gibbs, F. A.; Sapozink, M. D.; Kapp, D. S.; Stewart, R. J.; Emami, B.; Oleson, J.; Senzer, N.; Slater, J.; Astrahan, M., Regional hyperthermia for advanced tumors: A clinical study of 353 patients. *International Journal of Radiation Oncology*Biology*Physics* **1989,** *16* (3), 601-607.
16. Mahmoudi, M.; Sant, S.; Wang, B.; Laurent, S.; Sen, T., Superparamagnetic iron oxide nanoparticles (SPIONs): development, surface modification and applications in chemotherapy. *Advanced drug delivery reviews* **2011,** *63* (1-2), 24-46.
17. Wang, Y.-X. J., Superparamagnetic iron oxide based MRI contrast agents: Current status of clinical application. *Quantitative Imaging in Medicine and Surgery* **2011,** *1* (1), 35-40.
18. http://hyperphysics.phy-astr.gsu.edu/.
19. http://www.ndt-ed.org/EducationResources/.
20. Butler, R., Ferromagnetic minerals. In *Paleomagnetism: magnetic domains to geologic terranes*, Electronic ed.; 2004; pp 16-20.
21. Pankhurst, Q. A.; Connolly, J.; Jones, S. K.; Dobson, J., Applications of magnetic nanoparticles in biomedicine. *Journal of Physics D: Applied Physics* **2003,** *36* (13), R167.
22. Tartaj, P.; Morales, M. P.; Gonzalez-Carreno, T.; Veintemillas-Verdaguer, S.; Serna, C. J., The iron oxides strike back: from biomedical applications to energy storage devices and photoelectrochemical water splitting. *Advanced materials* **2011,** *23* (44), 5243-9.
23. Sidhu, P. S., Transformation of trace element -substituted maghemite to hematite *Clays and Clay Minerals* **1988,** *36* (1), 31-38.

24. Laurent, S.; Forge, D.; Port, M.; Roch, A.; Robic, C.; Vander Elst, L.; Muller, R. N., Magnetic iron oxide nanoparticles: synthesis, stabilization, vectorization, physicochemical characterizations, and biological applications. *Chemical reviews* **2008,** *108* (6), 2064-110.

25. Grau-Crespo, R.; Al-Baitai, A. Y.; Saadoune, I.; Leeuw, N. H. D., Vacancy ordering and electronic structure of γ - Fe 2 O 3 (maghemite): a theoretical investigation. *Journal of Physics: Condensed Matter* **2010,** *22* (25), 255401.

26. LaMer, V. K.; Dinegar, R. H., Theory, Production and Mechanism of Formation of Monodispersed Hydrosols. *Journal of the American Chemical Society* **1950,** *72* (11), 4847-4854.

27. Burda, C.; Chen, X.; Narayanan, R.; El-Sayed, M. A., Chemistry and properties of nanocrystals of different shapes. *Chemical reviews* **2005,** *105* (4), 1025-102.

28. Park, J.; Joo, J.; Kwon, S. G.; Jang, Y.; Hyeon, T., Synthesis of monodisperse spherical nanocrystals. *Angewandte Chemie (International ed. in English)* **2007,** *46* (25), 4630-60.

29. Voorhees, P. W., The theory of Ostwald ripening. *J Stat Phys* **1985,** *38* (1-2), 231-252.

30. Xu, C.; Sun, S., New forms of superparamagnetic nanoparticles for biomedical applications. *Advanced drug delivery reviews* **2013,** *65* (5), 732-43.

31. Basak, S.; Chen, D.-R.; Biswas, P., Electrospray of ionic precursor solutions to synthesize iron oxide nanoparticles: Modified scaling law. *Chemical engineering science* **2007,** *62* (4), 1263-1268.

32. Bhargava, A.; Jain, N.; Barathi, M.; Akhtar, M.; Yun, Y.-S.; Panwar, J., Synthesis, characterization and mechanistic insights of mycogenic iron oxide nanoparticles. *Journal of nanoparticle research* **2013,** *15* (11).

33. Massart, R., Preparation of aqueous magnetic liquids in alkaline and acidic media. *Magnetics, IEEE Transactions on* **1981,** *17* (2), 1247-1248.

34. Gupta, A. K.; Gupta, M., Synthesis and surface engineering of iron oxide nanoparticles for biomedical applications. *Biomaterials* **2005,** *26* (18), 3995-4021.

35. Chin, A. B.; Yaacob, I. I., Synthesis and characterization of magnetic iron oxide nanoparticles via w/o microemulsion and Massart's procedure. *Journal of Materials Processing Technology* **2007,** *191* (1–3), 235-237.

36. Okoli, C.; Sanchez-Dominguez, M.; Boutonnet, M.; Järås, S.; Civera, C.; Solans, C.; Kuttuva, G. R., Comparison and Functionalization Study of Microemulsion-Prepared Magnetic Iron Oxide Nanoparticles. *Langmuir : the ACS journal of surfaces and colloids* **2012,** *28* (22), 8479-8485.

37. Ge, S.; Shi, X.; Sun, K.; Li, C.; Uher, C.; Baker, J.; Banaszak Holl, M.; Orr, B., Facile Hydrothermal Synthesis of Iron Oxide Nanoparticles with Tunable Magnetic Properties. *The journal of physical chemistry. C* **2009,** *113* (31), 13593-13599.

38. Takami, S.; Sato, T.; Mousavand, T.; Ohara, S.; Umetsu, M.; Adschiri, T., Hydrothermal synthesis of surface-modified iron oxide nanoparticles. *Materials letters* **2007,** *61* (26), 4769-4772.

39. Hyeon, T.; Lee, S.; Park, J.; Chung, Y.; Na, H., Synthesis of Highly Crystalline and Monodisperse Maghemite Nanocrystallites without a Size-Selection Process. *Journal of the American Chemical Society* **2001,** *123* (51), 12798-12801.

40. Peng, S.; Wang, C.; Xie, J.; Sun, S., Synthesis and Stabilization of Monodisperse Fe Nanoparticles. *Journal of the American Chemical Society* **2006,** *128* (33), 10676-10677.

41. Babes, L.; Denizot, B.; Tanguy, G.; Le Jeune, J. J.; Jallet, P., Synthesis of Iron Oxide Nanoparticles Used as MRI Contrast Agents: A Parametric Study. *Journal of colloid and interface science* **1999,** *212* (2), 474-482.

42. Sun, C.; Lee, J. S.; Zhang, M., Magnetic nanoparticles in MR imaging and drug delivery. *Advanced drug delivery reviews* **2008,** *60* (11), 1252-65.

43. Lu, A. H.; Salabas, E. L.; Schuth, F., Magnetic nanoparticles: synthesis, protection, functionalization, and application. *Angewandte Chemie (International ed. in English)* **2007,** *46* (8), 1222-44.

44. Cheng, F.-Y.; Su, C.-H.; Yang, Y.-S.; Yeh, C.-S.; Tsai, C.-Y.; Wu, C.-L.; Wu, M.-T.; Shieh, D.-B., Characterization of aqueous dispersions of Fe3O4 nanoparticles and their biomedical applications. *Biomaterials* **2005,** *26* (7), 729-738.

45. Santra, S.; Tapec, R.; Theodoropoulou, N.; Dobson, J.; Hebard, A.; Tan, W., Synthesis and Characterization of Silica-Coated Iron Oxide Nanoparticles in Microemulsion: The Effect of Nonionic Surfactants. *Langmuir : the ACS journal of surfaces and colloids* **2001,** *17* (10), 2900-2906.

46. Müller, B. W.; Müller, R. H., Particle size distributions and particle size alterations in microemulsions. *Journal of Pharmaceutical Sciences* **1984,** *73* (7), 919-922.

47. Deng, H.; Li, X.; Peng, Q.; Wang, X.; Chen, J.; Li, Y., Monodisperse magnetic single-crystal ferrite microspheres. *Angewandte Chemie (International ed. in English)* **2005,** *44* (18), 2782-5.

48. Xuan, S.; Wang, Y.-X.; Yu, J.; Leung, K., Tuning the Grain Size and Particle Size of Superparamagnetic Fe3O4Microparticles. *Chemistry of materials* **2009,** *21* (21), 5079-5087.

49. Wang, X.; Zhuang, J.; Peng, Q.; Li, Y., A general strategy for nanocrystal synthesis. *Nature* **2005,** *437* (7055), 121-4.

50. Khollam, Y. B.; Dhage, S. R.; Potdar, H. S.; Deshpande, S. B.; Bakare, P. P.; Kulkarni, S. D.; Date, S. K., Microwave hydrothermal preparation of submicron-sized spherical magnetite (Fe3O4) powders. *Materials Letters* **2002,** *56* (4), 571-577.

51. Sun, S.; Zeng, H.; Robinson, D. B.; Raoux, S.; Rice, P. M.; Wang, S. X.; Li, G., Monodisperse MFe2O4 (M = Fe, Co, Mn) nanoparticles. *Journal of the American Chemical Society* **2004,** *126* (1), 273-9.

52. Park, J.; An, K.; Hwang, Y.; Park, J. G.; Noh, H. J.; Kim, J. Y.; Park, J. H.; Hwang, N. M.; Hyeon, T., Ultra-large-scale syntheses of monodisperse nanocrystals. *Nature materials* **2004,** *3* (12), 891-5.

53. Roca, A. G.; Morales, M. P.; O'Grady, K.; Serna, C. J.; Ogrady, K., Structural and magnetic properties of uniform magnetite nanoparticles prepared by high temperature decomposition of organic precursors. *Nanotechnology* **2006,** *17* (11), 2783-2788.

54. Sun, S.; Zeng, H., Size-Controlled Synthesis of Magnetite Nanoparticles. *Journal of the American Chemical Society* **2002,** *124* (28), 8204-8205.

55. Park, J.; Lee, E.; Hwang, N. M.; Kang, M.; Kim, S. C.; Hwang, Y.; Park, J. G.; Noh, H. J.; Kim, J. Y.; Park, J. H.; Hyeon, T., One-nanometer-scale size-controlled synthesis of monodisperse magnetic iron oxide nanoparticles. *Angewandte Chemie (International ed. in English)* **2005,** *44* (19), 2873-7.

56. Taboada, E.; Rodríguez, E.; Roig, A.; Oró, J.; Roch, A.; Muller, R. N., Relaxometric and Magnetic Characterization of Ultrasmall Iron Oxide Nanoparticles with High Magnetization. Evaluation as Potential T1 Magnetic Resonance Imaging Contrast Agents for Molecular Imaging. *Langmuir : the ACS journal of surfaces and colloids* **2007,** *23* (8), 4583-4588.

57. Mejias, R.; Perez-Yague, S.; Roca, A. G.; Perez, N.; Villanueva, A.; Canete, M.; Manes, S.; Ruiz-Cabello, J.; Benito, M.; Labarta, A.; Batlle, X.; Veintemillas-Verdaguer, S.; Morales, M. P.; Barber, D. F.; Serna, C. J., Liver and brain imaging through dimercaptosuccinic acid-coated iron oxide nanoparticles. *Nanomedicine (London, England)* **2010,** *5* (3), 397-408.

58. Bilecka, I.; Niederberger, M., Microwave chemistry for inorganic nanomaterials synthesis. *Nanoscale* **2010,** *2* (8), 1358-1374.

59. Baghbanzadeh, M.; Carbone, L.; Cozzoli, P. D.; Kappe, C. O., Microwave-Assisted Synthesis of Colloidal Inorganic Nanocrystals. *Angewandte Chemie International Edition* **2011,** *50* (48), 11312-11359.

60. Bilecka, I.; Elser, P.; Niederberger, M., Kinetic and Thermodynamic Aspects in the Microwave-Assisted Synthesis of ZnO Nanoparticles in Benzyl Alcohol. *ACS nano* **2009,** *3* (2), 467-477.

61. Na, H. B.; Song, I. C.; Hyeon, T., Inorganic Nanoparticles for MRI Contrast Agents. *Advanced materials* **2009,** *21* (21), 2133-2148.

62. Sosnovik, D.; Nahrendorf, M.; Weissleder, R., Magnetic nanoparticles for MR imaging: agents, techniques and cardiovascular applications. *Basic Research in Cardiology* **2008,** *103* (2), 122-30.

63. Himmelreich, U.; Dresselaers, T., Cell labeling and tracking for experimental models using Magnetic Resonance Imaging. *Methods* **2009,** *48* (2), 112-124.

64. Shubayev, V.; Pisanic, T.; Jin, S., Magnetic nanoparticles for theragnostics. *Advanced drug delivery reviews* **2009,** *61* (6), 467-77.

65. Arruebo, M.; Fernández-Pacheco, R.; Ibarra, M. R.; Santamaría, J., Magnetic nanoparticles for drug delivery. *Nano Today* **2007,** *2* (3), 22-32.

66. Brigger, I.; Dubernet, C.; Couvreur, P., Nanoparticles in cancer therapy and diagnosis. *Advanced drug delivery reviews* **2002,** *54* (5), 631-51.

67. Hundt, W.; Petsch, R.; Helmberger, T.; Reiser, M., Signal changes in liver and spleen after Endorem administration in patients with and without liver cirrhosis. *European radiology* **2000,** *10* (3), 409-16.

68. Sigal, R.; Vogl, T.; Casselman, J.; Moulin, G.; Veillon, F.; Hermans, R.; Dubrulle, F.; Viala, J.; Bosq, J.; Mack, M.; Depondt, M.; Mattelaer, C.; Petit, P.; Champsaur, P.; Riehm, S.; Dadashitazehozi, Y.; de Jaegere, T.; Marchal, G.; Chevalier, D.; Lemaitre, L.; Kubiak, C.; Helmberger, R.; Halimi, P., Lymph node metastases from head and neck squamous cell carcinoma: MR imaging with ultrasmall

superparamagnetic iron oxide particles (Sinerem MR) -- results of a phase-III multicenter clinical trial. *European radiology* **2002,** *12* (5), 1104-13.

69. Thorek, D. L.; Chen, A. K.; Czupryna, J.; Tsourkas, A., Superparamagnetic iron oxide nanoparticle probes for molecular imaging. *Annals of biomedical engineering* **2006,** *34* (1), 23-38.

70. Morishige, K.; Kacher, D.; Libby, P.; Josephson, L.; Ganz, P.; Weissleder, R.; Aikawa, M., High-resolution magnetic resonance imaging enhanced with superparamagnetic nanoparticles measures macrophage burden in atherosclerosis. *Circulation* **2010,** *122* (17), 1707-15.

71. Arbab, A. S.; Liu, W.; Frank, J. A., Cellular magnetic resonance imaging: current status and future prospects. *Expert review of medical devices* **2006,** *3* (4), 427-39.

72. Jendelova, P.; Herynek, V.; Urdzikova, L.; Glogarova, K.; Kroupova, J.; Andersson, B.; Bryja, V.; Burian, M.; Hajek, M.; Sykova, E., Magnetic resonance tracking of transplanted bone marrow and embryonic stem cells labeled by iron oxide nanoparticles in rat brain and spinal cord. *Journal of neuroscience research* **2004,** *76* (2), 232-43.

73. Kyrtatos, P. G.; Lehtolainen, P.; Junemann-Ramirez, M.; Garcia-Prieto, A.; Price, A. N.; Martin, J. F.; Gadian, D. G.; Pankhurst, Q. A.; Lythgoe, M. F., Magnetic tagging increases delivery of circulating progenitors in vascular injury. *JACC. Cardiovascular interventions* **2009,** *2* (8), 794-802.

74. Sykova, E.; Jendelova, P.; Herynek, V., Magnetic resonance imaging of stem cell migration. *Methods in molecular biology* **2011,** *750*, 79-90.

75. Li, Q.; Tang, G.; Xue, S.; He, X.; Miao, P.; Li, Y.; Wang, J.; Xiong, L.; Wang, Y.; Zhang, C.; Yang, G. Y., Silica-coated superparamagnetic iron oxide nanoparticles targeting of EPCs in ischemic brain injury. *Biomaterials* **2013,** *34* (21), 4982-92.

76. Carenza, E.; Barcelo, V.; Morancho, A.; Levander, L.; Boada, C.; Laromaine, A.; Roig, A.; Montaner, J.; Rosell, A., In vitro angiogenic performance and in vivo brain targeting of magnetized endothelial progenitor cells for neurorepair therapies. *Nanomedicine* **2014,** *10* (1), 225-34.

77. Connolly, J.; Dobson, J.; Pankhurst, Q. A.; Jones, S. K., Applications of magnetic nanoparticles in biomedicine. *Journal of physics. D, Applied physics* **2003,** *36* (13), R167-R181.

78. Schopf, B.; Neuberger, T.; Schöpf, B.; Hofmann, H.; Hofmann, M.; von Rechenberg, B., Superparamagnetic nanoparticles for biomedical applications: Possibilities and limitations of a new drug delivery system. *Journal of magnetism and magnetic materials* **2005,** *293* (1), 483-496.

79. Ma, W.; Xu, S.; Li, J.; Guo, J.; Lin, Y.; Wang, C., Hydrophilic dual-responsive magnetite/PMAA core/shell microspheres with high magnetic susceptibility and ph sensitivity via distillation-precipitation polymerization. *Journal of polymer science. Part A, Polymer chemistry* **2011,** *49* (12), 2725-2733.

80. Choi, W. S.; Koo, H.; Chang, S.; San Choi, W.; Park, J.-H.; Kim, D.-Y.; Velev, O., Emulsion-Based Synthesis of Reversibly Swellable, Magnetic Nanoparticle-Embedded Polymer Microcapsules. *Chemistry of materials* **2006,** *18* (14), 3308-3313.

81. Mishra, B.; Patel, B. B.; Tiwari, S., Colloidal nanocarriers: a review on formulation technology, types and applications toward targeted drug delivery. *Nanomedicine: Nanotechnology, Biology and Medicine* **2010,** *6* (1), 9-24.

82. Arias, J. L.; Gallardo, V.; Gomez Lopera, S. A.; GÃ³mez Lopera, S. A.; Plaza, R. C.; Delgado, A. V., Synthesis and characterization of poly(ethyl-2-cyanoacrylate) nanoparticles with a magnetic core. *Journal of controlled release* **2001,** *77* (3), 309-21.

83. Jain, T.; Richey, J.; Strand, M.; Leslie Pelecky, D.; Flask, C.; Labhasetwar, V., Magnetic nanoparticles with dual functional properties: drug delivery and magnetic resonance imaging. *Biomaterials* **2008,** *29* (29), 4012-21.

84. Nasongkla, N.; Bey, E.; Ren, J.; Ai, H.; Khemtong, C.; Guthi, J.; Chin, S.-F.; Sherry, A. D.; Boothman, D.; Gao, J., Multifunctional polymeric micelles as cancer-targeted, MRI-ultrasensitive drug delivery systems. *Nano letters* **2006,** *6* (11), 2427-30.

85. Alexiou, C.; Schmid, R.; Jurgons, R.; Kremer, M.; Wanner, G.; Bergemann, C.; Huenges, E.; Nawroth, T.; Arnold, W.; Parak, F., Targeting cancer cells: magnetic nanoparticles as drug carriers. *European biophysics journal* **2006,** *35* (5), 446-50.

86. Butoescu, N.; Seemayer, C.; Foti, M.; Jordan, O.; Doelker, E., Dexamethasone-containing PLGA superparamagnetic microparticles as carriers for the local treatment of arthritis. *Biomaterials* **2009,** *30* (9), 1772-80.

87. Fortin, J. P.; Gazeau, F.; Wilhelm, C., Intracellular heating of living cells through Neel relaxation of magnetic nanoparticles. *European biophysics journal : EBJ* **2008,** *37* (2), 223-8.

88. Fortin, J. P.; Wilhelm, C.; Servais, J.; Menager, C.; Bacri, J. C.; Gazeau, F., Size-sorted anionic iron oxide nanomagnets as colloidal mediators for magnetic hyperthermia. *Journal of the American Chemical Society* **2007,** *129* (9), 2628-35.

89. Guardia, P.; Di Corato, R.; Lartigue, L.; Wilhelm, C.; Espinosa, A.; Garcia Hernandez, M.; Gazeau, F.; Manna, L.; Pellegrino, T., Water-soluble iron oxide nanocubes with high values of specific absorption rate for cancer cell hyperthermia treatment. *ACS nano* **2012,** *6* (4), 3080-91.

90. Laurent, S.; Dutz, S.; Haefeli, U.; Mahmoudi, M.; HÃ¤feli, U., Magnetic fluid hyperthermia: focus on superparamagnetic iron oxide nanoparticles. *Advances in colloid and interface science* **2011,** *166* (1-2), 8-23.

91. Jordan, A.; Scholz, R.; Maier-Hauff, K.; van Landeghem, F. K.; Waldoefner, N.; Teichgraeber, U.; Pinkernelle, J.; Bruhn, H.; Neumann, F.; Thiesen, B.; von Deimling, A.; Felix, R., The effect of thermotherapy using magnetic nanoparticles on rat malignant glioma. *Journal of neuro-oncology* **2006,** *78* (1), 7-14.

92. Jordan, A.; Maier-Hauff, K.; Wust, P.; Johannsen, M., Nanoparticles for Thermotherapy. In *Nanotechnologies for the Life Sciences*, Wiley-VCH Verlag GmbH & Co. KGaA: 2007.

93. Ho, D.; Sun, X.; Sun, S., Monodisperse Magnetic Nanoparticles for Theranostic Applications. *Accounts of Chemical Research* **2011,** *44* (10), 875-882.

94. Wang, Y. X.; Hussain, S. M.; Krestin, G. P., Superparamagnetic iron oxide contrast agents: physicochemical characteristics and applications in MR imaging. *European radiology* **2001,** *11* (11), 2319-31.

CHAPTER 2

SUPERPARAMAGNETIC IRON OXIDE NANOPARTICLES (SPIONs): SYNTHESIS AND CHARACTERIZATIONS IN WATER AND IN BIOLOGICAL MEDIA

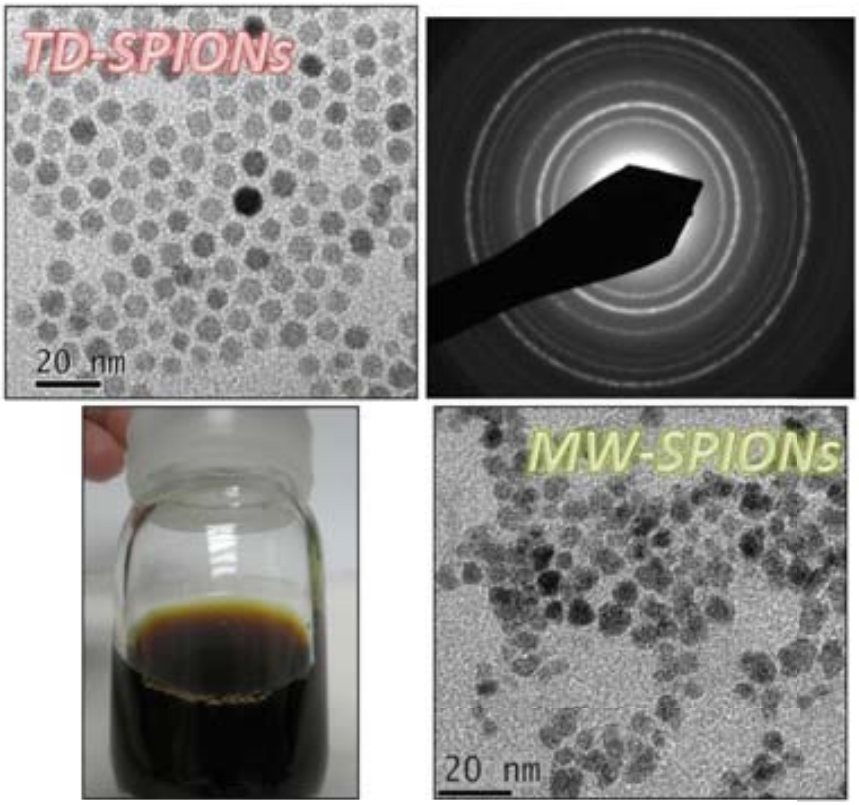

CHAPTER SUMMARY

To succeed in cellular uptake and cellular magnetic labeling SPIONs should be monodisperse, with high saturation magnetization and susceptibility. They should also be smaller than a critical size (typically 20 nm) in order to present superparamagnetism at room temperature. All these properties are related to particle crystal structure and they can vary very much with the synthetic process. For instance, in the coprecipitation method which is run at room temperature, saturation magnetization value of maghemite nanoparticles is in the range of 30–50 emu/g, which is lower than values obtained using the thermal decomposition route and much lower than 90 emu/g reported for their bulk form[1]. **For that in this thesis we selected two pathways to synthesize maghemite nanoparticles at high temperature in order to obtain material with high saturation magnetization and narrow size distribution**.

The first selected method is the thermal decomposition, the second is the microwave assisted non hydrolytic sol-gel process. We compared the magnetic properties, surface reactivity and colloidal stability of the SPION dispersions obtained by these two synthetic approaches aiming to achieve formulations for a safe and effective cellular labeling.

The choice of thermal decomposition was motivated by the easily attainment of monodisperse nanoparticles, with very precise size control and high experimental reproducibility. Nevertheless, nanoparticles synthesized by this method require laborious purification steps in order to be dispersible in water at physiological pH.

The choice of microwave route was motivated by the interest in a more straightforward and environmentally friendly approach to obtain magnetic nanoparticles dispersible in water.

SPIONs are of great interest in Nanomedicine, still efforts have to be made to achieve a more efficient fabrication and "transfer" from the lab bench to the market[2]. Referring to it, some of the commercialized products for cancer diagnosis have been recently withdrawn from the market. For instance, Feridex I.V.® (also known as Endorem® and Ferumoxide®) was discontinued by AMAG Pharma in November 2008 and Resovist® (also known as Cliavist®) was approved for the European market in 2001, but its production was abandoned in 2009.

CHAPTER INDEX

pag.

2.1. SYNTHESIS BY THERMAL DECOMPOSITION TECNIQUE

2.1.1. REACTION MECHANISM: GENERAL CONCEPTS

Thermal decomposition of iron precursors is one of the most extensive synthetic processes used to obtain monodisperse particles with high crystallinity[3,4,5]. Thermal decomposition route is preferred when precise size control, high crystallinity, and high magnetic saturation magnetization are required.

Generally, the reaction is performed by heating up the mixture of the organic precursor, solvent and surfactants. In the first step the temperature reaches the value at which organo-metallic decomposition started; in the second step the temperature increases up to the solvent boiling point. The high temperature allows surfactant molecules to be reversible linked to nanoparticle surface.[3] Oleic acid and oleylamine are two well known surfactants used in SPIONs synthesis. Oleic acid forms stronger interactions than oleylamine with the metal cations of the nanoparticle surface through the carboxylate groups.[6] The significance of the carboxylic acid headgroup in facilitating uniform nucleation and growth of γ-Fe_2O_3 nanocrystals is clarified by substituting methyl oleate instead of oleic acid and keeping unchanged all other conditions. The products from this reaction observed by TEM exhibit poor yield and high polydispersity.[7] It has been demonstrated that oleylamine acts as capping agent and reducing agent. More recently oleylamine has been used alone in the thermal decomposition synthesis in the place of 1,2-hexadecanediol.[8]

The final material consist of magnetic nanoparticles covered by organic surfactants which have to be exchanged with more hydrophilic molecules (tetramethylammonium hydroxide TMAOH, sodium citrate) before being used for biomedical purposes (Fig. 1)[9,10,11].

2.1.2. SYNTHESIS OF IRON OXIDE NANOPARTICLES BY THERMAL DECOMPOSITION

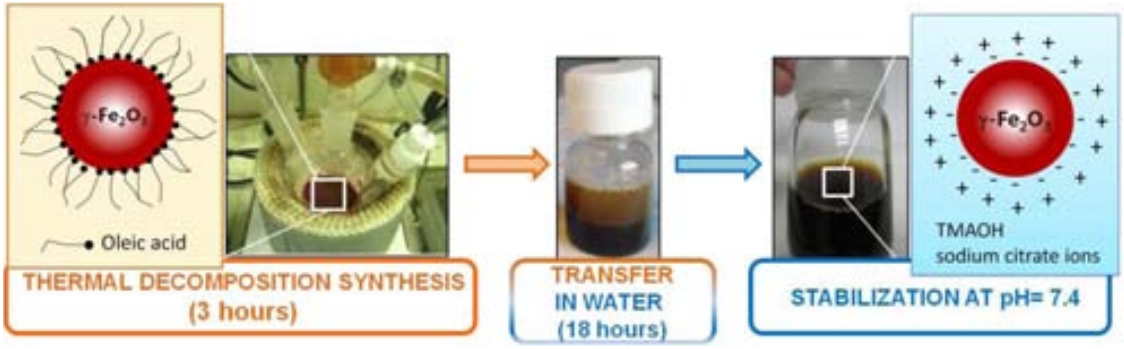

Figure 1. Schematic description of the thermal decomposition process used for TD-SPIONs synthesis. The first step is the formation of magnetic material in the high temperature boiling solvent, in presence of organic surfactants. The second step is the ligand exchange with the anionic surfactant TMAOH which takes place during 18 h. In the last step there is the separation and stabilization at pH=7.4 of the colloidal aqueous phase.

Following the protocol reported elsewhere[3,12] in a three well neck $Fe(acac)_3$ (2 mmol),1,2-hexadecanediol (10 mmol), oleic acid (6 mmol), oleylamine (6 mmol), benzylether (20 mL) were mixed and magnetically stirred under a flow of argon (Fig. 1). The mixture was heated to 200 °C for 2 h and then heated to reflux (300 °C) for 1 h. The black-colored mixture was cooled

down to room temperature. Under ambient conditions, ethanol (40 mL) was added and a black material was precipitated and separated with centrifugation. The separated product was dispersed in hexane in the presence of oleic acid (0.05 mL) and oleylamine (0.05 mL) and another centrifugation was applied to remove any residue. These steps were repeated twice to achieve nanoparticles with optimal monomodal size distribution. Finally stable nanoparticle hexane dispersion was obtained with an average yield of 79% and nanoparticle mean size of 6.2 nm ± 0.68 nm (mean value of 6 different batches).

To use SPIONs for cellular internalization we need to transfer them in water at physiological pH. This procedure is performed through the addition of two different stabilizers in two consecutive steps: first, tetramethyl ammonium hydroxide (TMAOH), an anionic surfactant with OH^- groups and $NH(Me)^{4+}$ which create a double charged shell around SPIONs surface, was selected as first stabilizer during the ligand exchange process (see discussion, next paragraph), that gives SPION aqueous suspension with basic pH. Then, sodium citrate, a well known chelating agent with three carboxylate groups, is used as stabilizer in the second step of particle stabilization in water when the electrostatic charges of the TMAOH which previously avoided particle agglomeration have been "removed" by pH neutralization with strong acid (nitric acid, HNO_3) to reach acceptable pH values for *in vitro* experiments.

In the first step of the ligand exchange process our system of nanoparticles covered by oleic acid and oleylamine in organic solvent is mixed in water with a basic aqueous solution of TMAOH. The high temperature of thermal decomposition reaction allows surfactant molecules to be reversible linked to nanoparticle surface, without being covalently attached. To achieve the highest amount of particles transferred in aqueous phase we tried different ratios γ-Fe_2O_3 : TMAOH solutions. The best ratio was 1:10 with a starting concentration of nanoparticles in hexane of 45 mM of γ-Fe_2O_3 (see next paragraph for further details). In that way the yield of the ligand exchange procedure is increased up to 90% (Table 1). The elemental microanalysis at 1200 °C in oxygen atmosphere reveals that only a small amount of organic surfactant is still present after ligand exchange process (see annex of chapter 2, paragraph 2.7.1. for further details).

Table 1. Different conditions of maghemite ligand exchange process to disperse particles from hexane to water. The best option was find to be the batch d. In the picture it is shown the final aqueous colloidal suspension at pH=7.4.

Batch	γ-Fe_2O_3 (mM) in Hex	γ-Fe_2O_3 : TMAOH molar ratio	Yield of transfer	Concentration of γ-Fe_2O_3 at pH= 7.4
a	17	1:10	around 50%	Less than 10 mM
b	25	1:08	around 50%	Less than 10 mM
c	41	1:20	81%	Amount of TMAOH too high
d	45	1:10	89%	Concentration ≥ 10 mM

Briefly, 3 mL of SPIONs in hexane (45 mM) are added to 3 mL of TMAOH 0.45 M and the mixture is kept for 18h under magnetic stirring. After that, the mixture is separated into two phases: the upper phase (yellow colored) mainly contains hexane and oleic acid, the lower one (brown colored) nanoparticles coated by TMAOH. SPIONs are precipitated with acetone (40 mL) and centrifuged (4500 rpm with centrifuge rotor radius 7 cm, 20 minutes), the supernatant is discarded and 20 µL of TMAOH 25% are added to 5 mL of sterile water to ensure colloidal stability. The pH of SPIONs dispersion is lowered from 12 to 7.4 using HNO_3 (0.1 M) and to ensure electrostatic repulsions between nanoparticles during neutralization of the OH^- groups, sodium citrate (4 mM) with volume ratio 1:1 is also added to the SPIONs. The iron concentration of the final colloidal suspension at pH= 7.4 for a typical batch is 10 mM (0.55 mg/mL). The amounts of TMAOH and nitric acid have a major influence in determining particle negative zeta potential for the electrostatic stabilization of the suspension. NO^{3-} anions, besides OH^- participate in the interaction with the metal cations of the particle surface.[13] In the next chapter it is described how different salt concentrations can affect cellular viability.

The batch was finally sterilized by filtering (0.2 µm pore size membranes, Millipore) before being used for cell cultures.

Particle core composition is made of maghemite/magnetite phase as confirmed by electron diffraction and particle core measures around 6 nm (Fig. 2).

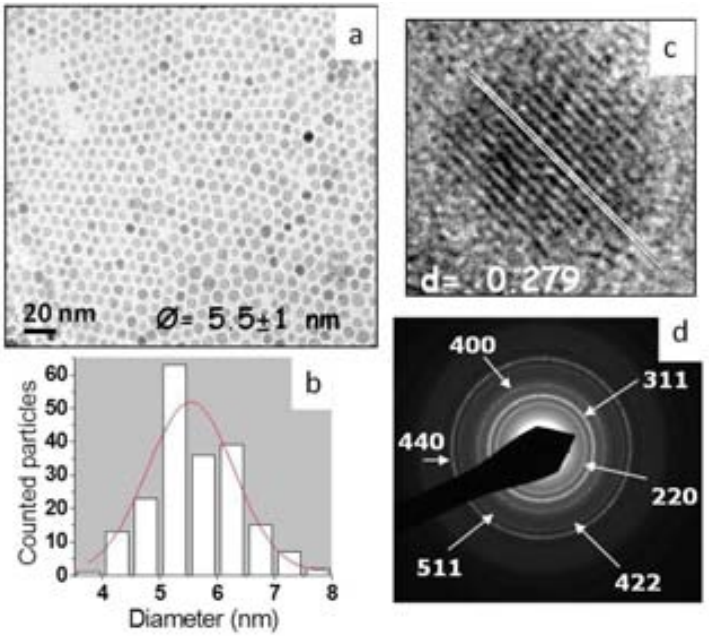

Figure 2. Nanoparticle core characterizations a) TEM image of TD-SPIONs; b) Histogram of particle size distribution fitted to a Gaussian function; c) High resolution (HR) TEM showing crystalline planes; d) Electron diffraction pattern indicating magnetite/maghemite material.

Quality of nanoparticles in terms of crystallinity has a major influence on their magnetic properties and in particular on their saturation magnetization values and their permittivity at low fields.

Sample aliquots of aqueous colloidal suspension are analyzed to check the superparamagnetic properties and the magnetization values. The magnetic properties of the nanoparticles are

evaluated by magnetization versus magnetic field measurements at 5 K and 300 K and by zero-field-cooling (ZFC), field-cooling (FC) temperature dependent magnetization curves using a 50 Oe field. Figure 3a shows a typical magnetization curve at 300 K for superparamagnetic nanoparticles in which neither remnant magnetization (magnetization at zero field, M_R) nor coercivity (hysteresis loop, H_C) are observed. Saturation magnetization at room temperature is 64 emu/g of Fe_2O_3 which indicates the high degree of nanoparticle crystallinity. As expected, saturation magnetization is higher at 5 K and the material presents ferromagnetic features (M_R, H_C). Superparamagnetism is also proved by the ZFC-FC magnetization curves (Fig. 3b). The ZFC magnetization increases with temperature until reaching the maximum value corresponding to the blocking temperature (T_B) which is 47 K for the TD-SPIONs (Fig. 3b). Above this temperature, the thermal energy becomes larger than magnetic anisotropy energy barrier and the nanoparticles enter in the superparamagnetic domain.

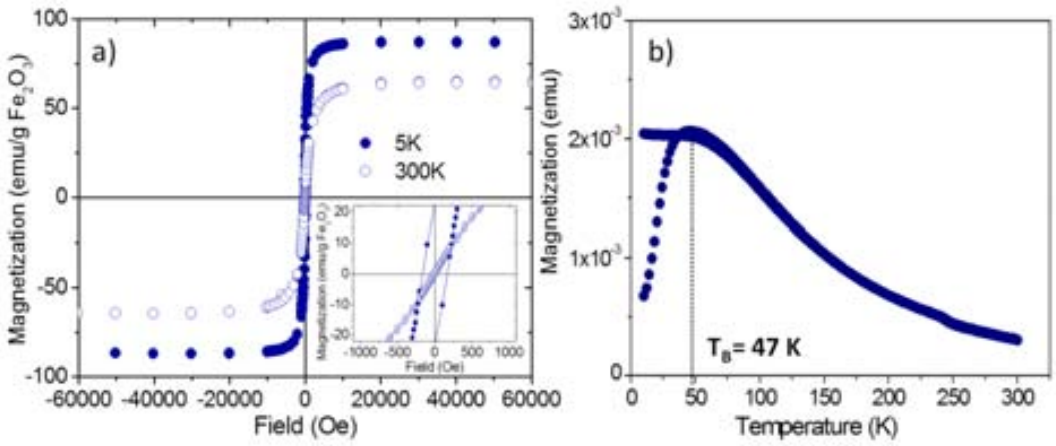

Figure 3. Nanoparticle magnetic characterization: a) TD-SPIONs magnetization curves at 5K and 300K as function of the magnetic applied field. b) Zero field cooled and Field cooled magnetization at 50 Oe.

2.1.3. BATCHES OF SPIONs USED FOR CELL LABELING: EFFECT OF TMAOH CONCENTRATION

In the literature it is reported that high nitrate concentration in combination with ammonium may induce cell toxicity[14] and for this reason nitric acid was added in low amounts. Tables 2 and 3 show SPIONs batches synthesized by thermal decomposition using two different conditions of ligand exchange process. The batches differ from one another in the molar ratios γ-Fe_2O_3:TMAOH 1:10 and 1:20 which indicate the amount of anionic surfactant exceeding nanoparticle concentration during the ligand exchange process. The presence of TMAOH which is an anionic basic surfactant is crucial to guarantee the colloidal stability of the magnetic nanoparticle dispersion during the pH adjustments from basic to neutral pH. The resulting batches with higher content of TMAOH and nitric acid also show in water at pH=7.4 more negative zeta potentials (Table 2). During *in vitro* experiments we found that endothelial progenitor cells labeled with TD-SPIONs showed enhanced ROS (reactive oxygen species) production compared to non-treated cells (see paragraph 3.3.3. chapter 3) and cytotoxicity at high TD-SPIONs concentrations (see paragraph 3.3.1.). These effects may be related to the iron

oxide nanoparticles themselves and also to the high TMAOH and nitric acid concentrations. For that reason we started to synthesize nanoparticles batches with lower ion amounts (Table 3).

Table 2. First batches were prepared using high concentration of nitric acid and γ-Fe_2O_3:TMAOH 1:20. Concentrations of nitric acid and sodium citrate at 100 μg/mL of iron. DLS diam= hydrodynamic diameter measured by DLS, PD%= polydispersity %, Z pot= zeta potential, [HNO_3]= nitric acid concentration, [sodium citrate]= sodium citrate concentration.

	DLS diam (nm)	PD%	Z pot (mV)	[HNO_3] (mg/mL)	γ- Fe_2O_3:TMAOH	[Sodium citrate] (mg/mL)
EC4-3	20	19	-48	6.2	1:20	0.04
EC5	31	29	-52	6.3	1:20	0.06
EC6-2	26	27	-49	6.2	1:20	0.06

Table 3. Batches prepared using low concentration of nitric acid and γ-Fe_2O_3:TMAOH 1:10. Concentrations of nitric acid and sodium citrate at 100 μg/mL of iron. DLS diam= hydrodynamic diameter measured by DLS, PD%= polydispersity %, Z pot= zeta potential, [HNO_3]= nitric acid concentration, [sodium citrate]= sodium citrate concentration.

	DLS diam (nm)	PD%	Z pot (mV)	[HNO_3] (mg/mL)	γ- Fe_2O_3:TMAOH	[Sodium citrate] (mg/mL)
EC10-2	30	25	-37	3.2	1:10	0.05
EC11	31	23	-30	4.9	1:10	0.07

2.2. SYNTHESIS BY MICROWAVE IRRADIATION

2.2.1. REACTION MECHANISM: GENERAL CONCEPTS

Microwave irradiation has been widely used in inorganic and organic synthesis[15,16]. Compared to the traditional heating method microwave irradiation presents numerous advantages as for instance, a more homogeneous inner core heating with no solvent convective currents due to temperature gradients, lower energy consumption and short time of reaction[17]. In seconds or minutes (for traditional heating methods hours), it is possible to reach high temperatures at which there is complete dissolution of the starting reagents, formation of reactive species (monomers), nucleation and growth.

Microwave chemistry is based on efficient heating of the material that is the ability of solvent and reagents to adsorb microwave energy and to convert it into heat. The microwave at frequency of 2.45 GHz generates too low energy to cleave chemical bonds, but enough to affect molecular rotations. Actually, the mechanism of microwave assisted synthesis seems to consist in increasing reaction rates by the thermal effect due to dielectric loss and ionic conduction.

Microwave irradiation creates an oscillating electric field in which polar molecules behave as rotating dipoles. Depending on the irradiation frequency and the time needed for the dipoles

to realign with the electric field, friction is generated and part of the microwave input energy is lost as heat. This mechanism is defined as dielectric loss. The microwave thermal effect due to ionic conduction comes from the collisions of dissolved charged molecules or ions when following the electric field direction. This mechanism is more efficient in generating heat compared to the dielectric loss (Fig. 4).

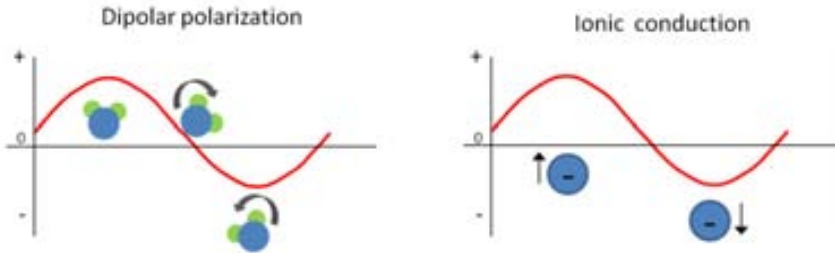

Figure 4. Mechanisms of microwave irradiation: on the left dipolar polarization, dipoles are oscillating in an electric field; on the right ionic conduction, ions are orienting in the electric field.

The dielectric properties of a substance are defined by two parameters: the dielectric constant (ε) which is the tendency of a substance to be polarized in an electric field, and the dielectric loss (ε') which is the ability of a substance to convert the microwave irradiation into heat. The ratio between these two parameters defines the dielectric loss $\tan\delta = \frac{\varepsilon'}{\varepsilon}$ which provides an indication on the ability of the material to absorb and convert electromagnetic irradiation into heat. Organic solvents are classified following this definition in high, medium and low absorbing electromagnetic materials. Here it is showed a table (Table 4) with the dielectric tangent properties of some organic solvents. We chose as ideal solvent benzyl alcohol with a tan δ= 0.667.

Table 4. List of solvents with their correspondent dielectric tangent properties tan δ. Solvents with high tan δ are high absorbing electromagnetic materials and are preferred in microwave reactions.

Solvent	tan δ
Ethylene glycol	1.350
Ethanol	0.941
2-Propanol	0.799
Benzyl alcohol	0.667
Methanol	0.659
Water	0.123
Chloroform	0.091
Ethyl acetate	0.059
Acetone	0.054
Toluene	0.040

Moreover, it has been proposed that benzyl alcohol has an active role in particle nucleation and growth through coordination of acetate function and esterification reaction.[18]

In microwave assisted colloidal synthesis, concentration of metal precursor, power and time of irradiation are critical factors to achieve size control[8,19]. It has been demonstrated that by increasing irradiation time and precursor concentrations, particles with larger sizes and

different shapes can be produced[20]. By selecting well defined experimental values of power, temperature and time of reaction we could obtain particles of around 6 nm in size, ready dispersible in water that were further used for an efficient cellular uptake and cell labeling.

2.2.2. SYNTHESIS OF WATER DISPERSABLE NANOPARTICLES BY MICROWAVE ASSISTED SOL-GEL METHOD

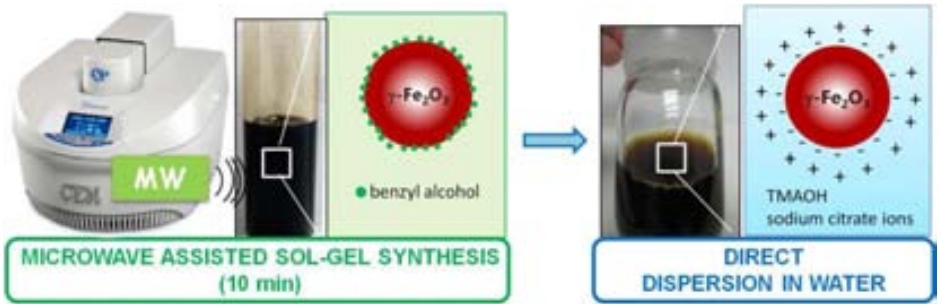

Figure 5. Schematic description of the microwave assisted sol-gel process used for MW-SPIONs synthesis. At the beginning the formation of the magnetic material occurs in the polar solvent without any surfactant. Afterward particles were stabilized at pH=7.4 with the addition of TMAOH and sodium citrate.

In a glass-tube suitable for microwave reaction (Fig. 5) 0.35 mmoL of the iron precursor $Fe(acac)_3$ are added to 4.5 mL benzyl alcohol, mixed with a spatula and ultrasonicated for few minutes. The vial is closed and the microwave irradiation takes place with power set at 250 W. The solution is kept at 60 °C for 5 min to achieve complete dissolution of the organic precursor and subsequently heated up to 180 °C and kept at this temperature for 10 min (Fig. 6).

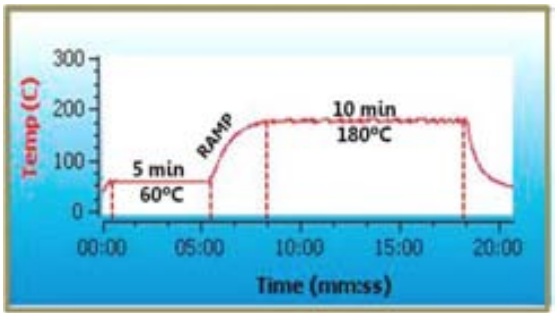

Figure 6. Temperature variations in time during a microwave reaction using CEM equipment.

The final result is a black colored dispersion, which suggests the formation of magnetic material. Acetone is added to precipitate the particles in presence of 20 µL of anionic stabilizer TMAOH 25% and centrifuged at 6000 rpm (centrifuge rotor radius 7 cm) for 30 min. The supernatant is discarded and another 20 µL of TMAOH 25% are added before centrifuging. The final black precipitate is dried at 60 °C for 1h and dispersed in MilliQ water. As synthesized, the pH of the colloidal aqueous dispersion is basic due to the presence of TMAOH. To be compatible for cellular labeling it is necessary to lower the pH to 7.4 by adding HNO_3 0.04 M.

At the same time, an anionic stabilizer, sodium citrate, is added to counterbalance inter particle attractive interactions. A typical batch with 76% of yield consists of a stable dispersion of magnetic nanoparticles with hydrodynamic size of 14 nm (18% polydispersity), zeta potential of -35 mV. Particle size is monitored during time and no precipitation is noticed even after 6 months. Furthermore, microwave synthesis allows us to obtain stable aqueous dispersions with concentrations up to 10 mg/mL. The batch is sterilized by filtering (0.2 μm pore size membranes, Millipore) before being used for cell cultures. Particle core composition is made of maghemite/magnetite phase as confirmed by electron diffraction and the average particle diameter is around 6 nm (Fig. 7). High resolution TEM of nanoparticles shows crystalline planes at a 0.267 nm distance that can be ascribed to the (311) plane of maghemite/magnetite. A typical batch in water at pH=7.4 has iron concentration of 35 mM and sodium citrate concentration of 0.3 mM.

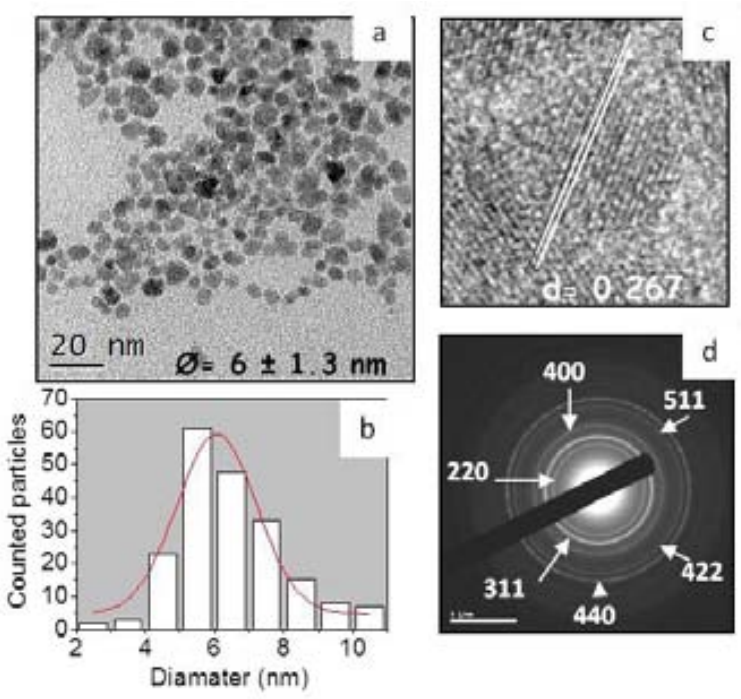

Figure 7. Nanoparticle core characterizations: a) TEM image of MW-SPIONs; b) Histogram of particle size distribution fitted to a Gaussian function; c) HR-TEM picture showing crystalline planes; d) Electron diffraction pattern typical of magnetite/maghemite material.

The saturation magnetization at room temperature is 60 emu/g which is comparable to the one found for TD-SPIONs, pointing to the high degree of crystallinity of the nanoparticles. Superparamagnetism is also proved by the ZFC-FC magnetization curves (Fig. 8). The ZFC magnetization increases with temperature until reaching the maximum value corresponding to the blocking temperature (T_B) which is 57 K for the MW-SPIONs.

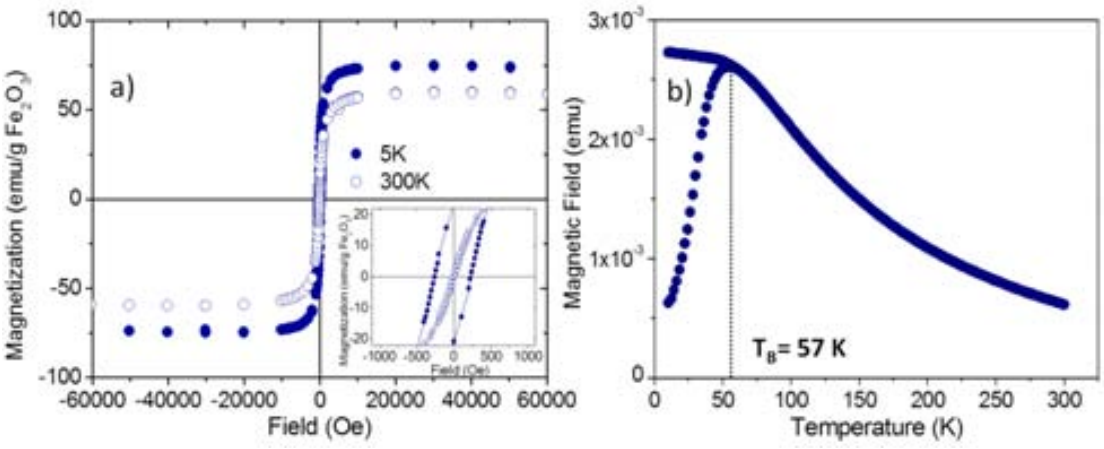

Figure 8. Nanoparticle magnetic characterization: a) MW-SPIONs magnetization curves at 5K and 300K as function of the magnetic applied field. b) Zero field cooled and Field cooled magnetization at 50 Oe.

2.3. CHARACTERIZATION OF IRON OXIDE NANOPARTICLE CRYSTALLINE PHASE: POWDER XRD AND CHEMICAL ANALYSIS.

Powder X-ray diffraction (XRD) patterns of TD-SPIONs and MW-SPIONs are presented in Figure 9[21]. The reflections in the XRD patterns can be indexed with the inverse spinel structures of magnetite or maghemite. The distinction between both phases was not possible due to the closeness of its reflections and the broad reflection peaks observed (Fig. 9). Titration analyses indicated the presence of 5% of Fe^{2+} relative to the total Fe in MW-SPIONs and 10% of Fe^{2+} for TD-SPIONs in both cases lower than the expected 33% for pure magnetite (see annex of chapter 2 for more details). We thus conclude that the materials consist of a mixture of the two phases. This is in agreement with previous works where detailed X-ray absorption spectroscopy and X-ray magnetic circular dichroism spectroscopy indicated that γ-Fe_2O_3 was the major phase for 5 nm iron oxide nanoparticles while the proportion of Fe_3O_4 rose from 20% to 60% with an increase in particle size from 5 nm to 9 nm[22] .

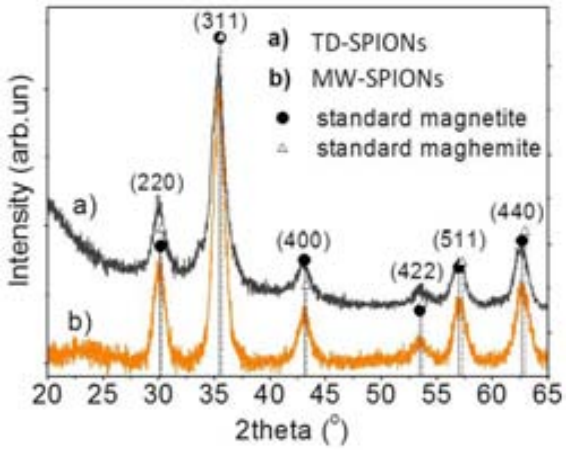

Figure 9. X-ray diffraction patterns corresponding to iron oxide synthesized by (a) thermal decomposition (TD-SPIONs) and (b) by microwave sol-gel route (MW-SPIONs).

2.4. MECHANISM OF STABILIZATION OF COLLOIDAL SUSPENSIONS IN WATER AT pH=7.4

As it is well known, several mechanisms may occur at the particle surface: chemical exchanges (anions, cations), electrochemical exchanges (electrons, protons), adsorption/desorption reactions of water and molecules in solution. The atoms that are exposed at the nanoparticle surface are oxygen atoms with a more or less basic character depending on the equilibrium:

$$Mn\text{-}O^{(nv-2)} + H^{+} \rightarrow Mn\text{-}OH^{(nv-1)},\ Kn_1$$
$$Mn\text{-}OH^{(nv-1)} + H^{+} \rightarrow Mn\text{-}OH_2^{(nv)},\ Kn_2$$

K_1, K_2 are the protonation constants, n is the number of the metal cations (M) bounded to the oxygen atom, v is the formal bound valence defined by Pauli.

Aquo ions are commonly formed at the particle-water interface of 3d transition metals and at the same time oxo-complexes are formed for metals in high oxidation states, particularly at high pH[23]. The adsorption of anions and weak acids in solution on the surface of metal oxides occurs by substitution of the aquo or oxo ligands.

Tetramethylammonium hydroxide readily dissolves to form $N(CH_3)_4^+$ and OH^- ion species in an aqueous environment. OH^- are directly adsorbed onto the maghemite surface forming an inner negative charged layer, while $N(CH_3)_4^+$ are contributing to particle stabilization forming an outer positive charged layer. Thus in a stable colloidal dispersion, the double electrostatic layer onto maghemite surface provides electrostatic repulsion forces to counterbalance the attractive Van deer Walls and dipole-dipole interactions (Fig. 10).

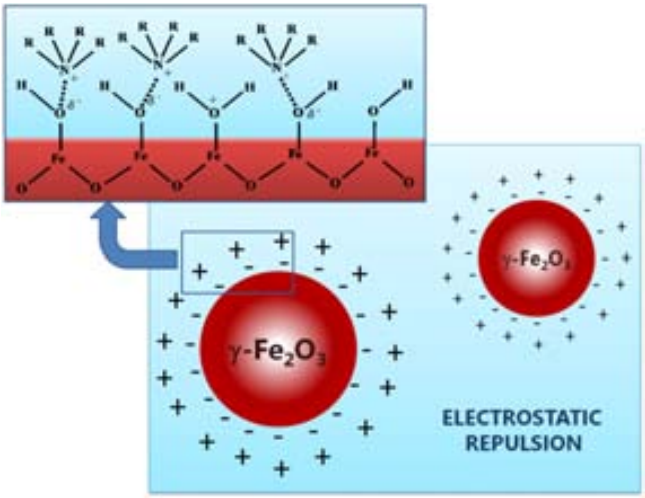

Figure 10. Schematic representation of the double electrostatic layer formed by $N(CH_3)_4^+$ and OH^- onto SPION surface.

As already mentioned, prior to be used for biomedical applications, the pH of the colloidal dispersion stabilized with TMAOH has to be lowered to physiological pH=7.4. By adding nitric acid without a further stabilizer, the groups NO^{3-} would neutralize $N(CH_3)_4^+$ leaving Fe–OH exposed. Without $N(CH_3)_4^+$ coverage, the ferrofluid would turn out to an unstable system and to coagulate readily[24]. In fact, maghemite/magnetite uncoated nanoparticles show isoelectric

point at pH=7.4 (the isoelectric point refers to the pH value at which zeta potential is zero)[25]. For that reason it is required a further ionic stabilizer to make sufficiently charged SPION surface at pH= 7.4 and we use sodium citrate. Sodium citrate is a polycarboxylate molecule which has good affinity with iron oxide surface due to its three carboxylate groups which replace aquo groups by bridging coordination. Moreover sodium citrate is biocompatible, widely used in food and drug industry and citric acid is one of products from tricarboxylic acid cycle, a normal metabolic process in human body[26].

The pKa constants of deprotonation for the three carboxylic groups of citric acid are pka1= 2.79, pka2= 4.3, pka3= 5.65. Sodium citrate adsorption onto SPION surface (that means its efficacy as colloidal stabilizer) depends on pH, particle concentration and temperature of the suspension. The pH of the suspension imposes both level of deprotonation of the carboxylate groups and surface charge of the iron oxide surface. The adsorption isotherm at room temperature of citrate molecules onto nanoparticles surface follows a saturation profile with the maximum charge density at salt concentration equal to 4 mM (Fig. 11)[27].

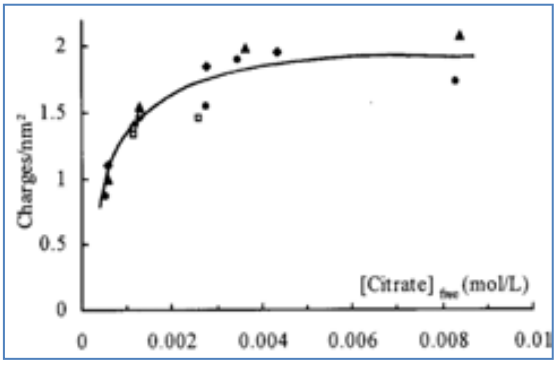

Figure 11. Adsorption isotherm showing citrate density onto maghemite nanoparticles versus citrate concentration in aqueous phase. Dubois, *The Journal of Chemical Physics 1999*, 111 (15), 7147-7160.

In a study on the adsorption of carboxylic acids on colloidal maghemite at different pHs of the aqueous suspension, R was defined as molar ratio percentage of the ligand added to the total iron ferrofluid:

$$R = \frac{[L]}{[Fe]} \cdot 100$$

R is the molar ratio percentage, [L] is the citric acid concentration and [Fe] is the iron concentration of the ferrofluid.

The maximum of citric acid adsorption was found to be at pH close to the pKa= 2.8. In Figure 12 it is showed the adsorption curve of citric acid on maghemite nanoparticles. The adsorptivity profile follows a saturation model with a maximum of adsorption of citric acid at R= 6% (Fig. 12)[28]. Moreover, it was affirmed that the R parameter had be no more than 10% in order to avoid particle precipitation.

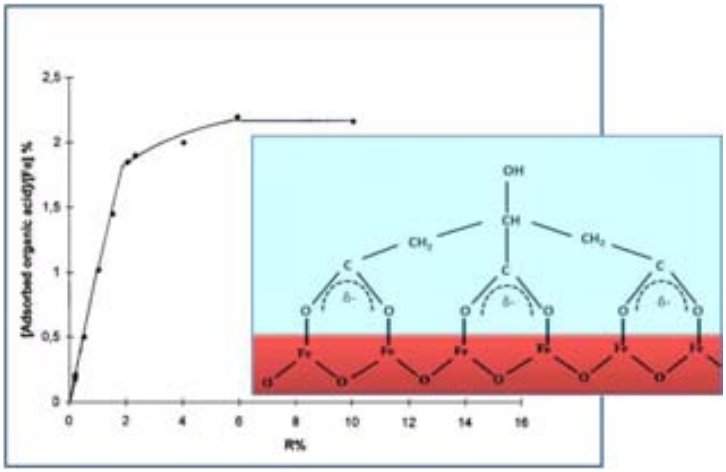

Figure 12. Percentage of adsorbed citric acid onto maghemite nanoparticles versus the amount introduced. Fauconnier, *Trends in Colloid and Interface Science X*, Steinkopff: 1996; Vol. 100, pp 212-216.

These references were useful to calculate the amount of sodium citrate to achieve a stable colloidal dispersion at pH=7.4. A batch solution of sodium citrate 4 mM was prepared and considering a final SPIONs concentration in water of [Fe]= 10 mM (0.55 mg/mL of γ-Fe_2O_3) it was calculated that the amount of sodium citrate to stabilize the dispersions should be between 0.25 mM and 1 mM. Experimentally it was found that for TD-SPIONs it was needed about 1.4 mM of sodium citrate to stabilize particles, maybe due to the ligand exchange process with oleic acid and TMAOH addition, while to stabilize MW-SPIONs only 0.3 mM of sodium citrate was needed (Table 5). Following this recipe the prepared samples were stable and no flocculation (for the neutralization of surface charges) or precipitation was observed even after 6 months.

Table 5. Concentrations of nitric acid and sodium citrate calculated at 10 mM of Fe for TD-SPION (batch EC12) and MW-SPION (batch MW8). Z pot= zeta potential, PD= polydispersity %.

	Diameter TEM (nm) ±PD%	Diameter DLS (nm) ±PD%	Z pot (mV)	HNO_3 (mM)	Sodium citrate (mM)
TD-SPION (EC12)	6.4 ± 11%	36 ±21%	-33	490	1.4
MW-SPION (MW8)	6 ± 22%	14 ± 19%	-36	20	0.3

Fourier transform infrared spectrometry (FTIR) was performed to check the presence of adsorbed molecules after centrifuging the suspension at 14000 rpm (centrifuge rotor radius 6 cm) for 90 minutes and drying the precipitated particles. As showed in FTIR picture (Fig. 13) the surface of TD and MW-SPIONs is coordinated by sodium citrate and TMAOH molecules. Sodium citrate typical bands are asymmetric and symmetrical stretches of the anionic carboxylate groups (1580 cm^{-1} C=O asymmetric stretches, 1404 cm^{-1} symmetric stretches). TMAOH typical bands are 1506 and 950 cm^{-1} C-N stretches. The peak at 583 cm^{-1} for both TD-SPIONs and MW-SPIONs is corresponding to the vibration of Fe−O bonds.

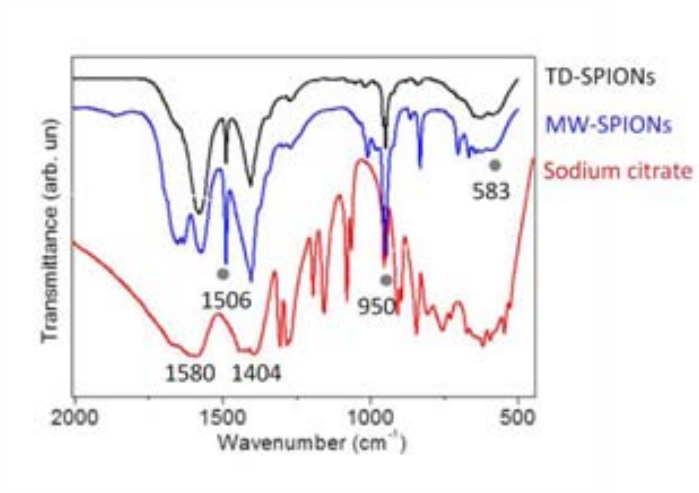

Figure 13. FT-IR spectra of TD-SPIONs, MW-SPIONs, and pure sodium citrate. The grey dots at 1506 and 905 cm^{-1} indicate TMAOH C-N stretches. The grey dot at 583 cm^{-1} indicates the Fe-O vibration bond.

From Cryo-TEM images (Fig. 14) it can be seen that TD-SPIONs in water at pH=7.4 are in form of small aggregates formed during the ligand exchange process, while MW-SPIONs are more dispersed since no ligand exchange was needed.

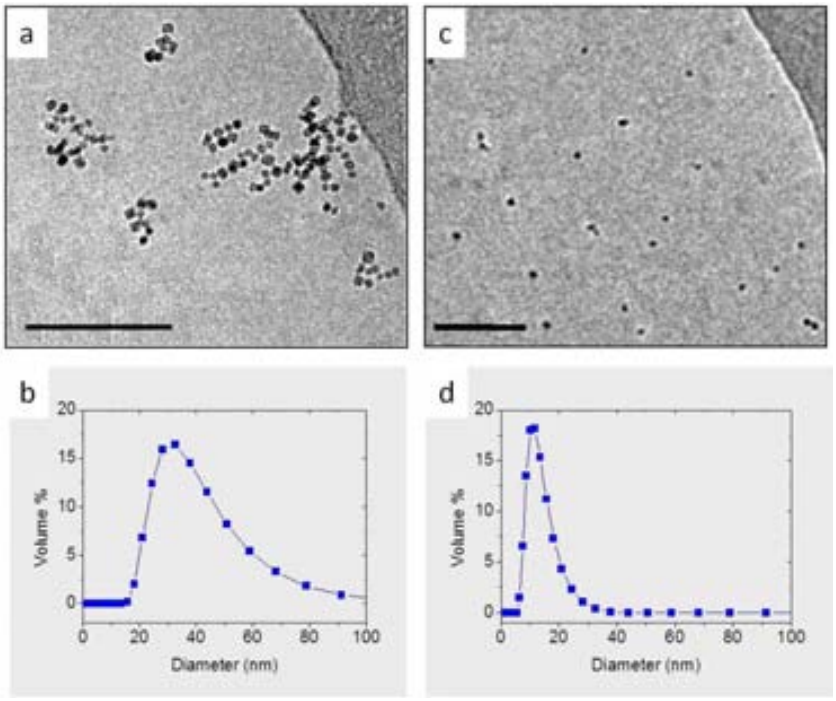

Figure 14. Cryo-TEM and DLS analysis of particle aggregates in water a) cryo-TEM picture of TD-SPIONs in water at pH=7.4; b) DLS hydrodynamic diameter (referred to sample in figure a): 36 nm (21% PD); c) cryo TEM picture of MW-SPIONs in water at pH=7.4; d) DLS hydrodynamic diameter of sample in (referred to sample in figure c): 14 nm (18% PD). Scale bar 100 nm.

The most evident differences between TD and MW-SPIONs were the DLS hydrodynamic diameters at pH=7.4: for TD-SPIONs sizes are bigger indicating that they tend to form aggregates even though the amount of sodium citrate added is higher than in MW-SPIONs formulations. These differences may arise from the different synthetic approaches: for TD-SPIONs it was needed to perform a previous ligand exchange in order to disperse them in

water, while MW-SPIONs were directly dispersed without any further surface modification. Colloidal particles randomly collide with each other at a rate determined by their Brownian motion. The collision can result in the formation of an aggregate if the particles remain in contact after the encounter[29]. The magnetic stirring for 18 hours during the ligand exchange process can affect TD-SPION colloidal stability in water by increasing the number of particle collisions. Moreover in TD-SPIONs formulations there is a higher amount of nitrate (Table 5). Nitrate increases the ionic strength in the TD-SPIONs suspension more than 10 fold compared to MW-SPIONs. This is also a consequence of the ligand exchange process where TD-SPIONs in organic phase were mixed with an excess of basic anionic surfactant (γ-Fe_2O_3: TMAOH molar ratio 1:10), so it was necessary a high amount of nitric acid to lower the pH.

Initially, the as-prepared colloidal suspensions at pH= 7.4 were sterilized using autoclave with temperature of 121ºC for 30 minutes. The final batch consisted of a sterile suspension whose hydrodynamic size distribution was slightly larger than the non-sterilized sample. Moreover, after 1 month it was found that aggregate size increased about 20%. It has been demonstrated that autoclave heating can destabilize nanoparticles suspensions[30]. Their physical stability depends on the composition of stabilizing surfactant or surfactant mixture. Methods of preventing clumping induced by heat stress generally include the use of excipients during the autoclaving process. Groman et al.[31], used low molecular weight carbohydrates such as mannitol to prevent clumping during autoclaving. However, the use of excipients increases the cost and complexity of manufacturing the product.

In conclusion, to ensure a long lasting colloidal stability we preferred as method of sterilization the membrane filtration using filters with pore diameters of 0.2 μm. We found that for TD-SPIONs as well as MW-SPIONs the size of aggregates did not substantially change after 6 months (Fig.15).

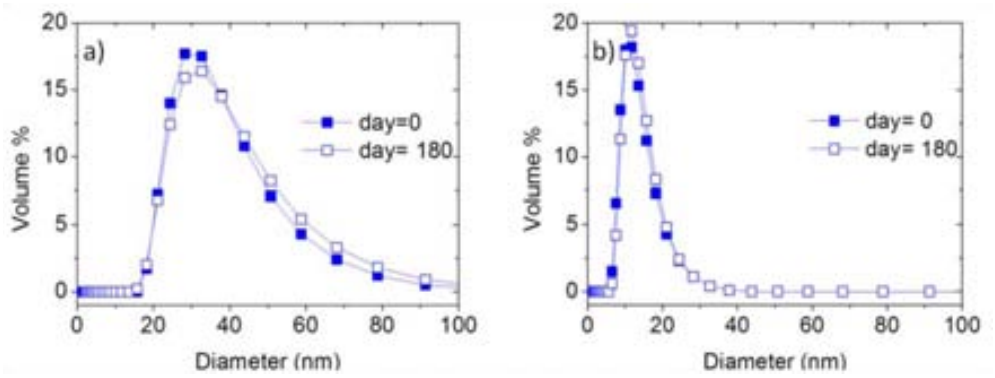

Figure 15. DLS measurements a) of as-prepared TD-SPIONs (day= 0) and after 6 months (day=180); b) of as-prepared MW-SPIONs (day= 0) and after 6 months (day=180).

2.5. SPIONs IN CULTURE MEDIA

When as-synthesized nanoparticles get in contact with biological media (PBS, blood, cellular media) proteins present in media interact and even attach to particle surface forming the as-known "protein corona".

2.5.1. THE ROLE OF PROTEIN CORONA

There are a considerable number of studies demonstrating that nanoparticle coated by protein corona is the real active biological entity, influencing biological responses such as cellular labeling and uptake (Fig. 16)[32].

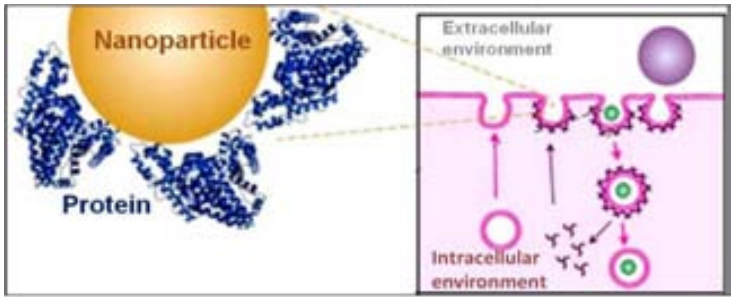

Figure 16. Nanoparticles are coated by protein corona. Depending on their size, nanoparticles either remain at the cell surface or are taken up into the cell via receptor mediated endocytosis, mediated by clathrin. Internalized particles are guided into specific cellular compartments. Lynch, *Adv Colloid Interface Sci 2007*;134-135:167-74.

Human plasma is made of around 3700 proteins[33]. At any moment, the composition of the corona is due to the concentration of the proteins in plasma as well as to the binding constants for a selected nanoparticle formulation. It is stated that to know the specific protein adsorption pattern onto a particle surface can help in predicting particle *in vivo* targeting and biodistribution[34]. There are specific plasma proteins like the apolipoprotein E which seems to facilitate drug targeting in the blood brain barrier. A well known example of protein-mediated drug delivery is albumin which is the most abundant protein in plasma and it has been successfully used in drug delivery of anticancer drugs like as Paclitaxel (Abraxane ®): the protein-drug complex induces less toxicity and enhances the uptake by tumor cells[35].

Another example was reported by Müller and coworkers who demonstrated that citrate-triethylene glycol-coated SPIONs of about 7 nm incubated with different fetal bovine serum aqueous dilutions are making a rather stable corona in time (measurements taken between 4 min and 4 h). Immunoglobulin and fibrinogen were the most abundant protein adsorbed onto the particle surface[36].

Often, particle surface functionalization with polymers (eg. with PEG, polaxamer, dextran) are required to minimize particle–serum protein interactions when long blood circulation time and reduced opsonization (process by which a pathogen is marked for ingestion and destruction by a phagocyte) by the reticuloendothelial system are needed[37]. However, impurities and product of oxidative degradation of used polymers were associated with certain pharmacological and immunological effects[17]. In our study, in which the nanoparticles have not to be directly injected in the blood stream, it is not the main requirement to avoid SPIONs-protein interactions since their final destination will be the cell cytoplasm. For this reason we preferred the use of easily fabricated citrate-coated SPIONs suitable for cellular labeling and to control their aggregation in culture media by the addition of limited amounts of salt.

The identification of key parameters controlling nanoparticle uptake by a selected cell type is extremely important. Hinderliter and coworkers developed a computational model describing

the amount of particle available per cell considering the physical and chemical properties of particles in the media[38]. In a standard liquid-based cell culture, the number of particles associated with cells is a function of the rate of delivery of particles to cells and how strongly particles adhere to the cell surface. Particle size, shape, density and surface-coating influence transport properties. Transport of particles with diameter less than 10 nm is controlled principally by diffusion. Transport of particles greater than 200 nm is controlled by sedimentation. Slower transport is expected to occur between 10 and 200 nm where both diffusion and sedimentation control transport. Moreover, they found a linear dependence between the mass of the iron oxide agglomerated nanoparticles and macrophages uptake used in their *in vitro* studies. Moreover, several *in vitro* studies have demonstrated that by choosing adequate core sizes, concentration of the magnetic material and chemical composition of the particle coating, it is possible to regulate the iron cellular uptake minimizing potential cytotoxic effects [39,39b,40]. Of particular importance is the nanoparticle surface coating composition since it plays a key role in the mechanism of cellular uptake. For instance, large uptakes of positively charged nanoparticles have been reported, although higher levels of cytotoxicity have often been observed[41,42]. Anionic citrate-coated iron oxide nanoparticles have also been used for cell labeling due to their simple molecular surface-coating and their high adsorption/internalization rates found in different mammalian cell types.

2.5.2. STABILITY IN WATER AND IN CULTURE MEDIA OF THERMAL DECOMPOSITION AND MICROWAVE SPIONs

SPIONs in culture media perform differently than in water and their performance strongly depends on media composition. Not only the formation of protein corona on particle surface has a major effect on particle aggregation, but also the high ionic forces due to high salt and amino acid concentration can lead to colloidal instability and aggregation. For instance Safi and coworkers[43] demonstrated that high concentrations of cations such as calcium and magnesium can induce destabilization of citrate-coated nanoparticles due to citrate desorption from particle surface. For this reason more anionic stabilizer was necessary in cell media to avoid particle precipitation[33].

To check particle stability in cell media the average hydrodynamic diameter of TD- and MW-SPIONs (Table 6) were monitored in time by DLS in PBS (phosphate buffer saline, calcium and magnesium free), DMEM F12 10% FBS (Dulbecco modified eagle medium supplemented with F12 and 10% of fetal bovine serum) and EGM-2 10% FBS (endothelial growth medium containing VEGF and other factors of unknown concentration supplemented with 10% of fetal bovine serum). Sodium citrate concentration was found to be a determinant factor in inducing particle stabilization: when sodium citrate concentration is lower than 1.3 mM (per 10 mM of Fe), microwave synthesized SPIONs tend to aggregate quite fast in all media, while at concentration of sodium citrate 1.3 mM particle aggregation could be easily controlled[44]. The following batches were analyzed by DLS:

Table 6. Concentrations of sodium citrate in TD-SPION (batch EC12), MW-SPION (batches MW8 and MW9), calculated at 10 mM of iron. Z pot= zeta potential, PD= polydispersity %.

	Diameter TEM (nm) ±PD%	Diameter DLS (nm) ±PD%	Z pot (mV)	Sod. citrate (mM) at 10 mM Fe
TD-SPIONs (EC12)	6.4 ± 11%	36 ±21%	-33	1.4
MW-SPIONs (MW8)	6 ± 22%	14 ± 19%	-36	0.3
MW-SPIONs_SC (MW9)	6.5 ± 21%	13± 17%	-52	1.3

MW-SPIONs stabilized in water at pH=7.4 with an amount of sodium citrate of 0.3 mM had rather stable hydrodynamic diameters of less than 100 nm after thirty minutes in PBS and DMEM F12 10% FBS (Fig. 17). An invariable size was maintained for longer time in the case of DMEM F12 10% FBS, while particles become unstable in PBS after one hour. In the case of EGM-2 10% FBS, SPIONs rapidly formed large clusters which sedimented within 2 hours.

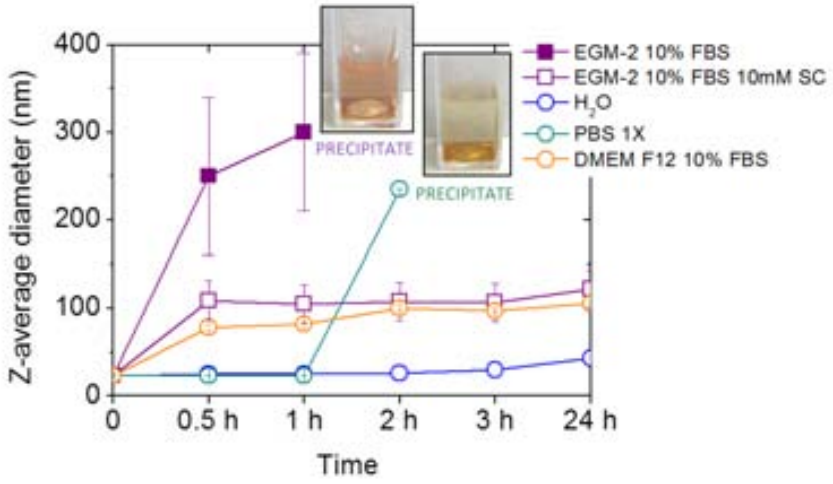

Figure 17. MW-SPIONs (batch MW8) hydrodynamic size measurements in different media, at different periods of time.

To control the aggregation extra sodium citrate was added in EGM-2 10% FBS at different concentrations: 0.2 mM, 5 mM and 10 mM, and the aggregates were imaged by optical microscopy (pictures in the Fig. 18) and by DLS (graphs in Fig. 18). From the pictures it can be observed that the higher is the sodium citrate concentration the smaller are particle aggregates.

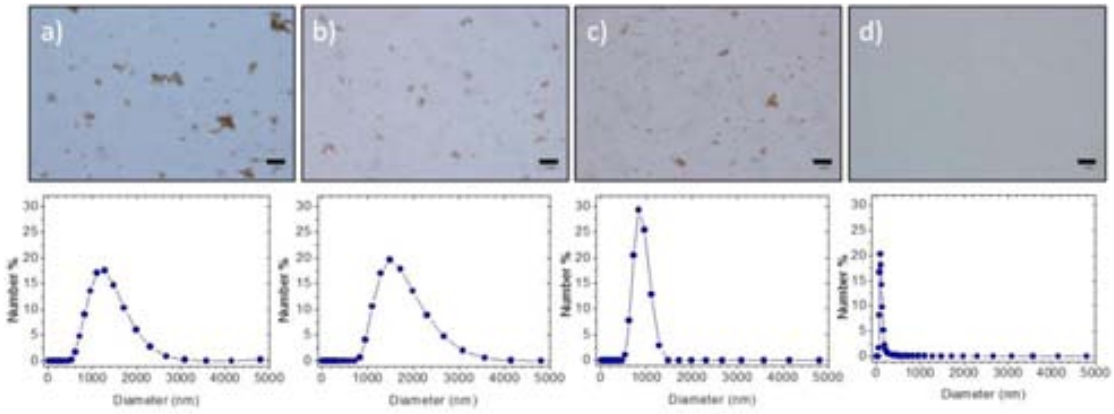

Figure 18. MW-SPIONs in different media: (a) control particles; particles with (b) 0.2 mM, (c) 5 mM and (d) 10 mM of sodium citrate. Scale bar 100 μm.

Since increasing sodium citrate concentration leads to less particle aggregation we started synthesizing batches of MW-SPIONs with a higher amount of sodium citrate directly added in the colloidal suspension at pH=7.4. MW-SPIONs with the salt concentration 1.3 mM were quite stable in time forming aggregates of less than 100 nm in DMEM F12 10% FBS and PBS 1X. It is worth noting that they precipitated in PBS only after 24h. In EGM-2 10% FBS the size of aggregates rapidly grew up to 300 nm but then it stayed rather constant during 24h. The suspension was rather turbid but precipitation did not occur. However we were expecting smaller aggregate size than 300 nm, in the range of 100 nm.

In conclusion comparing Figures 17 and 19 it can be concluded that the addition of sodium citrate resulted in a more efficient aggregate stabilization when it was added in EGM-2 medium rather than in the aqueous colloidal suspension at pH=7.4.

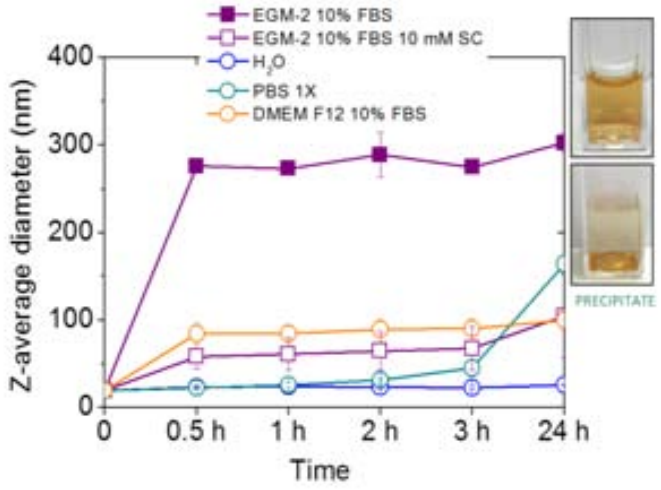

Figure 19. MW-SPIONs_SC (batch MW9) hydrodynamic size measurements in different media, at different periods of time.

TD-SPIONs stabilized in water at pH=7.4 with an amount of sodium citrate of 1.4 mM had an average hydrodynamic diameter lower than 100 nm in DMEM F12 10% FBS as well as in EGM-2 10% FBS 10 mM sodium citrate for the first 30 min. While in EGM-2 10% FBS the size increased

up to 150 nm after 30 minutes and stayed rather constant over 24h, without any visible precipitation. Particles in PBS 1X precipitated after 1h (Fig. 20).

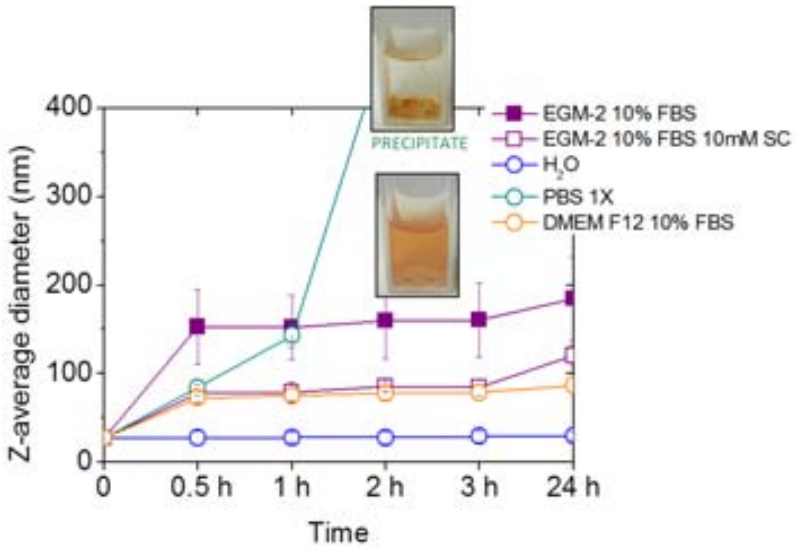

Figure 20. TD-SPIONs (batch EC12) hydrodynamic size measurements in different media, at different periods of time.

After DLS measurements, it can be highlighted the different behavior of SPIONs synthesized by microwave and thermal decomposition route in culture media. It can be concluded that there is a difference in the surface reactivity between MW-SPIONs and TD-SPIONs. The amount of sodium citrate required to stabilize MW-SPIONs in water (0.3 mM) was not enough for particle stabilization in culture media, where an extra-amount of sodium citrate was added (10 mM, with final sodium citrate concentration of 1.3 mM). On the contrary, in the case of TD-SPIONs it was not necessary to add any extra-amount of sodium citrate to stabilize particles in culture media. This fact may be related to different purification processes used to obtain aqueous MW-SPIONs and TD-SPIONs dispersions at pH=7.4: in the case of MW-SPIONs it was not necessary the ligand exchange process. Moreover, particles have different shape, being MW-SPIONs slightly less spherical and regular than TD-SPIONs.

2.5.3. DEGRADATION OF SPIONs IN LYSOSOMAL MIMICKED ENVIRONMENT

This study was preliminarily conducted to check SPIONs degradation kinetics in sodium citrate buffer at pH=4.5 in order to mimic the acidic environment after cellular uptake and particle internalization into cytoplasmatic vesicles (endosomes and lysosomes)[45,46]. It was useful to test our SPIONs formulation suitability for cellular labeling and guiding tool in angiogenic therapies with a duration time of minimum 1 week[47].

SPIONs sample were prepared keeping into account seven different periods of time to monitor particle degradation: day 0, day 1, day 2, week 1, week 2, week 4, week 6. Known aliquots of TD, MW and silica SPION aqueous dispersions were divided respectively into 7 different vials. 3 mL of sodium citrate buffer (citric acid 20 mM, trisodium citrate 20 mM in sterile water) were added to each vial in order to obtain a final iron concentration of 0.5 mg/ml. At every fixed period of time the color of the TD, MW and silica SPIONs dispersions were analyzed and

compared. Subsequently the samples were centrifuged at 14000 rpm (centrifuge rotor radius 6 cm) for 90 minutes to ensure nanoparticles precipitation. Later the supernatants were filtered through 0.1 µm porous filters and analyzed by ICP-OES (Fig. 21). From the experiment it can be noticed that particles degraded in few days and MW-SPIONs particles showed faster dissolution in time (2 days), compared with TD-SPIONs whose dissolution occurred after 8 days, while silica SPIONs were almost unchanged during the analyzed period of 43 days (Fig. 22). Silica SPIONs are core-shell nanocomposites which are made up by a silica shell (SiO_2) and an inner core of SPIONs (γ-Fe_2O_3) of around 6 nm in diameter[48]. Silica is known to be a biocompatible material, resistant to basic or acidic pH and is studied for the development of drug delivery formulations[49]. Measurements were repeated once and the error bar corresponds to the standard deviation during the analysis of each batch done in triplicate. For that reason more evidences are needed to corroborate such conclusions.

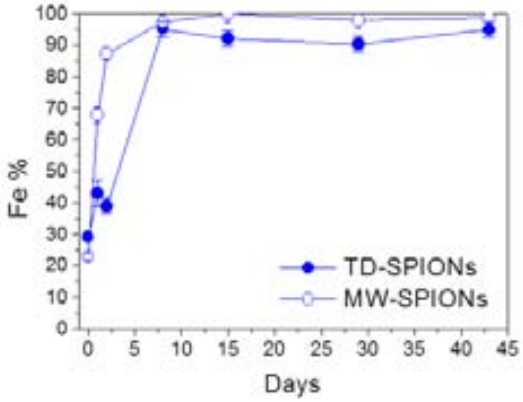

Figure 21. Degradation profiles of TD- and MW-SPIONs in time reported as Fe% found in the supernatant after centrifuge and further nanoparticle separation by filtration.

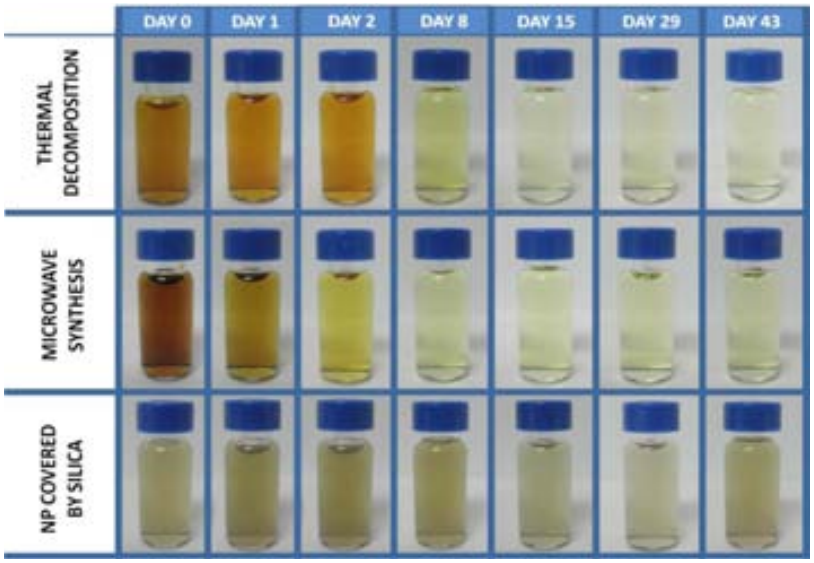

Figure 22. SPION suspensions in citrate buffer at pH=4.5. The pictures were taken at different times. Note the color changes for TD- and MW-SPIONs indicating particle degradation.

2.6. CHAPTER CONCLUSIONS

We synthesized SPIONs by two different synthetic approaches, thermal decomposition and microwave sol-gel method. Our purpose was to obtain particles with diameter of less than 20 nm, narrow size distribution, high crystallinity and good magnetic properties for an efficient cell labeling. Both selected methods allowed us to achieve our aim; moreover microwave yields particles ready dispersible in water without laborious ligand exchange or purification steps compared to the thermal decomposition method. In terms of "eco-design" applied to the fabrication of nanoparticles it can be stated that the microwave approach yields an energy consumption reduced by a factor of 10 and 40% lower overall cost.

It is important to highlight that from the magnetic point of view, iron oxide nanoparticles prepared by such simple technique as microwave synthesis can be as good as those prepared by more complex and costly thermal decomposition (comparable saturation magnetization). In these regards the microwave technique is clearly superior compared to other simple synthetic techniques such as coprecipitation which tend to yield less well crystallized nanoparticles with lower saturation magnetization. Such characteristics can be considered attractive for scaling-up nanoparticle fabrication.

Finally, by comparing the microwave particle stability in culture media with the stability of thermal decomposition particles of the same size, it was found a difference in particle surface reactivity. This surface characteristic certainly plays an important role in time aggregation and amount of protein corona adsorption. Cytotoxicity studies as well as cell labeling results for both particles systems will be presented in Chapter 3.

2.7. ANNEX OF CHAPTER 2

This annex describes the main techniques used for the characterization of thermal decomposition (TD-SPIONs) and microwave (MW-SPIONs) synthesized batches. We analyzed their chemical composition (iron oxide core), size in dried state or dispersed in water/culture media, surface coating and zeta potential. Finally, tables are included summarizing the main nanoparticle properties.

2.7.1. ELEMENTAL MICROANALYSIS

We used this technique to measure the residual amount of organic surfactant after ligand exchange process of SPIONs synthesized by thermal decomposition.

Accurately weighed samples of approximately 1 mg in a tin capsule are dropped at preset intervals of time into a vertical quartz combustion tube maintained at 1200 ºC, through which a constant flow of helium is run. When the sample is introduced, the helium stream is temporarily enriched with pure oxygen. Flash combustion takes place, primed by the oxidation of the tin container. Gases produced passes through a chromatographic column onto a detector. The gases eluted are N_2, CO_2, H_2O. Carbon, nitrogen and hydrogen percentage were measured for one nanoparticle batch synthesized by thermal decomposition (EC11), using Eurovector EA3011 equipment. Measurements were repeated twice and results were normalized to the weighted amount of nanoparticles. The final percentages obtained were: 17% C, 2.7% H, 0.23% N for TD-SPIONs.

2.7.1.1 EVALUATION OF THE RESIDUAL MASS OF ORGANIC SURFACTANT AFTER LIGAND EXCHANGE PROCESS

The percentages of carbon, hydrogen and nitrogen obtained by elemental microanalysis were used to calculate the residual amount of organic surfactants (oleylamine and oleic acid) onto TD-SPIONs surface after ligand exchange process.

Percentages of the elements obtained by elemental microanalysis in nanoparticle pellet of 1 mg:
Carbon= 17%
Hydrogen= 2.7%
Nitrogen= 0.23%
Number of carbons in oleic acid and oleylamine = 18
267.5 g/mol = molar weight of oleylamine
282.26 g/mol = molar weight of oleic acid
12 g/mol= molar weight of carbon
14 g/mol = molar weight of nitrogen

Since the moles of nitrogen atoms in oleylamine and oleylamine are in ratio 1:1 (1 molecule: 1 nitrogen: 18 carbons) it was possible to calculate the grams of carbon in the sample due to oleylamine doing:

0.23% = 0.23 x 10^{-2} mg of nitrogen in 1 mg of nanoparticle pellet= 0.23 x 10^{-5} g.
0.23 x 10^{-5} g / 14 g/mol = 1.64 x 10^{-7} mol nitrogen.
1.64 x 10^{-7} mol nitrogen * 18= 0.29 x 10^{-5} mol carbon
= 0.29 x 10^{-5} mol * 12 g/mol= 3.55 x 10^{-5} g of carbon due to oleylamine molecules.

The total milligrams of carbon in 1 mg of nanoparticle pellet due to oleylamine and oleic acid molecules are 0.17 mg, so the amount of carbon for oleic acid molecules is:
(0.17 -0.035)= 0.135 mg carbon of oleic acid molecules.

- Percentage of residual oleylamine:

1.64 x 10^{-7} mol * 267.5 g/mol = 0.43 x 10^{-4} g of residual oleylamine

The starting amount of oleylamine used for the thermal decomposition synthesis was
= 6 x 10^{-3} mol *267.5 g/mol= 1.6 g
Percentage of residual oleylamine= (0.43 x 10^{-4} / 1.6) * 100= 0.003%.

- Percentage of residual oleic acid:

0.135 x 10^{-3} g carbon / 12 g/mol= 0.011 x 10^{-3} mol of carbon
0.011 x 10^{-3} /18 * 282.46 g/mol = 1.7 x 10^{-4} g of residual oleic acid

The starting amount of oleic acid used for the thermal decomposition synthesis was
= 6 x 10^{-3} mol * 282.46 g/mol= 1.69 g
Percentage of residual oleic acid= (1.7 x 10^{-4} / 1.69) * 100= 0.01%.

2.7.2. FOURIER TRANSFORM INFRARED SPECTROSCOPY (FTIR)

FTIR is extensively used for quantitative as well as for qualitative analysis of organic compounds. The infrared sources used emit a band of different wavelengths in the mid-infrared (4000-400 cm^{-1}). The vibrational frequencies of most molecules correspond to the frequencies of mid-infrared light and each chemical bond vibrates at a specific frequency. For that FTIR is useful to identify the presence of a particular functional group, for instance C=O of aldehydes, or N-H of amines. The sample is irradiated by the infrared beam and it is measured how much of the beam is absorbed by the sample. Afterwards, the equipment works the absorption value at each corresponding wavelength by using a mathematical process (Fourier transform) to convert the raw data into the spectrum.
We used FTIR to verify the surface coating composition of SPIONs after synthesis and purification steps. Samples were prepared as follows: 0.5 mL of aqueous TD-SPIONs and MW-SPIONs were dried in oven at 60ºC for 2 hours. Subsequently they were mixed with anhydrous KBr to form a pellet which was analyzed by Spectrometer Perkin-Elmer Spectrum One equipment.

2.7.3. DETERMINATION OF SPION CORE COMPOSITION

Through different techniques we checked the SPION core composition (magnetite, Fe_3O_4 or maghemite, γ-Fe_2O_3) soon after nanoparticle synthesis.

2.7.3.1 CHEMICAL TITRATION

A redox titration was performed in order to evaluate the amount of Fe^{2+} and Fe^{3+} ions forming nanoparticle core. About 1 ml of the colloidal dispersion was dissolved in hydrochloric acid 37% giving a yellow colored solution (with Fe^{2+} and Fe^{3+} ions). When 5mM of potassium dichromate ($K_2Cr_2O_7$, oxidizing solution) were added for the first time the amount of Fe^{2+} in solution was titrated by oxidation to Fe^{3+} (Volume of $Fe^{2+:}$ V_{Fe2+}). This step was indicated by a color change (from colorless to violet) of the indicator (sodium diphenylamine sulphonate). By adding tin chloride ($SnCl_2$ reductive agent) ions were reduced to Fe^{2+}, so when $K_2Cr_2O_7$ was added a second time the total amount of iron was titrated (volume of total iron: V_{totFe}).

At last the concentration of Fe^{3+} was estimated as follows: V_{totFe} - V_{Fe2+} = V_{Fe3+}, by subtracting the amount of Fe^{2+} to the total amount of iron.

Chemical reactions occurred during the described redox titration:

- Fe^{3+} reduction:

$2Fe^{3+} + Sn^{2+} \rightarrow 2Fe^{2+} + Sn^{4+}$

- Total Fe oxidation:

$6Fe^{2+} + Cr_2O_7^{2-} + 14H^+ \rightarrow 6Fe^{3+} + 2Cr^{3+} + 7H_2O$

2.7.3.2 FLAME ATOMIC ABSORPTION SPECTROMETRY (FAAS)

FAAS is a quantitative analysis which is commonly used to detect amount of metals in a range of mg/L. In flame AAS, the measured absorbance depends on the absorptivity (characteristic of each kind of element), the concentration of that element in the flame and the optical pathlength through the flame. The sample is atomized in the flame (generally obtained by gas mixtures of air/acetylene), through which a radiation of a chosen wavelength is sent. The sample molecules broken into atoms adsorb an amount of radiation which is proportional to the concentration of the analyzed element.

Samples analyzed by FAAS were aqueous dispersions of SPIONs and solid pellets of cells with internalized SPIONs. Aqueous dispersions of SPIONs were previously diluted with hydrochloric acid 1%, while solid pellets were dissolved into a known volume of hydrochloric acid 37%. Analyses were run with Perkin-Elmer, model 2100 and repeated three times.

2.7.3.3. INDUCTIVELY COUPLED PLASMA OPTICAL EMISSION SPECTROMETRY (ICP-OES)

Inductively coupled plasma optical emission spectrometry (ICP-OES) or inductively coupled plasma atomic emission spectroscopy (ICP-AES) is a sensitive technique used for the detection of small amounts of metals (picograms). This type of emission spectroscopy uses a system at high temperature (8000 °C) as energy source to excite specimens, produced when an electrically conductive material (plasma, like argon gas) is exposed to strong electromagnetic

fields. When the sample is introduced in the plasma flame, atomic collisions generated with the plasma result in emission of ions and atoms. The formed radiation is characteristic of a particular element and its intensity indicates the concentration of that element in the sample.
We mainly used this technique when a precise evaluation of iron concentration within SPION dispersions was needed (sensitivity up to μg/L), for instance in the case of nanoparticle degradation study. Analyses were realized by a Perkin-Elmer, Optima 4300DV instrument.

2.7.3.4. SUPERCONDUCTIVE QUANTUM INTERFERENCE DEVICE (SQUID)

SQUID is a sensitive magnetometer used to measure the magnetization of magnetic materials like ferromagnets. SQUIDs are sensitive enough to measure fields as low as 5×10^{-18} Tesla. The magnetometer requires cryogenic refrigeration.
A magnetometer Quantum Design MPMS5XL was used to perform magnetization measurements of SPIONs at 5 K and 300 K. Magnetic measurements performed at room temperature (300 K) were useful to check particle superparamagnetic features (like the absence of coercivity or remnant magnetization) and saturation magnetization value (M_S).
Measurements at 5 K were conducted to calculate the amount of SPIONs (referred as γ-Fe_2O_3) contained in a specimen, like magnetically labelled cells or magnetic nanocapsules (see chapters 3 and 4). At low temperatures SPIONs behave as ferrimagnets showing remnant magnetization (M_R), for that to know the amount of SPIONs per mass of sample the remnant magnetization of the sample (emu/g_{SAMPLE}) was divided by the remnant magnetization of SPIONs (emu/$g_{\gamma\text{-}Fe2O3}$).
In general, samples were prepared by depositing few drops of a SPION aqueous dispersion of known concentration into a polycarbonate capsule to let water to evaporate until the material was completely dried. The capsule was inserted in the SQUID magnetometer sample holder and magnetization was measured at 5 K or 300 K with applied magnetic fields up to 6 Tesla.
Zero field cooled-field cooled magnetization versus temperature analyses (with applied field of 50 Oe) were performed to determine SPIONs blocking temperature (T_B).

2.7.3.5. POWDER X-RAY DIFFRACTION

Powder diffraction is used in the identification and characterization of crystalline solids (powders, microcrystalline samples), which produce distinctive diffraction patterns when irradiated by an X-ray beam (X-ray wavelengths comprised between 0.1 and 0.2 nm). During the analysis the orientation of a sample is rotated around the beam axis and the produced diffracted radiation (X-ray) is collected on a flat plate detector forming smooth diffraction rings around the beam axis. The angle between the beam axis and the ring is called diffracted angle and is denoted as 2Θ. Powder diffraction data are presented as "diffractogram" in which the diffracted intensity is shown as function of the angle 2Θ.
Powder X-ray diffraction patterns of SPIONs were measured on dried samples with a Rigaku, "rotaflex" RU-200B model using a Cu anode with $\lambda_{K\alpha1}$=1.5406 Å and $\lambda_{K\alpha2}$=1.5444 Å in the 2Θ range of 20-70°. The patterns were analyzed using Rietveld refinement with the Fullprof

program 30 which includes modules to calculate the apparent crystal size and strain. An experimental resolution function was obtained from the refinement of a quartz reference in order to take into account the instrumental broadening[21].

2.7.4 NANOPARTICLE SIZE DETERMINATION

SPIONs hydrodynamic size was characterized in water and culture media by DLS. Moreover nanoparticle core size was measured by TEM. To visualize different aggregation state of SPIONs in culture media an optical microscope was used.

2.7.4.1. DYNAMIC LIGHT SCATTERING (DLS) AND ZETA POTENTIAL

DLS is the most used analytic technique to measure hydrodynamic diameter of particles in sub-micron region. DLS measures the size of submicron particles dispersed in a liquid that constantly collide with solvent molecules and move randomly in different directions with different speeds (Brownian motion). The more particles are smaller the more collisions are generating with the solvent and the more rapid they diffuse in the liquid. The size of a particle is calculated from the translational diffusion coefficient by the Stokes-Einstein equation:

$$d = kT / 3\pi\eta D,$$

where d is the hydrodynamic diameter, k is Boltzmann's constant, T is temperature, η is viscosity of colloidal suspension and D is the translational diffusion coefficient.

A laser irradiates the sample and the beam is diffracted by particles in Brownian motion. The detector measures the rate at which the intensity of the scattered light changes with the time due to particle movement (smaller particles induces more rapid fluctuations of light than larger particles). This intensity fluctuation of diffracted light is transformed into the final curve by instrument calculations (correlation function. you can checks on Malvern website for further informations).

Zeta potential is the electrical potential that exists at the interface of particle-liquid. SPION dispersed in a solution are electrically charged due to their ionic composition (Fe^{2+}, Fe^{3+}) and surface coating (TMAOH, sodium citrate). The development of a net charge at the particle surface affects the distribution of ions at the interfacial region, resulting in an increased concentration of counter ions (anions) close to the SPIONs surface. Each particle dispersed in a solution is surrounded by oppositely charged ions called fixed layer (also called Stern Layer). Outside the fixed layer, there are varying compositions of ions of opposite polarities. Thus an electrical double layer is formed in the region of the particle-liquid interface which is made by two parts: an inner region with ions bound relatively strongly to the surface and an outer, or diffusion region, in which the ion distribution is determined by a balance of electrostatic forces and random thermal motion. Therefore, the potential in this region decays with the distance from the surface and at certain distance it becomes zero (Fig. 23). During a zeta potential measurement an electric field is applied to a dispersion of particles, which move toward the opposite electrode at a speed related to their charge. Finally, through calculations the equipment converts speed of particles into their zeta potential value.

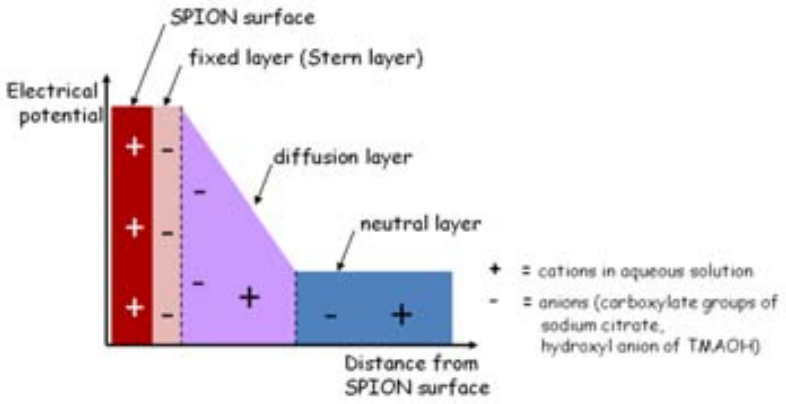

Figure 23. Graphic representation of zeta potential with double charged layer: fixed layer (Stern layer) and diffusion layer.

Dynamic light scattering and zeta potential experiments were performed using a Zetasizer Nano ZS instrument (Malvern Corporation) with a He/Ne 633 nm laser. The final hydrodynamic size is obtained by filling a plastic cuvette with 1 mL of colloidal dispersion analyzed with 15 scans, repeated three times. Laser Doppler Micro-electrophoresis is the technique used to measure zeta potential. The zeta potential of a colloidal dispersion in aqueous media at pH=7.4 was obtained by filling a disposable cell with 1 mL of colloidal dispersion, and measuring 15 scans repeated three consecutive times.

2.7.4.2. TRANSMISSION ELECTRON MICROSCOPY (TEM)

TEM is a microscopic technique used to visualize materials in of size less than 1 nm. It uses an electron beam which passes through an ultrathin sample. The interaction of a specimen with the electron beam forms an image which is magnified and projected onto a fluorescent screen. The sample has to withstand the penetration of the electron beam and the high vacuum (10^{-4} Pa) used to reduce collisions of electrons with gas molecules.

TEM was performed on SPIONs to measure their core size diameter. Samples were prepared as follows: few drops of diluted suspensions were deposited onto copper grids and liquid was left to evaporate at room temperature. Images were acquired using a transmission electron microscope JEOL 1210 at 120 kV and particle diameter was measured by counting 200 nanoparticles with ImageJ software.

2.7.4.3. CRYO-TEM

For TEM analysis of biological specimens like proteins or phospholipidic vesicles in aqueous solution in their "native state" it is needed to vitrify them, allowing electron beam penetration through the specimen with minimal energy loss.

Cryo-TEM analyses were used to visualize SPION dispersions in water and biological media at iron concentration of 10 mM. TEM images of water-born nanoparticles at pH= 7.4 were taken after rapid vitrification of particle suspensions. This was achieved by depositing a drop of SPION sample onto a Quantifoil® grid, and rapidly quenching it into liquid ethane. The grid

was then transferred into the TEM microscope (JEM-2011 operating at 200 kV) where the temperature is kept under -140 °C during the imaging.

2.7.4.4. OPTICAL MICROSCOPY

Optical microscope, often referred as "light microscope", uses visible light and a system of lenses to magnify images of samples with micrometric dimensions (1-100 µm).

We used optical microscopy to visualize the formation of SPION aggregates in culture media. In a multiwell plastic plate SPIONs at concentration of 50 µg/mL were dispersed in 1 mL of the following media: PBS 1X, DMEM F12 10% FBS and EGM-2 10% FBS, with or without 10 mM sodium citrate. Control wells consisted of the same media without SPIONs. Particle size aggregation was monitored during 1h using an optical microscope Olympus BX51 connected to a digital camera Olympus DP20. Images were taken with a 5x magnification objective.

2.7.5. TABLES WITH CHARACTERIZATIONS OF TD-SPION AND MW-SPION

This section includes two tables with TEM diameter, DLS hydrodynamic diameter, zeta potential, iron concentration, saturation magnetization at 300 K and blocking temperature of the main TD-SPION and MW-SPION batches used for nanoparticle characterizations and for *in vitro, in vivo* experiments.

Table 7. Characterizations of TD-SPION batches. Hydrodynamic diameter, zeta potential and iron concentration were determined using aqueous suspensions of SPIONs. Remaining measurements were done with dried samples. Ms= saturation magnetization; TB= blocking temperature.

batch	TEM diameter (nm)	Hydrodynamic diameter (nm) ± PD%	Zeta potential (mV)	Concentration (mg/mL Fe)	M_S (emu/g Fe_2O_3 at 300K)	T_B (K)
EC5-3	6.6 ± 1.3	20 ± 25%	-41	0.54	62	69
EC9	7.3 ± 1.2	28 ± 25%	-45	0.84	59	77
EC10-2	5.3 ± 1.2	30 ± 25%	-37	0.89	53	40
EC11	5.7 ± 1.3	31 ± 23%	-30	0.83	65	47
EC12	6.4 ± 1.4	36 ± 21%	-33	0.71	67	46

Table 8. Characterizations of MW-SPION batches. Hydrodynamic diameter, zeta potential and iron concentration were determined using aqueous nanoparticle suspensions of SPIONs. Remaining measurements were done with dried samples. M_S= saturation magnetization; T_B= blocking temperature.

batch	TEM diameter (nm)	Hydrodynamic diameter (nm) ± PD%	Zeta potential (mV)	Concentration (mg/mL Fe)	M_S (emu/g Fe_2O_3 at 300K)	T_B (K)
MW5	5.7 ± 1	15.6 ± 21%	-38	2.68	45	54
MW8	6.1 ± 1.1	14 ± 19%	-36	3.1	60	53
MW9	6.5 ± 1.6	13 ± 17%	-52	1.97	64	90
MW10	9 ± 2	16 ± 22%	-34	1.97	84	172
MW11	6.1 ± 1.3	15 ± 21%	-35	1.99	50	62

2.7. CHAPTER REFERENCES

1. Lu, A. H.; Salabas, E. L.; Schuth, F., Magnetic nanoparticles: synthesis, protection, functionalization, and application. *Angewandte Chemie* **2007,** *46* (8), 1222-44.
2. Osborne, E. A.; Atkins, T. M.; Gilbert, D. A.; Kauzlarich, S. M.; Liu, K.; Louie, A. Y., Rapid microwave-assisted synthesis of dextran-coated iron oxide nanoparticles for magnetic resonance imaging. *Nanotechnology* **2012,** *23* (21), 215602.
3. Sun, S.; Zeng, H.; Robinson, D. B.; Raoux, S.; Rice, P. M.; Wang, S. X.; Li, G., Monodisperse MFe2O4 (M = Fe, Co, Mn) nanoparticles. *Journal of the American Chemical Society* **2004,** *126* (1), 273-9.
4. Park, J.; Joo, J.; Kwon, S. G.; Jang, Y.; Hyeon, T., Synthesis of monodisperse spherical nanocrystals. *Angewandte Chemie* **2007,** *46* (25), 4630-60.
5. Sun, C.; Lee, J. S.; Zhang, M., Magnetic nanoparticles in MR imaging and drug delivery. *Advanced drug delivery reviews* **2008,** *60* (11), 1252-65.
6. Hou, Y.; Xu, Z.; Sun, S., Controlled synthesis and chemical conversions of FeO nanoparticles. *Angewandte Chemie* **2007,** *46* (33), 6329-32.
7. Willis, A. L.; Turro, N. J.; O'Brien, S., Spectroscopic Characterization of the Surface of Iron Oxide Nanocrystals. *Chemistry of Materials* **2005,** *17* (24), 5970-5975.
8. Xu, Z.; Shen, C.; Hou, Y.; Gao, H.; Sun, S., Oleylamine as Both Reducing Agent and Stabilizer in a Facile Synthesis of Magnetite Nanoparticles. *Chemistry of Materials* **2009,** *21* (9), 1778-1780.
9. Peng, S.; Wang, C.; Xie, J.; Sun, S., Synthesis and Stabilization of Monodisperse Fe Nanoparticles. *Journal of the American Chemical Society* **2006,** *128* (33), 10676-10677.
10. Hyeon, T.; Lee, S. S.; Park, J.; Chung, Y.; Na, H. B., Synthesis of highly crystalline and monodisperse maghemite nanocrystallites without a size-selection process. *Journal of the American Chemical Society* **2001,** *123* (51), 12798-801.
11. Taboada, E.; Rodriguez, E.; Roig, A.; Oro, J.; Roch, A.; Muller, R. N., Relaxometric and magnetic characterization of ultrasmall iron oxide nanoparticles with high magnetization. Evaluation as potential T1 magnetic resonance imaging contrast agents for molecular imaging. *Langmuir : the ACS journal of surfaces and colloids* **2007,** *23* (8), 4583-8.
12. Taboada, E. Synthesis of gamma-Fe2O3-SiO2 composite nanoparticles targeting magnetic resonance imaging and magnetic hyperthermia applications. PhD thesis, ICMAB-CSIC, Campus UAB, Spain, 2009.
13. Jolivet, J. P., *Metal oxide chemistry & synthesis: from solution to oxide*. Wiley: 2000.
14. McGuigan, C. F. Effect of nitrate on human cell lines in culture. Master Thesis, University of Saskatchewan, Canada, 2007.
15. Kappe, C. O., Controlled microwave heating in modern organic synthesis. *Angewandte Chemie* **2004,** *43* (46), 6250-84.
16. Bilecka, I.; Niederberger, M., Microwave chemistry for inorganic nanomaterials synthesis. *Nanoscale* **2010,** *2* (8), 1358-74.
17. Baghbanzadeh, M.; Carbone, L.; Cozzoli, P. D.; Kappe, C. O., Microwave-assisted synthesis of colloidal inorganic nanocrystals. *Angewandte Chemie* **2011,** *50* (48), 11312-59.
18. Bilecka, I.; Elser, P.; Niederberger, M., Kinetic and thermodynamic aspects in the microwave-assisted synthesis of ZnO nanoparticles in benzyl alcohol. *ACS Nano* **2009,** *3* (2), 467-77.
19. Ling, H.; Aurelien, P.; Denis, C.; Claire-Helene, B., Microwave-assisted one-step hydrothermal synthesis of pure iron oxide nanoparticles: magnetite, maghemite and hematite. *Journal of Sol-Gel Science and Technology* **2011**.
20. Pascu, O. Synthesis of magnetic nanoparticles and strategies towards magneto-photonic materials. PhD Thesis, ICMAB-CSIC, Campus UAB, Spain, 2012.
21. Pascu, O.; Carenza, E.; Gich, M.; Estradé, S.; Peiró, F.; Herranz, G.; Roig, A., Surface Reactivity of Iron Oxide Nanoparticles by Microwave-Assisted Synthesis; Comparison with the Thermal Decomposition Route. *The Journal of Physical Chemistry C* **2012,** *116* (28), 15108-15116.
22. Park, J.; An, K.; Hwang, Y.; Park, J.-G.; Noh, H.-J.; Kim, J.-Y.; Park, J.-H.; Hwang, N.-M.; Hyeon, T., Ultra-large-scale syntheses of monodisperse nanocrystals. *Nat Mater* **2004,** *3* (12), 891-895.
23. Auffan, M. R., J.; Chanéac, C.; Jolivet, J. P. et al., Surface reactivity of manufactured nanoparticles, in Nanosciences. In *Nanotoxicology and Nanoethics*, Springer: 2011; Vol. 4.

24. Cheng, F. Y.; Su, C. H.; Yang, Y. S.; Yeh, C. S.; Tsai, C. Y.; Wu, C. L.; Wu, M. T.; Shieh, D. B., Characterization of aqueous dispersions of Fe(3)O(4) nanoparticles and their biomedical applications. *Biomaterials* **2005,** *26* (7), 729-38.

25. Yu, S.; Chow, G. M., Carboxyl group (-CO2H) functionalized ferrimagnetic iron oxide nanoparticles for potential bio-applications. *Journal of Materials Chemistry* **2004,** *14* (18), 2781-2786.

26. Liu, J.; Sun, Z.; Deng, Y.; Zou, Y.; Li, C.; Guo, X.; Xiong, L.; Gao, Y.; Li, F.; Zhao, D., Highly water-dispersible biocompatible magnetite particles with low cytotoxicity stabilized by citrate groups. *Angewandte Chemie* **2009,** *48* (32), 5875-9.

27. Dubois, E. C., V.; Boué F.; Perzynski, R., Structural analogy between aqueous and oily magnetic fluids. *The Journal of Chemical Physics* **1999,** *111* (15), 7147-7160.

28. Fauconnier, N.; Bee, A.; Roger, J.; Pons, J. N., Adsorption of gluconic and citric acids on maghemite particles in aqueous medium. In *Trends in Colloid and Interface Science X*, Steinkopff: 1996; Vol. 100, pp 212-216.

29. Di Marco, M.; Guilbert, I.; Port, M.; Robic, C.; Couvreur, P.; Dubernet, C., Colloidal stability of ultrasmall superparamagnetic iron oxide (USPIO) particles with different coatings. *International journal of pharmaceutics* **2007,** *331* (2), 197-203.

30. Li, L.; Mak, K. Y.; Shi, J.; Leung, C. H.; Wong, C. M.; Leung, C. W.; Mak, C. S. K.; Chan, K. Y.; Chan, N. M. M.; Wu, E. X.; Pong, P. W. T., Sterilization on dextran-coated iron oxide nanoparticles: Effects of autoclaving, filtration, UV irradiation, and ethanol treatment. *Microelectronic Engineering* **2013,** *111* (0), 310-313.

31. Groman, E. V. J., L. Low molecular weight carbohydrates as additives to stabilize metal oxide compositions US 5102652, 1992.

32. Lynch, I.; Cedervall, T.; Lundqvist, M.; Cabaleiro-Lago, C.; Linse, S.; Dawson, K. A., The nanoparticle-protein complex as a biological entity; a complex fluids and surface science challenge for the 21st century. *Advances in colloid and interface science* **2007,** *134-135*, 167-74.

33. Pieper, R.; Gatlin, C. L.; Makusky, A. J.; Russo, P. S.; Schatz, C. R.; Miller, S. S.; Su, Q.; McGrath, A. M.; Estock, M. A.; Parmar, P. P.; Zhao, M.; Huang, S. T.; Zhou, J.; Wang, F.; Esquer-Blasco, R.; Anderson, N. L.; Taylor, J.; Steiner, S., The human serum proteome: display of nearly 3700 chromatographically separated protein spots on two-dimensional electrophoresis gels and identification of 325 distinct proteins. *Proteomics* **2003,** *3* (7), 1345-64.

34. Aggarwal, P.; Hall, J. B.; McLeland, C. B.; Dobrovolskaia, M. A.; McNeil, S. E., Nanoparticle interaction with plasma proteins as it relates to particle biodistribution, biocompatibility and therapeutic efficacy. *Advanced drug delivery reviews* **2009,** *61* (6), 428-37.

35. Hawkins, M. J.; Soon-Shiong, P.; Desai, N., Protein nanoparticles as drug carriers in clinical medicine. *Advanced drug delivery reviews* **2008,** *60* (8), 876-85.

36. Jansch, M.; Stumpf, P.; Graf, C.; Ruhl, E.; Muller, R. H., Adsorption kinetics of plasma proteins on ultrasmall superparamagnetic iron oxide (USPIO) nanoparticles. *International journal of pharmaceutics* **2012,** *428* (1-2), 125-33.

37. Lee, H.; Lee, E.; Kim do, K.; Jang, N. K.; Jeong, Y. Y.; Jon, S., Antibiofouling polymer-coated superparamagnetic iron oxide nanoparticles as potential magnetic resonance contrast agents for in vivo cancer imaging. *Journal of the American Chemical Society* **2006,** *128* (22), 7383-9.

38. Hinderliter, P. M.; Minard, K. R.; Orr, G.; Chrisler, W. B.; Thrall, B. D.; Pounds, J. G.; Teeguarden, J. G., ISDD: A computational model of particle sedimentation, diffusion and target cell dosimetry for in vitro toxicity studies. *Part Fibre Toxicol* **2010,** *7* (1), 36.

39. (a) Mailander, V.; Landfester, K., Interaction of nanoparticles with cells. *Biomacromolecules* **2009,** *10* (9), 2379-400; (b) Petri-Fink, A.; Steitz, B.; Finka, A.; Salaklang, J.; Hofmann, H., Effect of cell media on polymer coated superparamagnetic iron oxide nanoparticles (SPIONs): colloidal stability, cytotoxicity, and cellular uptake studies. *European journal of pharmaceutics and biopharmaceutics : official journal of Arbeitsgemeinschaft fur Pharmazeutische Verfahrenstechnik e.V* **2008,** *68* (1), 129-37.

40. Wilhelm, C.; Gazeau, F., Universal cell labelling with anionic magnetic nanoparticles. *Biomaterials* **2008,** *29* (22), 3161-74.

41. Xiao, K.; Li, Y.; Luo, J.; Lee, J. S.; Xiao, W.; Gonik, A. M.; Agarwal, R. G.; Lam, K. S., The effect of surface charge on in vivo biodistribution of PEG-oligocholic acid based micellar nanoparticles. *Biomaterials* **2011,** *32* (13), 3435-46.

42. Huhn, D.; Kantner, K.; Geidel, C.; Brandholt, S.; De Cock, I.; Soenen, S. J.; Rivera Gil, P.; Montenegro, J. M.; Braeckmans, K.; Mullen, K.; Nienhaus, G. U.; Klapper, M.; Parak, W. J., Polymer-coated

nanoparticles interacting with proteins and cells: focusing on the sign of the net charge. *ACS Nano* **2013,** *7* (4), 3253-63.

43. Safi, M.; Courtois, J.; Seigneuret, M.; Conjeaud, H.; Berret, J. F., The effects of aggregation and protein corona on the cellular internalization of iron oxide nanoparticles. *Biomaterials* **2011,** *32* (35), 9353-63.

44. Carenza, E.; Barceló, V.; Morancho, A.; Montaner, J.; Rosell, A.; Roig, A., Fast synthesis of water-dispersible SPIONs by microwave assisted route for safe labeling of endothelial progenitor cells. *Acta Biomaterialia* **2014,** (0).

45. Levy, M.; Lagarde, F.; Maraloiu, V. A.; Blanchin, M. G.; Gendron, F.; Wilhelm, C.; Gazeau, F., Degradability of superparamagnetic nanoparticles in a model of intracellular environment: follow-up of magnetic, structural and chemical properties. *Nanotechnology* **2010,** *21* (39), 395103.

46. Arbab, A. S.; Wilson, L. B.; Ashari, P.; Jordan, E. K.; Lewis, B. K.; Frank, J. A., A model of lysosomal metabolism of dextran coated superparamagnetic iron oxide (SPIO) nanoparticles: implications for cellular magnetic resonance imaging. *NMR in biomedicine* **2005,** *18* (6), 383-9.

47. Carenza, E.; Barcelo, V.; Morancho, A.; Levander, L.; Boada, C.; Laromaine, A.; Roig, A.; Montaner, J.; Rosell, A., In vitro angiogenic performance and in vivo brain targeting of magnetized endothelial progenitor cells for neurorepair therapies. *Nanomedicine* **2013**.

48. Taboada, E.; Solanas, R.; Rodríguez, E.; Weissleder, R.; Roig, A., Supercritical-Fluid-Assisted One-Pot Synthesis of Biocompatible Core(γ-Fe2O3)/Shell(SiO2) Nanoparticles as High Relaxivity T2-Contrast Agents for Magnetic Resonance Imaging. *Advanced Functional Materials* **2009,** *19* (14), 2319-2324.

49. Slowing, II; Vivero-Escoto, J. L.; Wu, C. W.; Lin, V. S., Mesoporous silica nanoparticles as controlled release drug delivery and gene transfection carriers. *Advanced drug delivery reviews* **2008,** *60* (11), 1278-88.

CHAPTER 3

MAGNETICALLY LABELED ENDOTHELIAL PROGENITOR CELLS FOR TARGETED THERAPEUTIC ANGIOGENESIS IN THE BRAIN

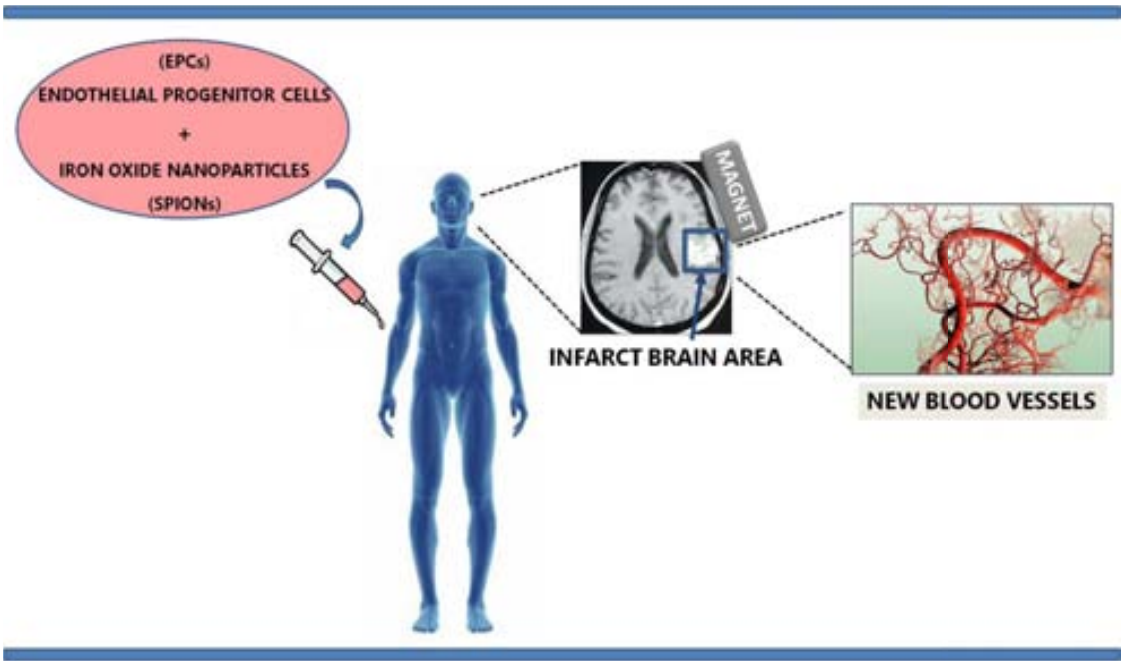

CHAPTER SUMMARY

In this chapter we firstly describe the essential role of endothelial progenitor cells (EPCs) in the angiogenic process which is the formation in adult subjects of new blood vessels from pre-existing ones, constituting an essential feature for tissue regeneration and growth. Secondly, we make a brief survey of recent studies based on non-invasive cellular therapy to induce angiogenesis in different organs and also in the brain. Finally, **we focus on our objective which is to obtain magnetically labeled EPCs that can be opportunely accumulated in a local area of the brain through a magnetic field created by a magnet implantation**. For this purpose we have developed protocols for an efficient and non-toxic cell labeling to achieve, as first step, functional magnetized EPCs.

CHAPTER INDEX pag.

3.1 PROGENITOR CELLS FOR ANGIOGENIC THERAPIES

3.1.1. ANGIOGENESIS: DEFINITION, MECHANISM AND THERAPEUTICAL APPLICATIONS

Blood vessels in skeletal animals are needed to transport oxygen and nutrients to the tissues. If the blood stream in the vascular system is reduced or obstructed it leads to deficits in tissue/organ functionality which can also be irreversible. This tissue condition is known as ischemia.

The angiogenesis, which is the physiological process through which the formation of new blood vessels occurs from preexisting ones, is fundamental during the embryonic growth carrying oxygen and nutrients to the organs in development. After birth, angiogenesis still contributes to organ growth but, during adulthood, most blood vessels remain quiescent. Nevertheless, angiogenesis can be triggered during the post-natal life for the maintenance of functional and structural integrity of the organism in particular circumstances as for instance wound healing or inflammation[1]. Angiogenesis activation or inhibition is the result of a complex regulation in the equilibrium between pro- and anti-angiogenic factors. When an excess of pro-angiogenic stimulation occurs it leads to disorders such as malignant, ocular and inflammatory disorders, cancer or autoimmune diseases. When the anti-angiogenic stimulation prevails it leads to ischemic heart disease, vessel malformation or regression.

Angiogenesis starts with endothelium activation determined by a balance of positive and negative regulators (cytokines, specialized molecules in intercellular communication) (Fig. 1). The cytokines involved in positive regulation of endothelial cells are VEGFs, FGFs among others which induce migration, proliferation, extracellular proteolytic activity or tube formation.

Figure 1. Sheme of the balance between negative and positive regulators of angiogenesis. When the pro-angiogenic stimulation prevails over the anti-angiogenic stimulation there is angiogenic activation.

In presence of a local angiogenic stimulus (such as ischemia) endothelial cells of pre-existing capillaries become activated: local vasodilatation, increased vascular permeability accumulation of extravascular fibrin, proteolytic degradation of the basal lamina and migration occur. Finally endothelial cell elongate and align with one another to form a capillary sprout (Fig. 2)[2].

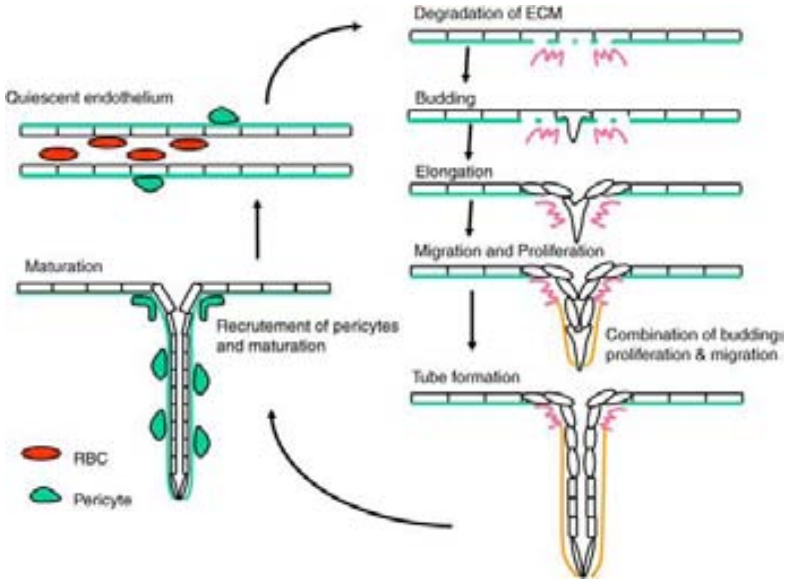

Figure 2. Angiogenic progression. Progression starts with degradation of extracellular matrix (ECM), followed by survival and budding of activated endothelial cell, migration and proliferation. By recruiting smooth muscle cells of microvessels, as pericytes, maturation proceeds. Dufraine, *Oncogene 2008,* 27, 5132–5137.

Why angiogenesis is an important therapeutic goal?

"Angiogenesis research will probably change the face of medicine in the next decades, with more than 500 million people worldwide predicted to benefit from pro- or anti-angiogenesis treatments."[3] Over the past decade, intensive efforts have been undertaken to develop therapeutic strategies to promote revascularization of ischemic tissues or to inhibit angiogenesis in cancer, ocular and skin disorders.

In adulthood, angiogenesis is activated in particular circumstances after wound healing, or fracture that means that not all tissues have the ability to start angiogenesis preserving their own structural and functional integrity after damage. For example coronary artery disease is a state of reduced transport of oxygen and nutrients to myocardic cells. The cardiac tissue has not the ability to induce local angiogenesis and if the blood flow is not restored in a short period of time, the tissue is irreversible damaged. That also happens in other tissues like limbs, retina and brain in conditions of reduced blood flow. Therapeutic angiogenesis strategies can stimulate revascularization in the ischemic tissues through different methods: direct administration of recombinant angiogenic factors[4,5] (VEGFs, FGFs, etc.), endothelial cells transplantation[6,7] or gene transfer[8,9]. The formers have the advantages of a more controlled toxicity and less secondary effects compared to the plasmids. However, the high costs of the synthesis of pyrogen-free recombinant proteins, the high cellular concentrations needed or the repeated administrations are important limiting factors for these methods[1].

We focused on two strategies to achieve revascularization in the brain: the endothelial cells transplantation (described in this chapter) and the encapsulation of pro-angiogenic factors into biodegradable nanoparticles (described in chapter 4).

3.1.2. ANGIOGENIC THERAPIES WITH ENDOTHELIAL PROGENITOR CELLS

Endothelial cells (ECs) cells make up the inner part of blood vessels, named endothelium, which could be surrounded by an external layer of smooth muscles or pericytes (Fig. 3). ECs are specialized cells involved in:

- regulation of blood pressure due to the ability of modulating the contraction of the smooth muscle, for instance by delivering the relaxing-factor nitric oxide;

- regulation of thrombosis-fibrinolysis processes for instance by exposing on the cellular surface molecules as like heparan sulfate,

- regulation of the metabolism acting like a semi-permeable barrier with active transport of molecules from the blood stream.[10]

Moreover the endothelium can be activated by angiogenic factors like VEGFs, FGFs and start angiogenesis.

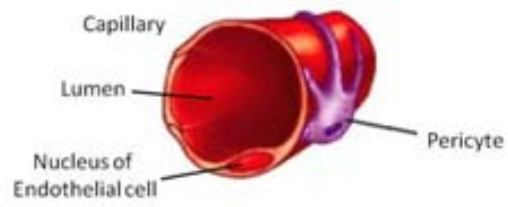

Figure 3. Structure of a small blood vessel (capillary). There is one layer (endothelium) made of endothelial cells which are connected among them throughout tight junctions. Pericytes are contractile cells found wrapped about capillary or small blood vessels. Dorland's Medical Dictionary for Health Consumers 2007.

Up to few years ago it was considered that the formation of new blood vessels during the adulthood was solely due to cell proliferation and migration from pre-existing blood vessels (angiogenesis). Vasculogenesis, which is the formation of new blood vessels from stem cells (progenitor cells) was believed to act only during the embryogenic state. An important breakthrough came with the demonstration of the existence in the peripheral blood of circulating endothelial progenitor cells (EPCs) which are cells with stemness characteristics that can differentiate in endothelial cells and which can be integrated into the endothelium promoting angiogenesis[11,12]. It was discovered the great potential of EPCs for therapeutic angio-vasculogenic purposes.

Initially, EPCs found in peripheral blood were proved to derive from bone marrow. EPCs under particular stimuli (chemokines, VEGF-A, FGFs) can be mobilized from the bone marrow, enter in the blood stream and reach ischemic sites where they complement the angiogenesis started by the endothelium (Fig. 4). This pool of cells is also named circulating EPCs to distinguish them from EPCs resident in the bone marrow[7,13,14,15].

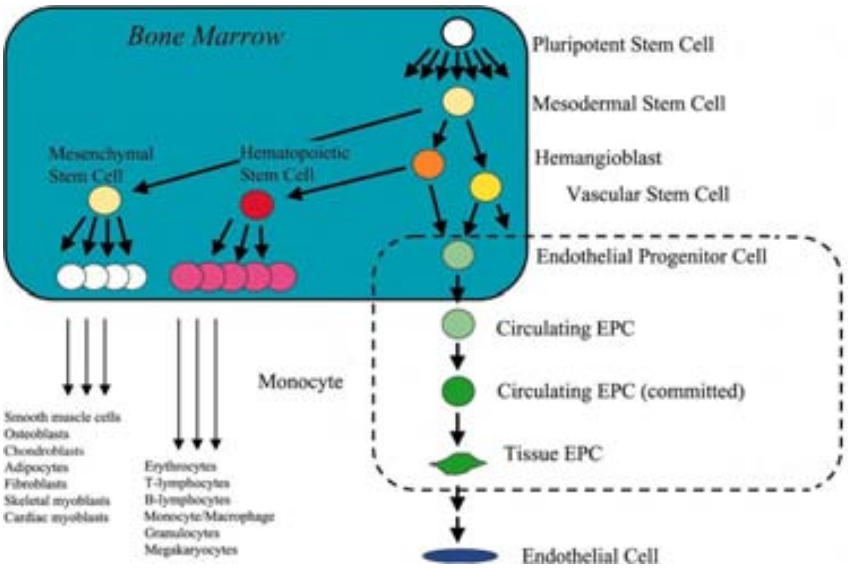

Figure 4. Picture showing the human bone marrow-derived endothelial progenitor cell differentiation. Asahara T., *Am J Physiol Cell Physiol 2004*, 287(3):C572-9.

The mobilization and incorporation of EPCs occur only in few organs as for instance in the vasculature of skin, liver, skeletal and muscles. In other organs like limbs, retina, myocardium and brain circulating EPCs cannot be easily integrated[7]. For this reason it has been proposed to inject external EPCs into these organs to facilitate the revascularization process.

Cell-culture techniques of EPCs from peripheral blood yield two populations with different characteristics (Fig. 5):

- Early-EPCs which are spindle shaped and appear in the first days of culture. They have no clonogenic potential and secrete a higher amount of angiogenic factors[16];
- Outgrowth EPCs (OECs), which appear in culture later, with endothelial-like shaped and clonogenic abilities. OECs are able to form capillary tubes, in vitro.[17,18]

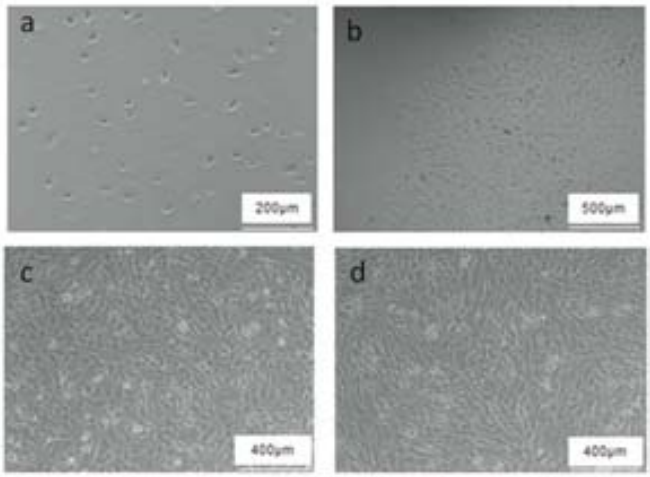

Figure 5. Images of EPCs at the optical microscope: a) early-EPCs from a mouse cell culture. b) early-EPCs growing colony from a human cell culture. c) mouse outgrowth EPCs. d) human outgrowth EPCs.

Kalka and coworkers demonstrate the possibility to isolate circulating EPCs from the peripheral blood in sufficient quantities to permit their harvest and after *ex-vivo* expansion, their intravenous administration for the purpose of enhancing revascularization in ischemic

tissues[19]. In particular they demonstrated perfusion enhancement within 28 days after EPCs transplantation in mice with hindlimb ischemia (Fig. 6).

Figure 6. Administration of EPCs leads to reduced limb loss and increased limb recover. Representative macroscopic photographs of mice showing three different outcomes observed in the study. (Left) autoamputation, characterized by loss of the ischemic hindlimb. (Middle) severe foot necrosis. (Right) most favorable outcome, complete salvage of ischemic hindlimb with intact function. Kalka, *PNAS 2000*, 97 (7):3422–3427.

Furthermore it was discovered that EPCs are present not only in the bone marrow, but also in the cord blood and adipose tissue opening to new sources for EPCs isolation and *in vitro* expansion (Fig. 7).[20]

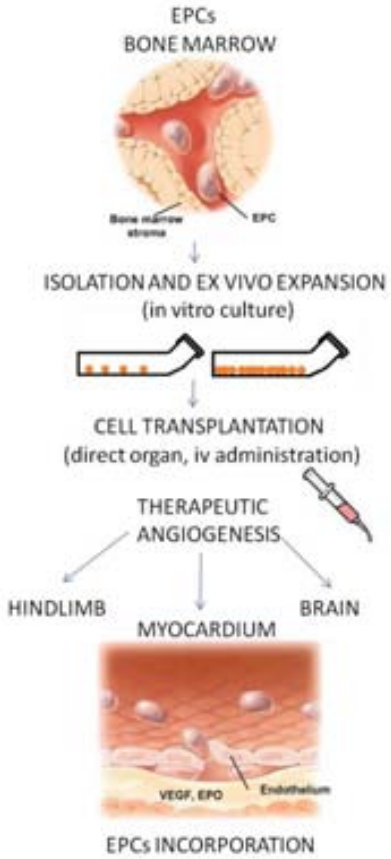

Figure 7. EPCs derived from the bone marrow, cord blood or peripheral blood can be isolated and expanded in suitable in vitro conditions, until reaching the sufficient number to be harvested and transplanted by direct injection or intravenous administration in the ischemic organ (hindlimb, myocardium, brain). The transplanted EPCs are incorporated into the endothelium and facilitate tissue revascularization by growth factors release and forming new endothelial cell connections. Modified pictures from Rabelink, *Arterioscler Thromb Vasc Biol 2004*; 24:834-838.

3.1.3. ANGIOGENIC THERAPY IN THE BRAIN: A PARTICULAR TARGET

Stroke, also known as "cerebrovascular accident," occurs when brain tissue is deprived of oxygen due to local reduction or interruption of blood perfusion. The oxygen-deprived area that leads to cell death is called infarct. Depending on which area of the brain has been affected, a stroke can cause neurological deficits related to speech, behavior, memory and might result in permanent brain damage, disability or death.

Differently from other organs, the wall of a cerebral blood vessel is more difficult to be permeated by exogenous molecules due to the blood brain barrier selectivity. For that it is difficult to find effective neuroprotective therapies in cerebral ischemia. After stroke, few treatment options are available and a high percentage of patients suffer of permanent disabilities (approximately 35% of cases). The only Food and Drug Administration (FDA)-approved treatment for ischemic strokes is tissue plasminogen activator (tPA). tPA works by dissolving the clot and improving blood flow toward the part of the brain which is hipoperfused. If administered within 4.5 hours, tPA may improve the chances of recovering from a stroke[21]. A significant number of stroke victims do not get to the hospital in time for tPA treatment; this is why it is so important to identify a stroke immediately[22].

Currently new strategies are under investigation to restore the blood flow into the ischemic brain region by stimulation of the area surrounding the infarct (named peri-infarct area which is not damaged) through chemokines release (erythropoietin, interleukines)[23].

Taguchi et al.[24] have demonstrated that the administration of EPCs after 48 hours of cerebral ischemia induces neurovascularization and a favorable environment for neuronal regeneration in animal models (mice). How transplanted cells work? After cell transplantation in the ischemic brain cells grow and secrete growth factors which are necessary for cell functional recovery. The brain recovers in two steps: an early stage of neuronal regeneration independent from neurovascularization and a delayed step which is VEGF dependent and coincident with vascularization.[25]

The administration route affects the migration and distribution of progenitor cells. Li and coworkers[26] verified through MRI studies that the intraarterial administration of neural progenitor cells increased migration with a high number of transplanted cells reaching the target brain area, but it also lead to high mortality (41%) compared to intracisternal (17%), and intravenous (8%) administration routes. In another study[27] it is argued that the major obstacle for intravenous administration of stem cells is the pulmonary filter, demonstrating that the majority of administrated stem cells are trapped in the lungs. Particularly, it has been estimated that less than 0.5% of administered cells reach the arterial system after standard intravenous administration and that only 0.0005% of intravenously administered stem cells reach the brain parenchyma in an animal model with brain injury[26]. Therefore, it is crucial to increase the number of stem cells reaching the arterial circulation to have an efficient stem cell therapy and subsequent tissue regeneration.

One strategy for increasing stem cells accumulation in the target area is by endowing stem cell with targeting capabilities. In the last 30 years numerous studies have been conducted on

engineered nanoparticles with the purpose, among others, to accomplish targeted drug delivery or targeted cellular therapy. Along with the targeting capabilities, "multifunctional nanoparticles"[28,29] have been developed to allow the real time tracking of transplanted cells during their migration (imaging properties). Iron oxide superparamagnetic nanoparticles (SPIONs) are multifunctional particles because they have the targeting capability due to their magnetic properties and can be visualized by means of Magnetic Resonance Imaging (MRI), acting like contrast agents. SPIONs are biocompatible materials approved by the Food and Drug Administration. There are examples in literature of transplanted stem cells efficiently labelled with magnetic nanoparticles *in vitro* (before being transplanted)[30,31]. The injected cells have been also guided by an external magnetic field until reaching the target area and they have been visualized in the host tissue[32].

Neural stem cells have also been successfully guided into the ischemic brain[33]. Kyrtatos and coworkers[34] described a successful external magnetic targeting using labelled EPCs with 5 fold enhanced cell retention at the site of vascular injury after 24 hours from the *in vivo* implantation. So far, encouraging results have been obtained in pre-clinical and clinical studies on therapeutic angiogenesis using EPCs, mainly in hindlimb[19,35] and myocardium[36,37] ischemia, and there are ongoing studies on monitoring EPCs distribution and engraftment after cell transplantation[38,39,40]. To date, little is known about magnetically labeled EPCs transplantation for targeted therapeutic angiogenesis in the brain. Only recently Li and et al. demonstrated that under an exterior magnetic field EPCs, labeled with silica-coated superparamagnetic iron oxide nanoparticles (SiO_4@SPIONs) could be guided to ischemic region of the brain and enhance therapeutic effect, suggesting that magnetic-guided SiO_4@SPIONs-EPCs delivery is a promising approach in cerebral ischemic therapy[41].

In this thesis, we have developed a protocol to obtain at the same time the guided-accumulation in the brain of magnetically labeled functional EPCs by external magnet implantation and the imaging of cell distribution using MRI[42] (Fig. 8).

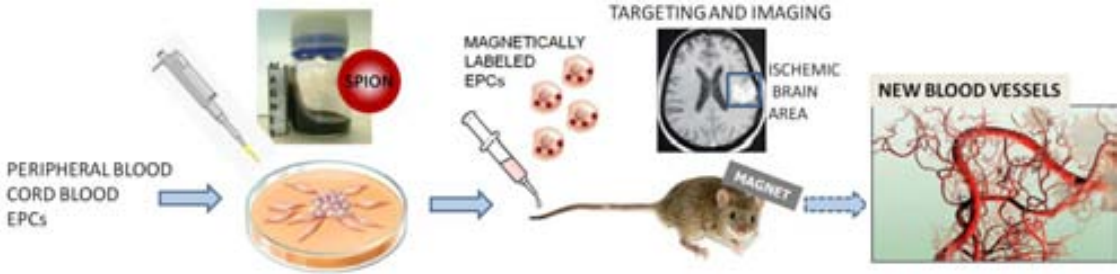

Figure 8. Used protocol to labeled EPCs: EPCs are isolated from peripheral blood, cord blood or other organs (spleen). They are *ex vivo* expanded and subsequently treated with SPIONs. Magnetically labelled EPCs are harvested and transplanted through intravenous injection in the mouse. Magnetically labeled cells are guided by an implanted magnet on the mouse skull and visualized by MRI. The angiogenic performance of magnetized EPCs in animal models of brain ischemia has still to be demonstrated.

3.2 NANOPARTICLE CELLULAR UPTAKE

3.2.1. CELLULAR UPTAKE MECHANISM

The plasma membrane is the interface between cells and their environment. At this interface uptake of nutrients, intercellular communications as well as cell-environment communication occur. Essential small molecules, such as amino acids, sugars and ions, can traverse the plasma membrane through the action of integral membrane protein pumps or channels. Macromolecules must be carried into the cell in membrane-bound vesicles derived by the invagination of the plasma membrane (endocytosis). Endocytosis has a crucial role in cellular development, immune responses, neurotransmission, intercellular communication, signal transduction, and cellular homeostasis. It occurs by multiple mechanisms that can be divided into two broad categories (Fig. 9):

- Phagocytosis, or cell "eating". Phagocytosis is typically restricted to specialized mammalian cells and it regards the uptake of large particles;
- Pinocytosis or cell "drinking" (the uptake of fluid and solutes) occurs in all cells by at least four basic mechanisms: macropinocytosis, clathrin-mediated endocytosis (CME), caveolae-mediated endocytosis, and clathrin- and caveolae independent endocytosis.

There are cells which are professionals of endocytosis, the macrophages, with an important role in the elimination of pathogens by phagocytosis[43].

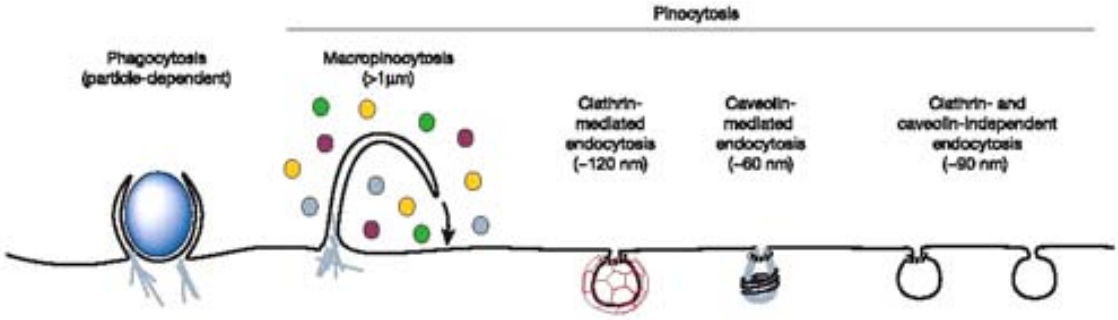

Figure 9. Schematic description of the principal mechanisms of cellular endocytosis. Conner, Nature (2003) 422, 37-44.

Uptake of particles into a wide variety of cells is an effect that seems to be specific for materials in the range of 50-200 nm based on the size of endocytic vesicles (Fig. 9). Along with the material size, the hydrophobic/hydrophilic surface characteristic also influences the type of receptor mediated endocytosis.[44,45]

Finally it has to be mentioned the important role of plasma proteins in the uptake mechanism. There are numerous studies demonstrating that the particle coated by protein corona is the real active biological entity influencing numerous cellular processes[46]. For example, 50-nm polystyrene particles pre-incubated in plasma are internalized by Kupffer cells (liver macrophages) via scavenger receptors and the plasma protein fetuin was shown to mediate this uptake[47].

3.2.2. STATE OF THE ART ON SPIONs UPTAKE

As previously mentioned, the type of internalization process into cells (phagocytosis, receptor mediated, etc.) is related to particle characteristics (particle size, surface coating). Gazeau and coworkers[48] proposed a general method to describe the uptake of citrate coated SPIONs of 30 nm in hydrodynamic diameter by different mammalian cells: adult, progenitors, immune and tumor cells. They analyzed and compared parameters like the binding constant of SPIONs to the cellular membrane (affinity constant), the cell diameter, the time of internalization for each cell type and they concluded the citrate coated SPIONs internalization can be divided into two steps: the first one cell-independent and the second one cell-dependent. The first step is the electrostatic adsorption onto reactive sites of the cell membrane (cationic sites) which occurs in the same way for all cell types; the second step is the internalization of saturated reactive sites by endocytosis with variable cell membrane invagination depending on cell dimensions[49]. It is worth mentioning that the binding affinity of citrate-coated SPIONs to the cell membrane is generally lower than the affinity of cationic liposomes, but it is comparable with the affinity of the free Fab fragment from 4D5 antibody on its membrane receptor.

However many details on SPIONs endocytosis mechanisms have not been clarified yet. For instance referring to citrated-coated SPIONs (hydrodynamic size of 30 nm) Gazeau states that clathrin mediated endocytosis occurs for a wide range of mammalian cells, whereas Hoffman reported on the integrin receptor MAC-1 contribution in the uptake of PVA-coated SPIONs (hydrodynamic size of 30 nm) by immune cells[50].

In conclusion, the definition of SPIONs endocytosis as specific- or non-specific receptor mediated pathway still remains controversial, nevertheless it seems generally accepted the hypothesis that different mechanisms can operate depending on particle characteristics and the type of cell.

Another important aspect influencing cell-SPIONs interactions is related to particle surface plasma protein adsorption. Müller and coworkers[51] demonstrated that citrate-triethylene glycol coated SPIONs of about 7 nm incubated with different fetal bovine serum aqueous dilutions formed rather stable corona in time: immunoglobulin and fibrinogen were the most abundant proteins adsorbed onto the particle surface. Often particle surface functionalization with polymers (eg. with PEG, polaxamer, dextran) are required to minimize particle–serum protein interactions when long blood circulation time and reduced opsonization by the reticuloendothelial system (RES system) are needed[52,53]. However, impurities and product of oxidative degradation of used polymers are associated with certain pharmacological and immunological effects[54]. In our study, in which nanoparticles do not have to be directly injected in the blood stream, it is not the major requirement to avoid SPIONs -protein interactions since particle final destination will be the cell cytoplasm. For this reason we preferred the use of easily fabricated citrate-coated SPIONs suitable for cellular labeling.

3.2.3. SPIONs INTO CELLULAR COMPARTMENTS AND MRI EFFECTS

In addition to the sample crystallinity, both particle size and aggregate size should be considered in order to explain the magnetic and relaxivity values of a suspension[55].

Superparamagnetic agents enhance both T_1 and T_2/T_2* relaxation. T_1 relaxivity can be improved (and so T_2/T_2* effect can be reduced) using small particles.[56,57]

Ultra small SPIONs have generally quite high r_1 longitudinal relaxivities and the r_2/r_1 ratio is low, less than 3. When there is particle aggregation longitudinal relaxivity r_1 tends to decrease and at the same time there is a big increase on transverse relaxivity (r_2). That is because transverse relaxation (T_2 spin-spin relaxation) is due to loss of phase coherence of the rotating spins in the plane and is fastened by "outside interferences". So, if particles cluster together the signal in the plane decays faster and the relaxivity r_2 increases. This has important consequences when considering the effects of contrast agent compartmentalization on imaging. The confinement of SPIONs into intracellular vesicles endosomes and lysosomes, implicates particle aggregation and for that reason the T_2 signal decays of cells labeled with SPIONs are greater than the signal decays of dispersed nanoparticles (comparing the same amount of magnetic material)[58].

3.3 ENDOTHELIAL PROGENITOR CELLS LABELING USING TD-SPIONs

The type of EPCs subpopulation used for the *in vitro* experiments has been specified as early-EPCs, outgrowth-EPCs (OECs) or the EPCs referring to any of them.

3.3.1. SPIONs LOADING AND CYTOTOXICITY

To find the best conditions for high labeling efficacy and low toxicity we tested different SPIONs concentrations and times of incubations on EPCs. SPIONs used were synthesized by thermal decomposition (see chapter 2) and labeled as TD-SPIONs. By magnetometry and chemical analysis we determined higher intracellular iron contents at longer incubation times (table 1). Regarding mouse OECs, even after 24 hours (the longest period of incubation time) the amount of intracellular iron was significantly lower when compared to the amount internalized by early EPCs (0.93± 0.05 pg/cell vs. 24.7± 3.4 pg/cell; p=0.04). Thus we can calculate the number of nanoparticles per cell after 24 hours of incubation being: $5.6x10^6$ SPIONs/early EPC and $2.5x10^5$ SPIONs/OEC (see annex of chapter 3, paragraph 3.6.3.1). Prussian blue stain was used to confirm iron uptake for both types of cells (Fig. 10). The explanation for the different extent of iron uptake could be related to the differences between the two cell populations: early-EPCs are a heterogeneous group of cells, while OECs are homogeneous and well differentiated[17,16]. Early-EPCs present analogies with monocyte/macrophages and for that reason they may also share phagocytic abilities.

Table 1. Iron content per cell after magnetization with TD-SPIONs at different incubation times. Values express mean±SD (n=3 per group). Measurements by magnetometry (SQUID).

Mouse Cells	Incubation time-with SPIONs	Iron Content (pgFe/cell)
Early EPCs	2 hours	7.7±1.7
Early EPCs	6 hours	10.7±2.9
Early EPCs	24 hours	24.7±3.4
OECs	24 hours	0.93±0.05

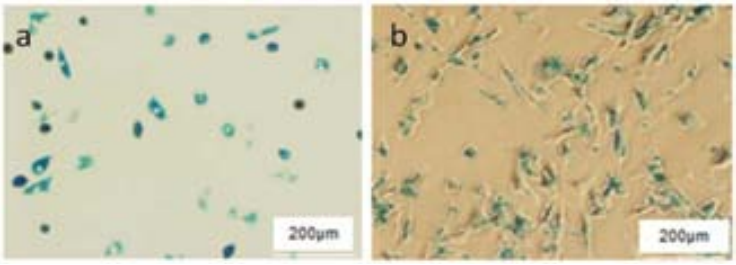

Figure 10. Prussian blue stain of early-EPCs (a) and OECs (b) from mouse after labeling for 24h with 50 µg/mL of TD-SPIONs.

MTT assays indicated that co-incubation of TD-SPIONs with mouse early-EPCs or OECs did not affect cell viability at any of the tested concentrations of 25, 50 and 100 µg/mL (Fig. 11a). However, a slight decrease in cell viability was observed for OECs obtained from stroke patients (83.6 ± 6.3%; $p<0.05$) in comparison to non-treated cells (Fig. 11b). To reach the highest contrast effect with the lowest toxicity for cells we selected as best concentration for EPCs labeling the 50 µg/mL for upcoming experiments.

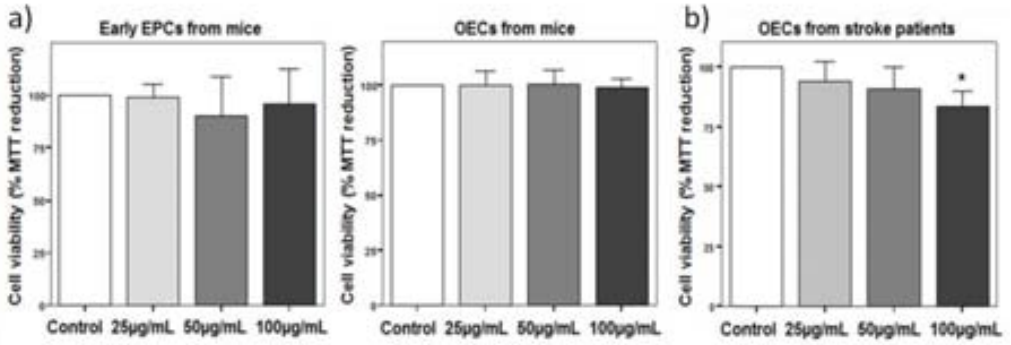

Figure 11. MTT tests on EPCs incubated with TD-SPIONs at concentrations between 25 and 100 µg/mL. a) early-EPCs and OECs from mouse do not show significant variations in cytoxicity compared to control cells; b) OECs obtained from human stroke patients show slight decrease in viability at the highest concentration.

Magnetic guidance after 24 hours cell magnetization was tested, in vitro, by applying a magnetic field near the pellet of EPCs collected from mice. We confirmed that magnetized EPCs were rapidly guided towards the magnet and remained there until the magnet was removed (Fig. 12).

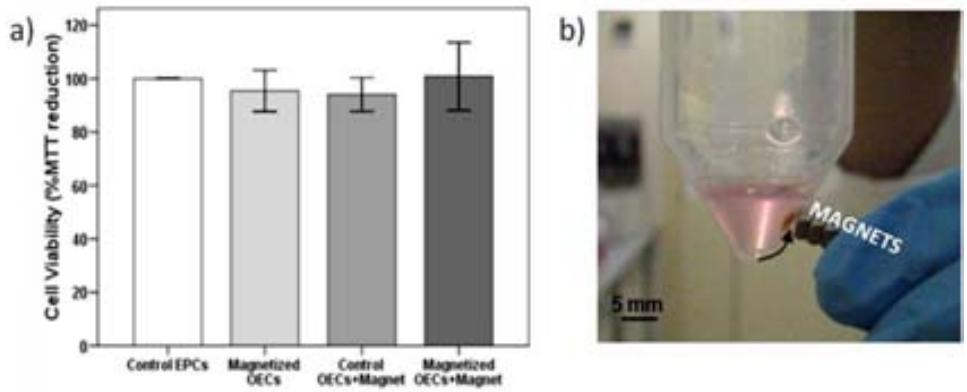

Figure 12. Cell viability determined by MTT assay: a) MTT assay after TD-SPIONs cell-magnetization and magnetic field exposure. Bar graphs represent cell viability for mouse OECs (n=4 independent experiments per treatment). EPCs treated with TD-SPIONs 50 µg/mL, 24 h; b) picture showing the movement of magnetically labeled EPCs (brown pellet) towards the magnets.

In literature it is reported that high nitrate concentration in combination with ammonium may induce cell toxicity[59]. TMAOH is proved to induce cytotoxicity[60,61]. During the labeling experiments we also found some toxicity associated to the "vehicle" media of SPIONs, obtained by separation of the solid phase (nanoparticles) from the aqueous medium containing TMAOH, nitric acid: the treatment of OECs from stroke patients with the vehicle solution resulted in reduced cell viability (86.6 ± 7.7%; $p<0.05$). For that reason, we preferred to synthesize nanoparticle batches with low amounts of TMAOH and nitric acid (see chapter 2, paragraph 2.1.3).

Electron microscopy demonstrated cellular uptake of TD-SPIONs and their confinement into intracellular vesicles endosomes/lysosomes (Fig. 13). Likewise, electron microscopy revealed that the amount of endosomes/lysosomes containing SPIONs was larger in early EPCs than in OECs (as shown in Fig. 13a and 13c, respectively) which is in agreement with the magnetometry results shown in Table 1. In both type of cells, diffraction pattern obtained on selected endosomes confirmed the presence of an iron oxide inverse spinel phase (Fig. 13b and 13d). The cytoplasmatic localization of TD-SPIONs matched with the iron localization found by standard Prussian blue staining (showed in Fig. 10).
About the possible identification of SPIONs into endosomes or lysosomes it is known that the material internalized by cells is initially confined into early endosomes which mature to late endosomes. Late endosomes are mainly spherical and contain many close-packed lumenal vesicles. They fuse their membrane with lysosomes which are denser and contain enzymes which start the material degradation[62]. Considering the outcomes of the degradation experiment described in chapter 2 and the TEM pictures (Fig. 13a-d) we can conclude that after 24 hours of incubation EPCs contain SPIONs into early and late endosomes. The presence of SPIONs into lysosomes and their enzymatic degradation is expected to become evident after 24 hours.

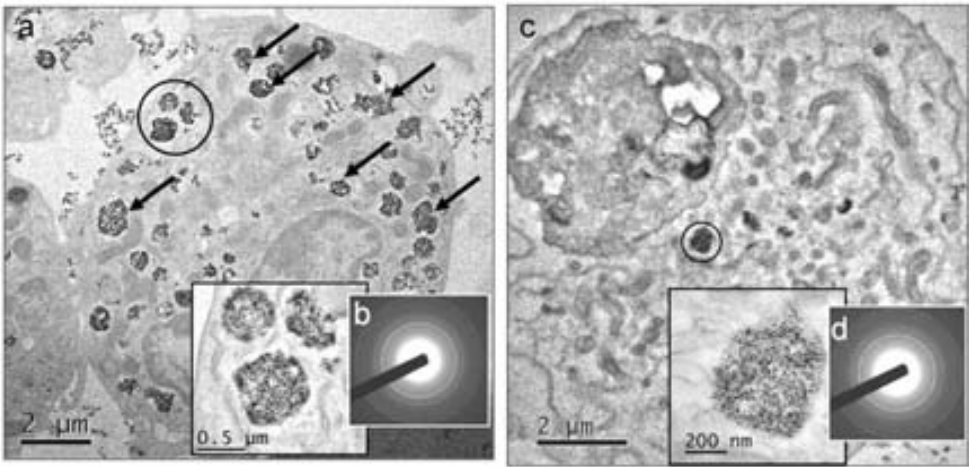

Figure 13. TEM pictures a) magnetized early-EPC (TD-SPIONs 50 µg/mL, 24 hours) with black arrows indicating intracellular vesicles with SPIONs. Inset: larger magnification with enhanced contrast between organic and inorganic components of a magnetized EPC; b) electron diffraction analysis of selected intracellular compartments; c) magnetized outgrowth-EPCs (TD-SPIONs 50 µg/mL, 24 hours). Inset: larger magnification with enhanced contrast between organic and inorganic components of a magnetized EPC; d) electron diffraction analysis of selected intracellular compartments.

3.3.2. MRI MEASUREMENTS

SPIONs synthesized by thermal decomposition had excellent T_2 relaxation properties. In this regard, the longitudinal (r_1) and transverse (r_2) relaxivities at 7 Tesla were found to be 1.6 mM^{-1} s^{-1} and 93 mM^{-1} s^{-1}, respectively, and relaxivity for r_{2*} was found to be 129 mM^{-1} s^{-1}. Moreover, the T_2 value was reduced in an iron dependent manner in the agarose phantoms visualized as dark signals in T2-weighted images (Fig. 14a).

Cells loaded with SPIONs were also visualized in T_2 weighted images. Phantoms prepared with suspensions of magnetized EPCs showed a clear signal decay in a cell-concentration dependent manner, becoming visible (dark signal) at dilutions as low as 1.3 x 10^4 cells/mL, while remaining invisible with non-magnetized EPCs (Fig. 14b).

Moreover, T_2 map quantifications showed clear signal decay at increased concentrations of magnetized EPCs compared to non-magnetized cells (Fig. 15).

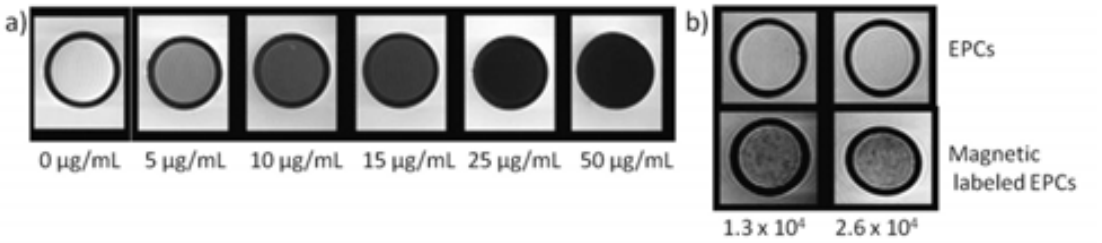

Figure 14. a) Agarose control and iron-dependent concentration of TD-SPIONs; b) Phantom images of early mouse EPCs (top) and magnetized early mouse EPCs (bottom). Note that magnetized cells can be detected as hypointense signals (dark dots).

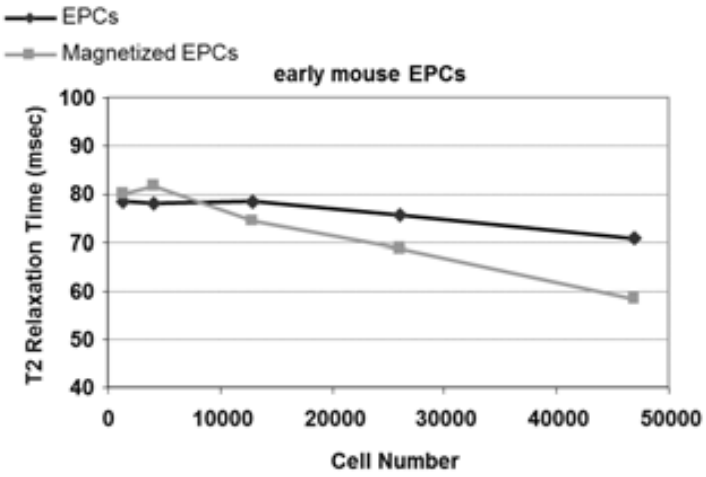

Figure 15. T_2 signal intensity quantified from corresponding T_2 maps obtained from phantoms containing increasing amounts of EPCs. Note that the signal decay is more significant for magnetized EPCs.

3.3.3. FUNCTIONALTY TESTS OF EPCs AFTER SPIONs LABELING

We verified through a set of *in vitro* experiments that EPCs after treatment with TD-SPIONs at concentration of 50 µg/mL (expressed as iron concentration), during 24 hours, does not show remarkably changes in cellular functionality compared to no treated cells (control). We tested the abilities of magnetized EPCs to form tubular connections (tubulogenesis) into Matrigel® substrate, to migrate following a magnetic field gradient and release growth factors as will be shown in the next pages.

3.3.3.1. IN VITRO TUBULOGENESIS

Using *in vitro* angiogenesis assays with Matrigel® matrix[63,64] we demonstrated the ability of magnetically labeled OECs to form tubes, named tubulogenesis (characteristic not expressed by Early-EPCs subpopulation). Indeed, our results indicated that magnetized OECs isolated from mice formed vessel-like structures similar to control cells in Matrigel® (Fig. 16). Interestingly it was found that human OECs from stroke patients also preserved their tube formation properties after magnetization (Fig. 17).

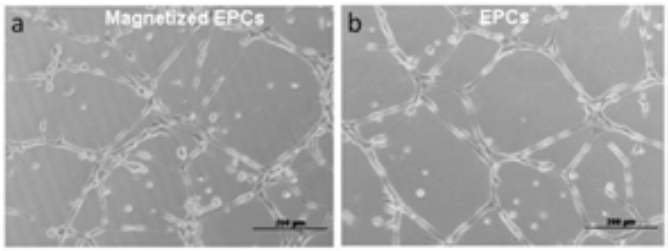

Figure 16. In vitro tubulogenesis, formation of vessel-like structures in Matrigel® matrix. a) Magnetized mouse OECs with 50 µg/mL of TD-SPIONs; b) control mouse OECs.

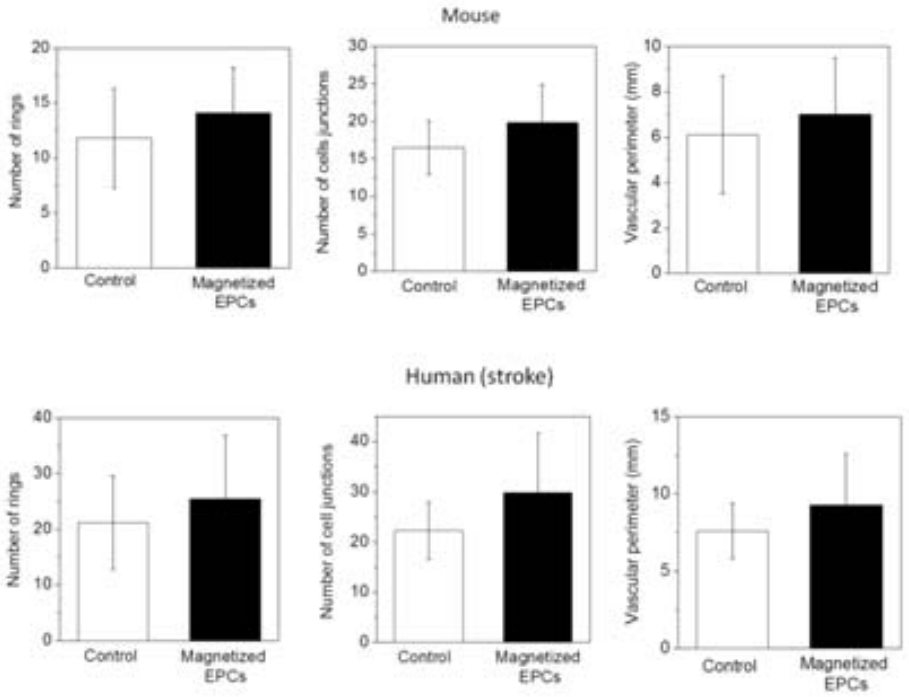

Figure 17. Quantified tubulogenesis: the number of complete rings (n=6 in mouse, n=4 in human), cell junctions and vascular perimeters were not significantly different between magnetized (with 50 µg/mL of TD-SPIONs, 24 h of incubation) and control EPCs.

3.3.3.2. CELL MIGRATION

Cell migration is essential for angiogenesis and is regulated by chemotactic, haptotactic, and mechanotactic stimuli.[2,65]

Transwell migration assays were performed to compare the ability of magnetized EPCs versus control EPCs to migrate in presence or in absence of a magnetic field (Fig. 18a). After 48 h of incubation (see details in annex of chapter 3, paragraph 3.6.5.1), the percentage of cells found in the lower part of the transwell insert was higher for magnetized cells and magnetized cells in presence of a magnet than control cells (2.19 ± 1.00 and 2.09 ± 0.83 vs. 1.52 ± 0.58; p=0.037 and p=0.077, respectively). Interestingly it was noticed that magnetized EPCs, once crossed the membrane pores, in presence of the magnetic field source migrated more efficiently toward the bottom of the well (Fig. 18b). Representative images of the transwell-migrated cells are shown in annex of chapter 3, paragraph 3.6.5.1.

Results of migration assays indicate that magnetized EPCs display enhanced endogenous migration ability compared to control cells and that magnetized EPCs migrated towards areas with larger magnetic field gradients. We believe that migration towards the lower chamber is clearly influenced by cell magnetization and that magnetic forces guide magnetized cells towards the bottom of the plate. If it is assumed an *in vivo* setting, we can hypothesize that circulating magnetized EPCs would be retained in the blood vessel wall close to the zone with highest magnetic attraction and then display enhanced migration abilities within the local region.

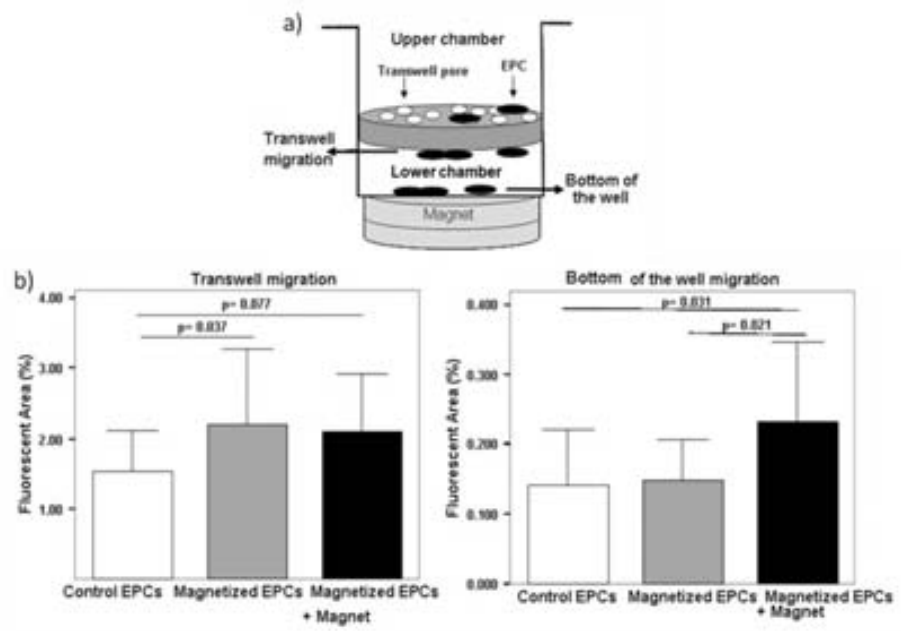

Figure 18. Transwell assay: a) schematic picture of a transwell set up and areas of quantification; b) Bar graphs showing percentage of fluorescent cells per field migrated through the transwell membrane (n=15) or to the bottom of the well (n=10).

3.3.3.3. QUANTIFICATION OF SECRETED GROWTH FACTORS

The ability of EPCs to secrete growth factors and participate in paracrine cell-signaling (the ability to release molecules which induce changes in nearby cells) after magnetic labeling is an important parameter to take into account for an effective angiogenic cellular therapy. As previously mentioned, beside vasculogenic activation, EPCs also promote angiogenesis by releasing VEGFs, FGFs, PDGF, SDF-1 and others pro-angiogenic factors (see chapter 4 for further details).

Through Searchlight® Multiplex Protein analysis that measure the protein content of VEGF, FGFb, HGF and PDGFbb we demonstrated that magnetized human and mouse OECs secreted more VEGF and FGF than control cells (table 2). The increment of FGF was around 35% in mouse and 55% in human magnetized OECs, while the increment of VEGF was 10 fold (1000%) in mouse and around 60% in human magnetized OECs. Similar amounts of HGF were secreted by magnetized and control mouse EPCs and we were unable to detect PDGF in our assay. We also confirmed the increased VEGF and FGF protein release by human magnetized OECs using western blotting technique (see annex of chapter 3, paragraph 3.6.5.3).

Table 2. Quantification of growth factors secreted by OECs. Mouse and human controls, and their corresponding magnetized OECs, were cultured for 24 h in basal media to collect EPC-conditioned media. A 4-plex protein array was used to measure growth factors content, independent experiments (n=2-3 per group). Values are corrected by the total protein amount (pg of growth factor/µg protein) and expressed as mean±SD; n.d.= not detected.

	Mouse		Human	
Growth Factor	Magnetized OECs	Control OECs	Magnetized OECs	Control OECs
FGF basic	23.23± 12.02	17.33± 1.87	25.60± 3.6	16.26± 4.48
VEGF	3.23± 2.34	0.27± 0.02	16.30± 4.64	10.08± 5.33
HGF	0.48± 0.19	0.50± 0.10	n.d.	n.d.
PDGF-bb	n.d.	n.d.	n.d.	n.d.

We found that OECs labeled by TD-SPIONs were able to secrete more FGF and VEGF than non-labeled cells. In conclusion magnetized EPCs preserved their paracrine potential showing also enhanced VEGF and FGF secretion. This effect is of great importance when evaluating our method for clinical translation. The fact that secretion of other growth factors, such as HGF and PDGF, was not altered suggests that there is preferential activation of specific pathways, which remain to be identified.

3.3.3.4. ROS FORMATION

ROS (reactive oxygen species, as like as hydroxyl radical OH·, hydrogen peroxide H_2O_2). It is well known that transition metal ions like Fe^{2+}/Fe^{3+} can generate ROS through Haber –Weiss reactions[66]:

$$Fe^{3+} + O_2^{\cdot-} \rightarrow Fe^{2+} + O_2$$

$$Fe^{2+} + H_2O_2 \rightarrow Fe^{3+} + OH^{\cdot} + OH^{-}$$

The net reaction is: $O_2^{\cdot-} + H_2O_2 \rightarrow OH^{\cdot} + OH^{-} + O_2$ with the generation of the hydroxyl radical OH· which induces lipid peroxydation (membrane breakage), DNA and protein damage.ROS also act in the regulation of growth factor release and in numerous physiological responses. For instance, together with other cytokines, ROS are intercellular signaling molecules in cellular migration and proliferation[67].

Subsequent to cell magnetization with SPIONs, increased intra-cellular ROS formation was observed (41% increase) in comparison to control cells (Fig. 19a). Importantly, ROS increase occurred without affecting cell viability (Fig. 11). Our findings on enhanced ROS production in magnetized cells could be considerate like a moderate increase, because treatments with antimycin, a well-known oxidative stress generator and cell-death inducer, further increased ROS levels in both control (176%) and magnetized cells (223%) (Fig. 19b).

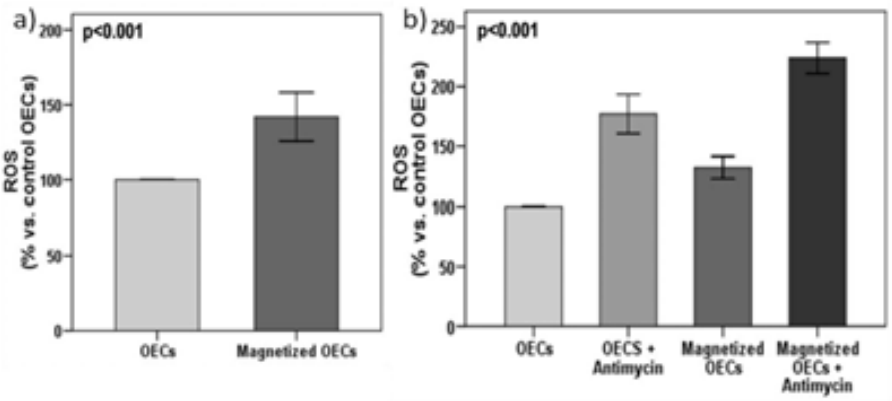

Figure 19. ROS production in OECs. a) Bar graph showing increased cellular ROS levels in magnetized cells after 24 h; n=7 independent experiments, p<0.001; b) Bar graphs showing that cellular ROS could be further enhanced with antimycin (a generator of ROS in biological samples), both in control and in magnetized cells; n=4 independent experiments, p<0.001. Data is expressed as percentage of the control group (named OECs).

It is already known that oxidative stress occurs when cells are exposed to iron oxide nanoparticles[68,69] and that ROS-dependent up-regulation of VEGF occurs in heart endothelial cells exposed to moderate levels of H_2O_2[70]. In addition, the concentration of TMAOH, nitric acid and sodium citrate may have a role in the increased ROS production due to the strong variation of medium ionic strength: it may affect the potential at the cell membrane and the regulation of flux of ions across the cell membrane inducing a cascade of intracellular events[71,72]. It can be concluded that compared to non treated cells, magnetized OECs present a predictable, moderate increase in ROS levels which may also have a role in the increased VEGF secretion and cell migration.[65]

3.3.4. IN VIVO CELL GUIDANCE AND CELL TRACKING OF MAGNETICALLY LABELLED ENDOTHELIAL PROGENITOR CELLS IN THE BRAIN

Song and coworkers demonstrated that a higher amount of neural stem cells can reach the target brain area after intravenous injection if labeled with magnetic nanoparticles in animal models with induced ischemia by middle cerebral artery occlusion[33].

Similarly we wanted to prove that a higher amount of EPCs can reach the target brain area if labeled with SPIONs in the presence of a local magnetic field. For that we compared cell accumulations in two mice: in the first one magnetized EPCs were injected in presence of a magnetic field (implantation on the left hemisphere of the mouse skull of small permanent neodymium–iron–boron magnets, Nd-Fe-B with a magnetic field of 0.3 T) (Fig. 20), while in the second animal magnetized EPCs were injected without applying the magnetic field (no magnet implantation). See annex of chapter 3, paragraph 3.6.7. for protocol details.

Figure 20. Image of implantation on the mouse skull of a small permanent Nd-Fe-B magnet with a magnetic field of 0.3 T. Mouse surgery was conducted under anesthesia.

Magnetized EPCs (3.5 x 10^4 cells) were injected and after twenty hours were successfully accumulated in cortical areas of the brain under the influence of the magnetic gradient created by the implanted magnets (Fig. 21a). In fact, T_2 weighted images in MRI confirmed the accumulation of hypointense signals in the most external cortical layers close to the magnetic field, visible as dark spots. Importantly, we did not observe these signals in other brain areas or in the control animal (Fig. 21c).

Moreover we used the Prussian blue stain of brain slices to verify that the hypointense signals observed by MRI indeed corresponded to the presence of the administered EPCs. The presence of blue cells, which were presumed to be our injected EPCs, was confirmed in matching cortical areas (Fig. 21b) but was not observed in brains of mice without magnet implantation (Fig. 21d). Importantly, magnet implantation at the surface of the skull along with injection of magnetized EPCs seemed to be safe as animals survived throughout the study period (24 hours). Additionally, no major sign of tissue injury was observed *in vivo* by MRI or *ex vivo* in the brain tissue. The total amount of iron injected with the magnetized cells was approximately 1 µg based on the amount of iron loaded in early-EPC (Table 1).

Our results prove that after appropriate magnetization, EPCs can be guided to precise cortical areas of the brain after intravenous administration of relatively low amounts of cells, which could be successfully tracked by MRI.

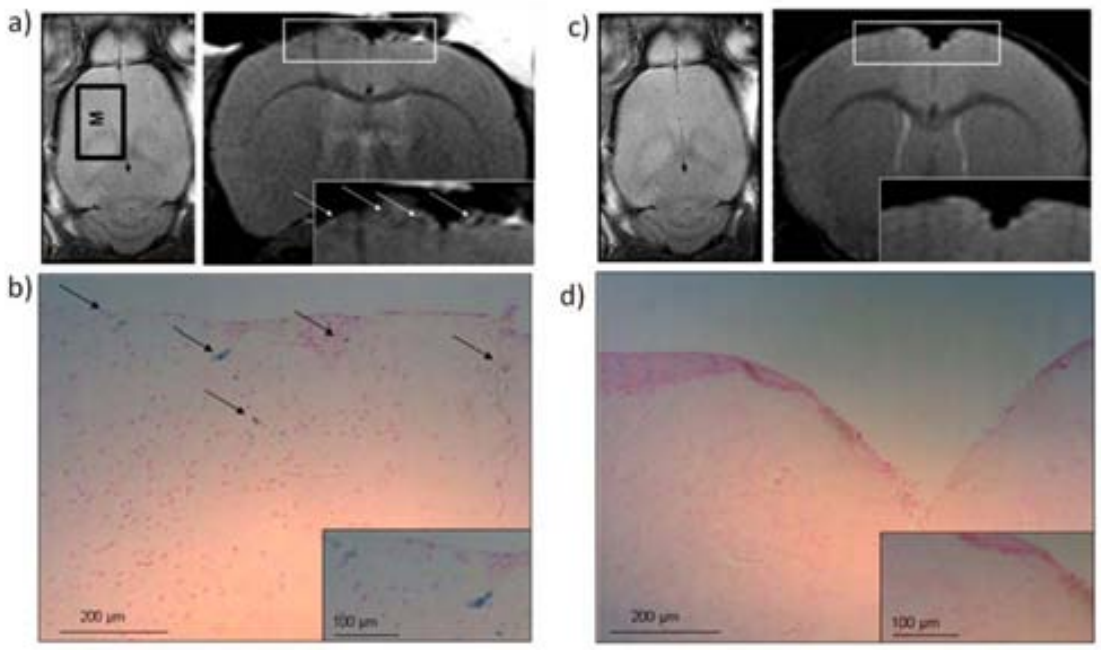

Figure 21. *In vivo* magnetic labeled EPCs imaging and guided accumulation in the left hemisphere of a mouse's brain: a) and c) Coronal section of a T_2 weighted image, showing the exact position of magnet implantation. T_2 weighted brain images corresponding to mice injected with 3.5 x 10^4 magnetized early-EPCs with (a) or without (c) magnet implantation. The inserts show areas under the influence of the magnetic field or corresponding area (white arrows). Prussian blue stain identified magnetized EPCs in the brain cortex under the influence of the magnetic field (b) which were no detected in brains not exposed to the magnetic field (d).

3.4. ENDOTHELIAL PROGENITOR CELL LABELING USING MW-SPIONs

As described in chapter 2 microwave route is a fast and reproducible synthetic route to obtain iron oxide magnetic particles where concentration of precursor, power and time of irradiation are critical factors to achieve size control[73,74]. This is of great importance if considering the interactions of nanoparticles in biological environment, such as the amount of protein corona adsorbed onto the particle surface[75]. Highly crystalline citrate-coated iron oxide nanoparticles readily dispersible in water were obtained by one-pot microwave-assisted sol-gel method, avoiding the inefficient and time-wasting ligand exchange steps[76]. The uptake of microwave synthesized SPIONs (MW-SPIONs) was investigated in endothelial progenitor cells (EPCs) to evaluate their labeling efficacy for potential application in cellular therapy[77]. Moreover we labeled a neuronal cell line (SHSY5Y) to test potential toxicity of nanoparticles in brain tissues (see annex of chapter 3, paragraph 3.6.4 for protocol details).

3.4.1. SPIONs LOADING AND CYTOTOXICITY

The system of MW-SPIONs was stabilized in EGM-2 (endothelial growth medium) using different amounts of sodium citrate. Two systems were studied: aggregated particles (batch prepared with 0.3 mM of sodium citrate) forming clusters larger than 200 nm and more dispersed particles (batch prepared with 1.4 mM of sodium citrate) with stable aggregates of approximately 100 nm (see chapter 2, paragraph 2.5). Figure 22 shows optical microscope images of OECs incubated for 24 hours at different MW-SPIONs concentrations in the

presence of high or low sodium citrate concentration, with the corresponding Prussian blue stain pictures to prove MW-SPIONs uptake. Particle aggregates are not observed in Figure 22c but they are evident in Figure 22a corresponding to cell medium without the extra sodium citrate. Noticeable is the higher stain intensity for cells incubated with aggregated particles (Fig. 22b) pointing out to higher iron uptake in this condition than for cells incubated with dispersed nanoparticles (Fig. 22d). No differences in cell morphology were observed between the two citrate-incubation conditions.

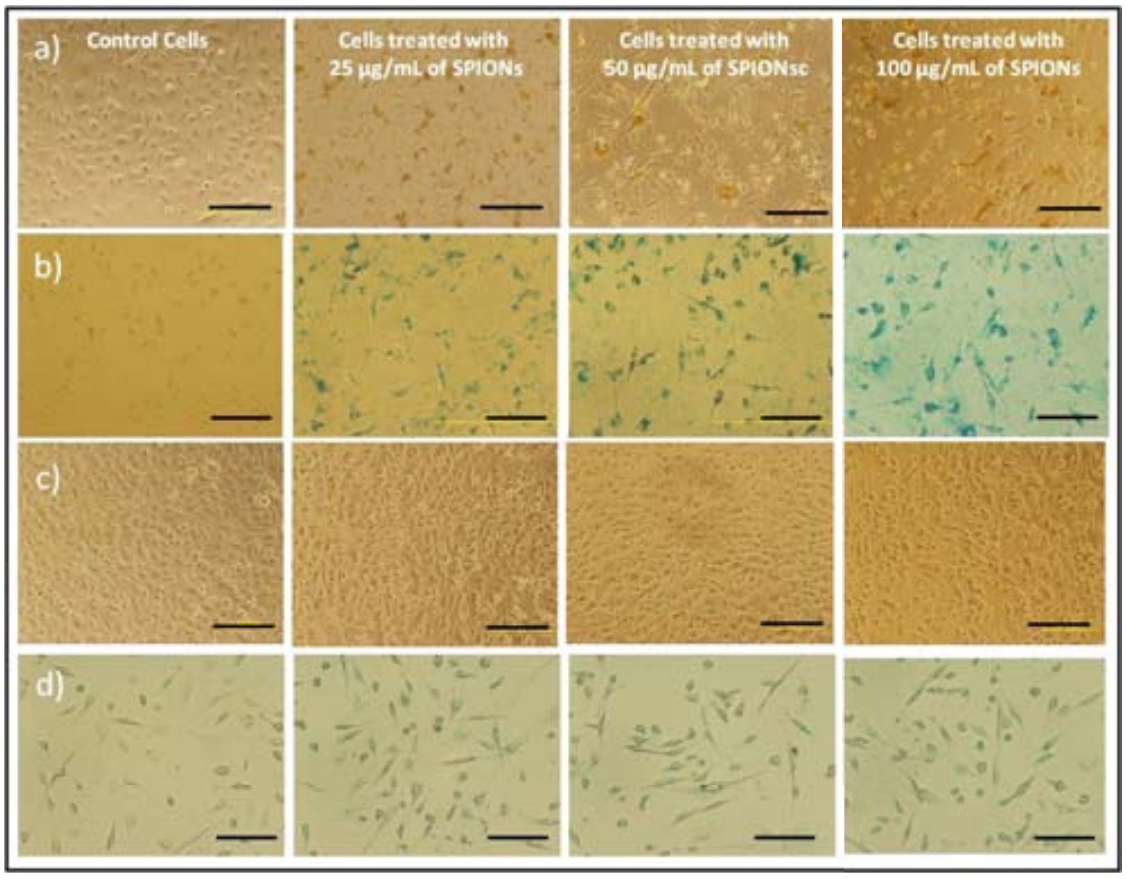

Figure 22. OECs labeled with MW-SPIONs at different sodium citrate concentrations. Row a) Optical microscope images of OECs incubated with SPIONs for 24h at 37ºC in absence of extra 10 mM sodium citrate. Scale bar 200 µm. Row b) Prussian Blue stain of OECs labeled with MW-SPIONs in absence of extra 10 mM sodium citrate. Scale bar 100 µm. Row c) Optical microscope images of OECs incubated with SPIONs for 24h at 37ºC in presence of extra 10 mM sodium citrate. Scale bar 200 µm. Row d) Prussian Blue stain of OECs labeled with MW-SPIONs in presence of extra 10 mM sodium citrate. Scale bar 100 µm. Number of seeded cells $2x10^5$.

By iron quantification measurements it was found that particles in aggregated state were uptaken in larger amounts (around seven fold) than the same particles in dispersed state (table 3). Furthermore, considering the same cell population (OECs) and the nanoparticle incubation conditions (50 µg/mL of SPIONs, 24 hours) we can conclude that the amount of iron internalized by cells using MW-SPIONs in aggregated conditions is higher than the amount of iron internalized using TD-SPIONs (see table 3).

Table 3. Comparison between OECs uptake and MRI contrast effect of aggregated and dispersed MW-SPIONs. Iron amount was quantified by magnetometry (SQUID measurements) and chemical analysis (ICP-OES), n=3 independent experiments.

	SQUID (pgFe/cell)	ICP (pgFe/cell)
control	0.03 ± 0.04	-
$MW_{aggregated}$	8.6 ± 1.0	7.2 ± 1.2
$MW_{dispersed}$	0.7 ± 0.2	1.1 ± 0.2

Cell viability has been evaluated using two populations of magnetic labeled cells, primary endothelial progenitor cells and neuron-like cells, at different iron concentrations. MTT tests on neuron-like cells (SHSY5Y cell line) were done at iron concentrations up to 100 µg/mL, incubating for 24 hours (Fig. 7a). We concluded that the presence of exogenous iron at the used concentrations does not significantly affect viability in SHSY5Y neuroblastoma cells line, very sensitive to iron loading[78].

Cell viability of labeled EPCs (OECs population) was examined in the presence or absence of 10 mM of sodium citrate. Results confirmed that MW-SPIONs were not toxic up to concentrations of 100 µg/mL for 24 hours (Fig. 23b, c). Only a slight decrease in viability at 100 µg/mL, without reaching statistical significance, was observed for particles in the aggregated state.

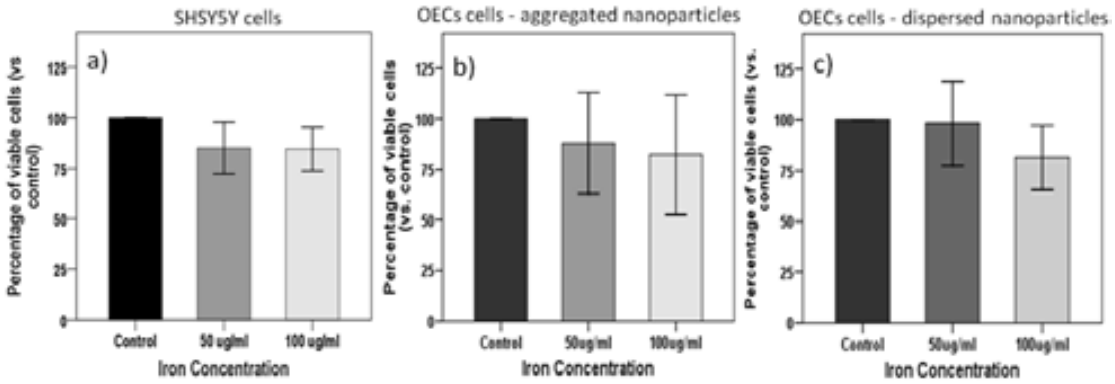

Figure 23. MTT cytotoxicity tests of cells after 24h of incubation with MW-SPIONs. a) SHSY5Y cells, statistical analysis by Anova one way test p> 0.05, n=7. b) OECs cells treated with MW-SPIONs in absence of extra sodium citrate (aggregated nanoparticles), statistical analysis by Anova one way test p> 0.05, n=5, analyzed by Muse, Millipore. c) OECs cells treated with MW-SPIONs in presence of 10 mM of extra sodium citrate (dispersed nanoparticles), statistical analysis by Anova one way test p> 0.05, n=7, analyzed by Muse Cell count and Viability Assay, Millipore**.**

3.4.2. MRI MEASUREMENTS

MRI is a powerful tool for cell tracking during migration, grafting and tissue proliferation after cell administration in pre-clinical studies[79]. Figure 24 displays agarose phantoms with the same number of labeled-cells containing dispersed or aggregated MW-SPIONS. If we define $\Delta T_2 = T_{2\ control\ cells} - T_{2\ cell+nanoparticles}$ (see table 4), we can calculate a $\Delta T_{2\ dispersed\ nanoparticles} = 4$ and $\Delta T_{2\ aggregated\ nanoparticles} = 38$ giving a ratio $\Delta T_{2\ aggregated\ nanoparticles} / \Delta T_{2\ dispersed\ nanoparticles} = 9.5$ in

accordance with a seven-fold increase in iron uptake by the cells when incubated with aggregated nanoparticles (Table 4).

Table 4. T_2 values (milliseconds) of MRI measurements on agarose phantoms with OECs labeled with MW-SPIONs dispersed (n=4 independent experiements) and aggregated nanoparticles (n=2 independent experiments). MW-SPIONs concentration of 50 µg/mL, time of incubation 24 hours, approximately 4.5 x 10^5 cells per agarose phantom.

	$MW_{Aggregated}$ T2 (msec)	$MW_{Dispersed}$ T2 (msec)
Control OECs	74.20± 3.11	59.16± 8.25
Magnetized OECs	36.05± 15.90	55.40± 6.56

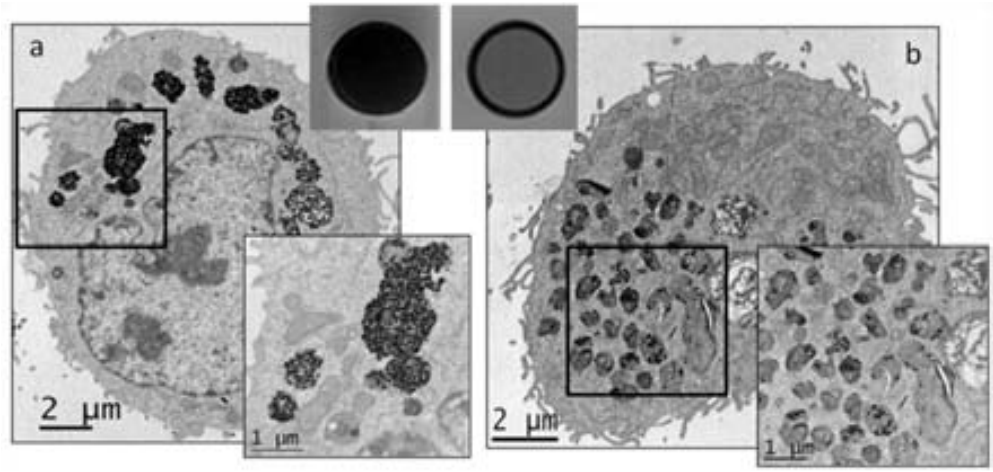

Figure 24. TEM images of OECs treated with MW-SPIONs. a) OECs incubated with aggregated MW-SPIONs at concentration of 50 µg/mL 24 h and corresponding T_2 weighted image of agarose phantom; b) OECs incubated with dispersed MW-SPIONs concentration of 50 µg/mL, 24 h and corresponding T_2 weighted image of agarose phantom. Approximately, 4.5 x 10^5 cells per agarose phantom.

3.4.3. FUNCTIONALTY TESTS OF EPCs AFTER SPIONs LABELING

3.4.3.1. IN VITRO TUBULOGENESIS.

To check if cell functionality can be affected by MW-SPIONs aggregation, *in vitro* vessel formation experiments were run in EBM-2 10% FBS (n=4). The number of complete rings (circular vessel-like structures), the total tube length (perimeter of the rings) and the number of cell connections (branching points between rings) were analyzed comparing three groups: not treated cells (control), cells labelled with SPIONs in absence of extra sodium citrate (aggregated particles) and cells labelled with SPIONs in presence of extra 10 mM sodium citrate (dispersed particles). Importantly, the assessed parameters in the three groups of cells were not statistically different, suggesting that particle aggregation has not a major effect on cell functionality during the analyzed period of 24 hours (Fig. 24).

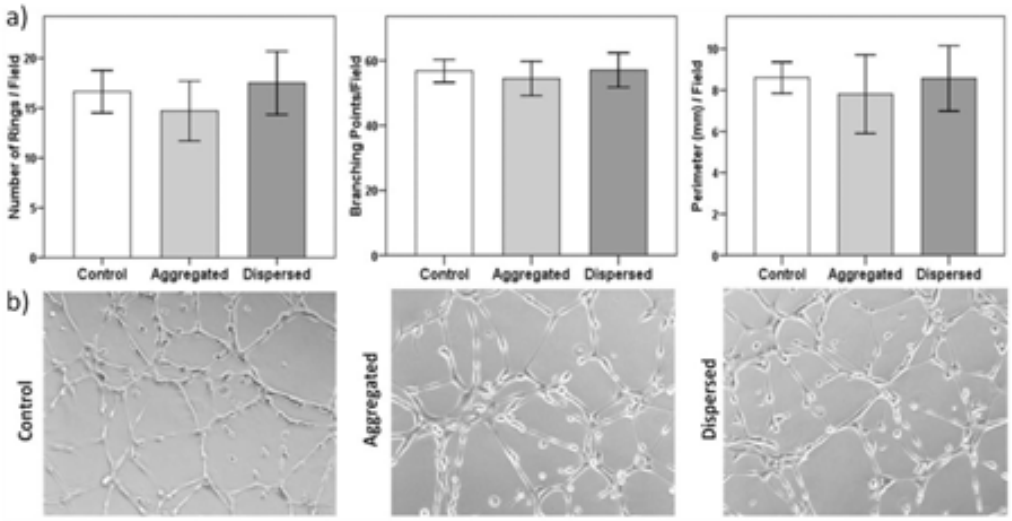

Figure 25. Matrigel Assay with human OECs labeled or not (control) with MW-SPIONs in the absence (aggregated particles) or presence (dispersed particles) of sodium citrate (10 mM). Row a): After 24 h tube-formation in Matrigel™ the number of structures (rings), the number of cell connections (branching points) and the extension of the vascular network (perimeter) were quantified using the automatic and blinded Wintube software. No differences were found between groups ($p>0.05$). Independent experiments n=4/group. Row b): Representative images of each group (100x).

3.5. CHAPTER CONCLUSIONS

The success of future repair therapies based on the angiogenic and vasculogenic potential of EPCs is dependent on the development of methods that allow effective delivery, arrival, engraftment, and trophic support in target tissues. We showed that EPCs could be safely magnetized with SPIONs synthesized by thermal decomposition synthesis and that intracellular iron content could be controlled depending on the incubation time. We also observed by TEM that synthesized SPIONs were internalized into the cytoplasm of EPCs within endosomes/lysosomes and were accumulated as nanoparticle clusters. Interestingly, our study reports for the first time that iron load was larger (about 20 fold) in the early EPC population compared to OECs under the same experimental conditions. This data is particularly relevant for cell magnetic targeting since differences in iron loads can lead to different cellular responses to a magnetic field. Therefore, it suggests that protocols should be "customized" for achieving an efficient magnetic labeling per each type of cell. Our results prove that after suitable magnetization, EPCs can be guided to precise cortical areas of the brain after intravenous administration of relatively low amounts of cells, which could be successfully tracked by MRI. In the context of ischemia, we might expect better engraftment into tissue due to increased blood– brain barrier permeability, even if further preclinical studies in animal models of stroke are needed to confirm EPC engraftment in diseased brains. It is worth to note that during our *in vivo* setting the total amount of cellular iron injected (1 µg) was about fifteen times lower the amount of iron administered as contrast agent for MRI studies, which have an advised dose of 0.56 mg/Kg for Feridex®. For that reason, considering a hypothetical clinical study, the amount of iron administered to a 70 kg human patient would be 39 mg which indicates 1×10^9 cells that could be safely injected.

Importantly, after cell magnetization with SPIONs, EPCs preserve their angiovasculogenic abilities, forming vessel-like structures *in vitro*. From migration assays we can conclude that after suitable magnetization EPCs have enhanced migration capacity compared to control cells. Additionally, magnetically labeled EPCs showed enhanced pro-angiogenic paracrine effects and increased ROS formation without affecting cell viability. In conclusion our results indicate that SPIONs-labeled EPCs can improve angiogenic performances through increased migration and paracrine secretion of growth factors, and that intravenously delivered EPCs can be accumulated in specific areas of the brain cortex by implanting an external magnet device. These results offer exciting possibilities for new non-invasive cell-based therapies that could potentiate neurorepair in specific brain areas. For that reason, additional studies are needed in animal models of cerebral ischemia to examine the potential engraftment of magnetized EPCs and whether angiogenesis stimulation occurs under the influence of a magnetic field.

Microwave synthesis showed to be a faster route to obtain citrate-coated iron oxide nanoparticles compared to thermal decomposition. Seven-fold more efficient uptake has been found for systems with large nanoparticle aggregates without compromising cell viability, cell morphology or cell functionality. The size of the aggregates found in intracellular compartments has a major influence on the MRI contrast effect that we can manipulate by changing the medium ionic strength. We demonstrated that microwave synthesized SPIONs can be better candidates compared with thermal decomposition synthesized SPIONs for a more effective endothelial progenitor cell labeling. Further experiments have to be done to confirm their potential in angiogenic targeted therapy to improve cell guidance, cell tracking, and pro-angiogenic stimulation in animal models.

3.6. ANNEX OF CHAPTER 3

In this section are described the protocols used for *in vitro* and *in vivo* experiments with SPIONs. The section is divided in paragraphs corresponding to experimental protocols of cell labeling, cell viability, cell functionality and cell guiding. Finally, general concepts on SPION pharmacokinetics are described.

3.6.1 ENDOTHELIAL PROGENITOR CELL CULTURES: ISOLATION AND *EX VIVO* EXPANSION PROTOCOL

The following protocol describes the procedure to obtain endothelial progenitor cells for *in vitro* and *in vivo* experiments with SPIONs. A pool of spleens obtained from male BALB/C mice (Charles River Laboratories, Spain) were mechanically minced, placed at 37ºC for 15 minutes in a 1 mM EDTA solution and run through a 40 mm nylon membrane to obtain a cell suspension. For human EPCs, 25 mL of venous blood were obtained from stroke patients or control subjects in EDTA tubes and mixed 1:1 with PBS containing 2% fetal bovine serum (FBS; Gibco BRL, CA, USA). For both mouse and human samples mononuclear cells (MNCs) were obtained by density gradient centrifugation with Ficoll-Paque Plus (GE Healthcare, Sweden), shortly washed with red blood cells lysis solution (150 mM NH_4Cl, 10 mM $NaHCO_3$ and 0.1 mM EDTA in distilled water) and gently washed with complete endothelial growth medium-2 (EGM-2; Lonza, Switzerland), which is composed of endothelial cell basal medium (EBM) containing 10% FBS, human endothelial growth factor (hEGF), vascular endothelial growth factor (VEGF), human basic fibroblast growth factor (hFGF-b), insulin like growth factor 1 (R3-IGF-1), GA-1000 (gentamicin and amphoterecin-B), heparin, hydrocortisone and ascorbic acid. Isolated MNCs were finally resuspended in EGM-2 and seeded on fibronectin-coated flasks or plates and incubated in a 5% CO_2 at 37ºC. Under daily observation, first media change was performed 2 days after plating and, thereafter, media was changed every 2/3 days until experiments were done. Cell cultures yield an EPC-enriched population at day 5/6 named early EPCs, whereas outgrowth EPCs (OECs) appeared from day 15 as proliferating colonies that were further expanded and frozen. For cultured OECs all experiments were done between passages 4-12.

3.6.2. PROTOCOLS OF CELL LABELING WITH SPIONs

For the experiments of cell labeling we used two cell populations: endothelial progenitor cells (EPCs) and neural cell (SHSY5Y).

3.6.2.1. LABELING OF ENDOTHELIAL PROGENITOR CELLS (EPCs)

EPCs were magnetized as follows: aliquots (25, 50 or 100 µg/mL) of an aqueous dispersion of SPIONs at pH=7.4 were added to growing early-EPCs or OECs (cell density 1 $x10^5$) in EGM-2 medium supplemented with 10% of fetal bovine serum (FBS) and incubated 2, 6 or 24 hours. Control EPCs (without SPIONs) were cultured in parallel.

3.6.2.2. LABELING OF NEURONAL CELLS (SHSY5Y)

SHSY5Y cells (5 x10^4) were cultured in DMEM F12 medium supplemented with 10% FBS. After 48h cells were washed twice with PBS and differentiation medium consisting of 1% retinoic acid (RA) in DMEM F12 supplemented with 1% FBS, was added. Medium with RA was changed every two days. After 5 days cells were washed twice with PBS, SPIONs were added at concentrations of 0, 25, 50, 100 µg/mL in DMEM F12 10 % FBS and incubated at 37ºC for 24h.

3.6.3. EVALUATION OF SPION UPTAKE BY CELLS

3.6.3.1. TRANSMISSION ELECTRON MICROSCOPY OF MAGNETICALLY LABELED CELLS

Specimens for TEM have to be dry and to withstand high vacuum conditions required for the analysis. Living cells and tissues usually need chemical fixation to preserve and stabilize their soft structures. Fixation is generally performed by incubation of samples in solutions of a buffered chemical fixative, such as glutaraldehyde, sometimes in combination with formaldehyde and other fixatives, and followed by postfixation with osmium tetroxide. The fixed specimen is then dehydrated with alcohols and embedded into epoxy resin.

We performed TEM analysis of EPCs labeled with SPIONs in order to check particle localization into cells and cellular morphology after treatment. Samples were prepared as follows: both mouse early EPCs and outgrowth EPCs (OECs) were seeded in 25 cm^2 flasks, grown and treated with SPIONs ([Fe] = 50 µg/mL for 24 h at 37ºC). Adhering cells were washed 1 time with EGM-2 and collected by centrifugation (1300 rpm, 4 min). The supernatant was discarded and 1.5 mL of glutaraldehyde 2% in cacodylate buffer was added to the pellet. The cells were incubated for 2 h in the fixation solution at 4ºC, and post-fixed in OsO_4 1 % for further 2h at 4ºC. Then cells were dehydrated in alcohol series and embedded in Epon resin. Ultrathin sections of 70 nm were used to perform TEM analysis to demonstrate nanoparticles uptake, while sections of 200 nm were used to perform electron diffraction (ED) analysis to check SPIONs crystalline structure. The ultrathin sections were transferred onto copper grids and analyzed by TEM microscope, JEM-2011 operating at 200 kV.

3.6.3.2. ESTIMATION OF THE NUMBER OF INTERNALIZED SPIONs INTO CELLS

An estimation of the number of SPIONs internalized after cell labeling with early-EPCs (SPION concentration corresponding to 50 µg/mL of iron, incubation for 24 hours) was done as follows:

Maghemite bulk density (ρ= m/v): 4.9 g/cm^3

Volume of spheric particle: 4/3π r^3

1 cm = 10^{-7} nm

Assuming the SPIONs as spherical particles, knowing the core diameter (for example 6 nm) we can calculate the particle volume: 904.8 x 10^{-21} cm^3= 9 x 10^{-19} cm^3

4.9 g/cm^3 * 9 x 10^{-19} cm^3= 44 x 10^{-19} g (grams of iron in one particle),

In mouse early EPCs the amount of SPION uptaken was found to be 24.7 x 10^{-12} g of iron (by ICP-OES analysis, see annex of chapter 2), so:

$24.7 \times 10^{-12} / 44 \times 10^{-19} = 0.56 \times 10^{7} = 5.6 \times 10^{6}$ number of particles.

3.6.3.3. EVALUATION OF SPIONs CONTENT BY SQUID

To determine the amount of SPIONs internalized by cells we performed magnetic measurements by SQUID magnometry onto dried pellets of cells. Pellets were obtained as follows: mouse early EPCs and mouse and human OECs were seeded in 25 cm^2 flasks, grown and treated with 50 µg/mL SPIONs. Then cells were deeply washed 3 times with basal media, trypsinized and counted. Cell pellets were dried with a speed vacuum for 60 minutes, at 1500 rpm and 60ºC in a capsule made of polycarbonate with a diameter less than 1 mm avoiding any scrabbling or transferring of cells. The as-prepared sample was inserted in the SQUID magnetometer sample holder. The uptake of the SPIONs can be evaluated by measuring the remnant magnetization value of treated cells (M_{Rcells}) after they were magnetized up to 5 Tesla. A dried pellet of around 1 mg was used and the M_{Rcells} of the treated cells (emu) was divided by the total number of cells giving the magnetization per cell (emu/cell). To know the amount of iron per cell, the magnetization per cell was divided by the remnant magnetization value of the SPIONs ($M_{R\ SPIONs}$) (emu/g Fe).

3.6.3.4. PRUSSIAN BLUE STAINING OF EPCs

Prussian blue is a ferric ferrocyanide ($Fe_7(CN)_{18}$) complex soluble in water. Ferric iron deposits in tissue (present mostly as ferric iron) react with the soluble ferrocyanide in the stain, to form insoluble Prussian blue dye in situ. They can be visualized by optical microscopy as blue deposits within cells.

Prussian Blue staining was conducted to check SPION internalization into EPCs. In a 12 well plate pre-coated with fibronectine, 2×10^5 cells were seeded. After 24 h, fresh medium EGM-2 10% FBS was added together with 25, 50 and 100 µg /mL of SPIONs in presence and in absence of 10 mM of extra sodium citrate. Cells were incubated for 24h at 37 ºC. Subsequently they were washed twice with PBS, and fixed for 30 minutes at room temperature with paraformaldehyde solution 2%. Lately, cells were washed twice with distilled water and a Perl's solution made of equal volumes of hydrochloric acid and potassium ferrocyanide at 2% was added. After incubation for 30 minutes at room temperature preserving the plate from light, cells were rinsed twice with distilled water and imaged with the light microscope (Olympus IX71). Photographs were taken using a 10x magnification objective.

3.6.4. MTT ASSAY PROTOCOL FOR CELL VIABILITY

Cytotoxicity is the quality of being toxic to cells. 3-(4,5-dimethylthiazol- 2-yl)2,5-diphenyl-tetrazolium bromide (MTT) assay measures cell metabolic activity, in particular mitochondrial function, to assess cell viability. Reductase enzymes of mitochondrial membrane reduce MTT (water soluble, yellow colored) to a formazan (insoluble, purple) which is measured by a spectrophotometer at 590 nm.

We tested SPION cytotoxicity on EPCs and neuronal cells (SHSY5Y) as follows: SPIONs were incubated with cells in a 24 well plate at concentrations of 0, 25, 50, 100 µg/mL at 37 °C for 24 hours. Afterwards cells were washed twice with PBS and 50 µL of MTT in 300 µL of complete EGM-2 were added. After incubation at 37 ºC for 90 minutes, at which the MTT reduction takes place, cell media was discarded and 200 µL of DMSO were added per each well. Absorbance on the isolated supernatant was measured at 590 nm by Bio Whittaker ELx808 Absorbance Microplate Reader. Experiments were run in duplicate and expressed as percentage of viable cells *versus* control condition (without SPIONs). For statistical analysis to determine differences between groups an ANOVA followed by Bonferroni PostHoc tests were run (statistical significance was considered when $p < 0.05$).

3.6.5. PROTOCOLS FOR CELL FUNCTIONALITY

To test EPCs functionality after treatment with SPIONs were measured cell migration ability, protein release and ROS (reactive oxygen species) formation.

3.6.5.1. MIGRATION ASSAY

FluoroBlock™ (BD, France) transwell inserts for 24 well-plates with a pore size of 8 µm were used to study the migratory response of magnetized EPCs in the presence or absence of a magnetic field. Both control and magnetized mouse OECs (50µg/mL of SPIONs during 24 hours) were additionally labeled with a red fluorescent dye according to manufacturer's instructions (PKH26, Sigma-Aldrich) and $1x10^4$ OECs were seeded on the upper chamber in EGM-2 media. The lower chamber was also filled with EGM-2 media and cells were allowed to attach to the transwell surface for 3 hours in an incubator at 37ºC. Afterwards media from the upper chamber was replaced with EBM, EGM-2 media was maintained in the lower chamber and cells were incubated for 48 hours. At 6, 24 and 48 hours images were taken (12 per condition and time-point) using a fluorescence inverted microscope to determine the migration capacity. Since the transwell membrane used was dark only migrated fluorescent cells are imaged from the bottom at the level of the membrane or at the bottom of the plastic well (Fig. 26A). in Figure 26B are showed the results for the migration ability of control cells (not treated with SPIONs) in presence and in absence of a magnet device.

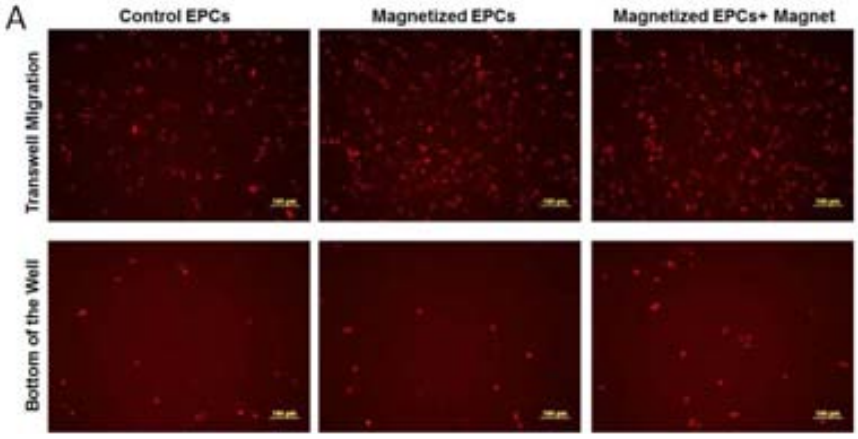

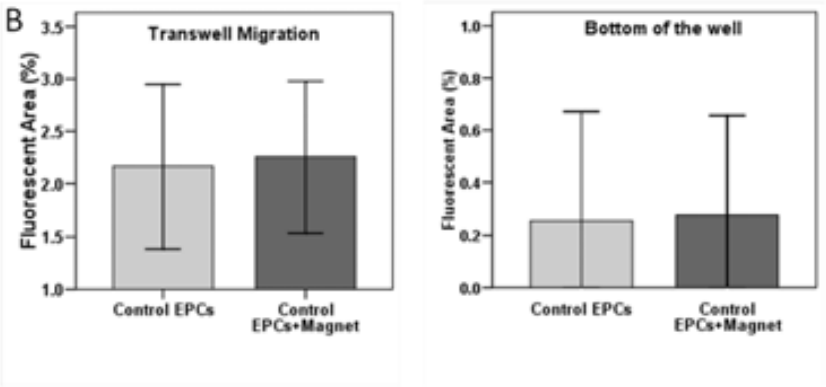

Figure 26. *In vitro* cell migration of mouse EPCs. Images obtained by fluorescent microscopy showing transwell-migrated cells (upper row in A) and cells further guided to the bottom of the transwell (lower row in A) at 48h under the different assayed conditions, scale bar 100 µm. In B bar graphs showing that migration of control cells was not influenced by the presence of a magnetic field at 48h (n=4).

3.6.5.2. MULTIPLEX PROTEIN ANALYSIS

This technique is a multiplex sandwich ELISA (Searchlight®), which consists in immunological assay for sensitive and specific detection of various target structures in biological samples. It is based on the specific antibody-antigen interaction which induces oxidation or reduction of a substrate with light emission at a specific wavelength which is proportional to the amount of protein detected.

Multiples protein analysis was conducted to measure the amount of proteins (VEGFs, FGFs, PDGFs) released by endothelial cells in normal and SPION treatment conditions (Fig. 2). Briefly, seeding density for OECs was $4x10^5$ cells/flask (25 cm^2) and grown for 2 days. Afterwards, cells were treated with 50 µg/mL of SPIONs for 24 hours in EGM-2 to allow cell magnetization. To obtain conditioned media, magnetized and non-magnetized cells were deeply washed 3 times with basal media and 4 mL of fresh basal media were added to collect growth factors. At 24 hours the basal media containing EPCs' secreting factors, named conditioned media, was collected and concentrated using Amicon Ultra® centrifugal filters (Millipore, Ireland) with a 3kDa membrane. Final conditioned media volume was around 600 microlitres and it was stored at -20ºC until use. Conditioned media were assayed to determine the amount of OECs-secreted growth factors using the SearchLight® Human Angiogenesis Array 2 (AushonBiosystems, MA, USA) as previously described for the simultaneous measure of four angiogenic factors: platelet derived growth factor (PDGF-bb), hepatocyte growth factor (HGF), FGF-b and VEGF. Samples were assayed twice and the mean value of the two measurements was used. The mean intra-assay coefficients of variation were <20%. The images were analyzed with Array Analyst software (Imaging Research, USA). The sensitivity limits were 1 pg/mL for PDGF-bb, 3.1 pg/mL for HGF, 2 pg/mL for FGF-b, and 4.9 pg/mL for VEGF. Importantly, concentrated EBM was also tested as a blank sample. Additionally, Bradford assay was performed to determine total protein concentration and the values were normalized to pg of factor/µg of protein. Assays were performed by personnel blinded for treatment.

3.6.5.3. WESTERN BLOTTING

Western blot is an analytic technique used to semi-quantify specific proteins in a biological sample. It uses gel electrophoresis to separate proteins by their size. Proteins are then transferred to a membrane (typically nitrocellulose or polyvinylidene difluoride PVDF), where they are detected by specific antibodies labeled with fluorescent or radioactive molecules.

The analysis was performed as follows: conditioned media was obtained and concentrated as described above for protein arrays and 5 µg of total protein were loaded in SDS-PAGE (12%) and transferred into PVDF (for VEGF blots) or Nitrocellulose (for FGF blots) membranes. Non-specific bindings were blocked with non-fat milk (10% in PBS-Tween), and membranes were incubated overnight with rabbit anti-VEGF (Santa Cruz; 1:200) or rabbit anti-FGF (Abcam; 1:1000) with non-fat milk (10% in PBS-Tween) at 4ºC. Secondary antibody was diluted 1:1000 with 5% BSA in PBS-Tween and membranes incubated at room temperature for 1 hour. The substrate reaction was developed with a chemiluminescent reagent and visualized with a luminescent image analyzer (Las-3000, FujiFilm; USA) (Fig. 27).

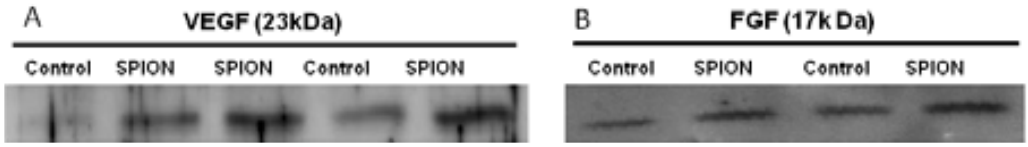

Figure 27. VEGF and FGF release by OECs. Western blots showing VEGF (A) and FGF (B) released by human control and magnetized cells (with SPION).

3.6.5.4. REACTIVE OXYGEN SPECIES (ROS) DETECTION ASSAY

Cellular Reactive Oxygen Species Detection Assay kit (Abcam®) uses the cell permeant reagent 2',7' –dichlorofluorescein diacetate (DCFDA), a fluorogenic dye that measures hydroxyl, peroxyl and other reactive oxygen species (ROS) activity within the cell. Samples for the analysis were prepared as follows: $5x10^3$ mouse OECs were seeded in 96 well plates in EGM-2 media, 24 hours after SPIONS were added at 50 µg/mL for cell magnetization as described above. Twenty-four hours after, cells were washed and DCFDA was added and let to permeate inside cells for 45 minutes. DCFDA is deacetylated by cellular esterases to a non-fluorescent compound, which is later oxidized by ROS into 2', 7' –dichlorofluorescin (DCF). DCF is a highly fluorescent compound which can be detected by fluorescence spectroscopy with excitation/emission wavelengths at 485/535, respectively. Antimycin, a ROS generator in biological systems, was used to assess if magnetized EPCs could be induced to produce more ROS (50µM of antimycin during 4h) as described in other endothelial cells. Control cells and magnetized cells (without DCFDA) were used as blanks of autofluorescence in all assays. Finally, triplicates were assayed per condition and mean values were obtained; data is given as percentage of cellular ROS of the control condition.

3.6.6. MRI RELAXOMETRY OF MAGNETIZED EPCs

Magnetic resonance imaging (MRI) of SPIONs or magnetized EPCs was performed using a quadrature 7.2 cm inner diameter volume coil on a 7 Tesla magnet (BioSpec 70/30 USR,

BrukerBioSpin, Ettlingen, Germany). Phantoms containing increasing concentrations of SPIONs (0, 5, 10, 15 and 25 ug/mL) were prepared in 1.5% agarose in distilled water. Cellular magnetization was performed with 50ug/mL during 20-24h in culture media. Phantom cell suspensions containing increasing concentrations of magnetized and non-magnetized early EPCs were prepared as follows: $1.3x10^3$, $4x10^3$, $1.3x10^4$, $2.6x10^4$, and $4.7x10^4$ cells/mL. Control phantoms containing 1.5% agarose were also imaged. Briefly, T2 map, T1 map and T2* maps were acquired to determine relaxation times using a multi-slice multi-echo (MSME) and variable repetition time (VTR) spin-echo and multi gradient echo (MGE) sequences respectively. Parameters for MSME (T2 maps) were: TR=3s, 30 TE values from 10ms-300ms (10ms echo spacing), matrix size=128x128. Parameters for VTR sequence (T1 maps) were: TE=7.5ms, seven TR values (1s, 1.3s, 1.7s, 2s, 2.6s, 3.5s, 5s), matrix size=128x128. Finally, parameters for multi-gradient echo MGE (T2* maps) were: TR=1500ms, 30 TE values from 4ms-300ms (7ms echo spacing), matrix size=128x128. T2-weighted, T1-weighted and T2*-weighted images were acquired as follows: high resolution T2WI was obtained using the fast spin echo sequence RARE (rapid acquisition with relaxation enhancement): TR=4s, TE_{eff}=16ms, 2 averages, matrix size=256x256; high resolution T2*WI was acquired using gradient echo sequence FLASH (Fast low angle shot): TR= 300ms, TE=7ms, flip angle= 30º, 2 averages, matrix size=256x256; high resolution T1WI was acquired with gradient echo sequence: TE=4ms, TR=250ms, flip angle= 50º, matrix size=256x256. The same geometry was used for all the scans: Field of view (FOV)= 8.5cmx8.5cm, 1.5mm slice thickness with a 1mm gap between slices (4 slices). Quantitative T1, T2 and T2* values were obtained by regions of interest obtained within the phantom volume. Relaxivities r1, r2 and r2* were determined by a linear fit of the inverse relaxation times as a function of the iron concentrations.

3.6.7. PROTOCOLS FOR *IN VIVO* CELL GUIDING

3.6.7.1. PREPARATION OF ANIMAL MODELS

Mice were anesthetized with isoflurane (4% induction, 1.5% maintenance) and two small permanent Nd–Fe–B (neodymium–iron–boron) magnets (3 x 4 x 2 mm) with a magnetic field of 0.3 T were implanted with glue in the left hemisphere. Afterwards, 3.5×10^4 early EPCs isolated from mice, which were previously magnetized using 50 µg/mL of SPIONs, were injected intravenously (tail vein; in 150 µL of phosphate buffered saline [PBS]). Control animals received an identical cell infusion without magnet implantation. Magnets were removed 24 hours later before MRI was carried out at 7 Tesla in a horizontal magnet (BioSpec 70/30 USR, Bruker BioSpin, Ettlingen, Germany).

Permanent Nd–Fe–B magnets used in our experiments were able to develop field gradients up to 70 T m^{-1} at a distance of 2 mm from the surface of the magnet (Fig. 28).

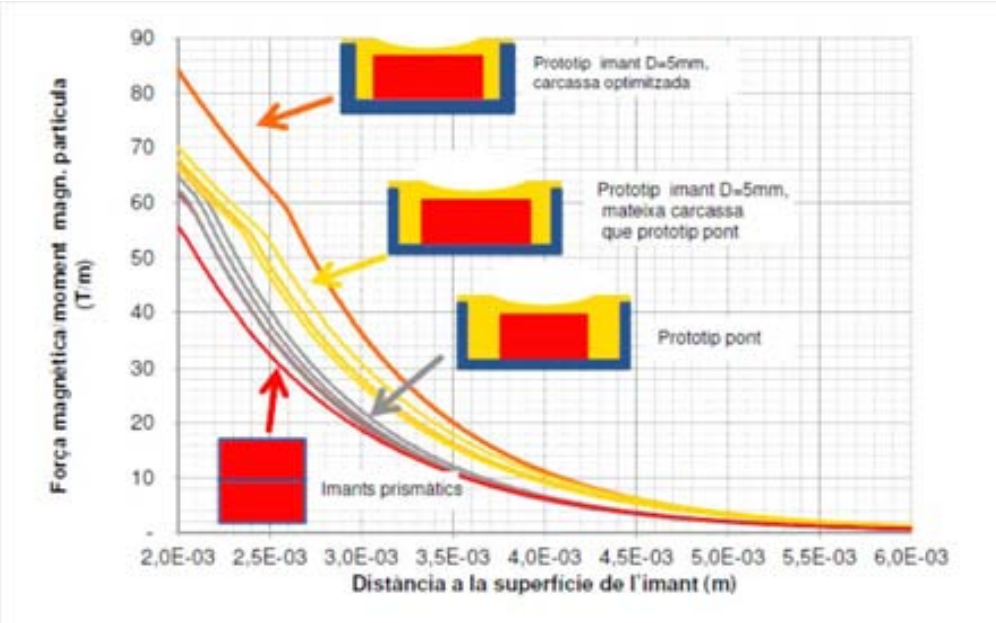

Figure 28. Magnetic field gradient developed by Nd-Fe-B magnets used for *in vivo* cell guiding experiments. y-axis: magnetic force/magnetic moment of particle; x-axis: distance from the surface of the magnet.

3.6.7.2. *IN VIVO* MAGNETIC CELL GUIDING AND MRI

MRI studies were carried out at 7 Tesla in a horizontal magnet (BioSpec 70/30 USR, BrukerBioSpin, Ettlingen, Germany) equipped with actively shielded gradients capable of 400 mT/m (B-GA12 gradient coil inserted into a B-GA20S gradient system) and a dedicated mouse brain quadrature receive surface coil, actively decoupled from a transmit volume coil with 72 mm inner diameter. Animals were positioned in the scanner bed, which allowed localized delivery of anesthesia (isoflurane, 0.5–1.5% in O2 at 0.8 L/min; respiratory frequency monitored with a pressure probe and kept between 50–80 breaths/min). A recirculation water system, integrated in the animal bed, was used to control the body temperature as measured with a rectal probe (37ºC±1ºC). T2-weighted fast spin-echo images were initially obtained in axial, sagittal and coronal planes to be used as reference scout images for reproducible slice selection at each MRI session. Imaging parameters for these images were: echo time (TE)=12 ms, echo train length (ETL)=8, effective echo time (TE_{eff})=36 ms, repetition time (TR)=4s, field of view (FOV)=1.92×1.92cm^2, matrix size (MTX)=128×128, and slice thickness (ST)=1 mm. Afterward, coronal MRI sections were performed over an 8.7 mm block starting 3.20 mm anterior to the bregma and towards the cerebellum. T2WI were acquired using a fast spin-echo sequence with ETL=8, TEeff/TR=36ms/4.2s, FOV=1.92×1.92cm^2, MTX= 256×256, 16 contiguous slices with ST=0.5 mm and 0.05 mm gap between them. T2 maps were also obtained using a multi-slice multi-echo sequence with 30 TE values ranging from 10 to 300ms, TR=4s, MTX=128×128,FOV=1.92×1.92cm^2, and slices covering exactly the same brain region as in high resolution T2w coronal images but with 8 continuous 1-mm slices and 0.1-mm gaps. All the procedures were approved by the ethics committee of Vall d'Hebron Research Institute.

3.6.7.3. PRUSSIAN BLUE STAINING OF *EX VIVO* BRAIN TISSUE

Prussian blue reaction was also conducted to verify magnetized EPCs accumulation in the brain after *in vivo* magnetic cell guiding. Brain tissue sections were re-hydrated in graded alcohols, rinsed in water and incubated 1 hour in 2% potassium ferrocyanide, washed in distilled water and counterstained with fast red for 5 minutes. Slices were dehydrated in grading alcohols and xylene and visualized under a light microscope.

3.6.8. SPIONs *IN VIVO* METABOLISM AFTER CELLULAR UPTAKE

Iron is always sequestrated to proteins in the body: in the blood plasma is bound to transferrin, into cells to ferritin. Under normal circumstances, only traces of "free iron ions" exist outside these physiologic sinks. In the cell, free iron ions or ions bound to low molecular weight compounds (citrate, adenosine diphosphate) can damage tissues by catalyzing the formation of reactive oxygen species (ROS) which damage plasma membranes, proteins and DNA. Iron is transported in plasma bound to transferring. The uptake into cells occurs by a receptor mediated endocytosis process. In hepatocytes (liver cells) is accumulated the amount of iron exceeding transferrin transport in the blood, while macrophages and reticuloendothelial systems in the spleen are the storage depots where the iron from erythrocyte degradation is accumulated and then bound to new transferrin molecules[80]. Particle cellular metabolism starts with the acidic (pH=5.5) degradation inside lysosomes (Fig. 29), where particles are partially digested within few days. They are subsequently mineralized as ferrihydrite, which is stored within ferritin cages: iron ions form crystallites together with phosphate and hydroxide ions. Each ferritin complex can store about 4500 iron (Fe^{3+}) ions. All particles released by the cells before completion of this digestion process should be cleared through the liver and spleen in a similar manner to clinically used contrast agents[30,81].

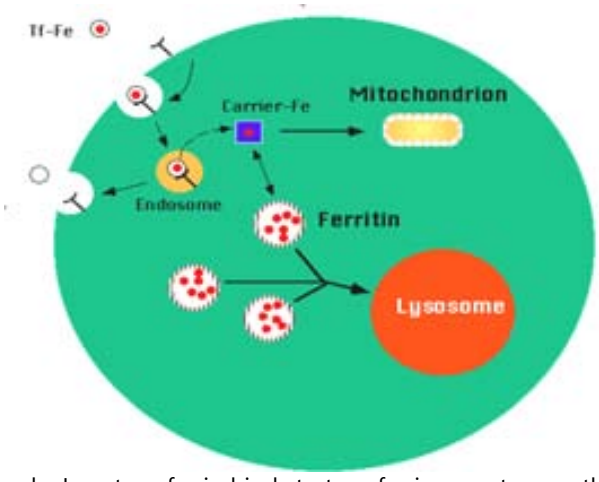

Figure 29. Iron cellular cycle. Iron-transferrin binds to transferrin receptors on the external surface of the cell. The complex is internalized into an endosome, where the pH is lowered to about 5.5. Iron separates from the transferrin molecule, moving into the cell cytoplasm. Here, an iron transport molecule shuttles the iron to various points in the cell, including mitochondria and ferritin. Ferritin molecules accumulate excess iron. Lysosomes engulf aggregates of ferritin molecules in a process termed "autophagy". Picture taken from the website: sickle.bwh.harvard.edu.

3.7. CHAPTER REFERENCES

1. Pepper, M. S., Manipulating angiogenesis. From basic science to the bedside. *Arteriosclerosis, thrombosis, and vascular biology* **1997,** *17* (4), 605-19.
2. Dufraine, J.; Funahashi, Y.; Kitajewski, J., Notch signaling regulates tumor angiogenesis by diverse mechanisms. *Oncogene* **2008,** *27* (38), 5132-7.
3. Carmeliet, P., Angiogenesis in life, disease and medicine. *Nature* **2005,** *438* (7070), 932-6.
4. Zhang, Z. G.; Zhang, L.; Jiang, Q.; Zhang, R.; Davies, K.; Powers, C.; Bruggen, N.; Chopp, M., VEGF enhances angiogenesis and promotes blood-brain barrier leakage in the ischemic brain. *The Journal of clinical investigation* **2000,** *106* (7), 829-38.
5. Hao, X.; Silva, E. A.; Mansson-Broberg, A.; Grinnemo, K. H.; Siddiqui, A. J.; Dellgren, G.; Wardell, E.; Brodin, L. A.; Mooney, D. J.; Sylven, C., Angiogenic effects of sequential release of VEGF-A165 and PDGF-BB with alginate hydrogels after myocardial infarction. *Cardiovascular research* **2007,** *75* (1), 178-85.
6. Asahara, T.; Kawamoto, A.; Masuda, H., Concise review: Circulating endothelial progenitor cells for vascular medicine. *Stem cells* **2011,** *29* (11), 1650-5.
7. Rafii, S.; Lyden, D., Therapeutic stem and progenitor cell transplantation for organ vascularization and regeneration. *Nature medicine* **2003,** *9* (6), 702-12.
8. Tarkka, T.; Sipola, A.; Jamsa, T.; Soini, Y.; Yla-Herttuala, S.; Tuukkanen, J.; Hautala, T., Adenoviral VEGF-A gene transfer induces angiogenesis and promotes bone formation in healing osseous tissues. *The journal of gene medicine* **2003,** *5* (7), 560-6.
9. Gowdak, L. H.; Poliakova, L.; Wang, X.; Kovesdi, I.; Fishbein, K. W.; Zacheo, A.; Palumbo, R.; Straino, S.; Emanueli, C.; Marrocco-Trischitta, M.; Lakatta, E. G.; Anversa, P.; Spencer, R. G.; Talan, M.; Capogrossi, M. C., Adenovirus-mediated VEGF(121) gene transfer stimulates angiogenesis in normoperfused skeletal muscle and preserves tissue perfusion after induction of ischemia. *Circulation* **2000,** *102* (5), 565-71.
10. Vanhoutte, P. M., Endothelium and control of vascular function. State of the Art lecture. *Hypertension* **1989,** *13* (6 Pt 2), 658-67.
11. Asahara, T.; Murohara, T.; Sullivan, A.; Silver, M.; van der Zee, R.; Li, T.; Witzenbichler, B.; Schatteman, G.; Isner, J. M., Isolation of putative progenitor endothelial cells for angiogenesis. *Science* **1997,** *275* (5302), 964-7.
12. Asahara, T.; Masuda, H.; Takahashi, T.; Kalka, C.; Pastore, C.; Silver, M.; Kearne, M.; Magner, M.; Isner, J. M., Bone marrow origin of endothelial progenitor cells responsible for postnatal vasculogenesis in physiological and pathological neovascularization. *Circulation research* **1999,** *85* (3), 221-8.
13. Asahara, T.; Kawamoto, A., Endothelial progenitor cells for postnatal vasculogenesis. *American journal of physiology. Cell physiology* **2004,** *287* (3), C572-9.
14. Takahashi, T.; Kalka, C.; Masuda, H.; Chen, D.; Silver, M.; Kearney, M.; Magner, M.; Isner, J. M.; Asahara, T., Ischemia- and cytokine-induced mobilization of bone marrow-derived endothelial progenitor cells for neovascularization. *Nature medicine* **1999,** *5* (4), 434-8.
15. Rabelink, T. J.; de Boer, H. C.; de Koning, E. J.; van Zonneveld, A. J., Endothelial progenitor cells: more than an inflammatory response? *Arteriosclerosis, thrombosis, and vascular biology* **2004,** *24* (5), 834-8.
16. Rehman, J.; Li, J.; Orschell, C. M.; March, K. L., Peripheral blood "endothelial progenitor cells" are derived from monocyte/macrophages and secrete angiogenic growth factors. *Circulation* **2003,** *107* (8), 1164-9.
17. Hur, J.; Yoon, C. H.; Kim, H. S.; Choi, J. H.; Kang, H. J.; Hwang, K. K.; Oh, B. H.; Lee, M. M.; Park, Y. B., Characterization of two types of endothelial progenitor cells and their different contributions to neovasculogenesis. *Arteriosclerosis, thrombosis, and vascular biology* **2004,** *24* (2), 288-93.
18. Yoon, C. H.; Hur, J.; Park, K. W.; Kim, J. H.; Lee, C. S.; Oh, I. Y.; Kim, T. Y.; Cho, H. J.; Kang, H. J.; Chae, I. H.; Yang, H. K.; Oh, B. H.; Park, Y. B.; Kim, H. S., Synergistic neovascularization by mixed transplantation of early endothelial progenitor cells and late outgrowth endothelial cells: the role of angiogenic cytokines and matrix metalloproteinases. *Circulation* **2005,** *112* (11), 1618-27.
19. Kalka, C.; Masuda, H.; Takahashi, T.; Kalka-Moll, W. M.; Silver, M.; Kearney, M.; Li, T.; Isner, J. M.; Asahara, T., Transplantation of ex vivo expanded endothelial progenitor cells for therapeutic neovascularization. *Proceedings of the National Academy of Sciences of the United States of America* **2000,** *97* (7), 3422-7.

20. Urbich, C.; Dimmeler, S., Endothelial progenitor cells functional characterization. *Trends in cardiovascular medicine* **2004,** *14* (8), 318-22.

21. Hacke, W.; Kaste, M.; Bluhmki, E.; Brozman, M.; Davalos, A.; Guidetti, D.; Larrue, V.; Lees, K. R.; Medeghri, Z.; Machnig, T.; Schneider, D.; von Kummer, R.; Wahlgren, N.; Toni, D., Thrombolysis with alteplase 3 to 4.5 hours after acute ischemic stroke. *The New England journal of medicine* **2008,** *359* (13), 1317-29.

22. http://www.strokeassociation.org.

23. Xiong, Y.; Mahmood, A.; Chopp, M., Angiogenesis, neurogenesis and brain recovery of function following injury. *Current opinion in investigational drugs* **2010,** *11* (3), 298-308.

24. Taguchi, A.; Soma, T.; Tanaka, H.; Kanda, T.; Nishimura, H.; Yoshikawa, H.; Tsukamoto, Y.; Iso, H.; Fujimori, Y.; Stern, D. M.; Naritomi, H.; Matsuyama, T., Administration of CD34+ cells after stroke enhances neurogenesis via angiogenesis in a mouse model. *The Journal of clinical investigation* **2004,** *114* (3), 330-8.

25. Horie, N.; Pereira, M. P.; Niizuma, K.; Sun, G.; Keren-Gill, H.; Encarnacion, A.; Shamloo, M.; Hamilton, S. A.; Jiang, K.; Huhn, S.; Palmer, T. D.; Bliss, T. M.; Steinberg, G. K., Transplanted Stem Cell-Secreted Vascular Endothelial Growth Factor Effects Poststroke Recovery, Inflammation, and Vascular Repair. *Stem cells* **2011,** *29* (2), 274-285.

26. Li, L.; Jiang, Q.; Ding, G.; Zhang, L.; Zhang, Z. G.; Li, Q.; Panda, S.; Lu, M.; Ewing, J. R.; Chopp, M., Effects of administration route on migration and distribution of neural progenitor cells transplanted into rats with focal cerebral ischemia, an MRI study. *Journal of cerebral blood flow and metabolism : official journal of the International Society of Cerebral Blood Flow and Metabolism* **2010,** *30* (3), 653-62.

27. Fischer, U. M.; Harting, M. T.; Jimenez, F.; Monzon-Posadas, W. O.; Xue, H.; Savitz, S. I.; Laine, G. A.; Cox, C. S., Jr., Pulmonary passage is a major obstacle for intravenous stem cell delivery: the pulmonary first-pass effect. *Stem cells and development* **2009,** *18* (5), 683-92.

28. Liong, M.; Lu, J.; Kovochich, M.; Xia, T.; Ruehm, S. G.; Nel, A. E.; Tamanoi, F.; Zink, J. I., Multifunctional inorganic nanoparticles for imaging, targeting, and drug delivery. *ACS nano* **2008,** *2* (5), 889-96.

29. Cheng, Z.; Al Zaki, A.; Hui, J. Z.; Muzykantov, V. R.; Tsourkas, A., Multifunctional nanoparticles: cost versus benefit of adding targeting and imaging capabilities. *Science* **2012,** *338* (6109), 903-10.

30. Arbab, A. S.; Bashaw, L. A.; Miller, B. R.; Jordan, E. K.; Lewis, B. K.; Kalish, H.; Frank, J. A., Characterization of biophysical and metabolic properties of cells labeled with superparamagnetic iron oxide nanoparticles and transfection agent for cellular MR imaging. *Radiology* **2003,** *229* (3), 838-46.

31. Jendelova, P.; Herynek, V.; Urdzikova, L.; Glogarova, K.; Kroupova, J.; Andersson, B.; Bryja, V.; Burian, M.; Hajek, M.; Sykova, E., Magnetic resonance tracking of transplanted bone marrow and embryonic stem cells labeled by iron oxide nanoparticles in rat brain and spinal cord. *Journal of neuroscience research* **2004,** *76* (2), 232-43.

32. Sykova, E.; Jendelova, P.; Herynek, V., Magnetic resonance imaging of stem cell migration. *Methods in molecular biology* **2011,** *750*, 79-90.

33. Song, M.; Kim, Y. J.; Kim, Y. H.; Roh, J.; Kim, S. U.; Yoon, B. W., Using a neodymium magnet to target delivery of ferumoxide-labeled human neural stem cells in a rat model of focal cerebral ischemia. *Human gene therapy* **2010,** *21* (5), 603-10.

34. Kyrtatos, P. G.; Lehtolainen, P.; Junemann-Ramirez, M.; Garcia-Prieto, A.; Price, A. N.; Martin, J. F.; Gadian, D. G.; Pankhurst, Q. A.; Lythgoe, M. F., Magnetic tagging increases delivery of circulating progenitors in vascular injury. *JACC. Cardiovascular interventions* **2009,** *2* (8), 794-802.

35. Yamahara, K.; Sone, M.; Itoh, H.; Yamashita, J. K.; Yurugi-Kobayashi, T.; Homma, K.; Chao, T. H.; Miyashita, K.; Park, K.; Oyamada, N.; Sawada, N.; Taura, D.; Fukunaga, Y.; Tamura, N.; Nakao, K., Augmentation of neovascularization [corrected] in hindlimb ischemia by combined transplantation of human embryonic stem cells-derived endothelial and mural cells. *PloS one* **2008,** *3* (2), e1666.

36. Assmus, B.; Schachinger, V.; Teupe, C.; Britten, M.; Lehmann, R.; Dobert, N.; Grunwald, F.; Aicher, A.; Urbich, C.; Martin, H.; Hoelzer, D.; Dimmeler, S.; Zeiher, A. M., Transplantation of Progenitor Cells and Regeneration Enhancement in Acute Myocardial Infarction (TOPCARE-AMI). *Circulation* **2002,** *106* (24), 3009-17.

37. Leistner, D. M.; Fischer-Rasokat, U.; Honold, J.; Seeger, F. H.; Schachinger, V.; Lehmann, R.; Martin, H.; Burck, I.; Urbich, C.; Dimmeler, S.; Zeiher, A. M.; Assmus, B., Transplantation of progenitor cells and regeneration enhancement in acute myocardial infarction (TOPCARE-AMI): final 5-year results

suggest long-term safety and efficacy. *Clinical research in cardiology : official journal of the German Cardiac Society* **2011,** *100* (10), 925-34.

38. Chavakis, E.; Urbich, C.; Dimmeler, S., Homing and engraftment of progenitor cells: a prerequisite for cell therapy. *Journal of molecular and cellular cardiology* **2008,** *45* (4), 514-22.

39. Agudelo, C. A.; Tachibana, Y.; Noboru, T.; Iida, H.; Yamaoka, T., Long-term in vivo magnetic resonance imaging tracking of endothelial progenitor cells transplanted in rat ischemic limbs and their angiogenic potential. *Tissue engineering. Part A* **2011,** *17* (15-16), 2079-89.

40. Yao, Y.; Li, Y.; Ma, G.; Liu, N.; Ju, S.; Jin, J.; Chen, Z.; Shen, C.; Teng, G., In vivo magnetic resonance imaging of injected endothelial progenitor cells after myocardial infarction in rats. *Molecular imaging and biology : MIB : the official publication of the Academy of Molecular Imaging* **2011,** *13* (2), 303-13.

41. Li, Q.; Tang, G.; Xue, S.; He, X.; Miao, P.; Li, Y.; Wang, J.; Xiong, L.; Wang, Y.; Zhang, C.; Yang, G. Y., Silica-coated superparamagnetic iron oxide nanoparticles targeting of EPCs in ischemic brain injury. *Biomaterials* **2013,** *34* (21), 4982-92.

42. Carenza, E.; Barcelo, V.; Morancho, A.; Levander, L.; Boada, C.; Laromaine, A.; Roig, A.; Montaner, J.; Rosell, A., In vitro angiogenic performance and in vivo brain targeting of magnetized endothelial progenitor cells for neurorepair therapies. *Nanomedicine* **2014,** *10* (1), 225-34.

43. Conner, S. D.; Schmid, S. L., Regulated portals of entry into the cell. *Nature* **2003,** *422* (6927), 37-44.

44. Mailander, V.; Landfester, K., Interaction of nanoparticles with cells. *Biomacromolecules* **2009,** *10* (9), 2379-400.

45. Dobrovolskaia, M. A.; McNeil, S. E., Immunological properties of engineered nanomaterials. *Nature nanotechnology* **2007,** *2* (8), 469-78.

46. Lynch, I.; Cedervall, T.; Lundqvist, M.; Cabaleiro-Lago, C.; Linse, S.; Dawson, K. A., The nanoparticle-protein complex as a biological entity; a complex fluids and surface science challenge for the 21st century. *Advances in colloid and interface science* **2007,** *134-135*, 167-74.

47. Nagayama, S.; Ogawara, K.; Minato, K.; Fukuoka, Y.; Takakura, Y.; Hashida, M.; Higaki, K.; Kimura, T., Fetuin mediates hepatic uptake of negatively charged nanoparticles via scavenger receptor. *International journal of pharmaceutics* **2007,** *329* (1-2), 192-8.

48. Wilhelm, C.; Gazeau, F., Universal cell labelling with anionic magnetic nanoparticles. *Biomaterials* **2008,** *29* (22), 3161-74.

49. Wilhelm, C.; Billotey, C.; Roger, J.; Pons, J. N.; Bacri, J. C.; Gazeau, F., Intracellular uptake of anionic superparamagnetic nanoparticles as a function of their surface coating. *Biomaterials* **2003,** *24* (6), 1001-11.

50. von Zur Muhlen, C.; von Elverfeldt, D.; Bassler, N.; Neudorfer, I.; Steitz, B.; Petri-Fink, A.; Hofmann, H.; Bode, C.; Peter, K., Superparamagnetic iron oxide binding and uptake as imaged by magnetic resonance is mediated by the integrin receptor Mac-1 (CD11b/CD18): implications on imaging of atherosclerotic plaques. *Atherosclerosis* **2007,** *193* (1), 102-11.

51. Jansch, M.; Stumpf, P.; Graf, C.; Rühl, E.; Müller, R. H., Adsorption kinetics of plasma proteins on ultrasmall superparamagnetic iron oxide (USPIO) nanoparticles. *International journal of pharmaceutics* **2012,** *428* (1–2), 125-133.

52. Harris, J. M.; Chess, R. B., Effect of pegylation on pharmaceuticals. *Nature reviews. Drug discovery* **2003,** *2* (3), 214-21.

53. Veiseh, O.; Gunn, J. W.; Zhang, M., Design and fabrication of magnetic nanoparticles for targeted drug delivery and imaging. *Advanced drug delivery reviews* **2010,** *62* (3), 284-304.

54. Soenen, S. J.; De Meyer, S. F.; Dresselaers, T.; Vande Velde, G.; Pareyn, I. M.; Braeckmans, K.; De Cuyper, M.; Himmelreich, U.; Vanhoorelbeke, K. I., MRI assessment of blood outgrowth endothelial cell homing using cationic magnetoliposomes. *Biomaterials* **2011,** *32* (17), 4140-50.

55. Roca, A. G.; Veintemillas-Verdaguer, S.; Port, M.; Robic, C.; Serna, C. J.; Morales, M. P., Effect of nanoparticle and aggregate size on the relaxometric properties of MR contrast agents based on high quality magnetite nanoparticles. *The journal of physical chemistry. B* **2009,** *113* (19), 7033-9.

56. Wang, Y. X.; Hussain, S. M.; Krestin, G. P., Superparamagnetic iron oxide contrast agents: physicochemical characteristics and applications in MR imaging. *European radiology* **2001,** *11* (11), 2319-31.

57. Taboada, E.; Solanas, R.; Rodríguez, E.; Weissleder, R.; Roig, A., Supercritical-Fluid-Assisted One-Pot Synthesis of Biocompatible Core(γ-Fe2O3)/Shell(SiO2) Nanoparticles as High Relaxivity T2-

Contrast Agents for Magnetic Resonance Imaging. *Advanced Functional Materials* **2009,** *19* (14), 2319-2324.

58. Billotey, C.; Wilhelm, C.; Devaud, M.; Bacri, J. C.; Bittoun, J.; Gazeau, F., Cell internalization of anionic maghemite nanoparticles: quantitative effect on magnetic resonance imaging. *Magnetic resonance in medicine : official journal of the Society of Magnetic Resonance in Medicine / Society of Magnetic Resonance in Medicine* **2003,** *49* (4), 646-54.

59. McGuigan, C. F. Effect of nitrate on human cell lines in culture. Master Thesis, University of Saskatchewan, Canada, 2007.

60. Mokrasch, L. C., Organic cations substituted for sodium are toxic to cultured rat glioma cells. *Molecular and cellular biochemistry* **1990,** *92* (1), 85-9.

61. Landauer, W., Cholinomimetic teratogens. II. Interaction with inorganic ions. *Teratology* **1975,** *12* (3), 271-6.

62. Russell, M. R.; Nickerson, D. P.; Odorizzi, G., Molecular mechanisms of late endosome morphology, identity and sorting. *Current opinion in cell biology* **2006,** *18* (4), 422-8.

63. Kleinman, H. K.; Martin, G. R., Matrigel: basement membrane matrix with biological activity. *Seminars in cancer biology* **2005,** *15* (5), 378-86.

64. Donovan, D.; Brown, N. J.; Bishop, E. T.; Lewis, C. E., Comparison of three in vitro human 'angiogenesis' assays with capillaries formed in vivo. *Angiogenesis* **2001,** *4* (2), 113-21.

65. Lamalice, L.; Le Boeuf, F.; Huot, J., Endothelial cell migration during angiogenesis. *Circulation research* **2007,** *100* (6), 782-94.

66. Kehrer, J. P., The Haber-Weiss reaction and mechanisms of toxicity. *Toxicology* **2000,** *149* (1), 43-50.

67. Ushio-Fukai, M.; Nakamura, Y., Reactive oxygen species and angiogenesis: NADPH oxidase as target for cancer therapy. *Cancer letters* **2008,** *266* (1), 37-52.

68. Stroh, A.; Zimmer, C.; Gutzeit, C.; Jakstadt, M.; Marschinke, F.; Jung, T.; Pilgrimm, H.; Grune, T., Iron oxide particles for molecular magnetic resonance imaging cause transient oxidative stress in rat macrophages. *Free radical biology & medicine* **2004,** *36* (8), 976-84.

69. Zhu, M. T.; Wang, Y.; Feng, W. Y.; Wang, B.; Wang, M.; Ouyang, H.; Chai, Z. F., Oxidative stress and apoptosis induced by iron oxide nanoparticles in cultured human umbilical endothelial cells. *Journal of nanoscience and nanotechnology* **2010,** *10* (12), 8584-90.

70. Chua, C. C.; Hamdy, R. C.; Chua, B. H., Upregulation of vascular endothelial growth factor by H2O2 in rat heart endothelial cells. *Free radical biology & medicine* **1998,** *25* (8), 891-7.

71. Lückhoff, A.; Busse, R., Calcium influx into endothelial cells and formation of endothelium-derived relaxing factor is controlled by the membrane potential. *Pflügers Arch* **1990,** *416* (3), 305-311.

72. Nilius, B.; Droogmans, G., Ion Channels and Their Functional Role in Vascular Endothelium. *Physiological Reviews* **2001,** *81* (4), 1415-1459.

73. Bilecka, I.; Elser, P.; Niederberger, M., Kinetic and thermodynamic aspects in the microwave-assisted synthesis of ZnO nanoparticles in benzyl alcohol. *ACS nano* **2009,** *3* (2), 467-77.

74. Hu, L.; Percheron, A.; Chaumont, D.; Brachais, C.-H., Microwave-assisted one-step hydrothermal synthesis of pure iron oxide nanoparticles: magnetite, maghemite and hematite. *J Sol-Gel Sci Technol* **2011,** *60* (2), 198-205.

75. Tenzer, S.; Docter, D.; Kuharev, J.; Musyanovych, A.; Fetz, V.; Hecht, R.; Schlenk, F.; Fischer, D.; Kiouptsi, K.; Reinhardt, C.; Landfester, K.; Schild, H.; Maskos, M.; Knauer, S. K.; Stauber, R. H., Rapid formation of plasma protein corona critically affects nanoparticle pathophysiology. *Nature nanotechnology* **2013,** *8* (10), 772-81.

76. Pascu, O.; Carenza, E.; Gich, M.; Estradé, S.; Peiró, F.; Herranz, G.; Roig, A., Surface Reactivity of Iron Oxide Nanoparticles by Microwave-Assisted Synthesis; Comparison with the Thermal Decomposition Route. *The Journal of Physical Chemistry C* **2012,** *116* (28), 15108-15116.

77. Carenza, E.; Barceló, V.; Morancho, A.; Montaner, J.; Rosell, A.; Roig, A., Fast synthesis of water-dispersible SPIONs by microwave assisted route for safe labeling of endothelial progenitor cells. *Acta Biomaterialia* **2014,** (0).

78. Pisanic, T. R., 2nd; Blackwell, J. D.; Shubayev, V. I.; Finones, R. R.; Jin, S., Nanotoxicity of iron oxide nanoparticle internalization in growing neurons. *Biomaterials* **2007,** *28* (16), 2572-81.

79. Weinstein, J. S.; Varallyay, C. G.; Dosa, E.; Gahramanov, S.; Hamilton, B.; Rooney, W. D.; Muldoon, L. L.; Neuwelt, E. A., Superparamagnetic iron oxide nanoparticles: diagnostic magnetic resonance imaging and potential therapeutic applications in neurooncology and central nervous system inflammatory

pathologies, a review. *Journal of cerebral blood flow and metabolism : official journal of the International Society of Cerebral Blood Flow and Metabolism* **2010,** *30* (1), 15-35.

80. Emerit, J.; Beaumont, C.; Trivin, F., Iron metabolism, free radicals, and oxidative injury. *Biomedicine & pharmacotherapy = Biomedecine & pharmacotherapie* **2001,** *55* (6), 333-9.

81. Weissleder, R.; Stark, D. D.; Engelstad, B. L.; Bacon, B. R.; Compton, C. C.; White, D. L.; Jacobs, P.; Lewis, J., Superparamagnetic iron oxide: pharmacokinetics and toxicity. *AJR. American journal of roentgenology* **1989,** *152* (1), 167-73.

CHAPTER 4

CO-ENCAPSULATION OF SPIONs AND RECOMBINANT HUMAN VASCULAR GROWTH FACTOR INTO PLGA NANOPARTICLES FOR TARGETED THERAPEUTIC ANGIOGENESIS

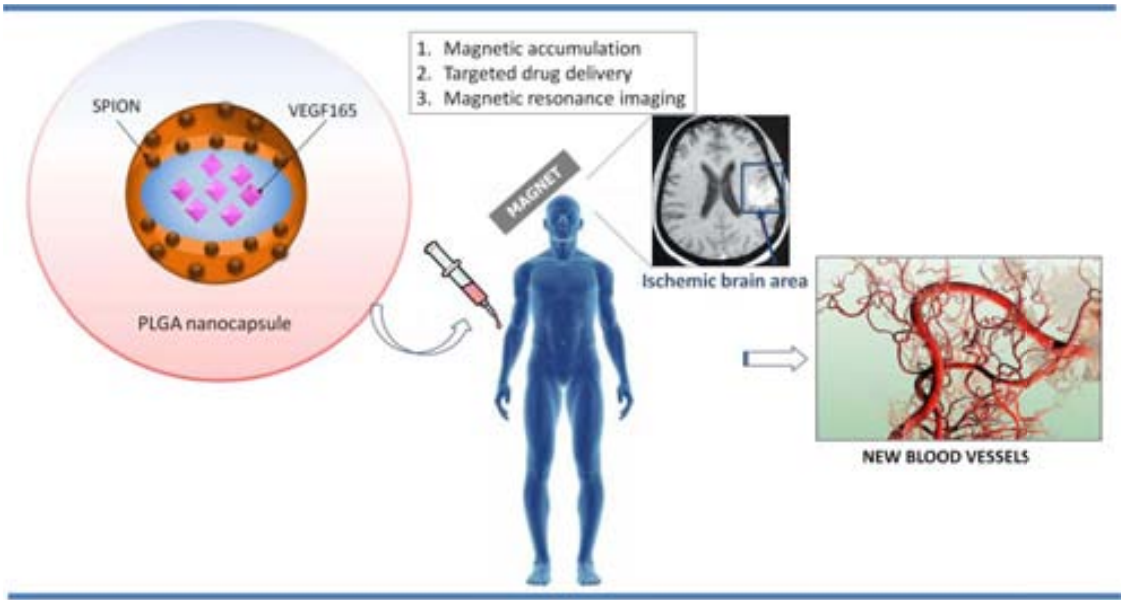

CHAPTER SUMMARY

The opportunity to rapidly assess and adjust therapeutic treatments to the needs of the individuals offers potential advantages in the view of a "personalized medicine"[1].

Nanotechnology is developing new strategies aiming to increase drug accumulation in the diseased area and reduce drug distribution in healthy tissues (targeted drug delivery). Compared with drug delivering systems or imaging agents alone, recently developed theranostic agents (useful for therapy and diagnosis) can simultaneously imaging and deliver therapeutic agents in specific sites or organs allowing detection and treatment in a single procedure[2]. **In this chapter we describe the successful synthesis of biodegradable poly(D,L-lactic-co-glycolic acid) (PLGA) nanocapsules with the encapsulation in the same formulation of a pro- angiogenic protein (recombinant human $VEGF_{165}$, $rhVEGF_{165}$) and magnetic nanoparticles**. This may be a promising strategy to combine:

- Local accumulation of the magnetic carriers in a target area under applied magnetic field,
- Targeted therapeutic angiogenesis by local delivery of pro-angiogenic factors,
- Simultaneous tissue monitoring by magnetic resonance imaging.

CHAPTER INDEX pag.

4.1. DRUG DELIVERY

4.1.1 TARGETED DRUG DELIVERY AND TYPE OF CARRIERS

Pharmaceutical technology has the objective to promote drug action as much as possible by improving drug distribution in the diseased area and avoiding drug penetration into healthy tissues. **Drug targeting needs carrier systems to bring therapeutic molecules to a target area in a controlled way**. This approach allows a series of advantages compared with the traditional drug formulations (capsules, tablets, etc.): reduction of the amount of drug required for the therapeutic effect, reduction of side-effects in healthy tissues and simplification of drug administration protocols. For instance, a drug into a suitable carrier can reside at the therapeutic dosage in blood without doing repeated intravenous injections [3,4].

The Nobel Prize Paul Ehrlich defined targeted drug delivery as the "magic bullet"[5] which at first recognizes and binds the target; secondly it delivers the drug in the target zone. The pharmaceutical components of the "magic bullet" are three: drug, carrier and targeting moiety. To date, numerous types of carriers are under investigation to load therapeutic agents: soluble polymers, nano- and microspheres, nano- and microcapsules, cells, liposomes, micelles, etc. The ideal carrier has to be slowly degradable, stimuli reactive, targeted and to have prolonged time circulation to keep constant the therapeutic level of the drug in the blood.

The targeting may occur without any specific recognition element (passive targeting) in the case of drug accumulation in a zone with enhanced permeability and retention like inflammation or tumor sites, or it may occur by specific targeting moiety (active targeting) with molecules which bind for instance specific receptors on the cellular membrane[6].

Moreover carriers may be sensitive to chemical or physical stimuli (Fig. 1) to promote the drug accumulation in a target zone and start drug release. Examples are variations in the pH values (e.g. the pH in inflamed or ischemic tissues is around 6.5 which is more acidic than 7.4 in healthy tissues)[7,8]; variations in temperature with application of local heat (hyperthermia)[9], magnetic field which retains carriers containing magnetic nanoparticles in the zone of interest[10,11] or ultrasounds which following to drug accumulation induce carrier disruption and drug liberation[12].

The active targeting is realized by attachment on the carrier surface of molecules or macromolecules like proteins (antibodies), nucleic acid (RNAs) or other receptor ligands directed to specific cellular components[13,14]. Generally it occurs through covalent binding of reactive groups as COOH- NH_2- or SH- of proteins with the carrier surface by bioconjugation strategies[15].

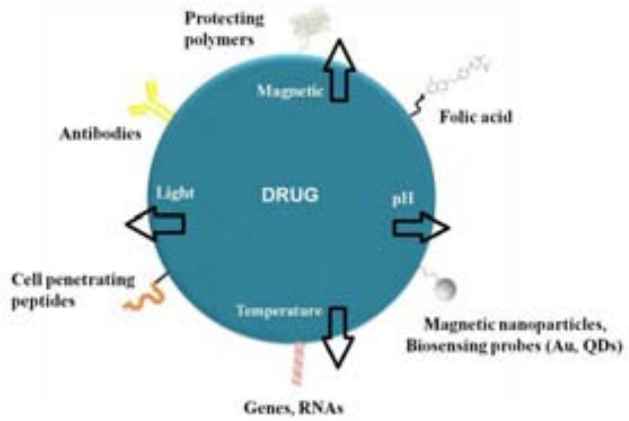

Figure 1. The three components of the "magic bullet" to achieve targeted drug release: drug, carrier (bleu colored) and targeting moieties. The sensitivity to chemical and physical stimuli (light, pH, temperature and magnetic field) after accumulation in the target zone allows controlled drug liberation. Modified picture from Yu-Cheng Chen et al. *Sci. Technol. Adv. Mater.* (2013), 14.

The carrier can be of micrometric or nanometric size, depending on the target site and it is usually made of biocompatible polymers. Biocompatibility as defined by Williams[16] concerns the effects of a material on the biological system: it should do not harm to the patient and it should perform with an appropriate response (specific for the application) into the host tissue. Examples of biocompatible materials used in drug delivery systems are polysaccharides like pectin[17], alginate[17b], which are natural polymers and polyesters[18], polyacrilate[19], polyethylenglycole (PEG)[20] which are synthetic polymers, phospholipids (liposomes)[21], mesoporous silica[22], etc.

Microspheres and microcapsules are carriers of size more than 1 μm. The former are homogeneous systems in which the drug is dispersed within the polymer matrix, whilst the latter are heterogeneous systems in which the drug is concentrated in the central core surrounded by a polymeric membrane. Nanospheres and nanocapsules (Fig. 2) have similar structures but smaller sizes, of less than 1 μm.

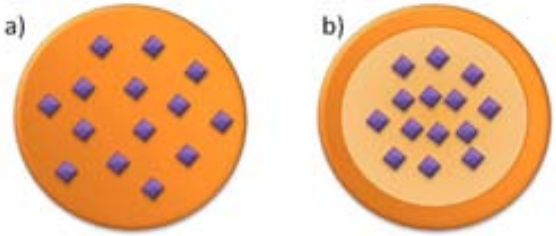

Figure 2. Scheme of cross sections in polymeric nanocarriers with different drug distributions (purple squares): (a) nanosphere with drug molecules embedded in the polymer matrix; (b) nanocapsule with drug molecules concentrated in the inner core.

The main advantage of nanocarriers (nanocapsules, nanospheres, liposomes) versus microcarriers is their smaller size: nanocarriers with good colloidal stability can be administered by general routes, including intravenous injection without the risk of embolization. Nanocapsules are preferred to nanospheres when it is needed to avoid the burst effect (rapid release) concentrating the drug in the central cavity to protect it from the degradation during storage or after administration. Compared to liposomes (artificial phospholipidic vesicles obtained by lipid dispersion in water), nanocapsules have enhanced

colloidal stability, better chemical resistance and they are easier to be synthesized[3]. Nanoparticles are also an attractive option for the targeted drug delivery into the brain. They may protect therapeutic agents from denaturation and increase the translocation efficiency across the blood brain barrier (BBB). Nanocapsules produced with poly(D,L-lactide-co-glycolide) (PLGA) have been evaluated as drug delivery carriers for stroke therapy[23,24] and have been produced by the double-emulsion method[25] among others. We chose to use PLGA because is a well known biodegradable polymer and it has numerous advantages compared with other carriers: it can be used to synthesize nanoparticles by reproducible, fast and economic procedures (see next paragraph), it is used as starting material rather than monomers.

4.1.2 BIODEGRADABLE POLYMERS AND PLGA

Biodegradable polymers are advantageous in many ways over other materials for use in drug delivery systems: they can be fabricated into various shapes and sizes, with tailored pore morphologies, mechanical properties, and degradation kinetics to suit a variety of applications. By selecting the appropriate polymer type, molecular weight, and copolymer blend ratio, the degradation/ erosion rate of the nanoparticles can be controlled to achieve the desired type and rate of release of the encapsulated drug. The common biodegradable polymers used in drug delivery include polyesters, such as lactide and glycolide copolymers, polycaprolactones, poly(hydroxybutyrates), polyamides, which includes natural polymers such as collagen, gelatin, and albumin, and semisynthetic pseudo-poly(amino acids) such as poly(N-palmitoyl hydroxyproline ester), polyorthoesters, polyanhydrides, and poly(alkyl cyanoacrylates).

Polymers are made of molecular chains and depending on the grade of order in their special distribution, polymers exhibit two states: crystalline and amorphous. The former is due to a more ordered chain distribution compared to the latter. Both states are conditioned by the temperature. At temperatures higher than the transition glass temperature (Tg) the molecular chains are randomly distributed and appear in a rubber-like state (Fig. 3).

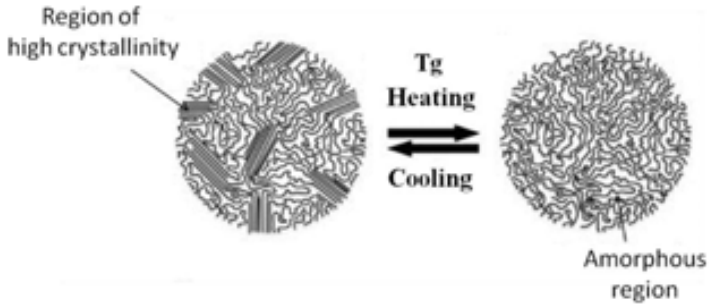

Figure 3. Transition of the polymer from more crystalline state (left) to the amorphous state (right) by changing the temperature. Tg is the transition glass temperature. Modified picture from Koichiro Uto et al (2012) *Sci. Technol. Adv. Mater.* 13.

The Tg is characteristic of each type of polymer because it depends on the presence of strong (H-bonds, electrostatic) or weak (Van der Waals) inter-chain interactions. Owing to the methyl groups the lactide polymer (PLA) (Fig. 4) is more hydrophobic than the glycolide polymer

(PGA), PLA is highly crystalline compared with PGA and erodes slowly since it is more resistant to hydrolysis[26].

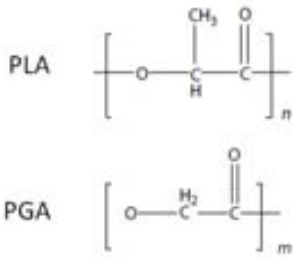

Figure 4. Chemical structures of poly-lactic acid (PLA) and poly-glycolic acid (PGA). Picture from "Targeted delivery of small and macromolecular drugs", CRC Press, (2010), book chapter number 17.

One of the most popular biodegradable polymers used in drug delivery are aliphatic polyester copolymers based on lactic and glycolic acids. Poly(D,L-lactic-co- glycolic acid) (PLGA) is used for the manufacture of implants and internal sutures and is known to be biocompatible[27]. PLGA is also the most used polymer in the formulation of nanoparticles as drug delivery systems for parenteral use. Danhier et al.[18] reviewed recent results in this field citing numerous preclinical *in vitro* and *in vivo* studies of targeted and untargeted nanoparticles for the treatment of different pathologies such as cancer, cerebral diseases and diabetes. PLGA nanoparticles undergo hydrolytic degradation to produce natural products lactic acid and glycolic acid. Polymer degradation is modulated by various factors such as chemical composition, porosity, hydrophilicity/hydrophobicity, morphology (crystalline/amorphous), molecular weight and molecular weight distribution.

PLGA copolymers (Fig. 5) undergo bulk hydrolysis/erosion of the ester bonds, wherein the molecular weight decreases while they are metabolized to lactic and glycolic acids which undergo elimination through Krebs cycle.

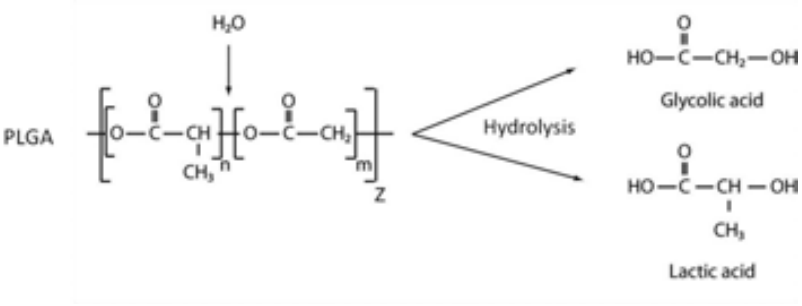

Figure 5. PLGA poly(D,L-lactic-co-glycolic) acid and its hydrolysis into glycolic acid and lactic acid molecules. Modified scheme from http://www.controlledreleasesociety.org.

The biodegradation *in vivo* and *in vitro* is different considering the presence of enzymes: it has been proved a more active enzymatic degradation of the polymer in the amorphous state than in the crystalline one[28]. For that, PLGA with increasing amounts of PLA (more crystalline) degrades slower than PLGA with increasing amounts of PGA (more amorphous). In fact, 50:50 lactide/glycolide copolymers have the fastest half-life of degradation, around 50 to 60 days, compared to 65:35, 75:25, and 85:15 lactide/glycolide copolymers which have progressively longer degradation half-lives *in vivo*. The 50:50 ratio of PLGA is thus advantageous as

compared with other polymers due to its fastest degradation rate, and as a result, fastest drug release from the nanoparticles. The evaluation of the biocompatibility for biodegradable polymers takes into account the incidence of the inflammatory and healing responses of the injected and implanted materials. Particles after an intramuscular or a subcutaneous injection usually have a high surface area/low volume ratio within a given tissue volume. Table 1 outlines the tissue responses to the polymer materials that are divided into three time phases (Phase I, II, III). The 50:50 PLGA nanoparticles have a phase II response of 50 to 60 days, whereas for the PLA microspheres, it takes around 350 to 400 days, thereby indicating its dependence on the rate of biodegradation of the nanoparticle. By modifying the polymer type, the copolymer composition, the polymer molecular weight, and the porosity of the microspheres, their degradation rate can be varied from days to months[28].

Table 1. Table showing the evaluation of biocompatibility for biodegradable polymers. It takes into consideration the incidence of the inflammatory and healing responses of the injected and implanted materials. From book chapter D'Mello S. et al., Drugs and the pharmaceutical sciences: "Drug Delivery Nanoparticles Formulation and Characterization", 2009, vol.. 191, Informa Healthcare.

Phase	Duration	Response
I	1–2 wk	Acute or chronic inflammatory responses that are independent of the degradation rate and the polymer composition.
II	0–3 wk	Response depends on the rate of polymer degradation and includes granular tissue development, foreign-body reaction, and fibrosis.
III	3 wk	Phagocytosis by macrophages and foreign-body giant cells.

Semete et al.[29] studied the extent of tissue distribution and retention following oral administration of PLGA particles was analyzed for 7 days. After 7 days, particles (between 0.3 and 1 μm in diameter) remained detectable in the brain, heart, kidney, liver, lungs, and spleen. The results show that a mean percentage of particles (40%) were localized in the liver, 25.97% in the kidney, and 12.86% in the brain. The lowest percentage was observed in the spleen. To avoid rapid particle clearance by the reticuloendothelial system and their accumulation in the liver particle surface modification is often needed, mainly achieved with PEG-PLGA blends or block copolymers.

4.1.3. PLGA NANOCAPSULES SYNTHESIS

The synthesis of PLGA nanoparticles can be typically done by a miniemulsion process starting from a liquid phase containing polymer in high concentration and a supernatant liquid phase depleted in the polymer. Polymeric nanoparticle synthesis can be divided into three steps:

- Formation of small liquid polymer droplets into a continuous phase by applying high shear stresses (e.g. sonication) in presence of surfactants to reduce surface tension (emulsification);
- Hardening of the small polymer droplets by solvent evaporation;

- Particle purification and lyophilization.

4.1.3.1 EMULSIFICATION PROCESS

Typically single emulsion processes are used to encapsulate drugs depending on their hydrophilic/hydrophobic properties: water in oil (W/O) emulsion with hydrophilic drug dissolved in the aqueous phase which is following added to the organic solvent containing polymer; whilst in the oil in water emulsion (O/W) the hydrophobic drug is dispersed in the organic phase together with the polymer. Usually low boiling point organic solvents are used in the emulsion process such as dichloromethane, isopropanol, chloroform.

Various variables such as the aqueous phase/organic phase volume ratio, stirring rate, polymer concentration, polymer solvent/nonsolvent ratio, affect the characteristics of nanoparticles such as morphology, internal porosity, and the size distribution. Emulsification is facilitated by high speed stirring such as sonication, differently from the macroemulsion process wherein simple mechanical stirring is used (ultraturrax)[30].

One challenge in the simple W/O emulsion is the low entrapment yield of hydrophilic drugs. A modification of the single-emulsion method is made by the preparation of a water-in-oil-in-water emulsion (W/O/W), which allows for the better incorporation of hydrophilic drugs; this process is termed as the double- or multiple-emulsion method. The process consists of adding the aqueous solution of the drug to the polymer dissolved in organic solvent with vigorous stirring to form the first W/O emulsion. This emulsion system is then added gently to a large quantity of water containing an emulsifier (e.g. poly(vinyl alcohol) PVA), resulting in a W/O/W double emulsion (Fig. 6).

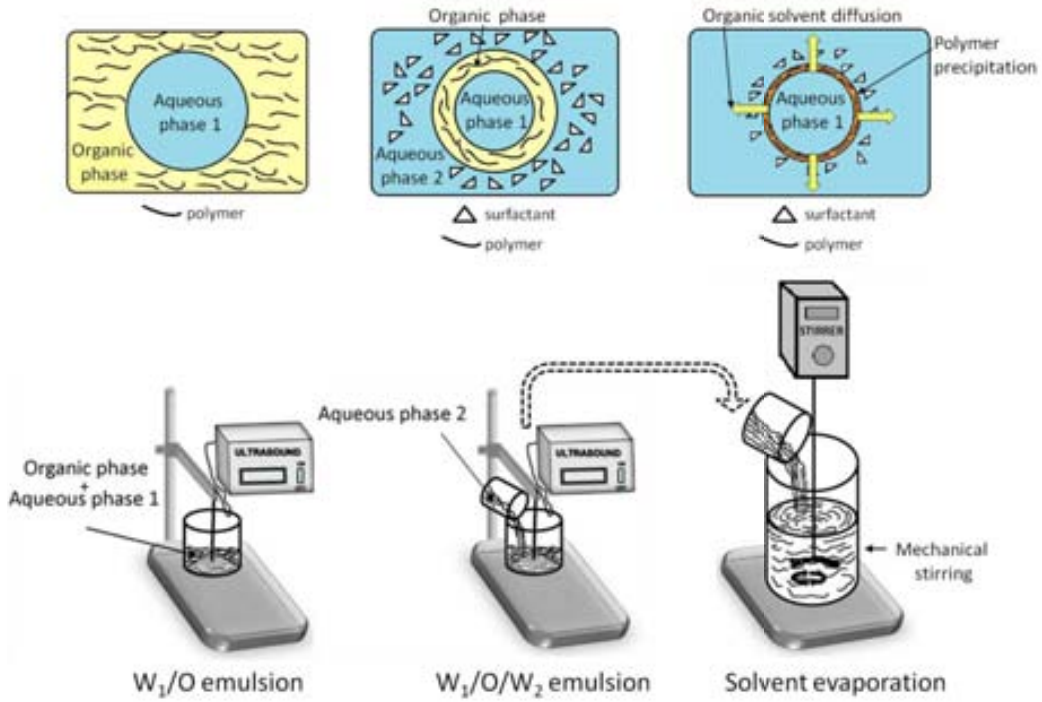

Figure 6. Set up used for the preparation of nanocapsules by the double emulsion method. Modified picture from Mora-Huertas C. E., *International Journal of Pharmaceutics 385* (2010) 113–142.

The double emulsion method allows the encapsulation of polypeptides and proteins with high efficiency yields[31], but it is also more difficult to control all synthetic parameters to achieve a uniform particle distribution with small size. Moreover the common organic solvents used to dissolve PLGA are class 2 solvents, classified as potentially toxic (e.g. dichloromethane). Attempts to overcome this issue have been done using less toxic solvents like ethyl acetate[28]. However, particles prepared by dichloromethane are spherical and more uniform, while the use of ethyl acetate results in particles which appear to be partly collapsed[32]. Moreover the drug **encapsulation efficiency** (EE%) which is the percentage of recovered drug over the initial loaded, reduces significantly compared to the particles made by dichloromethane. Li and coworkers[33] assumed that it is due to the high solubility of ethyl acetate in water, leading to the loss of drug for diffusion. Recently, Bilati et al.[34] demonstrated that for PLGA nanoparticles, formulation and processing parameters of W/O/W double- emulsion method affect their size and EE%. Blanco and Alonso[35,36] studied the effect of polymer type on drug content and mean size of the PLGA nanoparticles: it was found that high molecular weight PLGA gave the highest EE%.

4.1.3.2. SOLVENT EVAPORATION

After emulsification the formed liquid polymer droplets containing the drug are hardened by organic solvent removal inducing the formation of a solid polymer-rich phase. Solvent evaporation is realized by different methods, for instance by stirring the emulsion at high temperatures/low pressure conditions (distillation)[30,37] or by diluting the emulsion in an extensive amount of pure water under mechanical stirring at room temperature. In this case the organic solvent moves toward the emulsion interface, diffuses out into the aqueous phase and eventually evaporates into the air[33,38]. This process is accompanied by increased polymer concentration and subsequent polymer precipitation at the interface, droplet hardening and size reduction (Fig. 7).

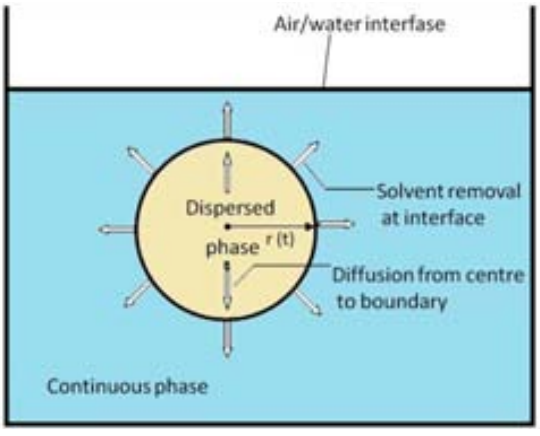

Figure 7. Scheme of solvent evaporation during a simple O/W emulsion. The yellow circle indicates a single polymer droplet (dispersed phase). r(t) is the average radius of drop that decreases with time. The continuous phase is water (blue colored). Modified picture from Li M. et al. (2008) *Int J Pharm 363*(1-2), 26-39.

In general the emulsion is formed using organic solvents partly soluble in water such as benzyl alcohol, propylene carbonate, ethyl acetate[35]. In this way the organic solvent contained in the polymer droplets can easily diffuse out of the droplets leading to the precipitation of the polymer. When dichloromethane (organic solvent less miscible with water) is used in the emulsification process the diffusion is facilitated by the presence of surfactants at the aqueous/organic interface[30]. The solvent evaporation by diffusion has been widely applied to prepare nanoparticles composed of PLA, PLGA using PVA, Pluronic F68 as surfactants. It can also be applied to formulate nanoparticles with amphiphilic copolymers including PEG-PLA. In this case there is no need to add a surfactant to insure the formation of the emulsion and the stability of the final nanoparticle suspension. Solvent diffusion in water is the most common method used for organic solvent evaporation. Recently it has been developed another technique, the spray drying, through which particle formation is achieved by atomizing the emulsion into a stream of hot air under vigorous solvent evaporation[36].

Normally, the rate of solvent evaporation has important effects on the porosity of nanoparticles, which significantly affects the drug release. Since the solvent evaporation at high temperatures or low pressures is faster than the evaporation at room temperature, the resultant porosity of the nanoparticle matrix prepared by the first method is usually greater than the nanoparticles prepared by using slow evaporation rates[28].

4.1.3.3. PARTICLE PURIFICATION AND LYOPHILIZATION

After solvent evaporation particles are collected and washed to eliminate organic solvent and surfactant traces. PVA is difficult to remove from particle surface: it has the ability to stay adsorbed on the polymer wall even after repeated washings. The residual PVA influenced different pharmaceutical properties of nanoparticles such as particle size, zeta potential, polydispersity index, surface hydrophobicity, protein loading and also slightly influenced the *in vitro* release of encapsulated protein. Importantly, nanoparticles with higher amount of residual PVA had relatively lower cellular uptake despite their smaller particle size[39,40].

Pluronics® which are commercial triblock copolymers made of polypropylene oxide (PPO) and polyethylene oxide (PEO) have also been largely used as stabilizers during the emulsification step[41,42]. Recently it has been proved that Pluronics® are not inert carriers but they have important biological effects *in vitro* and *in vivo*. The key attribute for the biological activity of Pluronics® is their ability to incorporate into cell membranes followed by subsequent translocation into the cells, affecting various cellular functions such as mitochondrial respiration, ATP synthesis, activity of drug efflux transporters, apoptotic signal transduction, and gene expression[43]. For those reasons they are currently studied as drug carriers and biological response modifier in tumor therapies.

After purification which generally occurs using pure water, the colloidal aqueous suspension containing the polymeric nanoparticles (PLGA) with the drug, have to be lyophilized in order to preserve them from hydrolytic degradation. The freeze-drying uses low temperatures to freeze the colloidal suspension and at the same time low pressures to sublimate water, which is

finally removed from the material (Fig. 8). It is a valid method to preserve nanoparticle fragile structures from degradation in time.

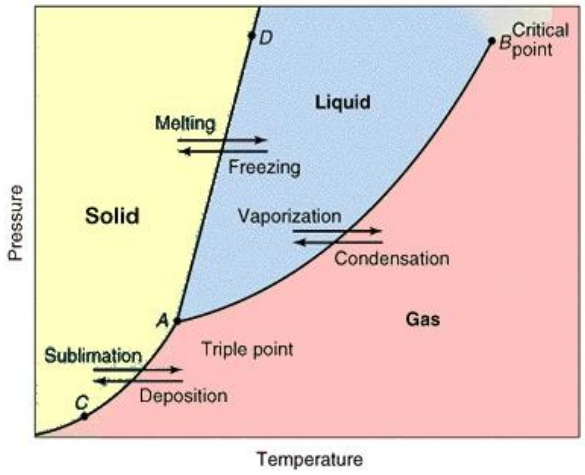

Figure 8. Graph of solid, liquid and gas states of a generic solution in function of temperature and pressure. Picture from http://lyophilizedproducts.com.

Freeze drying occurs in three steps:

- Product freezing at appropriate temperature (generally lower than -40°C) which depends on particle concentration in the colloidal suspension, polymer type and drug loading. Moreover a faster cooling-rate generally results in a solid with higher volume (lower density) and which is more amorphous compared to a slower cooling-rate;
- Primary drying which involves sublimation of ice from the frozen product. In this process the ice sublimes and water vapor formed passes to the surface of the dried sample. At the end of sublimation step a porous material is formed. Its pores correspond to the spaces that were occupied by ice crystals;
- Secondary drying which involves the removal of absorbed water from the product. This is the water fraction which did not separate out as ice during the freezing, and did not sublimate off in the primary step. It is performed at higher temperatures (between 25-50°C) to allow complete ice sublimation and water removal[44].

Freeze-drying may generate many stresses that could destabilize colloidal suspension of nanoparticles, especially, the stress of freezing and dehydration. It is well known that during the freezing of a sample there is a phase separation into ice and cryo-concentrated solution.

In the case of nanoparticle suspensions, the cryo-concentrated phase is composed of nanoparticles and other components as free surfactants, buffers, and unloaded drugs. This high concentration of particulate system may induce aggregation and in some cases irreversible fusion of nanoparticles. Furthermore, the crystallization of ice may exercise a mechanical stress on nanoparticles leading to their destabilization. For these reasons, special excipients must be added to the suspension of nanoparticles before freezing. These excipients are usually added in order to protect the product from freezing stress (cryoprotectant) or drying stress (lyoprotectant) and also to increase its stability upon storage. The most popular cryoprotectants for freeze-drying nanoparticles are sugars: trehalose, sucrose, glucose and

mannitol. These sugars in aqueous solutions are known to vitrify into amorphous states at a specific temperature denoted transition glass temperature (Tg).

The presence of a cryoprotectant during freezing creates a protective glassy layer around nanoparticles which can prevent their aggregation and protect them against the mechanical stress of ice crystals. Trehalose seems to be a preferable cryoprotectant for biomolecules. It has many advantages in comparison with other sugars: less hygroscopicity, very low chemical reactivity and higher Tg which means faster transition to the glassy state (Fig. 9).

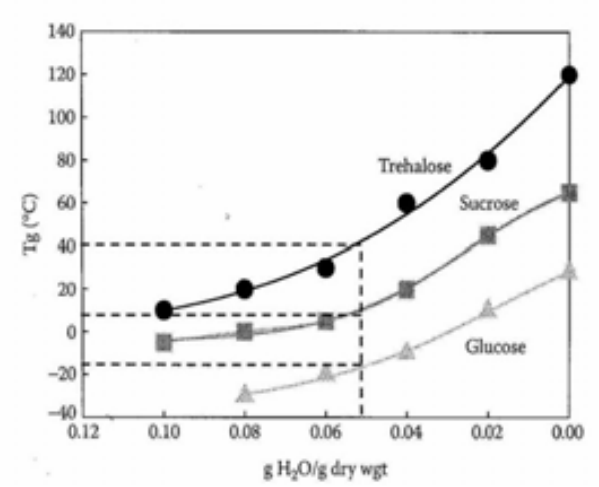

Figure 9. Trehalose has a higher glass transition temperature (T_g) than sucrose or any other disaccharide studied. At 5% water content, T_g for trehalose is about 40ºC whereas T_g for sucrose is about 15ºC. Image obtained from Vitrification in Cryonics, http://www.benbest.com/cryonics/vitrify.

If the freeze drying process is not performed in an accurate way, it can impair the performance of the drug delivery system by inducing collapse, or shrinkage of the final freeze-dried product, slow reconstitution after re-dispersion in water, higher nanoparticle hydrodynamic diameter (aggregation) and damage of drug integrity.

4.1.4. PROTEIN ENCAPSULATION INTO PLGA NANOCAPSULES

Proteins are attractive therapeutic molecules but are also more sensitive compared to common pharmaceutical drugs: they have complex architecture with primary, secondary, tertiary and in some cases quaternary structure. They often have labile bounds and chemically reactive groups on the side chains. Disruption or modification of these structures (by denaturation or aggregation) leads to loss of protein activity. For instance proteins can easily unfold due to changes in the environment conditions (pH, temperature, ionic force) and they have short half lives when administered *in vivo* [45]. The encapsulation of active proteins may preserve them from fast degradation but it presents many challenges associated with each step of the encapsulation procedure: from the protein emulsification using organic polymer solutions, to the solvent evaporation, lyophilization and storage. The emulsion obtained by adding a protein in aqueous solution to an organic solution induces the formation of aqueous/organic interface (e.g. water/ dichloromethane) which can lead to protein denaturation[46]. Approaches in stabilizing protein during encapsulation consist in adding molecules as surfactants or lyoprotctants (sucrose acetate isobutyrate, trehalose) which reduce the interfacial tension, or to

use organic solvents more miscible with water as ethylacetate and acetone[47]. Another approach consists in avoiding the formation of aqueous/organic interface by adding the protein in lyophilized state to the organic polymer phase (suspension method)[48,49,50]. Even though protein solubility in the organic solvent is not a favored thermodynamic condition, low temperatures together with the anhydrous environment may favorite protein suspension.

Bilati et al.[31] developed the nanoprecipitation technique which is performed using three basic ingredients: the polymer, the polymer solvent and the non-solvent of the polymer. The polymer solvent is chosen among organic solvents being miscible in water and easy to remove by evaporation. For this reason, acetone is the most frequently used polymer solvent in this method. Sometimes, it consists in binary blends of solvents, acetone with small amount of water, blends of ethanol and acetone. The polymer solution is added to the non-solvent and nanoparticles form instantaneously during the rapid polymer precipitation. However lower protein and drug encapsulation efficiencies have been found for these systems compared to traditional emulsion methods[47].

After the emulsification step nanoparticles, with the encapsulated protein, undergo solvent evaporation and repeated washings to reduce the amount of residual surfactants. Finally it is important to perform an accurate lyophilization to obtain a dried material, which has to be stored at 4°C under drying conditions (silica gel). In fact, the remaining humidity in the lyophilized material induces rapid PLGA degradation in time with the formation of an acidic environment which can modify protein structure and activity[46].

Another important drawback encountered in protein-nanoparticle formulation is the incomplete release due to the interaction of the protein (amphiphilic macromolecule) with the hydrophobic polymer (PLGA). To increase the release rates additives such as bovine serum albumin, polaxamers have been added during the emulsification step[51] or proteins have been encapsulated in PLGA-PEG copolymers[52] which has also the effect to increase nanoparticle circulation time *in vivo* [53].

In conclusion the double emulsion method using PLGA offers numerous advantages compared with other carriers in protein encapsulation because PLGA is a well known polymeric carrier accepted by FDA and nanoparticle synthesis is facile and reproducible.

4.2. PRO-ANGIOGENIC GROWTH FACTORS

In adults, angiogenesis (formation of new blood vessels from pre-existing ones) is started by a local angiogenic stimulus (such as ischemia), through which endothelial cells of pre-existing capillaries become activated: local vasodilatation, increased vascular permeability accumulation of extravascular fibrin, proteolytic degradation of the basal lamina, proliferation and migration occur. Finally endothelial cell elongate and align with one another to form a capillary sprout (see paragraph 3.1. chapter 3). Angiogenesis activation or inhibition is the result of a complex regulation in the equilibrium between pro- and anti-angiogenic factors[54]. The as-defined vascular endothelium growth factors include members of VEGF, angiopoietin, or ephrin families. In addition, many other growth factors that are not vascular endothelium-specific are also required for blood vessel formation, such as members of the platelet-derived

growth factor or transforming growth factor-b families, although these factors also have critical roles for many other systems as well.

VEGF, maintains its position as the most critical driver of vascular formation, as it is required to initiate the formation of immature vessels by vasculogenesis (formation of new blood vessels, commonly from stem cells) or angiogenic sprouting during embryonic development and in adulthood. Ang1 and ephrin-B2 are subsequently required for further remodeling and maturation of the initially immature vasculature with ephrin-B2 being particularly important in distinguishing developing arterial and venous vessels. VEGFs, angiopoietins and ephrin- B2 apparently repeat their developmental roles during vascular remodeling in the adult. The external administration of individual factors allows growth factors to continue but not to trigger the entire process. Thus VEGF administration can initiate vessel formation in adult animals, but by itself promotes formation of only leaky, immature and unstable vessels. In contrast, Ang1 simultaneous administration further stabilizes and protects the adult vasculature, making it resistant to the damage and leak induced by VEGF or inflammatory responses. In summary, all these factors act in a complementary and coordinated manner. Researchers are investigating the mechanisms through which these factors orchestrate pro-angiogenic and anti-angiogenic responses to develop new therapeutic strategies for numerous diseases (cancer, ischemia)[55, 56,57]. Di Santo et al.[58] demonstrated that by the administration of cell-free growth factors secreted by endothelial progenitor cells it is possible to achieve an angiogenic therapeutic effect equivalent to cell therapy in a rat model of hindlimb ischemia. More recently Rosell and coworkers described neurorepair effects of the administration of EPC-secreted growth factors in a mouse model of ischemic stroke[59].

Similarly, we aim to encapsulate endogenous growth factors (released by endothelial progenitor cells) together with magnetic nanoparticles (SPIONs) into suitable carriers for targeted therapeutic angiogenesis in brain stroke. Since the simultaneous encapsulation of more than one factor is challenging due to specific protein structures, interactions with the polymer matrix and release rates, we chose to start with the encapsulation of a single growth factor, the human recombinant $VEGF_{165}$ along with SPIONs.

4.2.1. VEGF ISOFORMS, RECEPTORS AND MECHANISM OF ANGIOGENESIS

VEGF is a family of polypeptide which is expressed almost exclusively by endothelial cells. The VEGF family currently comprises seven members: VEGF-A, VEGF-B, VEGF-C, VEGF-D, VEGF-E, VEGF-F, and PlGF (placent growth factor) (Table 2).

Table 2. Summary of VEGF family. Per each type of family member are explained main biological functions. EC = endothelial cells. Table from http://www.news-medical.net/health/VEGF-Classification.

Type	Function
VEGF-A	•Angiogenesis: ↑migration , mitosis EC. • Chemotactic for macrophages. • Vasodilatation.
VEGF-B	Embryonic angiogenesis.
VEGF-C	Lymphangiogenesis.
VEGF-D	Development of lymphatic vasculature surrounding bronchioles.
PlGF	Important for vasculogenesis, angiogenesis, wound healing, etc.

VEGFs induce proliferation exclusively of vascular endothelial cells, differently to PDGF (platelet -derived growth factor) which induces endothelial cell sprouting accompanied by extensive fibroblastic proliferation.

VEGF-A is a 34- to 42-kDa, dimeric glycoprotein. Activity of VEGF-A has been studied mostly on cells of the vascular endothelium, although it does have effects on a number of other cell types (e.g., stimulation of monocyte/macrophage migration, neurons, cancer cells, kidney epithelial cells). In vitro, VEGF-A has been shown to stimulate endothelial cell mitogenesis (proliferation) and cell migration. VEGF-A has also hemodynamic effects (vasodilatation) and increases microvascular permeability.

All members have a common VEGF homology domain. This core region is composed of a cystine knot motif, with eight invariant cysteine residues involved in inter- and intramolecular disulfide bonds at one end of a conserved central four-stranded β-sheet within each monomer, which dimerize in an antiparallel, side-by-side orientation[60] (Fig. 10).

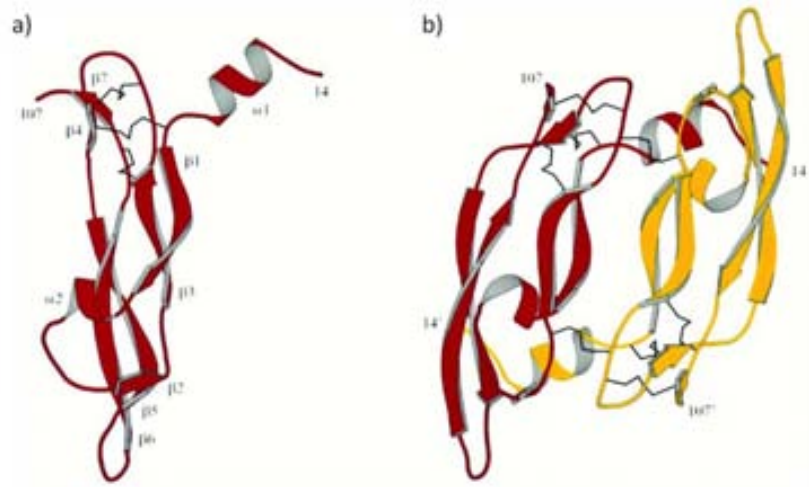

Figure 10. Ribbon representations of the receptor binding domain of VEGF, generated with program molscript showing the monomer in (a), with the secondary structural elements labeled, and the dimer in (b). In the monomer are visible the seven β sheets and the two α helixes. Cysteine bonds (black lines)

present in the dimer with the two monomers oriented in antiparallel way. Muller YA et al. *PNAS* (1997) *94*, 7192-7197.

VEGF-A exists in at least seven homodimeric isoforms. The monomers consist of 121, 145, 148, 165, 183, 189, or 206 amino acids respectively ($VEGF_{121}$, $VEGF_{145}$, $VEGF_{148}$, $VEGF_{165}$, $VEGF_{183}$, $VEGF_{189}$, $VEGF_{206}$)[61]. $VEGF_{165}$ is the predominant molecular specie; $VEGF_{206}$ is a very rare form. Native $VEGF_{165}$, the major isoform, is a basic (isoelectric point 8.5), heparin-binding, homodimeric glycoprotein. $VEGF_{121}$ is a weak acidic polypeptide that fails to bind to heparin. $VEGF_{189}$ and $VEGF_{206}$ are more basic and bind to heparin with greater affinity than $VEGF_{165}$. Previous studies demonstrated that such differences in the isoelectric point and in affinity for heparin may profoundly affect the bioavailability of VEGF[62].

VEGFs act binding two tyrosine kinase receptors causing them to dimerize and become activated. The main receptors that seem to be involved in signal transduction cascades in response to the VEGFs, comprise a family of closely related receptor tyrosine kinases (Fig. 11) consisting of three members termed VEGFR-1 (previously known as Flt-1), VEGFR-2 (previously known as KDR or Flk-1) and VEGFR-3 (previously known as Flt-3). In addition, there are a number of accessory receptors such as the neuropilins which seem to be involved primarily in modulating binding to the main receptors, although roles in signaling have not been ruled out. VEGFR-2 seems to mediate the major growth and permeability actions of VEGF, whereas VEGFR-1 is involved in the induction of matrix metalloproteinases (which destroy the extracellular matrix) and in the paracrine release of growth factors from endothelial cells[63,64]. VEGFR-3 may be important during blood vessel development, but its presence is almost limited to lymphatic vessels[55].

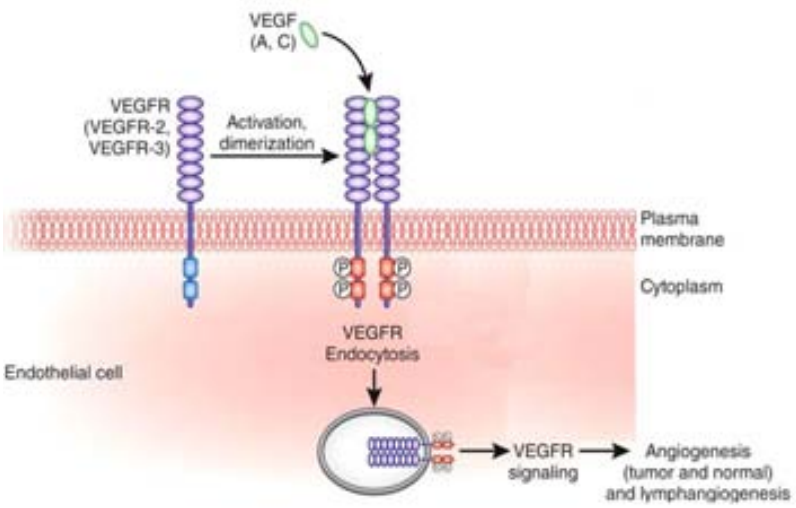

Figure 11. Mechanism of VEGF on tyrosine kinase receptors. Modified picture from S. Germain, *Nature Medicine* (2010) *16*, 752–754.

4.2.3. VEGF ENCAPSULATION INTO PLGA NANOCAPSULES

The administration of exogenous pro-angiogenic proteins is an attractive therapeutic strategy for ischemia treatment. Currently the most investigated VEGF for drug delivery purposes is VEGF-A (VEGF165 isoform) which has been incorporated or covalently linked to carriers as

alginate hydrogels[65], gelatin[66], polyethylenglycole[67], poly(D,L-lactide-co-glycolide) nanoparticles[68,69,70,71]), liposomes[72] and gold nanoparticles[73].

$VEGF_{165}$ has been encapsulated with high encapsulation efficiencies[70] (between 80% and 100%) into PLGA microspheres of 5 μm in diameter in presence of protein-stabilizers as bovine serum albumin (BSA). BSA is used to protect the VEGF from the acidic environment created by PLGA hydrolytic degradation during storage or during protein release *in vitro* which can modify protein structure reducing its biological activity. To prove encapsulated VEGF activity cell proliferation and sprouting formation of endothelial cells (EC) have been measured by *in vitro* experiments. Although the specific *in vivo* VEGF concentration required to elicit an EC response is unknown, the *in vitro* concentration of VEGF required to invoke an EC response is around 10 ng/ mL[71]. Importantly evidences of angiogenesis induced by delivered VEGF have also been confirmed by *in vivo* assays which show tissue revascularization and recover in animal models with ischemic hindlimb[74,75]. Recently it has been proved the angiogenic potential after stroke of PLGA microparticles with encapsulated VEGF in animal models[76].

4.3. SPIONs AND PROTEIN LOADED PLGA NANOCAPSULES: STATE OF THE ART

Water dispersible or oleic acid coated SPIONs have been recently encapsulated into PLGA particles by emulsion methods for improving non-invasive imaging by MRI. Most of studies have been done encapsulating hydrophobic SPIONs by single emulsion method in the polymeric phase of micro or nanospheres[77,78] or hydrophilic SPIONs in the aqueous core by double emulsion method[79]. Encapsulated SPIONs have also been used as theranostics (useful for therapy and diagnosis) with imaging purposes, targeted drug delivery and particle retention in specific tissues[11,80,81]. This strategy is of great interest because it may enhance particle accumulation in the target area and prolong the local drug release in time.

In literature there are few examples on the co-encapsulation of SPIONs with proteins[82]. VEGF-A has been encapsulated in PLGA particles together with gadolinium complexes for imaging purposes[83].

The lack of research in protein-SPION co-encapsulation can be due to proteins labile structure and possible inactivation by interaction with SPION surface. Generally, it is known that proteins adsorption onto nanoparticle surface can induce protein association with the formation of new protein clusters, which may be recognized as harmful products (and can potentially contribute to the progress of diseases such as amyloidoses) or could introduce new biological interactions, as a result of new protein surface presentations (new epitopes) at the bio/nano interface[84].

Very recently Niu and coworkers[85] have developed a new approach on the encapsulation of SPIONs with drugs: during the double emulsion process the drug is encapsulated in the inner core and the hydrophobic SPIONs are embedded in the polymeric layer of the nanocapsules. Our hypothesis is that this approach may be useful to reduce protein-SPIONs interactions keeping them separated, in different compartments. $VEGF_{165}$ is a glycoprotein of relative big size (38200 Da) soluble in aqueous media which can be incorporated in the aqueous core of

polymeric nanocapsules. SPIONs surface properties can be turned into hydrophobic ones by suitable coating (oleic acid) which makes possible to disperse them in the organic polymer phase. Figure 12 depicts our designed nanocapsules.

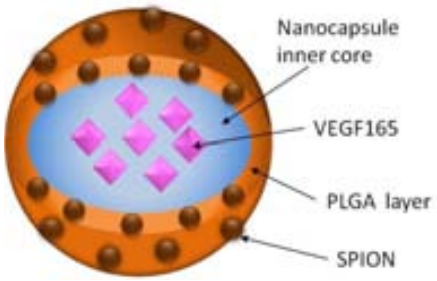

Figure 12. Scheme of nanocapsule cross-section: the aqueous inner core (blue colored) is filled with $VEGF_{165}$ molecules (purple squares), the PLGA layer embeds SPIONs (brown circles).

4.4. SYNTHESIS OF PLGA NANOCAPSULES WITH SPIONs AND $VEGF_{165}$

For the double emulsion we used the sonication with a digital sonifier microtip of 3 mm in diameter. Sonication produces high shear forces and may induce structural changes of proteins also due to the formation of free radicals by water sonolysis[34,86]. To overcome this drawback short sonication times were used during the first and second emulsion.

4.4.1. SET UP

In a small propylene tube the organic phase containing PLGA and SPIONs was prepared as follows: 50 mg of PLGA 50:50 (RG502 Boehringer Ingelheim, Mw 18000 Da, inherent viscosity 0.24 dL/g) were mixed with 0.45 mL of methylene dichloride using an ultrasonic bath. Oleic acid-coated SPIONs (0.94 mg) were dispersed in 50 µL of methylene dichloride and then mixed with the polymer solution using an ultrasonic bath.

The first W_1/O emulsion was carried out by adding to the organic phase 25 µg of lyophilized recombinant human $VEGF_{165}$ (Peprotech) dissolved in 50 µL of EBM (endothelial basal medium, Lonza) in one drop. The first emulsion took place by sonicating at 240 W for 28 seconds (Vibra-cell® VCX 500, Sonics & Materials) with microtip of 3 mm in diameter which was initially dipped close to the boundary surface to generate the maximum shear force between the two phases. The temperature during the whole emulsion process was kept at 4°C with an ice bath. The second emulsion $W_1/O/W_2$ was realized by adding 2 mL of polyvinyl alcohol (PVA) 2% w/v and by sonicating at 240 W for 28 seconds. Subsequently the as-formed colloidal suspension was poured into 50 mL of MilliQ water and kept under mechanical stirring at room temperature for 2 hours to allow complete evaporation of the organic solvent. Then the colloidal dispersion was collected in different polypropylene tubes and washed with MilliQ using a first centrifuge at 1000 rpm (rotor distance from the center of 6 cm) for 15 minutes to precipitate particles larger than 1 µm. Further three centrifugations at 11000 rpm, each time with addition of fresh water, were done to reduce the amount of PVA adsorbed on PLGA. Finally the particles were re-dispersed in an aqueous solution of trehalose 0.2% w/v before being rapidly frozen at -75°C and freeze-dried at -80°C for 2 days. Trehalose addition is

important for the nanocapsule preservation during the lyophilization step: it creates a protective glassy layer around nanocapsules which prevent their aggregation and protect them against the mechanical stress of ice crystals. The final lyophilized sample should not show any collapse or shrinkage but it should appear as an elegant cake, occupying the same volume of the starting aqueous suspension. The as obtained powder was stored at 4ºC with desiccant silica gel (Fig. 13).

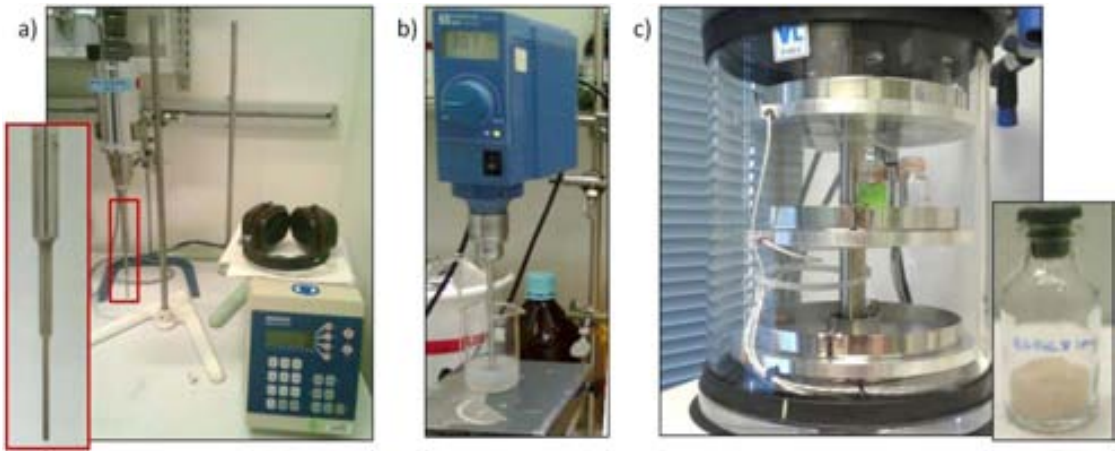

Figure 13. Steps of the synthesis of nanocapsules by double emulsion-solvent evaporation method: picture a) shows the digital sonifier with 3 mm microtip indicated in red rectangle; picture b) shows the evaporation step under vertical mechanical stirring; picture c) shows samples during freeze-drying at -80° at 0.05 mBar and on the right side the final lyophilized nanocapsules.

By previous encapsulation experiments using lysozyme (14300 Da, isoelectric point= 11) as model protein we checked if the used sonication conditions induced protein changes in the secondary structure using circular dichroism measurements (CD) (see annex of chapter 4, paragraph 4.6.3. for further details). The increase in time and power of sonication enhances the possibility of modifying protein structure. The condition used of 28 seconds at 240 Watts did not affect lysozyme structure.

4.4.2. CHARACTERIZATION OF rhVEGF$_{165}$ AND SPION LOADED PLGA NANOCAPSULES

4.4.2.1. SIZE AND STRUCTURE

Size was measured by dynamic light scattering after re-dispersion in water or culture media. The zeta potential of particles in water which resulted from the partially ionized –COOH for all samples was around -22 mV. Particles readily re-disperse in water and the suspension was stable in time, no precipitation occurred. Importantly the hydrodynamic size and polidispersity % of lyophilized particles were very similar and only slightly higher compared to as-synthesized particles. This fact indicated that during the lyophilization step no major particle aggregation for mechanical stress due to the formation of ice crystals took place. Particles re-dispersed in PBS 1X formed a rather unstable suspension and particle precipitation started after few minutes (Fig. 14). Attempts to stabilize them in PBS were done by using surfactants like TWEEN 80 at 0.1% without significant improvements. However PLGA nanocapsule instability in aqueous media (mainly after freeze-drying) is a common drawback due to the PLGA hydrophobic nature.

Nanocapsule size was measured by counting 200 particles of scanning electron microscopy images using ImageJ software (Fig. 15). The average diameter was 165 nm with 20% of polydispersity.

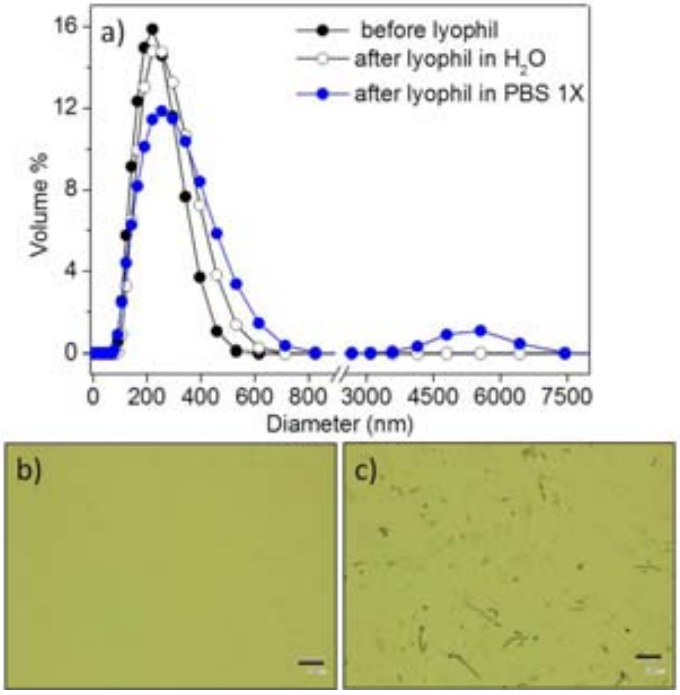

Figure 14. Nanocapsule (NCs) dispersions in water and PBS. Picture a): DLS measurements of as-synthesized NCs in water (before lyophilization) with mean size of 225 nm and 17% of polidispersity (black full circles); NCs after freeze-drying re-dispersed in water with mean size of 256 nm and 18% of polidispersity (black empty circles); NCs after freeze-drying re-dispersed in PBS1X showing two peaks: one at 270 nm and the other at 5000 nm indicating particle aggregation (blue circles). Picture b) shows NCs after freeze-drying re-dispersed in water analyzed by optical microscope: no particle precipitation occurs. Picture c) shows NCs after freeze-drying re-dispersed in PBS1X: particle aggregate and precipitate toward the bottom of the well after few minutes. Scale bar 100 μm.

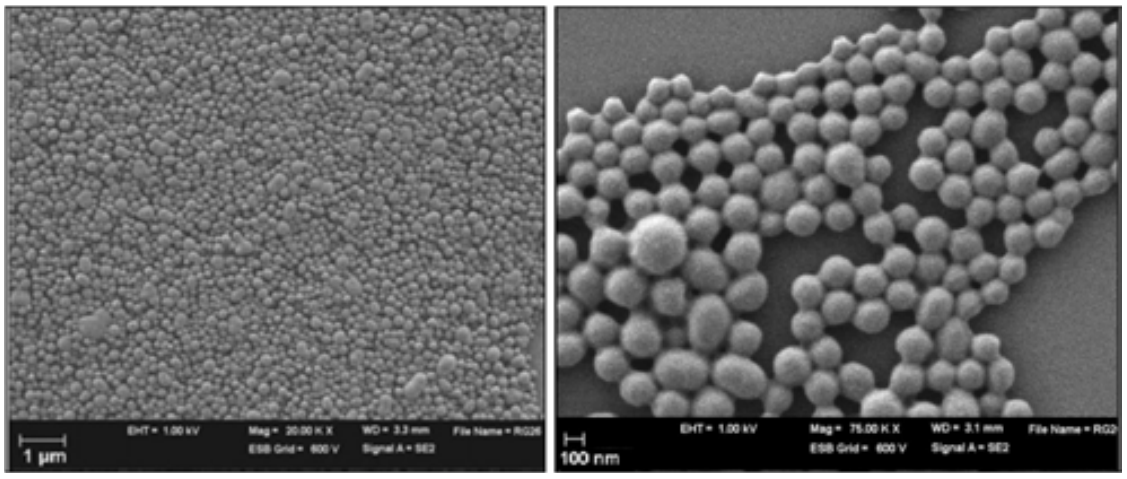

Figure 15. SEM images of PLGA nanocapsules synthesized by double emulsion-solvent evaporation method at different magnifications.

During SEM measurements it was also possible to visualize the inner structure of particles (accidently collapsed) which showed the hollow inner core and the polymeric layer with variable thickness (from 20 to 50 nm) depending on nanoparticle size (Fig. 16).

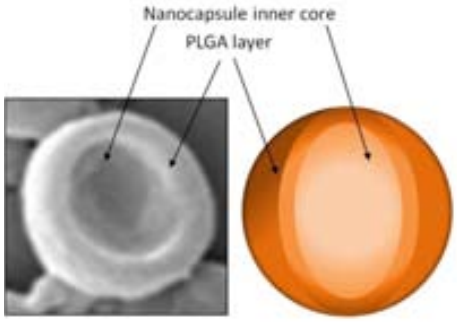

Figure 16. Nanocapsule structure synthesized by double emulsion method. On the left: SEM picture of lyophilized sample with a collapsed nanocapsule; on the right: scheme of nanocapsule cross section showing an empty inner core and the polymeric layer.

4.4.2.2. MAGNETIC AND IMAGING PROPERTIES OF rhVEGF$_{165}$ AND SPIONS LOADED PLGA NANOCAPSULES

We proved SPIONs encapsulation by MRI (see Table 3), ICP-OES (see Table 4), SQUID, cryo-TEM and FTIR. By cryo-TEM it was possible to visualize PLGA particles in the "native state" that exhibited a well defined spherical shape (Fig. 17a). Embedded SPIONs were uniformly distributed (visible as black spots) within the polymeric matrix (Fig. 17a). Moreover SPION encapsulation was confirmed by magnetic measurement at 5K and zero-field cooling field cooling (ZFC-FC) of nanocapsules in dried state. The resulting blocking temperature (T_B) was very close to the value of SPIONs in aqueous dispersion, demonstrating that nanoparticles did not aggregate during the encapsulation process (Fig. 17b).

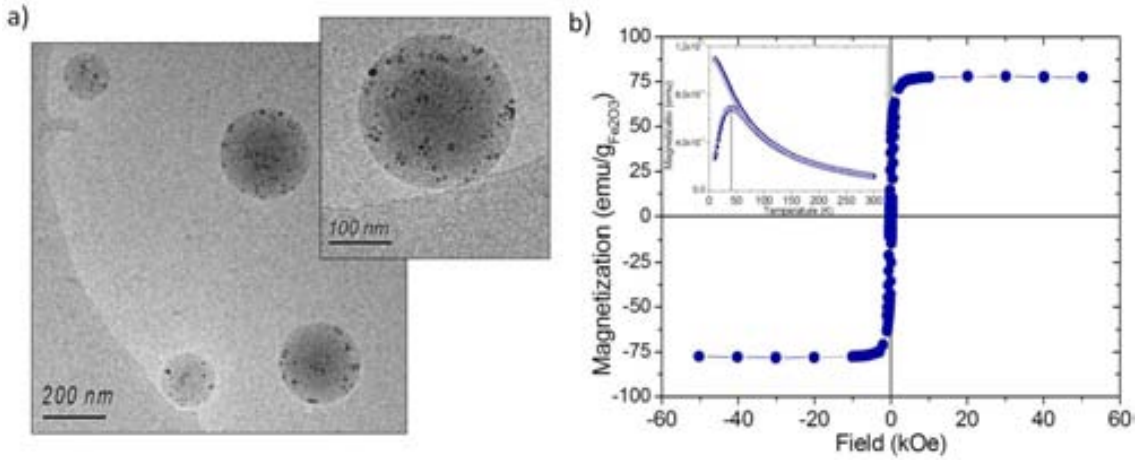

Figure 17. Characterizations of PLGA nanocapsule dispersion in water. a) Cryo-TEM images showing spherical nanocapsules containing SPIONs visible as black spots, uniformly dispersed in the polymer matrix; b) magnetic measurements of PLGA nanocapsules at 5K showing high saturation magnetization and ZFC-FC (inset). Embedded SPION have blocking temperature (T_B) of 44 K which is very close to the T_B value of nanoparticles in aqueous dispersion (46 K, batch EC12).

Moreover we compared FTIR spectra of pure PLGA and PLGA nanocapsules synthesized in presence of SPIONs. FTIR spectra of pure PLGA and PLGA with encapsulated SPIONs (PLGA_SPIONs) showed the "fingerprint" bands of the C=O stretching of lactic and glycolic carboxylic groups (peak at 1762 cm^{-1}), strong peaks between 1450-1300 cm^{-1} attributed to methyl and methylene bending and 1300-1000 cm^{-1} of C-O stretching of C-C-O and C-O-C

bonds in the polymer structure. Moreover PLGA_SPIONs sample showed the broad peak at 577 cm^{-1} typical of Fe-O stretch which was not observed in the pure PLGA.

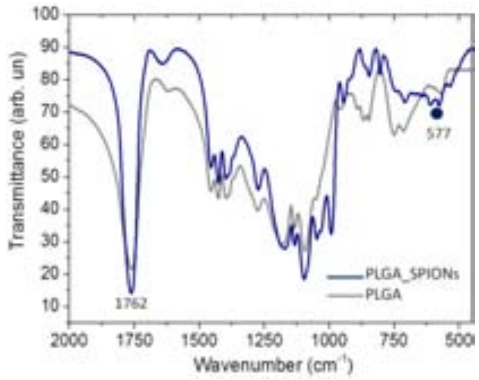

Figure 18. FTIR spectra of PLGA (RG502, 50:50) and PLGA with encapsulated SPIONs.

From MRI measurements we found optimal T_2 relaxation properties of SPIONs loaded PLGA nanoparticles with an average transverse relaxivity value (r_2) of 181 ± 37 mM^{-1} s^{-1} calculated over four samples obtained from four different batches (Table 3). Samples were prepared by mixing lyophilized nanocapsules with agarose at particle concentrations corresponding to 0, 0.6, 3, 6, 15 µg/mL of iron. In Figure 19 are showed T_2 weighted agarose phantoms with hypotense signal decay in a iron-concentration dependent manner.

Table 3. r_2 (mM^{-1} s^{-1}) values obtained by MRI analysis of lyophilized SPIONs and VEGF loaded PLGA nanoparticles in agarose phantoms. Samples RG502_23, 24, 25 contain $rhVEGF_{165}$ and SPIONs. Sample RG502_27 contains only SPIONs.

Sample	r_2 (mM^{-1} s^{-1})
RG502_23	180
RG502_24	130
RG502_25	201
RG502_27	213

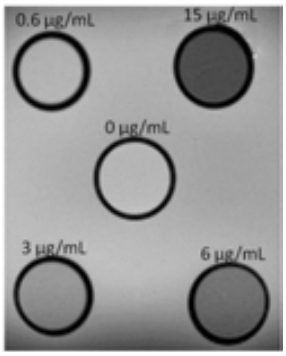

Figure 19. T_2 weighted phantoms obtained by mixing lyophilized SPIONs loaded PLGA nanocapsules with agarose at increasing iron concentrations. The image corresponds to phantoms of sample RG502_23.

With a simple experiment we checked the magnetic retention of particles under an applied magnetic field. We placed a strong magnet at 3 millimeters from the colloidal magnetic suspension contained into an eppendorf and after 24 hours we saw particle retention on the plastic wall close to the magnet (Fig. 20).

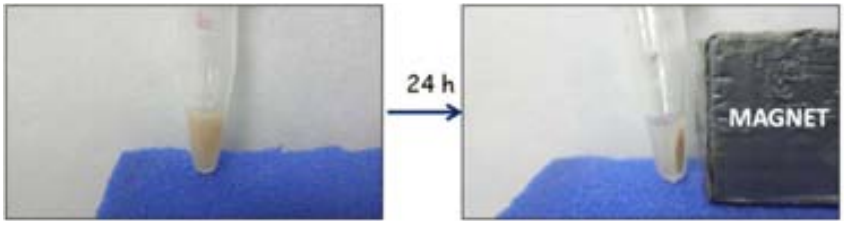

Figure 20. Eppendorf with 0.2 mL of PLGA nanocapsules with SPIONs suspension in water at concentration of 17 mg/mL. A strong magnet (dimensions 5x5x2 cm, field 0.4 Tesla) was placed near the eppendorf. After 24 hours particles were found to adhere to the wall, close to the magnet.

This experiment was a "proof of concept" on rhVEGF$_{165}$ and SPIONs loaded PLGA nanoparticles potential use as "magnetic guiding tools" under an applied magnetic field to achieve targeted drug delivery and targeted therapeutic angiogenesis.

4.4.2.3. ENCAPSULATION EFFICIENCIES OF rhVEGF$_{165}$ AND SPIONs IN PLGA NANOCAPSULES AND RELEASE STUDY

In pharmaceutical chemistry the amount of encapsulated drug is expressed using the definitions of drug loading and encapsulation efficiency. Drug loading (DL%) is defined as:

$$DL\% = \frac{mass\ of\ drug\ in\ nanocapsules}{mass\ of\ nanocapsules} \times 100$$

Entrapment efficiency (EE%) is defined as:

$$EE\% = \frac{experimental\ drug\ loading}{nominal\ drug\ loading} \times 100$$

EE% indicates the efficiency of the encapsulation process because it expresses the real amount of drug entrapped into particles (experimental drug loading) over the amount of drug initially used (nominal drug loading).

In literature the starting amount of VEGF$_{165}$ used for PLGA encapsulation is between 0.03 and 0.1% w/w[69,87]. In our experiments we used rhVEGF$_{165}$ loading of 0.05% w/w, and 2.6% w/w of SPIONs (expressed as γ-Fe_2O_3 weight over mass of nanocapsules).

Researchers achieved high VEGF encapsulation (EE%= 70%) in PLGA nanoparticles of around 300 nm in hydrodynamic diameter[69] and in other studies SPIONs concentration up to 1.4% w/w[79]. As expected, our process which combines drug with imaging agents in a unique formulation, yielded lower encapsulation efficiencies compared with the encapsulation of drug or imaging agents alone. We achieved VEGF EE% up to 58% and SPIONs EE% up to 68% (Table 4).

Table 4. Characterization of samples synthesized by double emulsion method-solvent evaporation with rhVEGF165 and SPIONs (from RG502_23 to RG502_25) and just with SPIONs (RG502_26, 27). $VEGF_{165}$ amount into PLGA nanocapsules was measured by ELISA immunoassay. EE%= encapsulation efficiency %; NCs= nanocapsules.

SAMPLE	PROTEIN	PROTEIN EE%	PROTEIN/NCs (ng/mg)	SPIONs EE%	SPION/ NCs (µg/mg)	SYNTHESIS YIELD%	DIAMETER (DLS, nm)
RG502_23	VEGF	58%	279	60%	10.8	62%	235 (17% PD)
RG502_24	VEGF	57%	273	60%	10.8	63%	225 (17% PD)
RG502_25	VEGF	44%	211	68%	12.2	68%	230 (18% PD)
RG502_26	_	_	_	57%	10.3	65%	215 (17% PD)
RG502_27	_	_	_	65%	11.7	63%	210 (15% PD)

Low weight eppendorfs (Eppendorf®) were used for the following experiments. Three samples loaded with $VEGF_{165}$ and SPIONs were analyzed together with one used as control (nanocapsules with only SPIONs). Lyophilized samples (5 mg) were previously sterilized under UV rays for 18 hours[88] and then dissolved at concentration of 10 mg/mL in an aqueous solution of 0.1 M NaOH, 10% DMSO, 0.2% w/v SDS for 1 hour[35] under magnetic stirring, until complete polymer dissolution. The as-obtained samples were centrifuged at 13000 rpm (sample distance from the rotor of 7 cm) for 5 minutes to precipitate SPIONs. The color of the solution turned from brown to colorless (Fig. 21).

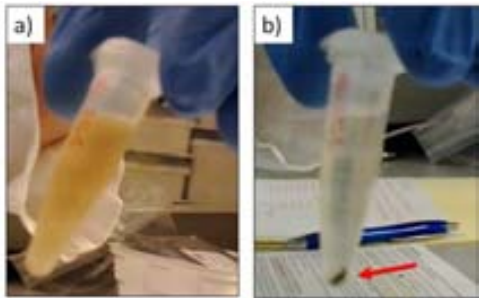

Figure 21. Solution of PLGA nanocapsules loaded with VEGF and SPIONs. In the picture a) is showed the solution with dissolved PLGA. The brow color is due to SPIONs presence. In the picture b) is showed the same sample after centrifuge at 13000 rpm for 5 min: the red arrow indicates a brown precipitate of SPIONs.

The supernatant was used to determine $VEGF_{165}$ content in the PLGA nanoparticles by ELISA immunoassay (samples seeded in duplicate, Quantikine® ELISA human VEGF immunoassay, catalog number DVE00, R&D Systems).

After the total protein determination, we studied protein release in time. The experiment of release was carried out for three different batches and the control at the same time. Lyophilized samples (5 mg) were previously sterilized under UV rays for 18 hours and subsequently dispersed in the release medium of PBS 1X, 0.1% w/v bovine serum albumin (BSA)[87], 1% penicillin-streptomycin at concentration of 10 mg/mL. Eppendorfs were put into plastic wells which were tightly closed and subsequently immersed in a bath at 37°C with

horizontal shaking at the maximum speed (80 pulses per minute). Aliquots of 100 µl were taken at established times (1 hour, 6 hours, 2 days, 6 days and 14 days), centrifuged at 13000 rpm (sample distance from the rotor of 7 cm) for 5 minutes to separate the PLGA particles, SPIONs from the supernatant and analyzed by ELISA immunoassay (samples seeded in duplicate, dilutions used 1:500 and 1:5000). We noted that the supernatant was colorless and not yellowish, indicating that during the time of the release experiment SPIONs did not degrade. The amount of $rhVEGF_{165}$ released was calculated as the sum of the amounts of drug released per each taken aliquot, defined as cumulative release:

$$\%\ Cumulative\ release = \sum(Mt \div M\infty) \times 100$$

Where Mt is the absolute amount of drug released at time t, M∞ is the absolute amount of drug released at infinite time which should be equal to the total amount of drug encapsulated. The absolute amount of drug is the mass of drug released divided by the mass of particles at the time t.

The results revealed a sustained protein release: during the 2 weeks the amount of release protein was around 35% of the total protein encapsulated (Fig. 22) (see annex of chapter 4, paragraph 4.6.2.1. for further details).

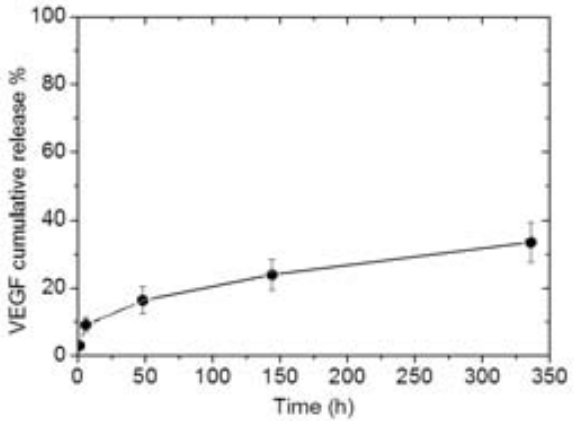

Figure 22. Release study over a period of 2 weeks nanocapsules loaded with of $rhVEGF_{165}$ and SPIONs analyzed by ELISA immunoassay. The measurement is expressed as the average release of three samples analyzed at the same time. Aliquots were taken after 1 hour, 6 hours, 2 days, 6 days and 14 days.

The slow protein release can be advantageous from a clinical point of view: it has been demonstrated that the time needed to induce consistent new vessel formation is around 2 weeks[71,89]. It has still to be checked SPIONs *in vitro* release in time. If SPIONs showed a slow sustained release (similar to VEGF profile), it would be possible to retain PLGA nanoparticles for a longer period of time in a specific area under an external magnetic field.

4.4.2.4. $rhVEGF_{165}$ AND SPIONs LOADED PLGA NANOCAPSULE *IN VITRO* BIOACTIVITY

We aimed to demonstrate that $rhVEGF_{165}$ is still bioactive after the whole encapsulation process and release step. We therefore used the collected aliquots of the $VEGF_{165}$ release study to prove endothelial cell proliferation *in vitro*. Human microvascular brain endothelial cells-D3 were cultivated in endothelial growth medium (EGM-2) for four days and then were treated with aliquots of $rhVEGF_{165}$ released at 1h, 6h, 2 days, 6 days, 14 days corresponding to a

protein concentration of 10 ng/mL (see annex of chapter 4, paragraph 4.6.2.2. for further details).

The number of cells treated with the collected aliquots of release media from rhVEGF$_{165}$ and SPIONs loaded PLGA nanoparticles, were compared with the cells treated with collected aliquots of release media from SPIONs loaded nanoparticles (release control) and basal medium (control media). Figure 23 shows that the number of cells treated with collected aliquots of release media from rhVEGF$_{165}$ and SPIONs loaded PLGA nanoparticles is significantly increased compared to control medium and basal medium.

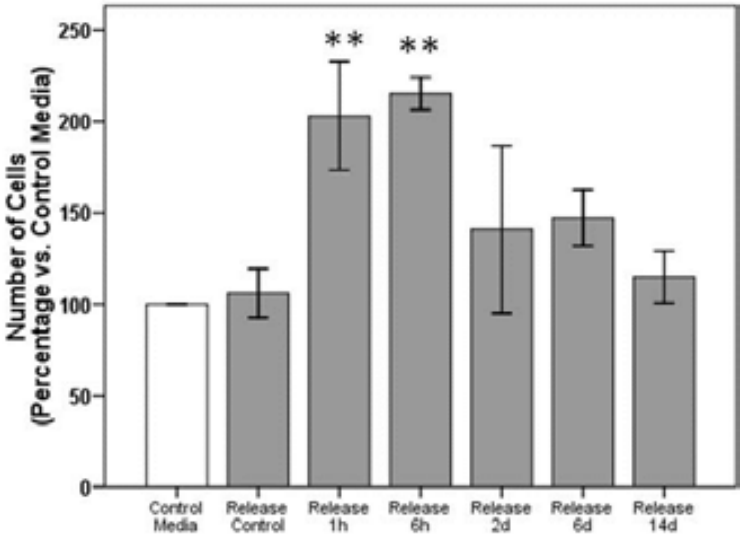

Figure 23. Bar Graphs representing the percentage of endothelial cells in each treatment condition vs. control treatment (basal media). Bars represent mean ±SD of n=3 independent experiments. ** p<0.001.

The highest cell proliferation occurred after cell treatment with aliquots collected at 1 hour and 6 hours of the release study with almost a double number of cells. Release media obtained at 2, 6, 14 days also produced cell proliferation although in less magnitude. This observation might be explained by partial protein inactivation over time in presence of acidic pH, coming from PLGA hydrolytic degradation. It is worthy to note that cell viability was not affected by our treatments since all conditions presented a mean number of viable cells over 90% vs. total cells. In particular, the release media from SPIONs loaded PLGA nanoparticles (release control in the graph) did not affect the viability of the cells compared to control media conditions (basal growing media).

4.5. CHAPTER CONCLUSIONS

We demonstrated that by easy and reproducible double emulsion-solvent evaporation method is possible to synthesize magnetic PLGA nanocapsules loaded with SPION and human recombinant vascular growth factor (VEGF$_{165}$) with size of around 200 nm. SPION were embedded in the polymer matrix as showed by cryoTEM pictures and magnetometry measurements indicated SPION encapsulation efficiencies of around 60%. The total protein encapsulated was around the 50% of protein loaded and *in vitro* studies demonstrated a sustained protein release with almost 35% of protein released in two weeks. Interestingly we

also found no PLGA particle cytotoxicity. After release, protein was proved to be still active by inducing high proliferation of human cerebral microvascular endothelial cells at concentration of 10 ng/mL after 48h of treatment and persisting up to day 14.

In conclusion this approach demonstrates the feasibility of VEGF and SPIONs co-encapsulation in a unique formulation. However further work it is needed to improve the obtained results and to test particle future application in targeted therapeutic angiogenesis *in vivo*.

We chose PLGA 50:50 (RG502) as well known polymeric carrier which offers numerous advantages compared with others, still it renders particle surface rather hydrophobic. New polymers can be used to enhance particle stability in PBS1X and culture media, as for instance PLGA-PEG blends. Moreover to accomplish a robust *in vivo* neovascularization it is necessary to administer more than one growth factor simultaneously. In this context future work will be focused in encapsulating a cocktail of endogenous growth factors released by endothelial cells.

4.6. ANNEX OF CHAPTER 4

In this section are described the techniques used to characterize PLGA nanocapsules and the encapsulated $VEGF_{165}$. Moreover, general concepts on circular dichroism and drug release kinetics are briefly described.

4.6.1. SCANNING ELECTRON MICROSCOPY (SEM) OF PLGA NANOCAPSULES

SEM uses a high energy electron beam which is scanned over the surface of a sample and the back scattering of the electrons is detected to compose the image. Dry samples can be observed in high vacuum or low vacuum conditions and have to be electrically conductive at the surface. The surface of non-conductive specimens can be modified by sputtering noble metal coating like gold, alloy of gold-palladium or platinum.

We used SEM to analyze morphology and diameter of polymeric nanocapsule. The sample was prepared as follows: 2 mg of the lyophilized powder were re-dispersed into 600 µl of MilliQ water and centrifuged twice at 4000 rpm (sample distance from the rotor center of 6 cm) for 20 minutes. Each time the supernatant was discarded and fresh water was added. Finally particles were re-dispersed in 1 mL of water and one drop of the slightly turbid suspension was deposited onto a small slice of silicon wafer stuck on a carbon layer. The sample was previously dried at room temperature and then covered with 2 nm of Au-Pd using Emitech K550 Sputter Coater equipment at 25 mA for 1 minute. Pictures were acquired at high vacuum condition, with FESEM Merlin de Zeiss using frame scan modality, repeated 15 times.

4.6.2. PROTOCOLS FOR PROTEIN DETERMINATION

4.6.2.1. RECOMBINANT HUMAN $VEGF_{165}$ ELISA IMMUNOASSAY

This analysis consists in a quantitative sandwich enzyme immunologic assay for specific detection of $VEGF_{165}$ in biological samples. It is based on the specific antibody-antigen interaction which induces oxidation or reduction of a substrate with light emission at a specific wavelength which is proportional to the amount of protein detected. It is a very sensitive analysis which allows detecting protein concentrations of pg/mL. We used Quantikine® ELISA recombinant human $VEGF_{165}$ (R&D systems, catalog. number DVE00) to measure the total VEGF encapsulated after the double emulsion-solvent evaporation process and the amount of protein released during the protein release study at 1h, 6h, 2 days, 6 days, 14 days.

Monoclonal antibodies specific for $VEGF_{165}$ have been pre-coated onto a microplate.

The calibration curve with concentrations between 1000 pg/mL and 0 pg/mL using VEGF standard (provided by the manufacturer) and nanocapsule samples of the release study were mixed in RD5K diluent provided by the manufacturer. Aliquots stored at -80 °C of nanocapsule batches RG502_23, 24, 25 (cointaining VEGF) and RG502_27 (control) obtained from protein release study (see chapter 4, paragraph 4.4.2.3) were slowly thaw at room temperature. Dilutions at 1:5000, 1:10000 for total protein determination and 1:500, 1:5000 for protein release study, were prepared in series starting from the stock solution and carefully mixed before the next transfer. VEGF standards and samples were run in duplicate (volumes of 200 µl)

and let to incubate for 2 hours. Afterward, wells were washed three times and dried by blotting the plate against a paper towel. Two-hundred µl of conjugate (polyclonal antibody linked to the enzyme) were added per each well and let to incubate for further 2 hours. Subsequently 200 µl of the enzyme substrate were added and let to incubate for 20 minutes protected from light. Finally, after addition of 50 µl of stop solution per each well, the color developed was spectrophotometrically measured by ELx800 96 well Microplate Reader set at 450 nm.

4.6.2.2. RECOMBINANT HUMAN $VEGF_{165}$ BIOACTIVITY ASSAY

One strategy to test protein bioactivity after encapsulation consists in adding the $VEGF_{165}$ containing sample to an endothelial cell culture and checking cellular proliferation. We used the remaining aliquots obtained from the protein release study (see chapter 4, paragraph 4.4.2.3) at 1h, 6h, 2 days, 6 and 14 days of RG502_23, 24, 25 or RG502_27 used as control. Since the available volume of sample at each time was not enough to repeat the analysis (n=3), all three aliquots of RG502_23, 24 and 25 were mixed together to make a single sample (pool) at 1h, 6h, 2 days, 6 and 14 days.

Human Cerebral Microvascular Endothelial Cells (hCMEC/D3)[90] cells were used to assess the functional effect of encapsulated VEGF on endothelial cell proliferation and viability. Briefly, 2.5 $x10^3$ cells were seeded in 24 well-plates in EGM-2 media (Lonza, Barcelona, Spain) containing basal media (EBM) plus ½ EGM-2 supplements VEGF, insulin-like growth factor, bovine FGF, hydrocortisone, ascorbate and 2% fetal bovine serum (FBS). After four days in culture cells were deeply washed with PBS and treated with pooled VEGF media obtained at 1h, 6h, 2 days, 6 days or 14 days at final concentration of 10 ng/mL of VEGF (according to the ELISA results). This concentration has shown to induce proliferation in endothelial cells by other authors[71]. Two controls were run in each experiment: EBM and control media from batch RG502_27. EBM was used to load all wells to a final volume of 0.4 mL. After 48 hours of treatment cells were washed, tripsinized and the total number of cells and number of viable cells were obtained with the Muse™ Cell Count and Viability Kit. Each experiment was run in duplicate in three independent experiments. Mean value of each independent experiment was used for statistics which consisted in One-Way ANOVA and Dunnett Post-Hoc test (SPSS 15.0 software was used). Proliferation data is expressed as percentage of control condition (basal media).

Cell Viability was not affected by our treatments since all conditions presented a mean number of viable cells over 90% vs. total cells (basal media: 93.64±1.69, RG27:93.72±1.19, VEGF release 1h: 94.08±1.89, VEGF release 6h: 95.75±087, VEGF release 2 days: 92.97±1.03, VEGF release 6 days: 93.75±0.57 and VEGF release 14 days: 92.34±1.78.

4.6.3. CIRCULAR DICHROISM

Circular dichroism (CD) is the differential adsorption of the left and the right polarized components of plane-polarized electromagnetic radiation. When these two opposite circularly polarized light waves (E_L, E_R) are combined, the result will be **elliptically polarized light** because the two components have different amplitudes. Ellipticity is defined as the arc tangent

of the ratio of the minor axis to the major axis of the ellipse. Θ = tan-1(b/a), where a and b are the semi-minor and semi-major axes of the ellipse. The ellipticity corresponds to optical rotation. The optical rotation of a sample can be measured at any wavelength (Fig. 24):

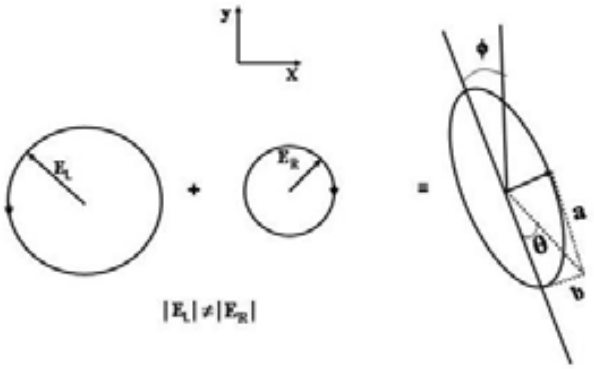

Figure 24. Plane polarized light components. In an optically active medium after passing through the sample, each component of the light is still circularly polarized, but the radii of the circles traced out by the electric vector of each (i.e., the amplitudes of the electric vectors) are different. Picture from http://www.physics.nus.edu.sg/.

Light passing through a chromophore solution is partially absorbed. Absorption is quantitated by the molar extinction coefficient, ε. Optically active samples have distinct molar extinction coefficients for left (ε_L) and right (ε_R) circularly polarized light, with $\varepsilon_L \neq \varepsilon_R$. The difference in absorbance, A, of the two components, is a measure of Circular Dichroism ($CD = A_L - A_R$).

The difference between ε_L and ε_R may be expressed as Δε. From Beer-Lambert Law the difference in the absorbance of left and right circularly polarized light ΔA, can be given by:

$$\Delta A = \Delta\varepsilon\, c\, l$$

c being the concentration and l, the path length. If Δε or ΔA or ellipticity, Θ, is plotted against wavelength, λ, a CD spectrum may be obtained. The ellipticity is proportional to the difference in absorbance of the two components, $A_L - A_R$. Thus, CD is equivalent to ellipticity.

The optical rotation of a sample depends on the presence of absorbing groups (chromophores) chirally active (as for instance phenylalanine, tryptophan and tyrosine)[91]. It provides structural and dynamic informations about biological macromolecules, particularly proteins (Fig. 25).

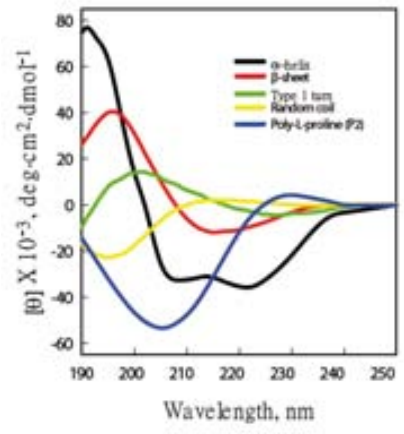

Figure 25. Far-UV CD spectra associated with various types of secondary structure in proteins. Picture from Kelly, SM et al. (2001) *Circular Dichroism: Studies of Proteins. In eLS, John Wiley & Sons.*

Protein spatial conformation can be influenced by a number of factors including temperature, pH, polarity of solvent, binding of ligands, mechanical stresses (e.g. sonication). CD is an extremely convenient technique to detect the extent of conformational changes that may be associated with the activity of the protein.

4.6.3.1. CD MEASUREMENTS OF LYSOZYME (MODEL PROTEIN)

We used lysozyme (lysozyme from chicken egg white, lyophilized powder, Sigma Aldrich) as model protein to find the best conditions for the co-encapsulation of rhVEGF$_{165}$ with SPIONs in PLGA nanocapsules. Before starting the double emulsion process with the formation of the emulsions by application of high shear stresses (ultrasounds) we investigated the effect of the sonication on protein structure. Lysozyme has mass of 14.3 kDa and most of its secondary structure consists of alfa helixes (41% against 6% of beta sheets). In order to test protein conformational changes induced by sonication we compared the CD spectrum of the starting aqueous solution of lysozyme (concentration of 1 µg/mL, control) with the same solution after sonication (Fig. 26).

We found that at the used sonication conditions (240 W and 30 seconds) any significant conformational changes occur, since the control curve and the one of the sample after sonication were overlapping.

CD measurements of rhVEGF$_{165}$ before and after sonication were also performed. Possibly, the aqueous solution used were too dilute (1 µM compared to 40 µM found in literature[92]) to give spectra with good resolution.

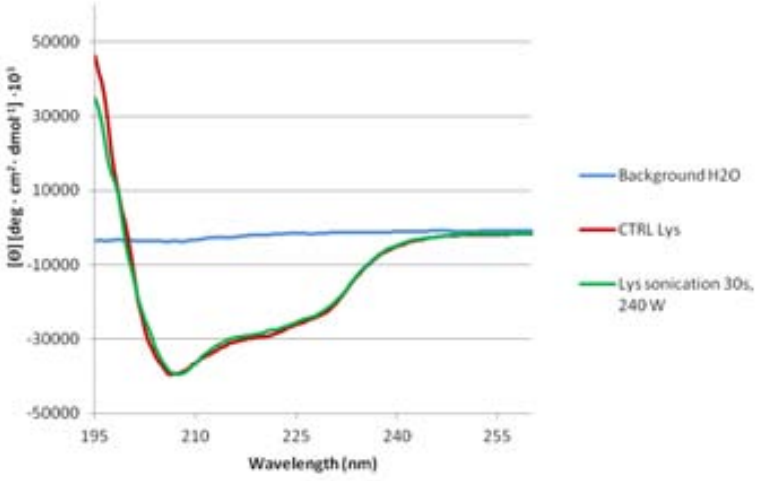

Figure 26. Far-UV CD spectra of lysozyme (concentration 1 µM in water). CTRL Lys= control solution, Lys sonication 30s, 240W= sample after sonication. Measurements made under nitrogen flow, at 20°C with Jasco J-815 spectrometer equipment.

4.6.4. GENERAL CONCEPTS ON DRUG RELEASE KINETICS

Drug release and polymer biodegradation are influenced by important factors[93] as (*i*) solubility of drug; (*ii*) desorption of the surface-bound/adsorbed drug; (*iii*) drug diffusion through the nanoparticle matrix; (*iv*) nanoparticle matrix erosion/degradation; and (*v*) combination of

erosion/diffusion process. Thus, solubility, diffusion, and biodegradation of the matrix materials govern the release process.

Diffusion is the movement of drug across concentration gradient until equalization takes place. Governed by Fick's first law, where flux is given as follows:

$$J = dM / dt = -DA\, dC / dx$$

where dM = mass of the drug diffused in time dt; D = diffusion coefficient; A = diffusion area; dx = the diffusion layer thickness; and dC / dx = the concentration gradient. Negative slope indicates movement from higher to lower concentration. Here D and C are assumed to be constant.

Diffusional exponent approach has been given by Peppas. It is applicable for hydrating or eroding systems in which *D (diffusion coefficient)* is not constant, thereby giving anomalous diffusion.

$$Mt / M_0 = kt^n$$

Where Mt/M_0 = fractional mass of drug released at time t; k= drug dissolution rate and n = diffusional exponent. Values greater than 0.5 indicate non-Fickian or anomalous diffusion, which are usually found in swellable systems. For Fickian release, n = 0.5 for the planar surface and n = 0.432 for spheres. For non-Fickian or anomalous diffusion, $n > 0.5$.

Sustained release implies a prolonged but not constant release of drug over a time period. It can be described by a biexponential equation with two different rate constants (K1>K2): initial fast drug release (K1) and subsequent slow release (K2).

Drug release from microcapsules and micro/nanoparticles involve mass transfer phenomenon with diffusion of the drug from higher to low concentration regions in the surrounding liquid. There are difficulties in modeling drug release data, as there is a great diversity in the physical form of micro/nanocapsules/particles with respect to size, shape, arrangement of the core and the coat, properties of core-like solubility, diffusivity, properties of coat-like porosity, thickness, crystallinity, inertness, etc. In addition, there are problems in translating kinetics of drug release from "micro" products of perfect geometry to various irregular micro/nanosystems. To describe the drug release from reservoir-type systems (micro/nanocapsules) various equations have been given depending on different situations.

Assuming that thermodynamic activity of the core material is constant within the microcapsule, which is spherical and has inert homogeneous coating, steady-state release rate is derived from Fick's first law of diffusion. If parameters are constant, drug release rate will be zero order. However, drug release rate decreases as coating thickness increases, therefore, drug release rate is dependent on the coating thickness. If thermodynamic activity of the core is not constant, with no inert or homogeneous coating, then release rate is exponential.

4.7. CHAPTER REFERENCES

1. Janib, S. M.; Moses, A. S.; MacKay, J. A., Imaging and drug delivery using theranostic nanoparticles. *Adv Drug Deliv Rev* **2010,** *62* (11), 1052-63.
2. Cheng, Z.; Al Zaki, A.; Hui, J. Z.; Muzykantov, V. R.; Tsourkas, A., Multifunctional Nanoparticles: Cost Versus Benefit of Adding Targeting and Imaging Capabilities. *Science* **2012,** *338* (6109), 903-910.
3. Couvreur, P.; Barratt, G.; Fattal, E.; Legrand, P.; Vauthier, C., Nanocapsule technology: a review. *Critical reviews in therapeutic drug carrier systems* **2002,** *19* (2), 99-134.
4. Schäfer-Korting, M., *Handbook of experimental pharmacology. Drug Delivery*. Springer: Germany, 2010; Vol. 197.
5. Strebhardt, K.; Ullrich, A., Paul Ehrlich's magic bullet concept: 100 years of progress. *Nat Rev Cancer* **2008,** *8* (6), 473-480.
6. Yuan, F.; Dellian, M.; Fukumura, D.; Leunig, M.; Berk, D. A.; Torchilin, V. P.; Jain, R. K., Vascular Permeability in a Human Tumor Xenograft: Molecular Size Dependence and Cutoff Size. *Cancer Research* **1995,** *55* (17), 3752-3756.
7. Wike-Hooley, J. L.; Haveman, J.; Reinhold, H. S., The relevance of tumour pH to the treatment of malignant disease. *Radiotherapy and oncology : journal of the European Society for Therapeutic Radiology and Oncology* **1984,** *2* (4), 343-66.
8. Kamada, H.; Tsutsumi, Y.; Yoshioka, Y.; Yamamoto, Y.; Kodaira, H.; Tsunoda, S.; Okamoto, T.; Mukai, Y.; Shibata, H.; Nakagawa, S.; Mayumi, T., Design of a pH-sensitive polymeric carrier for drug release and its application in cancer therapy. *Clinical cancer research : an official journal of the American Association for Cancer Research* **2004,** *10* (7), 2545-50.
9. Meyer, D. E.; Shin, B. C.; Kong, G. A.; Dewhirst, M. W.; Chilkoti, A., Drug targeting using thermally responsive polymers and local hyperthermia. *Journal of controlled release : official journal of the Controlled Release Society* **2001,** *74* (1-3), 213-24.
10. Béalle, G.; Di Corato, R.; Kolosnjaj-Tabi, J.; Dupuis, V.; Clément, O.; Gazeau, F.; Wilhelm, C.; Ménager, C., Ultra Magnetic Liposomes for MR Imaging, Targeting, and Hyperthermia. *Langmuir : the ACS journal of surfaces and colloids* **2012,** *28* (32), 11834-11842.
11. Butoescu, N.; Seemayer, C. A.; Foti, M.; Jordan, O.; Doelker, E., Dexamethasone-containing PLGA superparamagnetic microparticles as carriers for the local treatment of arthritis. *Biomaterials* **2009,** *30* (9), 1772-80.
12. Husseini, G. A.; Diaz de la Rosa, M. A.; Gabuji, T.; Zeng, Y.; Christensen, D. A.; Pitt, W. G., Release of doxorubicin from unstabilized and stabilized micelles under the action of ultrasound. *Journal of nanoscience and nanotechnology* **2007,** *7* (3), 1028-33.
13. Byrne, J. D.; Betancourt, T.; Brannon-Peppas, L., Active targeting schemes for nanoparticle systems in cancer therapeutics. *Advanced Drug Delivery Reviews* **2008,** *60* (15), 1615-1626.
14. Ni, S.; Stephenson, S. M.; Lee, R. J., Folate receptor targeted delivery of liposomal daunorubicin into tumor cells. *Anticancer research* **2002,** *22* (4), 2131-5.
15. Hermanson, G., *Bioconjugate techniques*. Second Edition ed.; Academic Press: 2008.
16. Williams, D. F., On the mechanisms of biocompatibility. *Biomaterials* **2008,** *29* (20), 2941-53.
17. (a) Garcia-Gonzalez, C. A.; Carenza, E.; Zeng, M.; Smirnova, I.; Roig, A., Design of biocompatible magnetic pectin aerogel monoliths and microspheres. *RSC Advances* **2012,** *2* (26), 9816-9823; (b) Saslawski, O.; Weingarten, C.; Benoit, J. P.; Couvreur, P., Magnetically responsive microspheres for the pulsed delivery of insulin. *Life sciences* **1988,** *42* (16), 1521-8.
18. Danhier, F.; Ansorena, E.; Silva, J. M.; Coco, R.; Le Breton, A.; Préat, V., PLGA-based nanoparticles: An overview of biomedical applications. *Journal of Controlled Release* **2012,** *161* (2), 505-522.
19. Liu, Y.; Wang, Y.; Zhuang, D.; Yang, J.; Yang, J., Bionanoparticles of amphiphilic copolymers polyacrylate bearing cholesterol and ascorbate for drug delivery. *Journal of colloid and interface science* **2012,** *377* (1), 197-206.
20. Cheng, J.; Teply, B. A.; Sherifi, I.; Sung, J.; Luther, G.; Gu, F. X.; Levy-Nissenbaum, E.; Radovic-Moreno, A. F.; Langer, R.; Farokhzad, O. C., Formulation of functionalized PLGA-PEG nanoparticles for in vivo targeted drug delivery. *Biomaterials* **2007,** *28* (5), 869-76.
21. Allen, T. M.; Cullis, P. R., Liposomal drug delivery systems: From concept to clinical applications. *Advanced Drug Delivery Reviews* **2013,** *65* (1), 36-48.

22. Slowing, I. I.; Vivero-Escoto, J. L.; Wu, C.-W.; Lin, V. S. Y., Mesoporous silica nanoparticles as controlled release drug delivery and gene transfection carriers. *Advanced Drug Delivery Reviews* **2008,** *60* (11), 1278-1288.

23. Chen, H.; Spagnoli, F.; Burris, M.; Rolland, W. B.; Fajilan, A.; Dou, H.; Tang, J.; Zhang, J. H., Nanoerythropoietin is 10-times more effective than regular erythropoietin in neuroprotection in a neonatal rat model of hypoxia and ischemia. *Stroke; a journal of cerebral circulation* **2012,** *43* (3), 884-7.

24. Reddy, M. K.; Labhasetwar, V., Nanoparticle-mediated delivery of superoxide dismutase to the brain: an effective strategy to reduce ischemia-reperfusion injury. *FASEB journal : official publication of the Federation of American Societies for Experimental Biology* **2009,** *23* (5), 1384-95.

25. Rhim, T.; Lee, D. Y.; Lee, M., Drug delivery systems for the treatment of ischemic stroke. *Pharmaceutical research* **2013,** *30* (10), 2429-44.

26. Picciochi, R.; Wang, Y.; Alves, N.; Mano, J., Glass transition of semi-crystalline PLLA with different morphologies as studied by dynamic mechanical analysis. *Colloid Polym Sci* **2007,** *285* (5), 575-580.

27. Pawar, R. S., N.; Andurkar, N.; Dake, S.; Domb, A., Injectable Polymers for Regional Drug Delivery. In *Targeted delivery of small and macromolecular drugs*, CRC Press: 2010; p 457.

28. D'Mello, S. D., S.; Das, N., Polymeric Nanoparticles for Small-Molecule Drugs: Biodegradation of Polymers and Fabrication of Nanoparticles. In *Drugs and the pharmaceutical sciences: "Drug Delivery Nanoparticles Formulation and Characterization"*, Informa Healthcare: 2009; Vol. 191.

29. Semete, B.; Booysen, L.; Lemmer, Y.; Kalombo, L.; Katata, L.; Verschoor, J.; Swai, H. S., In vivo evaluation of the biodistribution and safety of PLGA nanoparticles as drug delivery systems. *Nanomedicine: Nanotechnology, Biology and Medicine* **2010,** *6* (5), 662-671.

30. Vauthier, C.; Bouchemal, K., Methods for the preparation and manufacture of polymeric nanoparticles. *Pharmaceutical research* **2009,** *26* (5), 1025-58.

31. Bilati, U.; Allemann, E.; Doelker, E., Development of a nanoprecipitation method intended for the entrapment of hydrophilic drugs into nanoparticles. *European journal of pharmaceutical sciences : official journal of the European Federation for Pharmaceutical Sciences* **2005,** *24* (1), 67-75.

32. Herrmann, J.; Bodmeier, R., Biodegradable, somatostatin acetate containing microspheres prepared by various aqueous and non-aqueous solvent evaporation methods. *European Journal of Pharmaceutics and Biopharmaceutics* **1998,** *45* (1), 75-82.

33. Li, M.; Rouaud, O.; Poncelet, D., Microencapsulation by solvent evaporation: state of the art for process engineering approaches. *International journal of pharmaceutics* **2008,** *363* (1-2), 26-39.

34. Bilati, U.; Allemann, E.; Doelker, E., Sonication parameters for the preparation of biodegradable nanocapsules of controlled size by the double emulsion method. *Pharmaceutical development and technology* **2003,** *8* (1), 1-9.

35. Blanco, M. D.; Alonso, M. J., Development and characterization of protein-loaded poly(lactide-co-glycolide) nanospheres. *European Journal of Pharmaceutics and Biopharmaceutics* **1997,** *43* (3), 287-294.

36. Mundargi, R. C.; Babu, V. R.; Rangaswamy, V.; Patel, P.; Aminabhavi, T. M., Nano/micro technologies for delivering macromolecular therapeutics using poly(d,l-lactide-co-glycolide) and its derivatives. *Journal of Controlled Release* **2008,** *125* (3), 193-209.

37. Quintanar-Guerrero, D.; Allémann, E.; Fessi, H.; Doelker, E., Pseudolatex preparation using a novel emulsion–diffusion process involving direct displacement of partially water-miscible solvents by distillation. *International journal of pharmaceutics* **1999,** *188* (2), 155-164.

38. Bilati, U.; Allemann, E.; Doelker, E., Poly(D,L-lactide-co-glycolide) protein-loaded nanoparticles prepared by the double emulsion method--processing and formulation issues for enhanced entrapment efficiency. *Journal of microencapsulation* **2005,** *22* (2), 205-14.

39. Sahoo, S. K.; Panyam, J.; Prabha, S.; Labhasetwar, V., Residual polyvinyl alcohol associated with poly (D,L-lactide-co-glycolide) nanoparticles affects their physical properties and cellular uptake. *Journal of controlled release : official journal of the Controlled Release Society* **2002,** *82* (1), 105-14.

40. Vandervoort, J.; Ludwig, A., Biocompatible stabilizers in the preparation of PLGA nanoparticles: a factorial design study. *International journal of pharmaceutics* **2002,** *238* (1-2), 77-92.

41. Mora-Huertas, C. E.; Fessi, H.; Elaissari, A., Polymer-based nanocapsules for drug delivery. *International journal of pharmaceutics* **2010,** *385* (1-2), 113-42.

42. Santander-Ortega, M. J.; Jodar-Reyes, A. B.; Csaba, N.; Bastos-Gonzalez, D.; Ortega-Vinuesa, J. L., Colloidal stability of pluronic F68-coated PLGA nanoparticles: a variety of stabilisation mechanisms. *Journal of colloid and interface science* **2006,** *302* (2), 522-9.

43. Batrakova, E. V.; Kabanov, A. V., Pluronic block copolymers: evolution of drug delivery concept from inert nanocarriers to biological response modifiers. *Journal of controlled release : official journal of the Controlled Release Society* **2008,** *130* (2), 98-106.

44. Abdelwahed, W.; Degobert, G.; Stainmesse, S.; Fessi, H., Freeze-drying of nanoparticles: Formulation, process and storage considerations. *Advanced Drug Delivery Reviews* **2006,** *58* (15), 1688-1713.

45. Pinto Reis, C.; Neufeld, R. J.; Ribeiro, A. J.; Veiga, F., Nanoencapsulation II. Biomedical applications and current status of peptide and protein nanoparticulate delivery systems. *Nanomedicine : nanotechnology, biology, and medicine* **2006,** *2* (2), 53-65.

46. Panyam, J.; Labhasetwar, V., Biodegradable nanoparticles for drug and gene delivery to cells and tissue. *Advanced drug delivery reviews* **2003,** *55* (3), 329-347.

47. Coleman, J.; Lowman, A., Biodegradable Nanoparticles for Protein Delivery: Analysis of Preparation Conditions on Particle Morphology and Protein Loading, Activity and Sustained Release Properties. *Journal of biomaterials science. Polymer edition* **2011**.

48. Putney, S. D.; Burke, P. A., Improving protein therapeutics with sustained-release formulations. *Nat Biotech* **1998,** *16* (2), 153-157.

49. van de Weert, M.; Hennink, W.; Jiskoot, W., Protein Instability in Poly(Lactic-co-Glycolic Acid) Microparticles. *Pharmaceutical research* **2000,** *17* (10), 1159-1167.

50. Bilati, U.; Allemann, E.; Doelker, E., Strategic approaches for overcoming peptide and protein instability within biodegradable nano- and microparticles. *European journal of pharmaceutics and biopharmaceutics : official journal of Arbeitsgemeinschaft fur Pharmazeutische Verfahrenstechnik e.V* **2005,** *59* (3), 375-88.

51. Paillard-Giteau, A.; Tran, V. T.; Thomas, O.; Garric, X.; Coudane, J.; Marchal, S.; Chourpa, I.; Benoit, J. P.; Montero-Menei, C. N.; Venier-Julienne, M. C., Effect of various additives and polymers on lysozyme release from PLGA microspheres prepared by an s/o/w emulsion technique. *European journal of pharmaceutics and biopharmaceutics : official journal of Arbeitsgemeinschaft fur Pharmazeutische Verfahrenstechnik e.V* **2010,** *75* (2), 128-36.

52. Buske, J.; Konig, C.; Bassarab, S.; Lamprecht, A.; Muhlau, S.; Wagner, K. G., Influence of PEG in PEG-PLGA microspheres on particle properties and protein release. *European journal of pharmaceutics and biopharmaceutics : official journal of Arbeitsgemeinschaft fur Pharmazeutische Verfahrenstechnik e.V* **2012,** *81* (1), 57-63.

53. Avgoustakis, K., Pegylated poly(lactide) and poly(lactide-co-glycolide) nanoparticles: preparation, properties and possible applications in drug delivery. *Current drug delivery* **2004,** *1* (4), 321-33.

54. Mandriota, S. J.; Pepper, M. S., Vascular endothelial growth factor-induced in vitro angiogenesis and plasminogen activator expression are dependent on endogenous basic fibroblast growth factor. *Journal of cell science* **1997,** *110 (Pt 18)*, 2293-302.

55. Yancopoulos, G. D.; Davis, S.; Gale, N. W.; Rudge, J. S.; Wiegand, S. J.; Holash, J., Vascular-specific growth factors and blood vessel formation. *Nature* **2000,** *407* (6801), 242-8.

56. Niklason, L. E., Building stronger microvessels. *Nat Biotech* **2011,** *29* (5), 405-406.

57. Chen, R. R.; Silva, E. A.; Yuen, W. W.; Mooney, D. J., Spatio-temporal VEGF and PDGF delivery patterns blood vessel formation and maturation. *Pharmaceutical research* **2007,** *24* (2), 258-64.

58. Di Santo, S.; Yang, Z.; Wyler von Ballmoos, M.; Voelzmann, J.; Diehm, N.; Baumgartner, I.; Kalka, C., Novel cell-free strategy for therapeutic angiogenesis: in vitro generated conditioned medium can replace progenitor cell transplantation. *PloS one* **2009,** *4* (5), e5643.

59. Rosell, A.; Morancho, A.; Navarro-Sobrino, M.; Martinez-Saez, E.; Hernandez-Guillamon, M.; Lope-Piedrafita, S.; Barcelo, V.; Borras, F.; Penalba, A.; Garcia-Bonilla, L.; Montaner, J., Factors secreted by endothelial progenitor cells enhance neurorepair responses after cerebral ischemia in mice. *PloS one* **2013,** *8* (9), e73244.

60. Neufeld, G.; Cohen, T.; Gengrinovitch, S.; Poltorak, Z., Vascular endothelial growth factor (VEGF) and its receptors. *The FASEB Journal* **1999,** *13* (1), 9-22.

61. Hoeben, A.; Landuyt, B.; Highley, M. S.; Wildiers, H.; Van Oosterom, A. T.; De Bruijn, E. A., Vascular endothelial growth factor and angiogenesis. *Pharmacological reviews* **2004,** *56* (4), 549-80.

62. Ferrara, N.; Davis-Smyth, T., The biology of vascular endothelial growth factor. *Endocrine reviews* **1997,** *18* (1), 4-25.

63. Hiratsuka, S.; Nakamura, K.; Iwai, S.; Murakami, M.; Itoh, T.; Kijima, H.; Shipley, J. M.; Senior, R. M.; Shibuya, M., MMP9 induction by vascular endothelial growth factor receptor-1 is involved in lung-specific metastasis. *Cancer Cell* **2002,** *2* (4), 289-300.

64. Ferrara, N.; Kerbel, R. S., Angiogenesis as a therapeutic target. *Nature* **2005,** *438* (7070), 967-974.

65. Hao, X.; Silva, E. A.; Mansson-Broberg, A.; Grinnemo, K. H.; Siddiqui, A. J.; Dellgren, G.; Wardell, E.; Brodin, L. A.; Mooney, D. J.; Sylven, C., Angiogenic effects of sequential release of VEGF-A165 and PDGF-BB with alginate hydrogels after myocardial infarction. *Cardiovascular research* **2007,** *75* (1), 178-85.

66. Patel, Z. S.; Ueda, H.; Yamamoto, M.; Tabata, Y.; Mikos, A. G., In vitro and in vivo release of vascular endothelial growth factor from gelatin microparticles and biodegradable composite scaffolds. *Pharmaceutical research* **2008,** *25* (10), 2370-8.

67. DeVolder, R. J.; Kong, H.-J., Three dimensionally flocculated proangiogenic microgels for neovascularization. *Biomaterials* **2010,** *31* (25), 6494-6501.

68. Cleland, J. L.; Duenas, E. T.; Park, A.; Daugherty, A.; Kahn, J.; Kowalski, J.; Cuthbertson, A., Development of poly-(d,l-lactide–coglycolide) microsphere formulations containing recombinant human vascular endothelial growth factor to promote local angiogenesis. *Journal of Controlled Release* **2001,** *72* (1–3), 13-24.

69. Davda, J.; Labhasetwar, V., Sustained Proangiogenic Activity of Vascular Endothelial Growth Factor Following Encapsulation in Nanoparticles. *Journal of Biomedical Nanotechnology* **2005,** *1* (1), 74-82.

70. Formiga, F. R.; Pelacho, B.; Garbayo, E.; Abizanda, G.; Gavira, J. J.; Simon-Yarza, T.; Mazo, M.; Tamayo, E.; Jauquicoa, C.; Ortiz-de-Solorzano, C.; Prosper, F.; Blanco-Prieto, M. J., Sustained release of VEGF through PLGA microparticles improves vasculogenesis and tissue remodeling in an acute myocardial ischemia-reperfusion model. *Journal of controlled release : official journal of the Controlled Release Society* **2010,** *147* (1), 30-7.

71. Ennett, A. B.; Kaigler, D.; Mooney, D. J., Temporally regulated delivery of VEGF in vitro and in vivo. *Journal of biomedical materials research. Part A* **2006,** *79* (1), 176-84.

72. Bhansali, S. G.; Balu-iyer, S. V.; Morris, M. E., Influence of route of administration and liposomal encapsulation on blood and lymph node exposure to the protein VEGF-C156S. *Journal of Pharmaceutical Sciences* **2012,** *101* (2), 852-859.

73. Kim, J.; Cao, L.; Shvartsman, D.; Silva, E. A.; Mooney, D. J., Targeted Delivery of Nanoparticles to Ischemic Muscle for Imaging and Therapeutic Angiogenesis. *Nano Letters* **2010,** *11* (2), 694-700.

74. des Rieux, A.; Ucakar, B.; Mupendwa, B. P.; Colau, D.; Feron, O.; Carmeliet, P.; Preat, V., 3D systems delivering VEGF to promote angiogenesis for tissue engineering. *Journal of controlled release : official journal of the Controlled Release Society* **2011,** *150* (3), 272-8.

75. Borselli, C.; Ungaro, F.; Oliviero, O.; D'Angelo, I.; Quaglia, F.; La Rotonda, M. I.; Netti, P. A., Bioactivation of collagen matrices through sustained VEGF release from PLGA microspheres. *Journal of Biomedical Materials Research - Part A* **2010,** *92* (1), 94-102.

76. Bible, E.; Qutachi, O.; Chau, D. Y.; Alexander, M. R.; Shakesheff, K. M.; Modo, M., Neo-vascularization of the stroke cavity by implantation of human neural stem cells on VEGF-releasing PLGA microparticles. *Biomaterials* **2012,** *33* (30), 7435-46.

77. Liu, X.; Kaminski, M. D.; Chen, H.; Torno, M.; Taylor, L.; Rosengart, A. J., Synthesis and characterization of highly-magnetic biodegradable poly(d,l-lactide-co-glycolide) nanospheres. *Journal of controlled release : official journal of the Controlled Release Society* **2007,** *119* (1), 52-8.

78. Okassa, L. N.; Marchais, H.; Douziech-Eyrolles, L.; Herve, K.; Cohen-Jonathan, S.; Munnier, E.; Souce, M.; Linassier, C.; Dubois, P.; Chourpa, I., Optimization of iron oxide nanoparticles encapsulation within poly(d,l-lactide-co-glycolide) sub-micron particles. *European journal of pharmaceutics and biopharmaceutics : official journal of Arbeitsgemeinschaft fur Pharmazeutische Verfahrenstechnik e.V* **2007,** *67* (1), 31-8.

79. Wang, Y.; Ng, Y. W.; Chen, Y.; Shuter, B.; Yi, J.; Ding, J.; Wang, S. c.; Feng, S. S., Formulation of Superparamagnetic Iron Oxides by Nanoparticles of Biodegradable Polymers for Magnetic Resonance Imaging. *Advanced Functional Materials* **2008,** *18* (2), 308-318.

80. Estevanato, L. L.; Da Silva, J. R.; Falqueiro, A. M.; Mosiniewicz-Szablewska, E.; Suchocki, P.; Tedesco, A. C.; Morais, P. C.; Lacava, Z. G., Co-nanoencapsulation of magnetic nanoparticles and selol for breast tumor treatment: in vitro evaluation of cytotoxicity and magnetohyperthermia efficacy. *International journal of nanomedicine* **2012,** *7*, 5287-99.

81. Hamoudeh, M.; Diab, R.; Fessi, H.; Dumontet, C.; Cuchet, D., Paclitaxel-Loaded Microparticles for Intratumoral Administration via the TMT Technique: Preparation, Characterization, and Preliminary Antitumoral Evaluation. *Drug development and industrial pharmacy* **2008,** *34* (7), 698-707.

82. Shubhra, Q. T. H.; Mackova, H.; Horak, D.; Fodor-Kardos, A.; Toth, J.; Gyenis, J.; Feczko, T., Encapsulation of human serum albumin in submicrometer magnetic poly(lactide-co-glycolide) particles as a model system for targeted drug delivery. *e-Polymers* **2013**.

83. Faranesh, A. Z.; Nastley, M. T.; Perez de la Cruz, C.; Haller, M. F.; Laquerriere, P.; Leong, K. W.; McVeigh, E. R., In vitro release of vascular endothelial growth factor from gadolinium-doped biodegradable microspheres. *Magnetic resonance in medicine : official journal of the Society of Magnetic Resonance in Medicine / Society of Magnetic Resonance in Medicine* **2004,** *51* (6), 1265-71.

84. Mahmoudi, M.; Lynch, I.; Ejtehadi, M. R.; Monopoli, M. P.; Bombelli, F. B.; Laurent, S., Protein-nanoparticle interactions: opportunities and challenges. *Chemical reviews* **2011,** *111* (9), 5610-37.

85. Niu, C.; Wang, Z.; Lu, G.; Krupka, T. M.; Sun, Y.; You, Y.; Song, W.; Ran, H.; Li, P.; Zheng, Y., Doxorubicin loaded superparamagnetic PLGA-iron oxide multifunctional microbubbles for dual-mode US/MR imaging and therapy of metastasis in lymph nodes. *Biomaterials* **2013,** *34* (9), 2307-17.

86. Marchioni, C.; Riccardi, E.; Spinelli, S.; Dell'Unto, F.; Grimaldi, P.; Bedini, A.; Giliberti, C.; Giuliani, L.; Palomba, R.; Congiu Castellano, A., Structural changes induced in proteins by therapeutic ultrasounds. *Ultrasonics* **2009,** *49* (6–7), 569-576.

87. Simon-Yarza, T.; Formiga, F. R.; Tamayo, E.; Pelacho, B.; Prosper, F.; Blanco-Prieto, M. J., PEGylated-PLGA microparticles containing VEGF for long term drug delivery. *International journal of pharmaceutics* **2013,** *440* (1), 13-8.

88. Shearer, H.; Ellis, M. J.; Perera, S. P.; Chaudhuri, J. B., Effects of common sterilization methods on the structure and properties of poly(D,L lactic-co-glycolic acid) scaffolds. *Tissue engineering* **2006,** *12* (10), 2717-27.

89. Silva, E. A.; Mooney, D. J., Effects of VEGF temporal and spatial presentation on angiogenesis. *Biomaterials* **2010,** *31* (6), 1235-41.

90. Weksler, B. B.; Subileau, E. A.; Perriere, N.; Charneau, P.; Holloway, K.; Leveque, M.; Tricoire-Leignel, H.; Nicotra, A.; Bourdoulous, S.; Turowski, P.; Male, D. K.; Roux, F.; Greenwood, J.; Romero, I. A.; Couraud, P. O., Blood-brain barrier-specific properties of a human adult brain endothelial cell line. *FASEB journal : official publication of the Federation of American Societies for Experimental Biology* **2005,** *19* (13), 1872-4.

91. Kelly, S. M.; Price, N. C., Circular Dichroism: Studies of Proteins. In *eLS*, John Wiley & Sons, Ltd: 2001.

92. Gast, R.; König, S.; Rose, K.; Ferenz, K.; Krieglstein, J., Binding of ATP to vascular endothelial growth factor isoform VEGF-A165 is essential for inducing proliferation of human umbilical vein endothelial cells. *BMC Biochem* **2011,** *12* (1), 1-9.

93. Murthy, R. S., In vitro evaluation of NPDDs. In *Drugs and Pharmaceutical Sciences, Drug Delivery Nanoparticle Formulation and Characterization*, Informa Healthcare: 2009; Vol. 191, pp 154-164.

CHAPTER 5

CONCLUSIONS AND FUTURE WORK

5.1. GENERAL CONCLUSIONS

5.2. FUTURE WORK

5.1. GENERAL CONCLUSIONS

The main objectives achieved during this PhD thesis are summarized in the following three sections:

1- Two reproducible and potentially scalable methods of synthesis at high temperature (thermal decomposition and microwave assisted thermal decomposition) were selected for the fabrication of superparamagnetic iron oxide nanoparticles (SPIONs).

The thermal decomposition protocol (TD-SPIONs) was optimized with respect the previous one used in our lab[1] in order to achieve longer colloidal stability in time (up to six months). It was done by controlling the ratio between iron oxide nanoparticle and anionic surfactant (tetramethylammonium hydroxide, TMAOH) during the ligand exchange process and the amount of sodium citrate (anionic stabilizer) in the final dispersion at pH=7.4.

We showed that microwave assisted non-sol gel method is a simpler and less costly technique compared to traditional thermal decomposition. SPIONs obtained by microwave assisted route (MW-SPIONs) had also good saturation magnetization, but presented a slightly larger polydispersity factor and less spherical shape compared to TD-SPIONs. Importantly MW-SPIONs could be readily stabilized in water without any ligand exchange process, obtaining nanoparticle dispersions with concentrations as high as 10 mg/mL of iron.

Our results indicate that superparamagnetic iron oxide nanoparticles obtained by two high temperature synthetic methods are monodisperse in size and show good magnetic properties. Moreover, we have stabilized particles in water and culture media by choosing suitable amounts of anionic stabilizers.

2- We showed that endothelial progenitor cells (EPCs) could be safely magnetized with SPION aqueous dispersions at pH= 7.4 using the concentration of 50 μg/mL of iron and 24 hours of incubation time. SPIONs were internalized by cells as aggregates and confined into cytoplasmatic compartments (endosomes/lysosomes).

The amount of particles internalized by cells depended on the experimental conditions (concentration and time of incubation) used per each type of cell population (early-EPC and OECs). For the first time, we demonstrated that early-EPCs and OECs treated with the same labeling conditions (50 μg/mL of iron, 24 hours of incubation time) showed different uptake, being much higher in the case of early-EPCs (around 20 pgFe/cell *versus* 1 pgFe/cell).

Another important finding related to cellular labeling was that EPCs treated with MW-SPIONs, in different aggregation conditions, showed a more efficient uptake for systems with large nanoparticle aggregates without compromising cell viability, cell morphology or cell functionality.

After labeling EPCs with TD-SPIONs, we obtained:

- preserved angiovasculogenic abilities of magnetized EPCs, forming vessel-like structures *in vitro;*
- enhanced migration through the transwell membrane of the magnetized cells compared to the control cells, both in presence and in absence of a magnet. Importantly, more cells migrate through the transwell membrane in presence of the magnet device.
- increased paracrine effect, with more VEGF and FGF secreted by magnetized human and mouse OECs compared to the control cells;
- increased ROS (reactive oxygen species) formation in magnetized cells compared to the control cells. The moderate oxidative stress could also explain the increased paracrine effect detected in SPION-labeled EPCs.

Finally, we demonstrated that intravenously administered magnetized EPCs can be guided via magnet implantation to precise cortical areas of the brain in mouse animal models and can be successfully tracked by MRI.

In summary, we have obtained efficiently labeled and still functional magnetized EPCs. Our results indicate that SPION-labeled EPCs can improve angiogenic performances through increased migration and paracrine secretion of growth factors *in vitro* and that intravenously administered EPCs can be accumulated in specific areas of the brain cortex by implanting an external magnet device.

3- For the first time we demonstrated that by easy and reproducible double emulsion- solvent evaporation process it was possible to synthesize SPION-$VEGF_{165}$ loaded poly(D,L-lactic-co-glycolic acid) (PLGA) nanocapsules with core size of less than 200 nm, readily dispersible in water after freeze-drying. Through SEM and cryo-TEM images it was noticed that nanocapsules were spherical and did not aggregate in water. Moreover SPIONs embedded into the polymer matrix with encapsulation efficiencies of around 60%, confer magnetic properties to nanocapsules which were efficiently imaged by MRI and were also responsive to an applied magnetic field of 0.4 Tesla. The efficiency of protein encapsulation was around the 50%. *In vitro* studies demonstrated a sustained protein release with 35% of protein cargo released over a period of two weeks. The released protein was still active by inducing high proliferation of human cerebral microvascular endothelial cells at concentration of 10 ng/mL after 48h of treatment. For that, our results indicate that the co-encapsulation of $VEGF_{165}$ and contrast agents in the same formulation (PLGA nanocapsule) may be an interesting strategy for developing new targeted therapeutic treatments to enhance angiogenesis.

In conclusion, we have achieved efficiently co-encapsulation of $VEGF_{165}$ and SPIONs in poly(D,L-lactic-co-glycolic acid) nanocapsules with size of less than 200 nm (compatible with systemic administration), good contrast magnetic resonance imaging effects and

responsiveness to external magnetic fields. Moreover, encapsulated $VEGF_{165}$ is still bioactive after the release process in mimicked physiological condition.

5.2. FUTURE WORK

Future experiments on EPCs labeling with SPIONs could be performed to improve cellular accumulation at the target site. This may be achieved by improving cell response to magnetic stimuli (using larger particles with higher saturation magnetization values, identifying other mechanisms to enhance SPIONs cellular uptake) and by increasing the magnetic field gradient at the target site with new magnetic constructs. Moreover, ongoing *in vivo* experiments in animal models of stroke may confirm EPC engraftment in diseased brains, where it is expected better engraftment of transplanted cells due to increased blood– brain barrier permeability.
Another interesting point which could be further investigated is the higher amount of growth factors secreted by magnetically labeled EPCs compared to control cells. This is an important effect which should be considered in the view of new EPCs based pro-angiogenic therapies.
Nevertheless, it has to be taken into account that labeling cells with SPIONs requires careful analysis and validation by independent techniques (histology, electron microscopy) to minimize ambiguities and misinterpretations of T_2-weighted contrast[2]. For instance, hypodense dark signals during magnetic resonance imaging of transplanted cells may arise after blood vessel leakage or macrophage accumulation. For that, an important subject that should be considered is the dual cell labeling for identifying administered cells, unambiguously, in the target area.

Regarding the co-encapsulation of $VEGF_{165}$ and SPIONs into PLGA nanocapsules, it would be useful to improve particle stabilization in water and culture media, due to PLGA hydrophobic nature. It could be realized through particle surface functionalization with more hydrophilic polymers as polyethylene glycol (PEG) or by means of PEG-PLGA block copolymers.
Future work should be done to encapsulate more than one pro-angiogenic protein together with SPIONs in PLGA nanocapsules to attain a more robust tissue revascularization in time. In fact, the simultaneous administration of more than one growth factor has been considered an attractive therapeutic strategy for tissue repair after stroke in a mouse model of cerebral ischemia[3]. The same objective may be achieved by encapsulating endogenous growth factors (secreted by EPCs) into magnetic PLGA nanocarriers.
Finally, the whole synthesis of SPIONs-$VEGF_{165}$ loaded nanocapsules should be performed in controlled sterile environment to avoid bacterial or fungal contaminations.

5. 3. CHAPTER REFERENCES

1. Taboada, E.; Rodriguez, E.; Roig, A.; Oro, J.; Roch, A.; Muller, R. N., Relaxometric and magnetic characterization of ultrasmall iron oxide nanoparticles with high magnetization. Evaluation as potential T1 magnetic resonance imaging contrast agents for molecular imaging. *Langmuir : the ACS journal of surfaces and colloids* **2007,** *23* (8), 4583-8.

2. Himmelreich, U.; Dresselaers, T., Cell labeling and tracking for experimental models using Magnetic Resonance Imaging. *Methods* **2009,** *48* (2), 112-124.

3. Rosell, A.; Morancho, A.; Navarro-Sobrino, M.; Martinez-Saez, E.; Hernandez-Guillamon, M.; Lope-Piedrafita, S.; Barcelo, V.; Borras, F.; Penalba, A.; Garcia-Bonilla, L.; Montaner, J., Factors secreted by endothelial progenitor cells enhance neurorepair responses after cerebral ischemia in mice. *PloS one* **2013,** *8* (9), e73244.

CHAPTER 6

CURRICULUM VITAE OF THE AUTHOR

LIST OF PUBLICATIONS

Curriculum Vitae

Personal informations:
Name: Elisa
Surname: Carenza
Date of birth: 08/08/1983
Passport number: YA2174601

Academic records:
Degree: M. Sc. in Medicinal Chemistry with grade honor at "Universitá degli Studi di Bari", Italy.
Date: November 2008.
1-year training in the Laboratory Organic Chemistry at Department of Pharmacy under the supervision of Prof. Saverio Florio and Prof. Renzo Luisi.
Elaboration of the final thesis entitled: "Study on configurational stability of oxazoline aziridines alpha-lithiated".

Current position:
PhD candidate in Material Science at "Institute of Material Science of Barcelona" (ICMAB-CSIC), Nanoparticles and Nanocomposites group, "Campus Universidad Autónoma de Barcelona" (UAB).
Supervisors: Dr. Anna Roig (ICMAB-CSIC) and Dr. Anna Rosell (Neurovascular research group, Vall d'Hebron Research Institute).
Title of the Thesis: "Engineering iron oxide nanoparticles for angiogenic therapies".

Stage abroad:
Place: Ecole de Pharmacie Genève-Lausanne (EPGL), Geneva, Switzerland.
Supervisors: Prof. Gerrit Borchard, Dr. Olivier Jordan.
Subject: research on the co-encapsulation of superparamagnetic iron oxide nanoparticles (SPIONs) and vascular endothelial growth factor ($VEGF_{165}$) in poly(D,L-lactic-co-glycolic acid) nanocapsules.
Duration: 5 months.

List of publications:

1. **E. Carenza**, P. Martínez, O. Jordan, G. Borchard, A. Rosell, A. Roig.
   Successful co-encapsulation and bioactivity evaluation of recombinant human $VEGF_{165}$ into PLGA magnetic nanocapsules.
   In preparation.

2. **E. Carenza**; V. Barceló; A. Morancho; J. Montaner; A. Rosell*; A. Roig*
   Rapid synthesis of water- dispersible SPIONs by microwave assisted route for safe labeling of endothelial progenitor cells.
   Accepted for publication in Acta Biomateralia. IF= 5

3. **E. Carenza**; V. Barceló; A. Morancho; L. Levander; C. Boada; A. Laromaine; A. Roig*; J. Montaner; A. Rosell*
   In vitro angiogenic performance and in vivo brain targeting of magnetized endothelial progenitor cells for neurorepair therapies.
   Nanomedicine NBM (2014) 10, 225-34. IF= 6.9.

4. O. Pascu; **E. Carenza**; M. Gich; S.Estrade; F. Peiro; G.Herranz, A. Roig*
   Surface reactivity of iron oxide nanoparticles by microwave-assisted synthesis; comparison with thermal decomposition route.
   Journal of Physical Chemistry C (2012) 116, 15108−15116. IF= 4.8

5. C. A. Garcıa-Gonzalez; **E. Carenza**; M. Zeng; I. Smirnova; A. Roig*
   Design of biocompatible magnetic pectin aerogel monoliths and microspheres.
   RSC advances (2012) 2, 9816-9823. IF= 2.5

6. L. Degennaro; R. Mansueto; **E. Carenza**; R. Rizzi; S. Florio; L. M. Pratt; R. Luisi*.
   Nitrogen Dynamics and Reactivity of Chiral Aziridines: Generation of Configurationally Stable Aziridinyllithium Compounds.
   Chemistry- A European Journal (2011) 17, 4992 – 5003. IF= 5.8

Short communications and presentations at conferences:

Poster
E. Carenza, V. Barceló, J. Montaner, A. Rosell, A. Roig
MRI cell tracking of endothelial progenitor cells
Symposium on Nanoparticle-Based Technologies for Cell Tracking, Liverpool, UK, Julio **2013**.

Poster
E. Carenza, V. Barceló, A. Morancho, L. Levander, C. Boada, A. Laromaine, J. Gibert, A. Roig, J. Montaner, A. Rosell
Magneticaly labelled iron oxide nanoparticles for brain ischemia treatment
Colloids and Nanomedicine 2012, Amsterdam, Holland, July **2012**.

Short communication and poster
E. Carenza, V. Barceló, A. Morancho, L. Levander, C. Boada, A. Laromaine, J. Gibert, A. Roig, J. Montaner, A. Rosell
Magneticaly labelled iron oxide nanoparticles for brain ischemia treatment
CEICS Nobel Campus-Chemistry for Life, Tarragona, Spain, July **2012**.

Poster
E. Carenza, V. Barceló, L. Levander, J. Montaner, A. Rosell, A. Roig
Anionic magnetic nanoparticles for cell tracking
Nanoselect Annual Meeting
Sant Feliu de Guíxols, Spain, July **2011**.

Poster
E. Carenza, V. Barceló, L. Levander, J. Montaner, A. Rosell, A. Roig
Anionic magnetic nanoparticles for cell tracking
Nanomedicine 2011 Summer School
Lutherstadt Wittenberg, Germany, June **2011**.

Technical Knowledge:

- Dynamic Light Scattering (DLS), Spectrophotomety (UV-vis; FTIR): self use;
- ^{1}H, ^{13}C NMR ; SEM, TEM; SQUID; liquid chromatography;
- Synthesis of inorganic nanoparticles (iron oxide magnetic nanoparticles) used as contrast agents;
- Synthesis of polymeric nanoparticles for controlled drug delivery;
- Use of microwave irradiation technology for synthesis of inorganic nanoparticles;
- Experience in pre-clinical studies: cell labeling, cytotoxicity assays, immunological assays (ELISA);
- Magnetic resonance imaging measurements;
- Stereoselective synthesis of chiral compounds in modified environment.

Languages:

Spanish: fluent written; fluent spoken.
English: fluent written; fluent spoken
French: good written; good spoken.
Catalan: fluent written; fluent spoken.
Italian: mother tongue

Barcelona, 10th May 2014

Signature

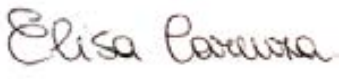

List of publications

Acta Biomaterialia xxx (2014) xxx–xxx

Contents lists available at ScienceDirect

Acta Biomaterialia

journal homepage: www.elsevier.com/locate/actabiomat

Rapid synthesis of water-dispersible superparamagnetic iron oxide nanoparticles by a microwave-assisted route for safe labeling of endothelial progenitor cells

Elisa Carenza [a], Verónica Barceló [b], Anna Morancho [b], Joan Montaner [b], Anna Rosell [b,*], Anna Roig [a,*]

[a] Institut de Ciència de Materials de Barcelona, Consejo Superior de Investigaciones Científicas (ICMAB-CSIC), Campus de la UAB, 08193 Bellaterra, Catalunya, Spain
[b] Neurovascular Research Laboratory and Neurovascular Unit, Vall d'Hebron Institut de Recerca, Hospital Universitari Vall d'Hebron, Universitat Autònoma de Barcelona, Passeig Vall d'Hebron, 119-129 Barcelona, 08035 Catalunya, Spain

ARTICLE INFO

Article history:
Received 30 December 2013
Received in revised form 17 March 2014
Accepted 8 April 2014
Available online xxxx

Keywords:
Iron oxide nanoparticles
Endothelial progenitor cells
Cellular uptake
Microwave synthesis
Magnetic resonance imaging

ABSTRACT

We synthesize highly crystalline citrate-coated iron oxide superparamagnetic nanoparticles that are stable and readily dispersible in water by an extremely fast microwave-assisted route and investigate the uptake of magnetic nanoparticles by endothelial cells. Nanoparticles form large aggregates when added to complete endothelial cell medium. The size of the aggregates was controlled by adjusting the ionic strength of the medium. The internalization of nanoparticles into endothelial cells was then investigated by transmission electron microscopy, magnetometry and chemical analysis, together with cell viability assays. Interestingly, a sevenfold more efficient uptake was found for systems with larger nanoparticle aggregates, which also showed significantly higher magnetic resonance imaging effectiveness without compromising cell viability and functionality. We are thus presenting an example of a straightforward microwave synthesis of citrate-coated iron oxide nanoparticles for safe endothelial progenitor cell labeling and good magnetic resonance cell imaging with potential application for magnetic cell guidance and in vivo cell tracking.

1. Introduction

In the past decade or so, a number of studies on cellular therapy for tissue repair have shown that, under the influence of an external magnetic field, cells can be guided into areas of interest and their migration can be tracked by magnetic resonance imaging (MRI) [1–4]. Interestingly, enhanced cell functions, such as growth factor secretion or migration, have also been reported in the case of endothelial progenitor cells labeled with superparamagnetic iron oxide nanoparticles (SPIONs) for cellular-based approaches in angiogenic treatments [3]. Several in vitro experiments have demonstrated that, by choosing adequate core sizes, concentration of the magnetic material and chemical composition of the particle coating, it is possible to regulate the iron cellular uptake whilst minimizing potential cytotoxic effects [5–7].

To succeed in cellular uptake and cellular magnetic labeling, SPIONs should be monodisperse, with high magnetization and susceptibility. For this purpose, we selected a high-temperature microwave-assisted nonhydrolytic sol–gel process in order to obtain nanoparticles with high saturation magnetization and narrow size distribution. The microwave-assisted route has been widely used in inorganic and organic synthesis owing to its easier and more environmentally friendly set-up compared to other high-temperature synthetic approaches [8,9]. Moreover, there are numerous advantages compared with traditional heating methods, such as more homogeneous inner core heating with no solvent convective currents due to temperature gradients [10], lower energy consumption and shorter reaction time: it is possible to reach high enough temperatures to complete the dissolution of the starting reagents, formation of reactive species (monomers), nucleation and growth within seconds or minutes, rather than the hours in traditional heating methods. The microwave route is a fast and reproducible process by which to obtain magnetic iron oxide particles in which the concentration of the precursor, the power and the time of irradiation are critical factors to achieving size control [11,12]. This is of great importance when considering the interactions of nanoparticles in a biological environment, such as the amount of protein corona adsorbed onto the particle surface [13].

Here, we report on an extremely fast and simple method to obtain highly crystalline citrate-coated iron oxide nanoparticles

* Corresponding authors.
E-mail addresses: anna.rosell@vhir.org (A. Rosell), roig@icmab.es (A. Roig).

http://dx.doi.org/10.1016/j.actbio.2014.04.010
1742-7061/

that are readily dispersible in water by using a microwave-assisted sol–gel method, avoiding the inefficient and time-wasting ligand exchange steps. We have successfully labeled two cell populations: endothelial progenitor cells (EPCs), for use in future cell therapies, and a neuronal cell line, to test the potential toxic effects of SPIONs in brain tissues. Citrate-coated nanoparticles in culture medium formed aggregates and the aggregate size could be easily controlled by adjusting the medium ionic strength via the addition of citrate. We selected this approach rather than a polymer coating strategy to stabilize our particle formulation in vitro, aiming to minimize any possible cytotoxicity deriving from polymer degradation. It has been demonstrated that, depending on the amount of plasma in the medium and the temperature, a dynamic shell made of plasma protein (protein corona) with specific binding affinity constants is adsorbed onto the surface of maghemite nanoparticles, leading to the loss of electrostatic charge and particle precipitation [14]. In our study, in which nanoparticles do not have to be injected directly into the blood stream, it is not necessary to avoid SPION–protein interactions since the particles' final destination is inside the cell for cell labeling purposes. For this reason, limited particle aggregation (up to 200 nm) will not be considered a drawback if the particle aggregates were proved to be non-toxic to cells. The internalization of nanoparticles into endothelial cells was investigated. Sevenfold more efficient uptake has been found for cells exposed to aggregated nanoparticles, which also show significantly greater MRI effectiveness in terms of the T_2 contrast agent. We are thus presenting an example of straightforward microwave synthesis of citrate-coated iron oxide nanoparticles for successful endothelial progenitor cell labeling and good contrast MRI cell imaging, which could be useful in therapies aimed at promoting angiogenesis.

2. Materials and methods

2.1. Chemicals

The following chemicals were purchased from Sigma–Aldrich and were used as received: iron(III) acetylacetonate ($Fe(acac)_3$, 97%), benzyl alcohol, aqueous trimethylammonium hydroxide (TMAOH) solution (25 wt.%), trisodium citrate, nitric acid (65%), human plasma fibronectin, phosphate-buffered saline (PBS, 10×), trypsin from bovine pancreas lyophilized powder, 3-(4,5-dimethylthiazol-2-yl)-2,5-diphenyltetrazolium bromide (MTT, 98%), potassium ferrocyanide trihydrate and concentrated hydrochloric acid. MilliQ water was used to prepare all chemical dilutions.

2.2. Iron oxide nanoparticle synthesis and characterization

2.2.1. Microwave synthesis

In a glass tube suitable for microwave reactions, the iron precursor $Fe(acac)_3$ (0.35 mmol) was added to benzyl alcohol (4.5 ml) and ultrasonicated for a few minutes. No surfactant was added at this stage. The vial was closed and the microwave irradiation took place with the power set at 250 W. During the chemical reaction, the temperature and pressure were monitored by a volume-independent infrared built-in sensor. The solution was kept at 60 °C for 5 min to achieve complete dissolution of the organic precursor and subsequently heated to 180 °C and kept at this temperature for 10 min. The final result was a black colored dispersion, which suggested the formation of magnetic material. Acetone was added to precipitate the particles in the presence of a few microliters of the anionic stabilizer TMAOH and centrifuged at 2817g for 30 min. The supernatant was then discarded and another few more microliters of TMAOH was added before a further centrifugation. The final black precipitate was dried at 60 °C for 1 h and dispersed in MilliQ water. As synthesized, the pH of the colloidal aqueous dispersion was basic due to the presence of TMAOH. To be compatible for cellular labeling, it was necessary to reduce the pH to 7.5 by adding 0.1 M HNO_3. In addition, sodium citrate, an anionic stabilizer, was added to counterbalance inter-particle interactions. The final batch, with a yield of 76%, consisted of a stable colloidal dispersion of single core iron oxide nanoparticles with a hydrodynamic size of 14 nm (relative polydispersity 20%) and a zeta potential of −35 mV. Concentrations as high as 12 mg ml^{-1} can be achieved. The particle size was monitored throughout the experiment and no precipitation was found even after 6 months. Finally, the batch was sterilized by filtration (0.2 μm pore size membranes, Millipore) before being used for cell culture. The particle core is composed of maghemite phase (γ-Fe_2O_3), as confirmed by electron diffraction. A typical batch had a particle concentration of 2.8 mg ml^{-1}, with a sodium citrate concentration of 0.03 mM.

2.2.1.1. Transmission electron microscopy. TEM was performed on the SPIONs. A few drops of the diluted suspensions were deposited onto copper grids and water was left to evaporate at room temperature. Images were acquired using a JEOL 1210 transmission electron microscope operated at 120 kV.

2.2.2. Cryo-transmission electron microscopy (cryo-TEM)

Cryo-TEM analysis was performed on particle dispersions in water and biological medium (EGM-2 medium (Lonza, Switzerland) containing 10% fetal bovine serum (FBS) in the presence and absence of an excess of 10 mM sodium citrate) at an iron concentration of 10 mM. TEM images of water-borne nanoparticles at pH 7.5 could be visualized by rapid vitrification of the particle suspension. This was achieved by depositing a drop of the SPION sample onto a Quantifoil® grid and rapidly quenching it in liquid ethane. The grid was then transferred to the TEM microscope (JEM-2011 operating at 200 kV), with the temperature being kept under −140 °C during the imaging.

2.2.3. Dynamic light scattering (DLS)

Measurements were done with Zetasizer Nano ZS from Malvern Instruments equipped with an He/Ne 633 nm laser using 1 ml of particle dispersion in a disposable plastic cuvette. Measurements were run in triplicate, each one of 15 scans, at room temperature. Zeta potential measurements were run three times at room temperature.

2.2.4. Superconductive quantum interference device (SQUID)

A magnetometer from Quantum Design MPMS5XL was used to take magnetization measurements of the SPIONs. A few drops of the aqueous colloidal dispersion were deposited into a polycarbonate capsule and left at room temperature for the water to evaporate until the material was completely dry. The as-prepared sample was inserted in the SQUID magnetometer sample holder and the cell remanent magnetization was measured at 5 K after the material has been magnetically saturated up to 6 T. The zero field cooled-field cooled magnetization vs. temperature with a 50 Oe applied field was also plotted for the synthesized SPIONs. The blocking temperature of the superparamagnetic assembly was 58 K.

2.2.5. Optical microscopy

In a multiwell plate, SPIONs at a concentration of 50 μg ml^{-1} were dispersed in 1 ml of the following medium: PBS 1×, Dulbecco's modified Eagle's medium with Ham's F-12 (DMEM F12; Gibco, CA, USA)–10% FBS and EGM-2–10% FBS, in the presence and absence of an excess of 10 mM sodium citrate. Control wells consisted of the same medium without SPIONs. Particle size aggregation was monitored for 1 h using an Olympus BX51 optical

Please cite this article in press as: Carenza E et al. Rapid synthesis of water-dispersible superparamagnetic iron oxide nanoparticles by a microwave-assisted route for safe labeling of endothelial progenitor cells. Acta Biomater (2014), http://dx.doi.org/10.1016/j.actbio.2014.04.010

microscope connected to an Olympus DP20 digital camera. Images were taken with a 5 × objective.

2.3. Cell cultures

Outgrowth endothelial progenitor cell (OEC, a type of EPC) cultures were obtained from the spleens of male BALB/c mice (Charles River Laboratories, Spain) or human blood as previously described [15,16], grown in EGM-2 complete medium, which is endothelial cell basal medium (EBM-2) supplemented with human endothelial growth factor, vascular endothelial growth factor, human basic fibroblast growth factor, insulin-like growth factor 1, gentamicin + amphoterecin-B, heparin, hydrocortisone, and ascorbic acid with 10% FBS (Gibco, CA, USA). SHSY5Y neuroblastoma cells were purchased from ATCC (LCG Standards S.L.U.) and grown in DMEM F12–10% FBS.

2.3.1. Cell labeling with SPIONs

SHSY5Y cells (5×10^4) were cultured in DMEM F12–10% FBS. After 48 h, cells were washed twice with PBS and differentiation medium, consisting of 1% retinoic acid (RA) in DMEM F12–1% FBS, was added. The differentiation medium was changed every 2 days. After 5 days, cells were washed twice with PBS, then SPIONs were added at concentrations of 0, 25, 50, 100 μg ml^{-1} in DMEM F12–10% FBS and incubated at 37 °C for 24 h.

OECs between passage 3 and 6 were seeded onto fibronectin-coated 24-well plates (1×10^5 cells per well) and incubated for 2 days in EGM-2–10% FBS. SPIONs were added at concentrations of 0, 25, 50, 100 μg ml^{-1} and incubated at 37 °C for 24 h in the presence or absence of 10 mM sodium citrate.

2.3.2. Cell viability assays (MTT)

MTT is a yellow compound which turns into a purple formazan product after reduction by mitochondrial enzymes, which are only present in metabolically active live cells, and not in dead cells. The amount of formazan generated is proportional to the number of viable cells in the sample. The formazan product is photometrically quantified at 590 nm.

SPIONs were incubated with cells in a 24-well plate at concentrations of 0, 25, 50, 100 μg ml^{-1} at 37 °C for 24 h in the presence or absence of 10 mM sodium citrate, as described above for OECs and SHSY5Y cultures. Afterwards cells were washed twice with PBS and 50 μl of MTT in 300 μl of complete EBM-2 was added. After incubation at 37 °C for 90 min, during which the MTT reduction took place, the cell medium was discarded and 200 μl of dimethylsulfoxide was added to each well. Absorbance on the isolated supernatant was measured at 590 nm. Experiments were run in duplicate and expressed as percentage of viable cells vs. the control condition (without SPIONs). Differences between groups were subjected to analyses of variance followed by Bonferroni post hoc tests (statistical significance was considered when $p < 0.05$).

2.3.3. Muse™ count & viability assay

The assay utilizes a proprietary mix of two DNA intercalating fluorescent dyes in a single reagent. One of the dyes is membrane permeant and stains all cells with a nucleus. The second dye only stains cells which have membranes that have been compromised in dying or dead cells. This combination allows one to discriminate between nucleated cells and those without a nucleus or debris, and live cells from dead or dying cells, resulting in both accurate cell concentration and viability results (MuseTM cell analyzer http://www.millipore.com/userguides/tech1/8tut22). A Muse™ Cell Analyzer (Millipore, catalogue number MCH100102) was used to read the results. Briefly, after 24 h of cell labeling with SPIONs, OECs were trypsinized and resuspended in complete EGM-2 medium. Cells were stained following the manufacturer's instructions and the numbers of total cells and viable cells were counted by automatic reading. Data are expressed as percentage of viable cells vs. control.

2.3.4. Prussian blue staining

In a 12-well plate pre-coated with fibronectine, 2×10^5 cells were seeded. After 24 h, fresh EGM-2–10% FBS medium was added together with 25, 50 and 100 μg ml^{-1} SPIONs in the presence and absence of an excess of 10 mM sodium citrate. Cells were incubated for 24 h at 37 °C, then washed twice with PBS and fixed for 30 min at room temperature with 2% paraformaldehyde solution. Next, cells were washed twice with distilled water and a Perl's solution, made of equal volumes of hydrochloric acid and potassium ferrocyanide at 2%, was added. After incubation for 30 min at room temperature in the dark, cells were rinsed twice with distilled water and imaged with an optical microscope (Nikon). Photographs were taken using a 10 × objective.

2.3.5. Cell TEM

TEM of OECs was performed as follows: cells were seeded in 25 cm^2 flasks, grown and treated with SPIONs ([Fe] = 50 μg ml^{-1} for 24 h, at 37 °C). Cells were trypsinized, washed once with complete EGM-2 and collected by centrifugation (1300 rpm, 4 min). The supernatant was discarded and 1.5 ml of 2% glutaraldehyde in cacodylate buffer was added to the pellet. Cells were quickly incubated in the fixation solution at 4 °C for 1 h and post-fixed in 1% OsO_4; they were then dehydrated in an alcohol series and embedded in Epon resin. Finally, ultrathin sections (70 nm) were transferred onto copper grids and analyzed by TEM, using a JEM-2011 microscope operating at 200 kV.

2.3.6. Nanoparticles cell uptake determination: SQUID and Inductively coupled plasma atomic emission spectroscopy

A magnetometer from Quantum Design MPMS5XL was used to perform magnetization measurements of cells labeled with SPIONs. To quantify the iron uptake by OECs, cells were seeded in 25 cm^2 flasks, grown in complete EGM-2 medium until confluence and treated with 50 μg ml^{-1} SPIONs in fresh complete medium in the presence or absence of the extra 10 mM sodium citrate. After 24 h, cells were washed three times, trypsinized and counted. Cells were centrifuged at 1500 rpm for 5 min at room temperature and the cell pellet formed was dried at 60 °C using a speed vacuum centrifuge (1500 rpm for 60 min). The as-prepared sample was inserted into the SQUID magnetometer sample holder and the cell remanent magnetization was measured at 5 K after the material has been magnetically saturated up to 6 T. The uptake of SPIONs was evaluated using simple calculations: first, dividing the remanence magnetization value of the treated cells by the total number of cells, giving the magnetization per cell (emu cell^{-1}), then further dividing this value by the remanence magnetization of the SPIONs (emu g^{-1} Fe) at 5 K to give the amount of iron per cell. The zero field cooled-field cooled magnetization vs. temperature with an 50 Oe applied field was also plotted for magnetized cells that were exposed to both SPIONs in EGM-2–10% FBS medium and SPIONs in EGM-2–10% medium with extra sodium citrate.

Inductively coupled plasma atomic emission spectroscopy (ICP-AES). To quantify the iron uptake by OECs, cells were seeded in 25 cm^2 flasks, grown in EGM-2 complete medium until confluence and treated with 50 μg ml^{-1} SPIONs in fresh complete medium in the presence or absence of the extra 10 mM sodium citrate. After 24 h, cells were washed three times, trypsinized and counted. Cells were centrifuged at 1500 rpm for 5 min at room temperature and the cell pellet formed was dried at 60 °C using a speed vacuum centrifuge (1500 rpm for 60 min). The pellet was then weighed using a microbalance (MX5, Mettler Toledo) and subsequently digested in concentrated HNO_3 for 20 min at 150 °C. The dissolved sample was

Please cite this article in press as: Carenza E et al. Rapid synthesis of water-dispersible superparamagnetic iron oxide nanoparticles by a microwave-assisted route for safe labeling of endothelial progenitor cells. Acta Biomater (2014), http://dx.doi.org/10.1016/j.actbio.2014.04.010

diluted using 1% HNO_3 and the iron content was analyzed using a Perkin-Elmer Optima 4300DV spectrometer. The final iron concentration was expressed as weight percentage over the total weight of the pellet.

2.3.7. In vitro vessel formation

To assess the effect of the SPIONs on the angio-vasculogenic abilities of OECs, growth factor reduced Matrigel™ (BD Biosciences, NJ, USA) was used for an in vitro vessel formation assay (also named tubulogenesis). Twenty-four hours before the experiment, the cells were treated with complete medium alone (EGM-2–10% FBS), 50 μg ml^{-1} of SPIONs in EGM-2 or 50 μg ml^{-1} of SPIONs in EGM-2 with 10 mM sodium citrate, as described above. Experiments were performed with OECs obtained from a healthy human control between passages 10 and 12. Briefly, 24-well plates were coated with 200 μl of cold Matrigel™ and allowed to solidify at 37 °C for 30 min. Magnetic labeled cells were then tripsinized and 6×10^4 cells were transferred into the Matrigel™-coated wells in basal medium (a medium that does not contain growth factors or FBS). Each assay was performed in duplicate and the number of complete rings (circular vessel-like structures), the total tube length (perimeter of the rings) and the number of cell connections (branching points between rings) were counted by the Wintube automatic software (Wimasis GmbH, Munich, Germany) in six representative fields (100×) per well. The experiment was assayed in four independent plates.

2.3.8. MRI relaxometry

MRI of SPIONs and of labeled OECs was performed using a 7 T magnet (BioSpec 70/30 USR, Bruker BioSpin, Ettlingen, Germany). Cellular magnetization was achieved by standard incubation with 50 μg ml^{-1} SPIONs for 24 h in complete culture medium in the presence or absence of 10 mM sodium citrate. Phantom cell suspensions containing labeled and unlabeled OECs in 1.5% agarose were imaged. Briefly, and as previously described [3], T_2 maps were acquired to determine relaxation times using a multi-slice multi-echo method with the following parameters: *TR* (repetition time) = 3 s, 30 *TE* (echo delay time) values from 10 to 300 ms (10 ms echo spacing), matrix size = 128 × 128. High-resolution T2WI was obtained using the fast spin echo sequence RARE (rapid acquisition with relaxation enhancement): *TR* = 4 s, TE_{eff} (effective echo time) = 16 ms, average of two samples, matrix size = 256 × 256. T_2 values were obtained by regions of interest obtained within the phantom volume. The relaxivity, r_2, of the SPIONs was determined by a linear fit of the inverse relaxation times as a function of the iron concentrations, resulting in an r_2 value of 140 s^{-1} mmol Fe^{-1}.

3. Results and discussion

New synthetic processes to produce SPIONs with high quality, high yields and low environmental impact are of great interest for their potential industrial scale-up [17]. Microwave synthesis has been increasingly used during the last 30 years for its versatility in inorganic [18] and organic [19] synthesis, and its shorter duration and lower energy consumption compared to other traditional heating methods. Moreover, when considering nanoparticle synthesis, since sample heating is homogeneous and no solvent convective currents or temperature gradients are present in the reaction well, narrow particle size distributions can be achieved [10].

Microwave-assisted non-hydrolytic sol–gel decomposition of $Fe(acac)_3$ at 180 °C in benzyl alcohol [8] was used as a simple and extremely fast method (15 min) to synthesize water-soluble maghemite nanoparticles. We have previously demonstrated that particles with low surface reactivity are formed [20], allowing us to add surfactants (TMAOH) as a final step after the particle synthesis. TMAOH readily dissolves to form $N(CH_3)_4^+$ and OH^- ion species in an aqueous environment. OH^- ions are directly adsorbed onto the maghemite surface, forming an inner negatively charged layer, while $N(CH_3)_4^+$ contributes to particle stabilization, forming an outer positively charged layer. Thus, in a stable colloidal dispersion, the double electrostatic layer on the maghemite surface provides electrostatic repulsion forces to counterbalance attractive Van der Waals and dipole–dipole interactions. Prior to being used for biomedical applications, the pH of the basic solution of nanoparticles stabilized with TMAOH has to be lowered to physiological pH (7.5). By simply adding nitric acid, the groups NO_3^- would neutralize $N(CH_3)_4^+$, leaving Fe–OH exposed, and without the $N(CH_3)_4^+$ coverage the ferrofluid would readily sediment [21]. For this reason, an additional stabilizer is needed, and we used sodium citrate, which in great part replaces the initial TMAOH. In this way we attained colloidal solutions with very high Fe concentrations (up to 12 mg ml^{-1}) that were stable in time (up to 6 months). Thus, the final dispersion consisted of TMAOH-citrate-coated nanoparticles (cit-γ-Fe_2O_3) with a hydrodynamic diameter of 14 nm ± 20% polydispersity, a TEM diameter of 7.2 nm ± 18% polydispersity, a final pH of 7.5 and a zeta potential of −35 mV.

Two cell types – mouse and human OECs and human SHSY5Y neuroblastoma cells – were investigated. The OECs were selected for their potential use in promising novel cellular therapies, in particular those targeting angiogenesis [22]. The choice of SHSY5Y cells was motivated by their known sensitivity to external factors [23]; they were thus used to test cell toxicity when exposed to SPIONs. Nanoparticles with iron concentrations up to 100 μg ml^{-1} were incubated for 24 h in complete cell culture medium. Clear differences in particle aggregate sizes were observed, dependent on the medium composition. The hydrodynamic nanoparticle diameter was monitored by DLS (see discussion below) and showed that no major aggregation took place in DMEM–10% FBS (the growth medium for SHSY5Y), while large aggregates were observed when using EGM-2–10% FBS (growth medium for OECs). Control over nanoparticle aggregation in EGM-2 complete medium was achieved by adjusting its ionic strength via the addition of citrate. Hereafter, we refer to the SPIONs in EGM-2–10% FBS medium as the aggregate system and to the SPIONs in EGM-2–10% medium with extra sodium citrate as the dispersed system.

3.1. Iron oxide nanoparticles characterization

A TEM image of the as-obtained nanoparticles is depicted in Fig. 1a. The particles have a roundish lobular shape. Fitting the particle size histogram (Fig. 1b) to a Gaussian function, a mean particle diameter of 7.2 ± 1.3 nm is obtained. The 18% polydispersity, calculated as the percentage of the half width of the distribution over the mean diameter, indicates the narrow particle size distribution of the system. Electron diffraction (Fig. 1c) shows well-defined diffraction rings indexed to the maghemite spinel structure. The good crystallinity of the microwave-synthesized nanoparticles can also be seen in the high-resolution TEM image in Fig. 1d, where a plane interdistance of the spinel phase of d = 0.267 nm is identified. The well crystallized nanoparticles are likely the result of performing the synthesis at high temperature, in contrast to the co-precipitation method, which renders nanoparticles that are readily soluble in water with high concentrations but lower crystallinity (and thus low magnetization saturation values) [24,25]. Fig. 2 summarizes the magnetic properties of the as-obtained SPIONs. Zero field cooled–field cooled curve (ZFC–FC; upper inset of Fig. 2) signals the small size and superparamagnetic character of the material, with a ferrimagnetic transition at the blocking temperature (58 K). The sharp peak of the ZFC curve shows the narrow particle size distribution of the assembly. A high saturation magnetization of 60 emu g^{-1} Fe_2O_3 is measured at 300 K

Please cite this article in press as: Carenza E et al. Rapid synthesis of water-dispersible superparamagnetic iron oxide nanoparticles by a microwave-assisted route for safe labeling of endothelial progenitor cells. Acta Biomater (2014), http://dx.doi.org/10.1016/j.actbio.2014.04.010

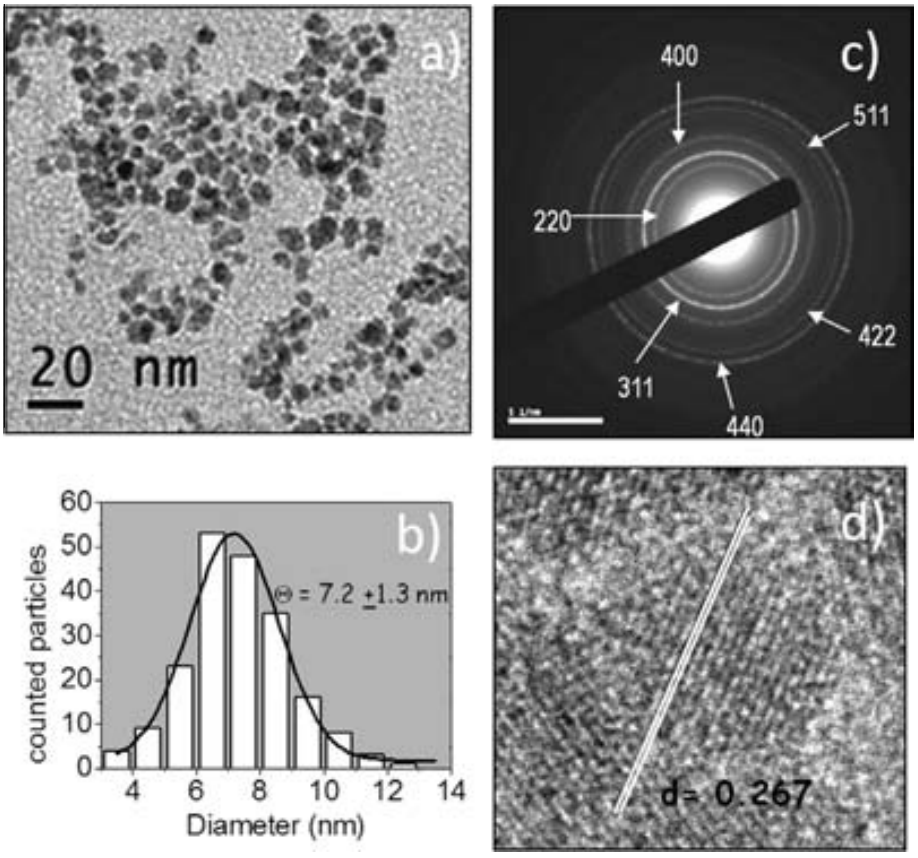

Fig. 1. (a) TEM image of microwave synthesized SPIONs in aqueous medium at pH 7.5, (b) particle size distribution histogram and mean particle size diameter, (c) electron diffraction pattern indexed to the inverse spinel phase of maghemite and (d) high-resolution TEM image showing few nanoparticles with the identification of a crystalline plane for maghemite.

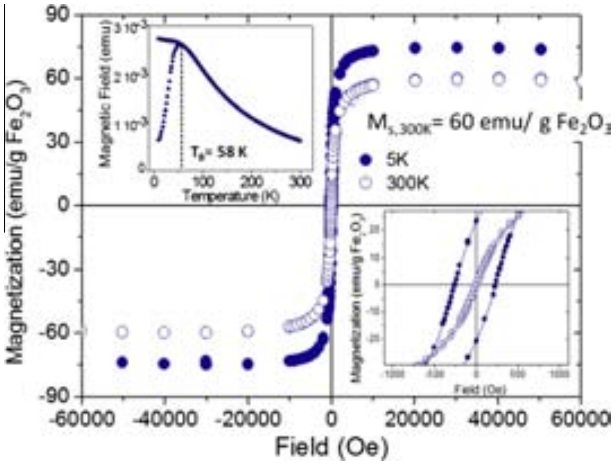

Fig. 2. (a) Hysteresis loops, M(H), of the synthesized SPIONs at 5 K and at room temperature. Saturation magnetization at room temperature is 60 emu g^{-1} Fe_2O_3. The upper inset depicts the ZFC–FC curves at 50 Oe; the blocking temperature is 58 K. The lower inset shows details of the hysteresis loops under small fields. The lack of a coercive field is observed at room temperature.

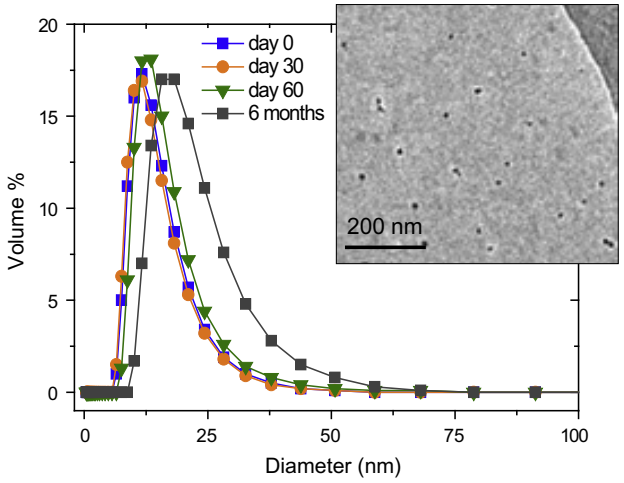

Fig. 3. DLS measurements of the same batch of SPIONs repeated at different times for nanoparticles in water at pH 7.5. Measurements show that there is no remarkable change in particle aggregation over a period of 6 months. Inset: cryo-TEM images of the frozen solution, showing that particles are not aggregated in the conditions used.

(Fig. 2). No coercive field is observed at 300 K, though a small coercive field is present at 5 K (lower inset Fig. 2).

3.2. Colloidal stability in biological medium

Nanoparticles in biological fluids are attracting increased attention from nanoscientists. There are numerous studies demonstrating that nanoparticles coated by a protein corona are active biological entities that influence such biological responses as cellular targeting and uptake [14,26]. Human plasma is made up of around 3700 proteins, each one having a different binding constant for a specific nanoparticle formulation. Importantly, if the specific protein adsorption pattern on a particle surface is

Please cite this article in press as: Carenza E et al. Rapid synthesis of water-dispersible superparamagnetic iron oxide nanoparticles by a microwave-assisted route for safe labeling of endothelial progenitor cells. Acta Biomater (2014), http://dx.doi.org/10.1016/j.actbio.2014.04.010

known, this can help in predicting particle targeting and biodistribution in vivo. For instance, the plasma protein apolipoprotein E seems to facilitate drug targeting when the blood–brain barrier has to be crossed. A well-known example of a protein that mediates drug delivery is albumin, which is the most abundant protein in plasma and has been successfully used in the delivery of paclitaxel (Abraxane®, an anticancer drug) [27]. Another example was reported by Jansch and co-workers, who demonstrated that citrate–triethylene glycol-coated SPIONs of about 7 nm incubated with different aqueous dilutions of FBS formed a quite stable corona over time, with immunoglobulin and fibrinogen being the most abundant proteins adsorbed onto the particle surface [28]. Often particle surface functionalization with polymers (e.g. poly(ethylene glycol), polaxamer, dextran) is required to minimize particle–serum protein interactions when a long blood circulation time and reduced opsonization by the reticuloendothelial system are needed [29,30]. However, impurities and the products of the oxidative degradation of used polymers have been associated with certain pharmacological and immunological effects [31]. In our study, in which nanoparticles do not have to be injected directly into the blood stream, it is not the major requirement to avoid SPION–protein interactions since the particles' final destination is

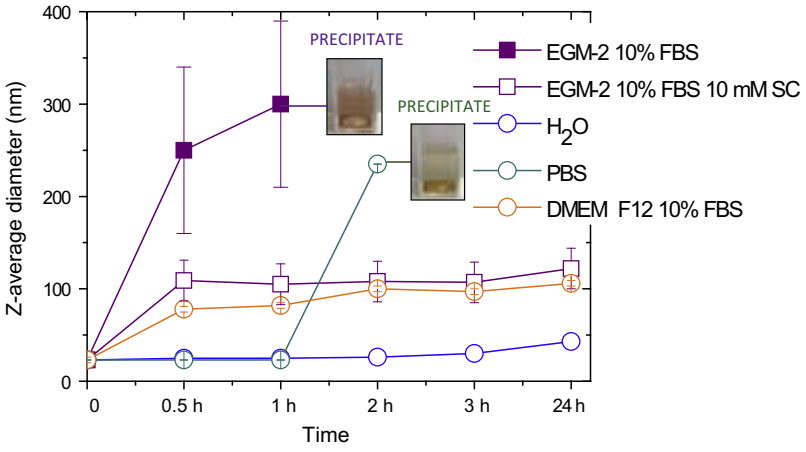

Fig. 4. DLS measurements of SPIONs in biological medium. Measurements at 37 °C, $n = 2$.

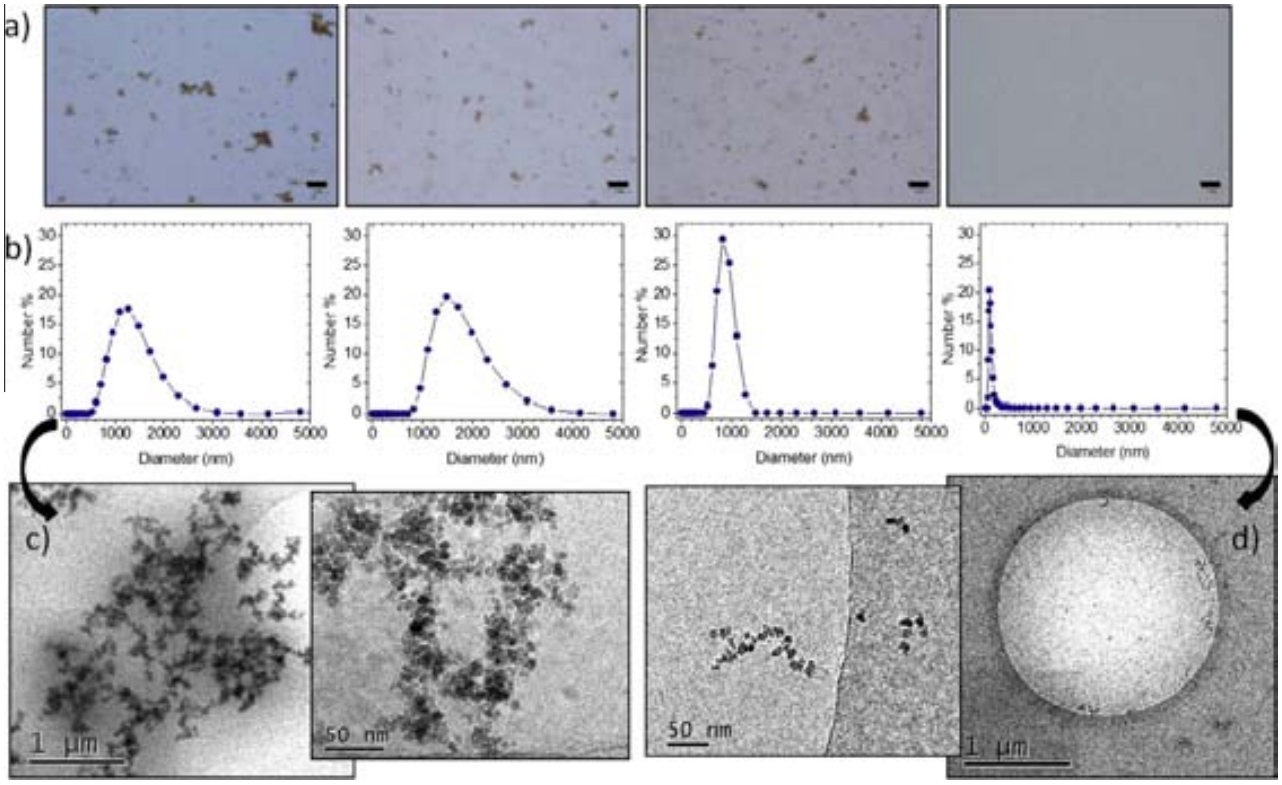

Fig. 5. Optical microscopy images of SPIONs incubated for 1 h at 37 °C in the biological medium studied. (a) Endothelial growth medium (EGM-2–10% FBS), EGM-2–10% FBS with extra 0.2 mM sodium citrate, EGM-2–10% FBS with extra 5 mM sodium citrate and EGM-2–10% FBS with extra 10 mM sodium citrate. Brown aggregates of different sizes can be seen in all images. Scale bar = 100 µm. (b) The corresponding DLS histograms. (c) Cryo-TEM pictures at two different magnifications, showing aggregated particles in EGM-2–10% FBS. (d) Cryo-TEM pictures at two different magnifications, showing dispersed particles in EGM-2–10% FBS with extra 10 mM sodium citrate.

Please cite this article in press as: Carenza E et al. Rapid synthesis of water-dispersible superparamagnetic iron oxide nanoparticles by a microwave-assisted route for safe labeling of endothelial progenitor cells. Acta Biomater (2014), http://dx.doi.org/10.1016/j.actbio.2014.04.010

inside the cell. For this reason, we preferentially used the easily fabricated citrate-coated SPIONs, which are suitable for cellular labeling, and controlled their aggregation in the culture medium by the addition of limited amounts of salt.

The nanoparticle's hydrodynamic diameter was measured by DLS in water at pH 7.5, which gave a value of 14 nm (with 20% polydispersity) for the as-prepared material. The system was colloidally stable, maintaining the same size even after 6 months as a consequence of the particle's low surface reactivity [18] (Fig. 3). Cryo-TEM images (inset of Fig. 3) show that the nanoparticles are individually stabilized. As mentioned above, SPIONs perform differently in biological medium than in water, and their performance strongly depends on the medium composition, which can vary for each cell type. Not only does the formation of a protein corona on the particle surface have a major effect on particle aggregation, but also the high ionic forces due to high salt and amino acid concentrations can lead to colloidal instability [32]. In addition to water, particle stability was also monitored by DLS over time in different media, such as PBS 1× (calcium and magnesium free), DMEM F12–10% FBS and EGM-2–10% FBS (Fig. 4). The chemical compositions of all the media were known except for EGM-2 (from Lonza), the ionic strength of which was impossible to determine. However, it was found that the pHs and potentials (expressed in millivolts) of PBS and DMEM F12 were significantly different from that of EGM-2 medium. For instance, PBS had a pH of 7.3 and a potential of −30 mV, while EGM-2 had a pH of 8.4 and a potential of −80 mV, suggesting a higher concentration of negatively charged molecules. When the hydrodynamic diameters of SPIONs were measured after 30 min in PBS and DMEM F12–10% FBS, the particles were found to be rather stable, with a hydrodynamic diameter of less than 100 nm. An invariable size was maintained for a longer time in the case of DMEM F12–10% FBS but the particles becoming unstable in PBS after 1 h. In the case of EGM-2–10% FBS, SPIONs rapidly formed large clusters, which started to precipitate after 2 h. To control the size of the aggregates, extra sodium citrate was added to the EGM-2–10% FBS at different concentrations (0.2, 5 and 10 mM). The aggregates were monitored by optical microscopy images, as shown in Fig. 5, which also contains the corresponding DLS curves. It can be seen that the higher the sodium citrate concentration, the smaller the particle aggregates. For the 10 mM sodium citrate concentration, the particles had an average hydrodynamic diameter of 100 nm according to DLS (Fig. 5d), and did not form large aggregates even after 2 days at 37 °C.

3.3. Cell labelling, SPION cell cytotoxicity and cell functionality

Fig. 6 show optical microscopy images of OECs incubated for 24 h at several SPION concentrations (0, 25, 50 and 100 μg ml−1) in EGM-2–10% FBS medium in the presence and absence of extra sodium citrate, with the related Prussian blue-stained images to

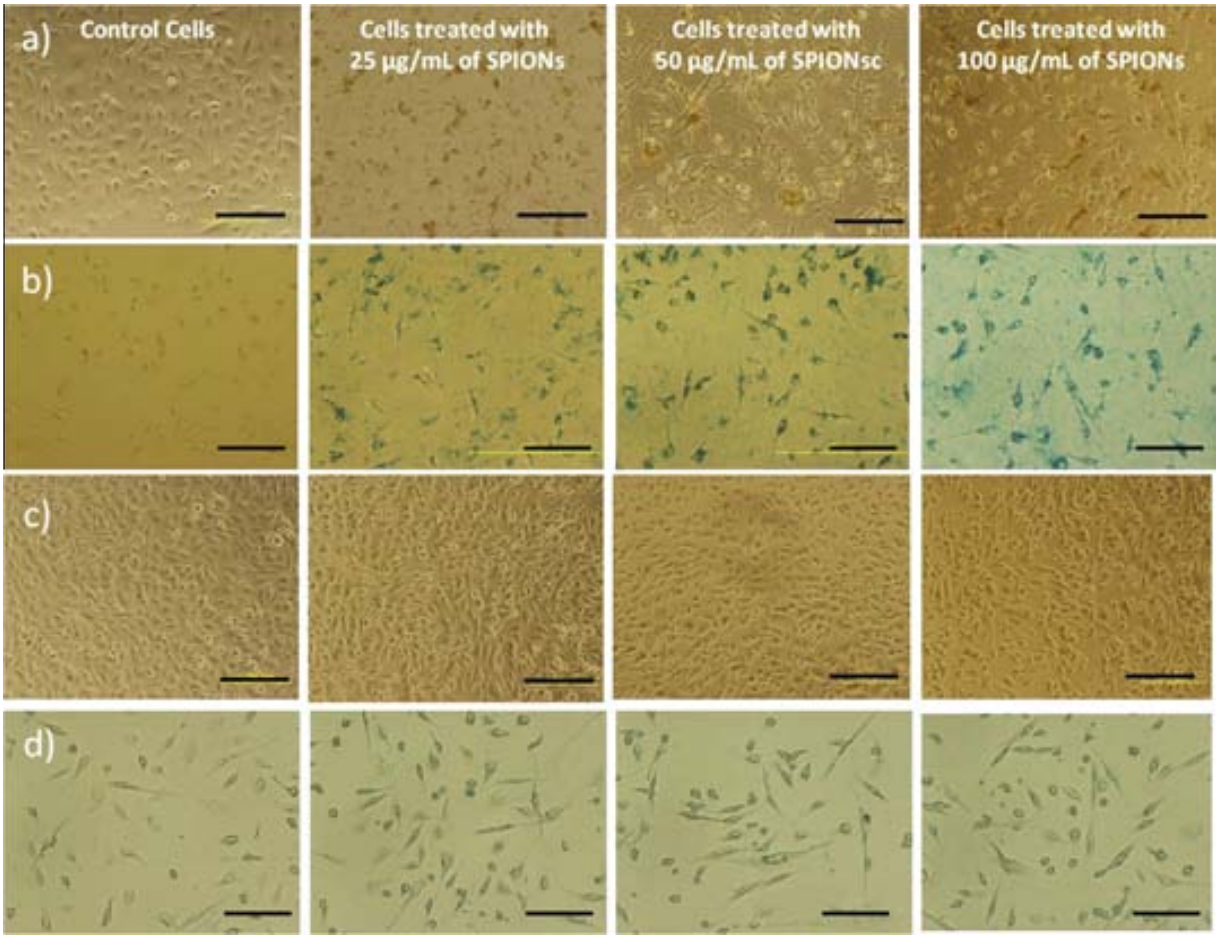

Fig. 6. (a) Optical microscopy images of OECs incubated with SPIONs for 24 h at 37 °C in the absence of extra 10 mM sodium citrate. Scale bar = 200 μm. (b) Prussian blue staining of OECs labeled with SPIONs in the absence of extra 10 mM sodium citrate. Scale bar = 100 μm. Row (c) Optical microscopy images of OECs incubated with SPIONs for 24 h at 37 °C in the presence of extra 10 mM sodium citrate. Scale bar = 200 μm. (d) Prussian blue staining of OECs labeled with SPIONs in the presence of extra 10 mM sodium citrate. Scale bar = 100 μm. For cell labeling, 1×10^5 cells in a 24-well plate were used, whilst for Prussian blue staining, 2×10^5 cells in a 12-well plate were used; thus the seeding density was 0.5×10^3 cells mm^{-2}.

Please cite this article in press as: Carenza E et al. Rapid synthesis of water-dispersible superparamagnetic iron oxide nanoparticles by a microwave-assisted route for safe labeling of endothelial progenitor cells. Acta Biomater (2014), http://dx.doi.org/10.1016/j.actbio.2014.04.010

show that the SPIONs had been up taken. Particle aggregates are not observed in Fig. 6c but they are evident in Fig. 6a, corresponding to the cell medium without any extra sodium citrate. The stain intensity for cells incubated with aggregated particles (Fig. 6b) is noticeable higher than in cells incubated with dispersed nanoparticles (Fig. 6d), signaling increased iron uptake. No differences in cell morphology were observed between the two incubation conditions.

SPION viability was evaluated using two populations of cells, including primary endothelial progenitor cells and neuron-like cells, at different iron concentrations. MTT tests on neuron-like cells (SHSY5Y cell line) were done at iron concentrations up to 100 μg ml^{-1}, incubating at 37 °C for 24 h (Fig. 7a). We concluded that the presence of exogenous iron at the concentrations used does not markedly affect viability even in neuron-like cells, which are very sensitive to iron loading [33].

The cell viability of the OECs treated with SPIONs in EGM-2–10% FBS was examined in the presence or absence of 10 mM of sodium citrate. The results confirmed that SPIONs were not toxic up to concentrations of 100 μg ml^{-1} at 37 °C for 24 h (Fig. 7b and c). Only a slight decrease (not statistically significant) in viability at 100 μg ml^{-1} was observed for particles in the aggregated state.

To check if cell functionality can be affected by SPION aggregation, in vitro vessel formation experiments were run in EBM-2–10% FBS ($n = 4$). The number of complete rings (circular vessel-like structures), the total tube length (perimeter of the rings) and the number of cell connections (branching points between rings) were analyzed and compared between three groups: non-treated cells

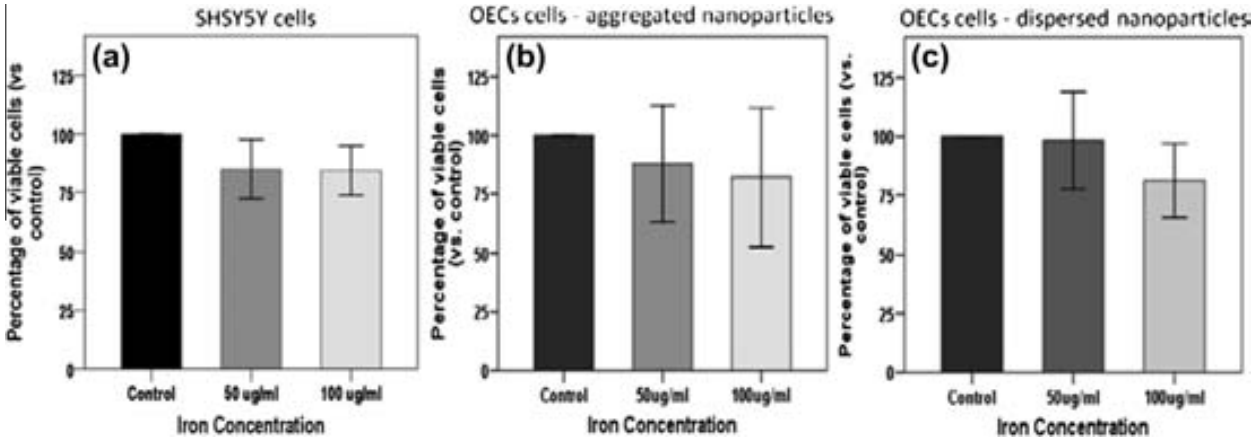

Fig. 7. Cytotoxicity tests of cells after 24 h of incubation with SPIONs. (a) SHSY5Y cells. Statistical analysis by ANOVA one-way test, $p > 0.05$, $n = 7$, analyzed by MTT test. (b) OECs treated with SPIONs in absence of extra sodium citrate (aggregated nanoparticles). Statistical analysis by ANOVA one-way test, $p > 0.05$, $n = 5$, analyzed by Muse (Millipore). (c) OECs treated with SPIONs in presence of 10 mM of extra sodium citrate (dispersed nanoparticles). Statistical analysis by ANOVA one-way test, $p > 0.05$, $n = 7$, analyzed by Muse.

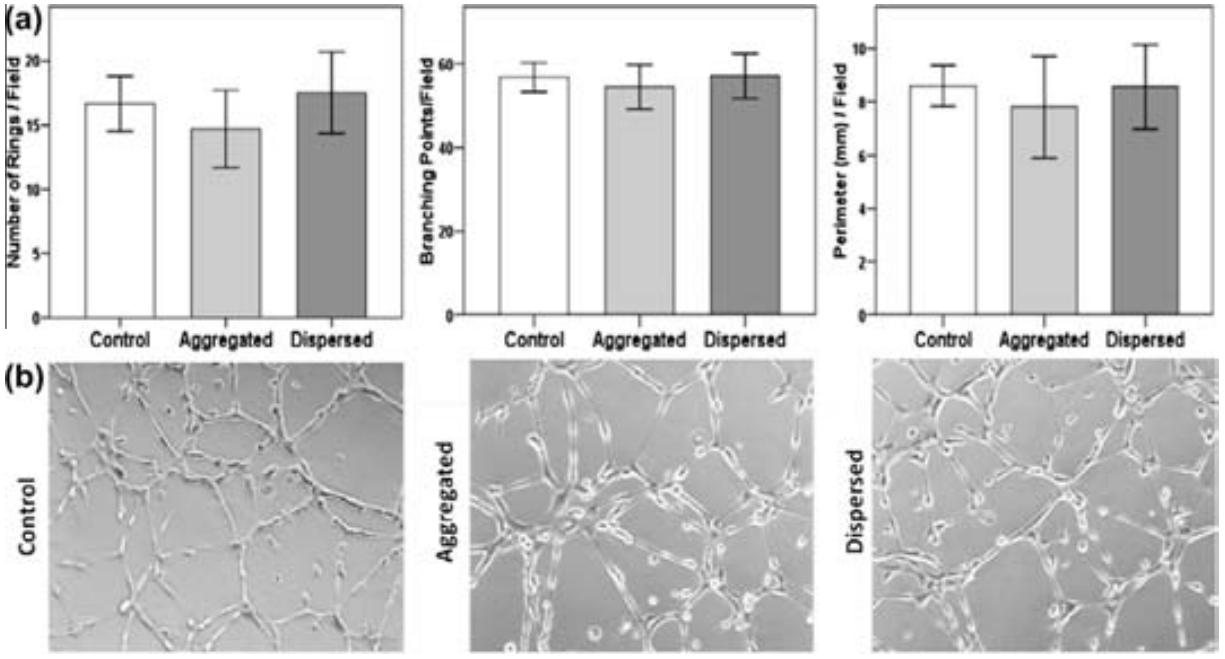

Fig. 8. A Matrigel assay with human OECs labeled or not (control) with SPIONs in the absence (aggregated particles) or presence (dispersed particles) of sodium citrate (10 mM). (a) After 24 h of tube-formation in Matrigel™, the number of structures (rings), the number of cell connections (branching points) and the extension of the vascular network (perimeter) were quantified using the automatic and blinded Wintube software. No differences were found between groups ($p > 0.05$). Independent experiments, $n = 4$ per group. (b) Representative images of each group (100×).

Please cite this article in press as: Carenza E et al. Rapid synthesis of water-dispersible superparamagnetic iron oxide nanoparticles by a microwave-assisted route for safe labeling of endothelial progenitor cells. Acta Biomater (2014), http://dx.doi.org/10.1016/j.actbio.2014.04.010

(control), cells labeled with SPIONs in the absence of extra sodium citrate (aggregated particles) and cells labeled with SPIONs in the presence of 10 mM sodium citrate (dispersed particles). Importantly, the parameters assessed in the three groups of cells were not statistically different, suggesting that particle aggregation did not have a major effect on cell functionality during the 24 h period of analysis (Fig. 8). Despite our study strongly demonstrating that NPs labeling preserves cell viability and function in vitro, we cannot discount changes in gene or protein expression patterns.

3.4. Iron cellular uptake

Hinderliter and co-workers have developed a computational model that describes the number of particles available per cell, considering the physical and chemical properties of the particles in the cell medium [34]. In a standard liquid-based cell culture, the number of particles associated with cells is a function of the delivery rate of particles to cells and how strongly the particles adhere to the cell surface. A particle's size, shape, density and surface coating influence its transport properties. The transport of particles with a diameter of less than 10 nm is controlled principally by diffusion. The transport of particles greater than 200 nm is controlled by sedimentation. Slower transport is expected to occur between 10 and 200 nm, where both diffusion and sedimentation control the transport of the nanoparticles. Moreover, Hinderliter et al. found a linear dependence between the mass of iron oxide agglomerated nanoparticles and particle uptake by RAW 264.7 macrophages.

SPIONs with an anionic coating of citrate molecules are efficiently internalized by different types of mammalian cells after a few hours of incubation at 37 °C [7]. By analyzing TEM images of cell cross-sections (Fig. 9), it was evident that cells cultured in the absence of 10 mM sodium citrate (aggregated particles) contained endosomes/lysosomes which were bigger in size and had more particles (Fig. 9a) than the endosomes in cells cultured with extra sodium citrate (dispersed particles) (Fig. 9b). Note that in both cases no particles were observed to be attached to the cell membrane, and no morphological change was evident in either of the two systems. Iron loading was determined by SQUID ($n = 3$) and ICP-AES ($n = 3$); the two techniques provided coincident values, as listed in Table 1. For cell cultures with aggregated particles, the total amount of iron per cell (~7 pg of Fe per cell) was sevenfold higher than for cells incubated with dispersed SPIONs (~1 pg of Fe per cell), as was already suggested from the Prussian blue staining images (Fig. 6). Cryo-TEM pictures of SPIONs in EBM-2–10% FBS confirm particle aggregation in branching and intertwining chains (Fig. 5). Particle clustering can affect the nanoparticle relaxation process, and thus the superparamagnetic blocking temperature, if strong inter-particle coupling exists [35]. For this reason, employing dry samples for the as-obtained nanoparticles' magnetic characterization increases the complexity of the analysis. Magnetization vs. temperature (FC–ZFC) measurements were used to monitor the magnetic properties of cells labeled with aggregated SPIONs and dispersed SPIONs. The ZFC–FC curves show very similar overall magnetic behavior of cells cultured in EBM-2–10% FBS (aggregated SPIONs) and cells cultured in EBM-2–10% FBS with extra sodium citrate (dispersed SPIONs). The sevenfold higher uptake for the aggregated nanoparticles is depicted in the values of the cell magnetization per gram of internalized iron (Fig. 10a). Note that the blocking temperature of the magnetized cells in EGM-2–10% FBS is the same (58 K) as for the initial water-borne SPIONs, while the blocking temperature of the magnetized cells in EGM-2–10% FBS with extra sodium citrate is slightly lower (33 K) (Fig. 10b). As mentioned above, this could be related to a different inter-particle coupling and size of aggregates.

From the results presented in Figs. 6 and 9, we argue that the pronounced SPIONs uptake exhibited by the cells is related to the destabilization of the initially dispersed nanoparticles and their accumulation by gravity in the vicinity of the cell membranes by greatly enhancing the internalization of nanoparticles [36]. At the same time, the sizes of such aggregates were not large enough to completely cover cells, or to attach to the cell membrane and compromise cell viability. The two systems studied here are in accord with the model proposed by Hinderliter et al. [33]. Aggregated

Table 1
Murine OECs treated with 50 μg ml^{-1} SPIONs, in the presence (dispersed) and absence (aggregated) of 10 mM sodium citrate, after 24 h of incubation.

	SQUID (pgFe/cell)	ICP (pgFe/cell)	
Control	0.03 ± 0.04	–	
$MW_{aggregated}$	8.6 ± 1.0	7.2 ± 1.2	
$MW_{dispersed}$	0.7 ± 0.2	1.1 ± 0.2	

SQUID analysis was performed at 5 K, $n = 3$. ICP analysis was also performed, $n = 3$. The right side of the table includes images of the polycarbonate capsules with dried cell pellets used for the SQUID measurements.

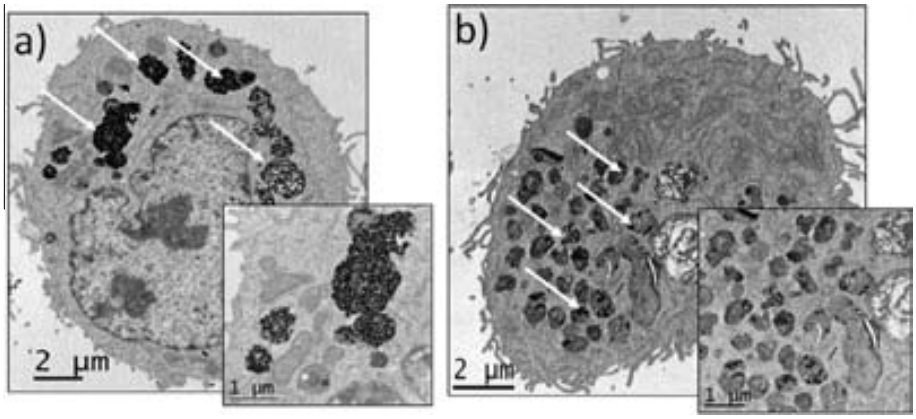

Fig. 9. (a) TEM picture of OECs treated in the absence of extra sodium citrate at a SPION concentration of 50 μg ml^{-1} after 24 h of incubation at 37 °C; (b) OECs treated in the presence of 10 mM sodium citrate at a SPION concentration of 50 μg ml^{-1} after 24 h of incubation at 37 °C. White arrows indicate endosomes containing particles. The insets show close-ups of these endosomes.

Please cite this article in press as: Carenza E et al. Rapid synthesis of water-dispersible superparamagnetic iron oxide nanoparticles by a microwave-assisted route for safe labeling of endothelial progenitor cells. Acta Biomater (2014), http://dx.doi.org/10.1016/j.actbio.2014.04.010

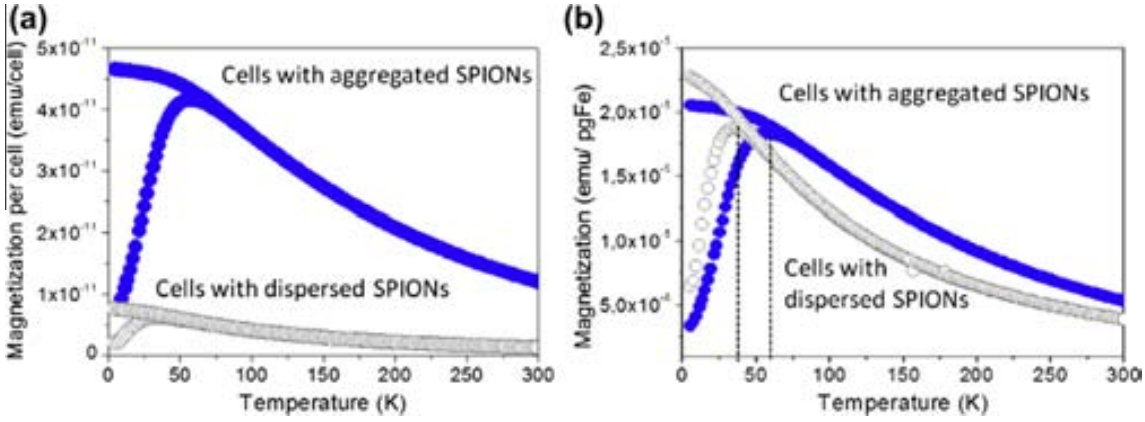

Fig. 10. ZFC–FC measurements of murine OECs treated with 50 μg ml^{-1} SPIONs. (a) Curves obtained in the presence (dispersed) and absence (aggregated) of 10 mM sodium citrate showing the magnetization per cell. The ratio between the two corresponding maximum magnetization values is above 7. (b) Curves obtained in the presence (dispersed) and absence (aggregated) of 10 mM sodium citrate showing the magnetization values per gram of iron added. In both cases particles still behave superparamagnetically, with slightly different blocking temperatures, perhaps due to a faster lysosomal degradation in the dispersed SPIONs system.

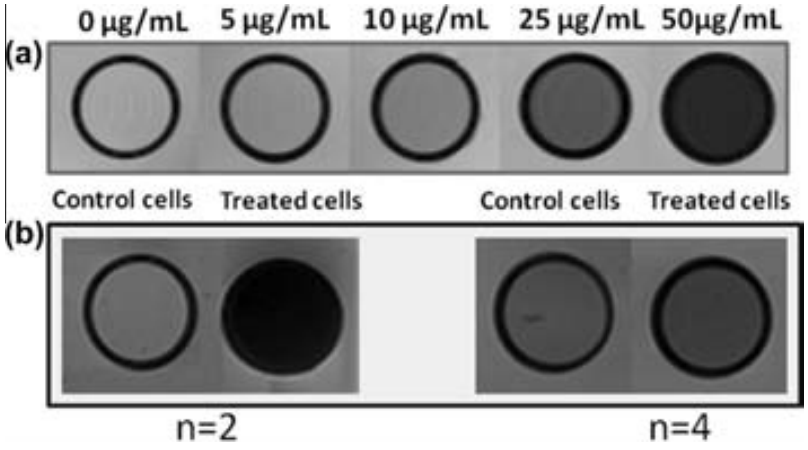

Fig. 11. (a) Agarose T2-weighted phantoms of SPIONs at different concentrations in 1.5% agarose. (b) Left: agarose T2-weighted phantoms for control cells (0 μg ml^{-1}) and cells treated with 50 μg ml^{-1} SPIONs at 37 °C for 24 h, using aggregated SPIONs in the absence of sodium citrate; right: T2-weighted phantoms for control cells (0 μg ml^{-1}) and cells treated with 50 μg ml^{-1} dispersed SPIONs, in the presence of 10 mM sodium citrate.

particles formed clusters larger than 200 nm and efficient uptake of particles was controlled by sedimentation. In the case of dispersed particles, stable aggregates of approximately 100 nm are formed and slower uptake was reported, since both diffusion and sedimentation control the transport of nanoparticles to the cells but neither process is particularly effective.

MRI is a powerful tool for tracking cells during migration, grafting and tissue proliferation after cell administration in pre-clinical studies [37]. For instance, EPCs labeled with SPIONs have been guided to specific tissues and monitored during the formation of new blood vessels [38]. We recently reported on SPION labeling of EPCs for magnetic field guidance and cellular tracking [3] in the brain. Fig. 11a includes the phantoms of agarose with water-borne SPIONs at several concentrations, where increasingly dark contrast is clearly seen as the iron concentration increases. Fig. 11b displays the agarose phantoms for the same number of labeled cells with dispersed or aggregated SPIONS. As expected, a much darker contrast image is observed for cells incubated with aggregated SPIONs. If $\Delta T_{2=}T_{2\ \text{cells}} - T_{2\ \text{cells+nanoparticles}}$, we can calculate that $\Delta T_{2\ \text{dispersed nanoparticles}} = 4$ and $\Delta T_{2\ \text{aggregated nanoparticles}} = 38$, giving a ratio of $\Delta T_{2\ \text{aggregated nanoparticles}}/\Delta T_{2\ \text{dispersed nanoparticles}}$ of 9.5, in accordance with the sevenfold increase in iron uptake by the cells when incubated with aggregated nanoparticles. This increase in the uptake could be extremely relevant when considering cell guiding applications using an external magnetic field.

4. Conclusions

Microwave-assisted nonhydrolytic sol–gel decomposition of $Fe(acac)_3$ in benzyl alcohol was used as a simple and extremely fast method to synthesize crystalline maghemite nanoparticles. Their low surface reactivity permits the addition of an electrostatic stabilizer after the particles have been synthesized. Iron oxide nanocrystals that are readily dispersible in water can be produced in the form of highly concentrated stable dispersions. Nanoparticles at iron concentrations up to 100 μg ml^{-1} were incubated for 24 h in complete cell medium. Differences in particle aggregation depending on the culture medium were observed. While in DMEM F12–10% FBS no major aggregation and sedimentation were seen, large aggregates occurred when using EGM-2–10% FBS. Control over the size of aggregates in EGM-2 complete medium was achieved by adjusting its ionic strength via citrate concentration. Comparison of the cellular uptake of identical nanoparticles in aggregated and dispersed state could be performed. The internalization of the two nanoparticle systems (dispersed and large aggre-

Please cite this article in press as: Carenza E et al. Rapid synthesis of water-dispersible superparamagnetic iron oxide nanoparticles by a microwave-assisted route for safe labeling of endothelial progenitor cells. Acta Biomater (2014), http://dx.doi.org/10.1016/j.actbio.2014.04.010

gates) in endothelial cells was investigated by TEM microscopy, and differences in size as well as in the number of cytoplasmatic vesicles were observed. Sevenfold more efficient uptake was found for systems with large nanoparticle aggregates, without compromising cell viability, cell morphology or cell functionality. We are thus presenting an example of a fast microwave synthesis of citrate-coated iron oxide nanoparticles for effective and safe endothelial progenitor cell labeling which is potentially suitable for in vivo cellular guiding and tracking.

Acknowledgements

This work was partially funded by the Spanish Government, MINECO projects MAT2012-35324 and CONSOLIDER-NANOSELECT-CSD2007-00041, and Instituto de Salud Carlos III Project PI10/00694, co-financed by the European Regional Development Fund (ERDF). A.R. is supported by the Miguel Servet program (CP09/00265) from the Instituto de Salud Carlos III. COST Action MP1202 is also kindly acknowledged.

Appendix A. Figures with essential colour discrimination

Certain figures in this article, particularly Figs. 2–6, and 10 are difficult to interpret in black and white. The full colour images can be found in the on-line version, at http://dx.doi.org/10.1016/j.actbio.2014.04.010.

References

[1] Frank JA, Miller BR, Arbab AS, Zywicke HA, Jordan EK, Lewis BK, et al. Clinically applicable labeling of mammalian and stem cells by combining superparamagnetic iron oxides and transfection agents. Radiology 2003;228(2):480–7.
[2] Chan KWY, Liu G, Song X, Kim H, Yu T, Arifin DR, et al. MRI-detectable pH nanosensors incorporated into hydrogels for in vivo sensing of transplanted-cell viability. Nat Mater 2013;12:268–75.
[3] Carenza E, Barceló V, Morancho A, Levander L, Boada C, Laromaine A, et al. In vitro angiogenic performance and in vivo brain targeting of magnetized endothelial progenitor cells for neurorepair therapies. Nanomed NBM 2014;1:225–34.
[4] Syková E, Jendelová P. Migration, fate and in vivo imaging of adult stem cells in the CNS. Cell Death Differ 2007;14:1336–42.
[5] Mailänder V, Landfester K. Interaction of nanoparticles with cells. Biomacromolecules 2009;10(9):2379–400.
[6] Petri-Fink A, Steitz B, Finka A, Salaklang J, Hofmann H. Effect of cell media on polymer coated superparamagnetic iron oxide nanoparticles (SPIONs): colloidal stability, cytotoxicity, and cellular uptake studies. Eur J Pharm Biopharm 2008;68(1):129–37.
[7] Wilhelm C, Gazeau F. Universal cell labelling with anionic magnetic nanoparticles. Biomaterials 2008;29(22):3161–74.
[8] Bilecka I, Niederberger M. Microwave chemistry for inorganic nanomaterials synthesis. Nanoscale 2010;2(8):1358–74.
[9] Kappe CO. Controlled microwave heating in modern organic synthesis. Angew Chem 2004;43(46):6250–84.
[10] Baghbanzadeh M, Carbone L, Cozzoli PD, Kappe CO. Microwave-assisted synthesis of colloidal inorganic nanocrystals. Angew Chem Int Ed 2011;50(48):11312–59.
[11] Bilecka I, Elser P, Niederberger M. Kinetic and thermodynamic aspects in the microwave-assisted synthesis of ZnO nanoparticles in benzyl alcohol. ACS Nano 2009;3(2):467–77.
[12] Hu L, Percheron A, Chaumont D, Brachais CH. Microwave-assisted one-step hydrothermal synthesis of pure iron oxide nanoparticles: magnetite, maghemite and hematite. J Sol–Gel Sci Technol 2011;60(2):198–205.
[13] Tenzer S, Docter D, Kuharev J, Musyanovych A, Fetz V, Hecht R, et al. Rapid formation of plasma protein corona critically affects nanoparticle pathophysiology. Nat Nanotechnol 2013;8(10):772–81.
[14] Mahmoudi M, Lynch I, Ejtehadi MR, Monopoli MP, Bombelli FB, Laurent S. Protein-nanoparticle interactions: opportunities and challenges. Chem Rev 2011;111(9):5610–37.
[15] Rosell A, Arai K, Lok J, He T, Guo S, Navarro M, et al. Interleukin-1beta augments angiogenic responses of murine endothelial progenitor cells in vitro. J Cereb Blood Flow Metab 2009;29(5):933–43.
[16] Navarro-Sobrino M, Rosell A, Hernandez-Guillamon M, Penalba A, Ribo M, Alvarez-Sabin J, et al. Mobilization, endothelial differentiation and functional capacity of endothelial progenitor cells after ischemic stroke. Microvasc Res 2010;80(3):317–23.
[17] Osborne EA, Atkins TM, Gilbert DA, Kauzlarich SM, Liu K, Louie AY. Rapid microwave-assisted synthesis of dextran-coated iron oxide nanoparticles for magnetic resonance imaging. Nanotechnology 2012;23(21):215602.
[18] Rao KJ, Vaidhyanathan B, Ganguli M, Ramakrishnan PA. Synthesis of inorganic solids using microwaves. Chem Mater 1999;11(4):882–95.
[19] Varma RS. Solvent-free organic syntheses. Using supported reagents and microwave irradiation. Green Chem 1999;1:43–55.
[20] Pascu O, Carenza E, Gich M, Estradé S, Peiró F, Herranz G, et al. Surface reactivity of iron oxide nanoparticles by microwave-assisted synthesis; comparison with the thermal decomposition route. J Phys Chem C 2012;116(28):15108–16.
[21] Cheng FY, Su CH, Yang YS, Yeh CS, Tsai CY, Wu CL, et al. Characterization of aqueous dispersions of Fe_3O_4 nanoparticles and their biomedical applications. Biomaterials 2005;26(7):729–38.
[22] Rosell A, Morancho A, Navarro-Sobrino M, Martínez-Saez E, Hernández-Guillamon M, et al. Factors secreted by endothelial progenitor cells enhance neurorepair responses after cerebral ischemia in mice. PLoS ONE 2013;8(9):e73244.
[23] Ke Y, Qian ZM. Brain iron metabolism: neurobiology and neurochemistry. Prog Neurobiol 2007;83(3):149–73.
[24] Xu C, Sun S. New forms of superparamagnetic nanoparticles for biomedical applications. Adv Drug Deliv Rev 2013;65(5):732–43.
[25] Park J, Joo J, Kwon SG, Jang Y, Hyeon T. Synthesis of monodisperse spherical nanocrystals. Angew Chem Int Ed 2007;46(25):4630–60.
[26] Lynch I, Cedervall T, Lundqvist M, Cabaleiro-Lago C, Linse S, Dawson KA. The nanoparticle–protein complex as a biological entity; a complex fluids and surface science challenge for the 21st century. Adv Colloid Interface Sci 2007;134–135:167–74.
[27] Aggawal P, Hall JB, McLeland CB, Dobrovolskaia MA, McNeil SE. Nanoparticle interaction with plasma proteins as it relates to particle biodistribution, biocompatibility and therapeutic efficacy. Adv Drug Deliv Rev 2009;61(6):428–37.
[28] Jansch M, Stumpf P, Graf C, Ruhl E, Muller RH. Adsorption kinetics of plasma proteins on ultrasmall superparamagnetic iron oxide (USPIO) nanoparticles. Int J Pharm 2012;428(1–2):125–33.
[29] Harris JM, Chess RB. Effect of pegylation on pharmaceuticals. Nat Rev Drug Discovery 2003;2(3):214–21.
[30] Veiseh O, Gunn JW, Zhang M. Design and fabrication of magnetic nanoparticles for targeted drug delivery and imaging. Adv Drug Deliv Rev 2010;62(3):284–304.
[31] Soenen SJ, De Meyer SF, Dresselaers T, Velde GV, Pareyn IM, Braeckmans K, et al. MRI assessment of blood outgrowth endothelial cell homing using cationic magnetoliposomes. Biomaterials 2011;32(17):4140–50.
[32] Safi M, Courtois J, Seigneuret M, Conjeaud H, Berret JF. The effects of aggregation and protein corona on the cellular internalization of iron oxide nanoparticles. Biomaterials 2011;32(35):9353–63.
[33] Pisanic TR, Blackwell JD, Shubayev VI, Finones RR, Jin S. Nanotoxicity of iron oxide nanoparticle internalization in growing neurons. Biomaterials 2007;28(16):2572–81.
[34] Hinderliter P, Minard K, Orr G, Chrisler WB, Thrall BD, Pounds JG, et al. Computational model of particle sedimentation, diffusion and target cell dosimetry for in vitro toxicity studies. Part Fibre Toxicol 2010;7(36).
[35] Jolivet JP. Metal oxide chemistry and synthesis. From solution to solid state. Chichester: John Wiley & Sons; 2000. p. 338.
[36] Safi M, Sarrouj H, Sandre O, Mignet N, Berret JF. Interactions between sub-10-nm iron and cerium oxide nanoparticles and 3T3 fibroblasts: the role of the coating and aggregation state. Nanotechnology 2010;21(14):145103.
[37] Weinstein JS, Varallyay CG, Dosa E, Gahramanov S, Hamilton B, Rooney WD, et al. Superparamagnetic iron oxide nanoparticles: diagnostic magnetic resonance imaging and potential therapeutic applications in neurooncology and central nervous system inflammatory pathologies, a review. J Cereb Blood Flow Metab 2010;30(1):15–35.
[38] Kyrtatos PG, Lehtolainen P, Junemann-Ramirez M, Garcia-Prieto A, Price AN, Martin JF, et al. Magnetic tagging increases delivery of circulating progenitors in vascular injury. JACC Cardiovasc Interv 2009;2(8):794–802.

POTENTIAL CLINICAL RELEVANCE

Nanomedicine: Nanotechnology, Biology, and Medicine
10 (2014) 225–234

Research Article

nanomedjournal.com

In vitro angiogenic performance and in vivo brain targeting of magnetized endothelial progenitor cells for neurorepair therapies

Elisa Carenza, MSc[a], Verónica Barceló[b], Anna Morancho, MSc[b], Lisa Levander, MSc[a], Cristina Boada[b], Anna Laromaine, PhD[a], Anna Roig, PhD[a,*], Joan Montaner, MD, PhD[b], Anna Rosell, PhD[b,*]

[a]*Institut de Ciència de Materials de Barcelona, Consejo Superior de Investigaciones Científicas (ICMAB-CSIC), Campus de la UAB, Bellaterra, Catalunya, Spain*
[b]*Neurovascular Research Laboratory and Neurovascular Unit, Vall d'Hebron Institut de Recerca, Hospital Universitari Vall d'Hebron, Universitat Autònoma de Barcelona, Passeig Vall d'Hebron 119-129, Barcelona, Catalunya, Spain*

Received 3 March 2013; accepted 11 June 2013

Abstract

Endothelial progenitor cells (EPCs) represent a promising approach for cell-based therapies to induce tissue repair; however, their effective delivery into the brain has remained a challenge. We loaded EPCs with superparamagnetic iron oxide nanoparticles (SPIONs), assessed their angiogenic potential and evaluated their guidance to the brain using an external magnet. SPIONs were stored in the cytoplasm within endosomes/lysosomes as observed by transmission electron microscopy (TEM) and could be visualized as hypointense signals by magnetic resonance imaging (MRI) T_2-weighted images. In vitro SPION-loaded EPCs were fully functional, forming vessel-like structures in Matrigel®, and displayed enhanced migration and secretion of growth factors (VEGF and FGF), which was associated with a moderate increase in reactive oxygen species production. Furthermore, in vivo MRI of treated mice showed accumulated hypointense signals consistent with SPION-loaded EPCs engraftment. Thus, we demonstrate that loading EPCs with SPIONs represents a safe and effective strategy for precise cell guidance into specific brain areas.

From the Clinical Editor: This study investigates the potential role of endothelial progenitor cells in neuro-repair strategies of the central nervous system using SPION-loaded EPCs and magnetic guidance to the target organ. The authors demonstrate ex vivo cellular viability and maintained function following SPION load as well as successful guidance of the EPCs to the target site via MR imaging in a murine model.

Key words: Endothelial progenitor cell; Iron oxide nanoparticle; Angiogenesis; MRI; Growth factor; Magnetic field guidance

According to the World Health Organization, stroke annually affects more than 15 million people worldwide, with 10 million dying or becoming permanently disabled. Nevertheless, only 5% of stroke patients receive thrombolytic treatment, which is the only approved therapy for the acute phase of ischemic stroke.[1] For this reason, researchers are currently investigating new treatments for potentiating neurorepair,[2,3] and it has been proposed that modulating angioneurogenic responses in peri-lesional areas could constitute a viable therapeutic strategy.[4,5]

The formation of new blood vessels was once thought to result from embryogenic vasculogenesis followed by an outbreak of endothelial cells from existing vessels.[6,7] However, this dogma was called into question upon the discovery of bone marrow-derived endothelial progenitor cells (EPCs) circulating in the blood of adult humans.[8] EPCs have been defined as non-endothelial cells that are capable of clonal expression, exhibiting stemness characteristics as well as the ability to differentiate into endothelial cells.[9] Various sub-populations have been identified, including early EPCs and outgrowth endothelial cells (OECs). These cells display in vivo vasculogenic capacity[10] and have become a new, promising model for promoting angiogenesis and endothelial regeneration.[11] Indeed, several in vitro and in vivo angiogenesis studies have confirmed the role of these EPCs as an alternative cell therapy for enhancing angiovasculogenic responses

Conflicts of interest: The authors have no conflicts of interest to declare.

Sources of support: A. Rosell is supported by the Miguel Servet program (CP09/00265) from the Spanish Ministry of Health (Instituto de Salud Carlos III) and A.L. by the Ramon y Cajal program 2010. This work has been funded by Instituto de Salud Carlos III: Grant PI10/00694 co-financed by the European Regional Development Fund (ERDF) and the stroke research network RENEVAS (RD06/0026/0010); the Spanish Ministry of Science and Innovation: EUROSALUD program, MAT2012-35324 and CONSOLIDER-Nanoselect-CSD2007-00041; and the European Commission FP7-People-2011-CIG 303630 project.

*Corresponding authors: Anna Rosell is to be contacted at Neurovascular Research Laboratory, Vall d'Hebron Institut de Recerca, Passeig Vall d'Herbon 119-129, 08035 Barcelona, Spain. Anna Roig, Institut de Ciència de Materials de Barcelona, Campus de la UAB, 08193 Bellaterra, Catalunya, Spain.

E-mail addresses: roig@icmab.es (A. Roig), anna.rosell@vhir.org (A. Rosell).

1549-9634/$ – see front matter
http://dx.doi.org/10.1016/j.nano.2013.06.005

after myocardial,[12] hindlimb,[13,14] or cerebral ischemia.[15,16] Moreover, it has been proposed that EPCs can influence angiogenesis through paracrine secretion of growth factors, such as VEGF[17] or cytokines.[18]

Cell-based therapies are becoming a reality. Therefore, control of the guidance, delivery and engraftment of stem cells into target tissues is crucial for the success of these treatments. So far, several preclinical studies have reported positive results with local administration of EPCs into the perilesional tissue.[19–21] However, local administration of EPCs in the areas of interest after brain injury remains complex in humans because of the risks and side effects associated with intraparenchymal delivery, such as bleeding and tissue injury. In fact, we have learned from animal models that although intra-arterial infusion can guarantee optimal delivery of cells to the brain, this technique increases mortality rates (up to 41%) following cell transplantation due to artery embolization.[22] Moreover, it has been suggested that the low efficacy associated with intravenous injection might be related to major obstacles, such as the pulmonary filter.[23,24] Specifically, it has been estimated that <0.5% of administered cells reach the arterial system after intravenous administration[24] and that only 0.0005% of intravenously administered mesenchymal stem cells reached the brain in an animal model of traumatic brain injury.[25] Therefore, the development of improved methods for delivery of functional EPCs to target areas is an important prerequisite for effective cell therapy treatments.

Recently, magnetic nanoparticle cell labeling was used to monitor and image stem cell engraftment.[26,27] This technique has also been employed to magnetically guide stem cell delivery for therapy of spinal cord injury[28] and after in situ intra-arterial EPC administration for treatment of vascular injury of the common carotid artery.[29] However, in the latter study, the authors suggested that less aggressive forms of administration, such as intravenous delivery, should be considered when translating their findings into clinical practice. Finally, other recent studies used anionic magnetic nanoparticle-loaded EPCs to successfully control the formation of vascular networks in vitro and in vivo using subcutaneously implanted Matrigel® plugs.[30] However, to the best of our knowledge, EPCs have never been magnetically guided into brain tissue.

In the present study, we labeled EPCs with superparamagnetic iron oxide nanoparticles (SPIONs), which are Food and Drug Administration (FDA) approved, and demonstrated that magnetized EPCs maintained their ability to form vessel-like structures. Strikingly, they also displayed enhanced migration and paracrine angiovasculogenic potential through increased production of vascular endothelial growth factor (VEGF) and fibroblast growth factor (FGF). We propose that this strategy can be used along with a local magnetic field to guide delivery of EPCs to specific areas of the brain in order to potentiate angiogenesis for efficient neurorepair.

Methods

Synthesis of the SPIONs in organic solvent and ligand transfer to aqueous dispersions

Synthesis of the SPIONs was adapted from a previous procedure of thermal decomposition of an iron precursor in organic media using oleic acid and oleylamine as surfactants.[31] Detailed information can be found in the Supplementary Materials. The final material consisted of a stable colloidal nanoparticle dispersion at pH 7.5. A typical batch was made up of 50-nm SPION aggregates, as determined by dynamic light scattering (DLS), and −40-mV *Z*-potential values.

Transmission electron microscopy (TEM)

SPIONs were examined using a JEOL1210 TEM microscope operating at 120 kV. Nanoparticle size distribution was monitored by analyzing images of 750 particles from the same sample. Early mouse EPCs and OECs were also visualized and analyzed using a JEM-2011 TEM microscope operating at 200 kV. Detailed protocols can be found in the Supplementary Materials.

Endothelial progenitor cell culture

Early EPCs and OECs isolated from mice, as well as human OECs from stroke patients, were obtained as previously described.[32,33] All procedures were approved by the ethics committee and the animal committee of our institution according to the Declaration of Helsinki. Detailed information can be found in the Supplementary Materials.

Cellular magnetization and viability

EPCs were magnetized with SPIONs as follows: 25, 50, or 100 μg/mL of iron was added to growing early EPCs or OECs in EGM-2 media for 2, 6, or 24 h. Control EPCs were grown in parallel. In addition, 3-(4,5-dimethylthiazol-2-yl)-2,5-diphenyltetrazolium bromide (MTT) reduction was measured to determine cell viability of EPCs and OECs. Additional experiments were performed to assess any potential effects of the vehicle solution using volumes that corresponded to the experimental concentrations, as well as to control for the presence of the magnetic field. Details can be found in the Supplementary Materials.

Determination of iron content

Magnetization vs. applied field at 298 and 5 K was performed with a superconducting quantum interference device (SQUID). Intracellular iron content of the EPCs was determined using the ratio between the remanent magnetization value at 5 K of a known number of magnetized cells and a known mass of SPIONs as described in the Supplementary Materials.

Magnetic resonance imaging (MRI) relaxometry

MRI of phantoms containing SPIONs or magnetized EPCs was performed using a quadrature 7.2-cm inner diameter volume coil on a 7-T magnet (BioSpec 70/30 USR, Bruker BioSpin, Ettlingen, Germany) according to the protocols described in the Supplementary Materials.

In vitro tubulogenesis assay

Matrigel® (reduced growth factors, BD; San Jose, CA, USA) was used as a substrate for assessing the tube formation capacity of mouse and human OECs as previously described.[33] Vessel-like structures were formed, and the number of complete rings,

number of joints, and vessel perimeters were counted for each treatment using imageJ software by blinded personnel.

Migration assay

To evaluate the migration of mouse control and magnetized OECs (labeled with 50 μg/mL of SPIONs), FluoroBlock™ (BD, France) transwell inserts were used in two sets of experiments. In the first set, three conditions were analyzed: control cells, magnetized cells, and magnetized cells in the presence of a magnetic field, consisting of an iron–neodymium–boron (FeNdB) magnet with circular shape (15 × 5 mm) placed at the bottom of the well. In the second set, either control OECs or control OECs in the presence of the magnetic field were assayed to test the effects of the magnetic field on control cells. Following incubation, the cells were imaged and the percentage of cells per field was calculated using ImageJ software. A detailed protocol is described in the Supplementary Materials.

Multiplex protein analysis

Secretion of growth factors from magnetized and non-magnetized mouse and human OECs was assessed. A Search-Light® multiplex protein array was performed to measure the level of platelet-derived growth factor (PDGF-bb), hepatocyte growth factor (HGF), FGF-b, and VEGF in EPC-conditioned media as described in Supplementary Materials.

Western blotting

To verify our findings regarding growth factor secretion, Western blot analysis of VEGF and FGF in human OEC-conditioned media was performed. The complete protocol can be found in the Supplementary Materials.

Reactive oxygen species (ROS) detection assay

ROS generation in magnetized OECs was measured using a ROS assay kit (Abcam, UK, ab113851), which uses a cell-permeant fluorogenic dye (2′,7′-dichlorofluorescein diacetate; DCFDA) to measure hydroxyl, peroxyl, and other ROS activity within cells. A detailed protocol is described in the Supplementary Materials.

In vivo magnetic cell targeting and MRI

Mice were anesthetized with isoflurane (4% induction, 1.5% maintenance) and two small permanent FeNdB magnets (3 × 4 × 2 mm) with a magnetic field of 0.3 T were implanted with glue in the left hemisphere. Afterwards, 3.5×10^4 early EPCs isolated from mice, which were previously magnetized using 50 μg/mL of SPIONs, were injected intravenously (tail vein; in 150 μL of phosphate buffered saline [PBS]). Control animals received an identical cell infusion without magnet implantation. Magnets were removed 24 h later, and MRI was carried out at 7 T in a horizontal magnet (BioSpec 70/30 USR, Bruker BioSpin, Ettlingen, Germany) following standard protocols, as described in the Supplementary Materials.

Statistical analyses

SPSS 15.0 was used for all statistical analyses. The Shapiro–Wilk test was used to check Gaussian distribution of the data. Statistical significance of the intergroup differences was assessed using Student's *t*-test or ANOVA followed by the Tukey's post hoc test. Non-parametric data were analyzed using the Kruskal–Wallis test followed by the Mann–Whitney test. Moreover, Bonferroni's correction was applied to account for multiple testing. A P-value <0.05 was considered statistically significant at the 95% confidence level. All values are expressed as mean ± standard deviation (SD) and represented as bar graphs. The number of independent experiments analyzed is stated in each figure legend or table footnote.

Results

SPION characterization

SPIONs were synthesized through thermal decomposition reactions of iron acetylacetonate [$Fe(acac)_3$] to yield nanoparticles, which were stabilized in hexane. SPIONs were found to display an average diameter of 6 nm and a polydispersity of 20% (Figure 1, *A*). Moreover, a redox titration procedure was used to determine the presence of Fe^{+3} and Fe^{+2} ions (85% and 15%, respectively), revealing a mixed composition of Fe_3O_4 and γ-Fe_2O_3. Following synthesis, the SPIONs were transferred to water using tetramethylammonium hydroxide (TMAOH) as an electrostatic stabilizer and the pH was lowered to 7.5 using 0.01 M HNO_3. A typical batch of SPIONs used for cell magnetization had an iron concentration of 0.50 mg/mL as measured by redox titration and a zeta potential of −40 mV. Moreover, the dispersions were stable for >2 months without any noticeable precipitation.

CryoTEM analysis of SPIONs in water at pH 7.5 showed nanoparticle aggregates of dendritic shape with an average length of ~60 nm (Figure 1, *B*). The hydrodynamic size of the aggregates was also measured by DLS, and revealed a mean diameter of 50 nm and a polydispersity of 30% (Figure 1, *C*). Also, magnetization vs. magnetic field measurements were performed at 5 K and at room temperature using a SQUID magnetometer (Figure 1, *D*). The absence of coercivity and remanence at room temperature confirmed the superparamagnetic character of the nanoparticles, and the saturation magnetization at 298 K was found to be 54 emu/g. At 5 K the particles behaved as ferrimagnets as revealed by the hysteresis loop, M(H), showing coercivity field and remnant magnetization (insert of Figure 1, *D*). Furthermore, we determined the intracellular iron content by comparing the remnant magnetization value of the magnetized cells and the nanoparticles at 5 K.

Co-incubation of SPIONs permits EPC magnetization

We next labeled EPCs with SPIONs via co-incubation. The presence of intracellular iron could be confirmed by Prussian blue staining (Supplementary Figure 1). Accordingly, quantification of intracellular iron content by magnetometry demonstrated that the amount of iron increased with longer incubation times for early EPCs isolated from mice: 7.7 ± 1.7 pg/cell at 2 h, 10.7 ± 2.9 pg/cell at 6 h, and 24.7 ± 3.4 pg/cell at 24 h (see Supplementary Table 1). These differences were statistically significant between 2 and 24 h ($P = 0.003$) and 6 and 24 h ($P =$

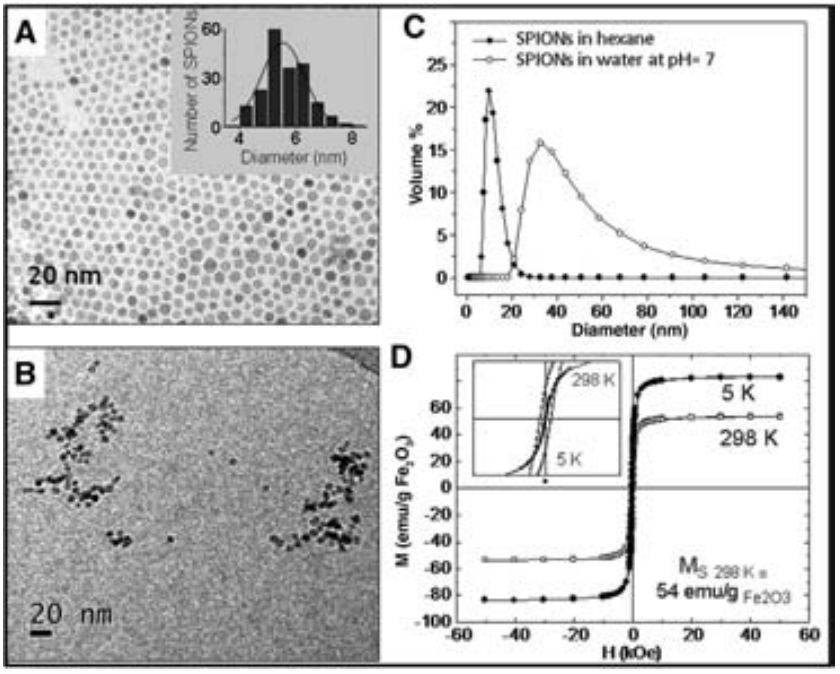

Figure 1. SPIONs characterization. **(A)** TEM image of SPIONs in hexane; the insert shows the particle size distribution histogram adjusted to a Gaussian function. **(B)** Cryo-TEM of SPIONs aggregates in water (pH 7.5). **(C)** DLS measurements of SPIONs in hexane and after transfer in water (pH 7.5). **(D)** M(H) curves for SPIONs at 298 K and 5 K. The insert shows a low field magnification where the lack of coercivity and remanence is evidenced at 298 K and values different from zero are evidenced at 5 K.

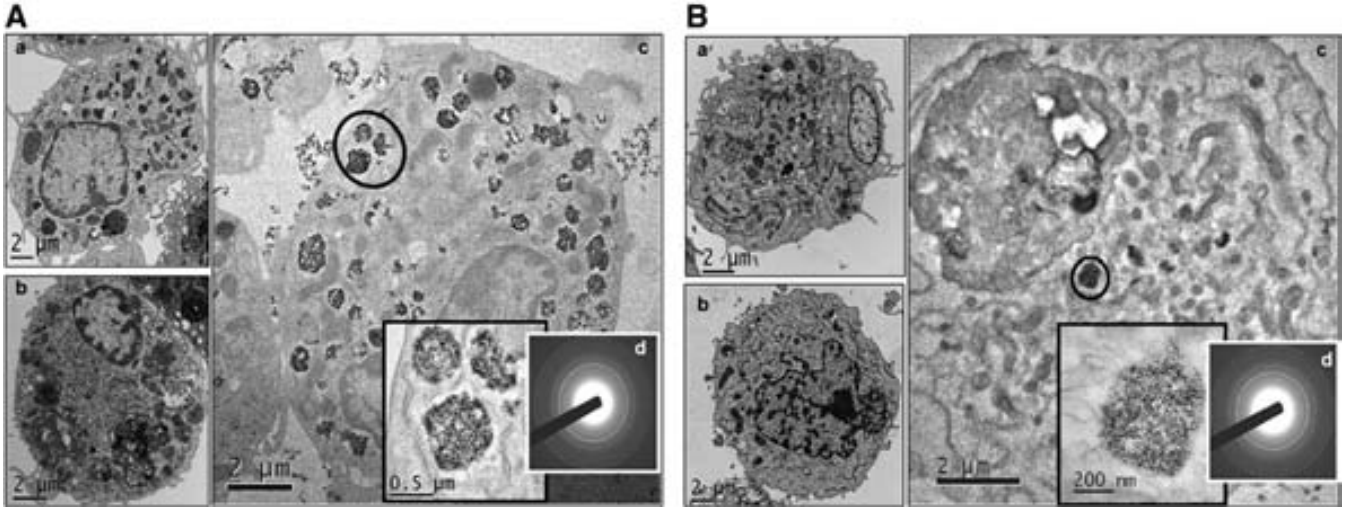

Figure 2. TEM imaging. Panel showing early mouse EPCs **(A)** and outgrowth of mouse EPCs **(B)**: **(a)** TEM image of a magnetized EPC (SPIONs 50 μg/mL, 24 h); **(b)** TEM image of a control EPC; **(c)** TEM image with enhanced contrast between organic and inorganic material of a magnetized EPC; **(d)** electron diffraction analysis of selected intracellular compartments identified as endosomes (circle) corresponding to the γ-Fe_2O_3 phase.

0.001), but not between 2 and 6 h ($P = 0.730$). Regarding outgrowth, the amount of intracellular iron at 24 h was significantly lower when compared to the amount initially internalized by early EPCs isolated from mice (0.93 ± 0.05 pg/cell vs. 24.7 ± 3.4 pg/cell, respectively; $P = 0.04$), whereas the amount of iron in non-magnetized outgrowth EPCs was 0.05 pg Fe/cell (Supplementary Table 1). In addition, the estimated amount of nanoparticles per cell after 24 h incubation was $5.3 \times 10^7 \pm 8 \times 10^6$ SPIONs/EPC and $2.5 \times 10^6 \pm 1 \times 10^5$ SPIONs/OEC.

Magnetic guidance following cell magnetization for 24 h was tested in vitro by applying a magnetic field near a pellet of mouse EPCs. The magnetized EPCs were rapidly guided toward the magnet and remained there until the magnet was removed (Supplementary Figure 2).

TEM demonstrated that cellular uptake of SPIONs occurred through plasmatic membrane invagination and that SPIONs were subsequently localized in endosomes within the cytoplasm of EPCs (Figure 2). Furthermore, TEM revealed a greater number of SPION-containing endosomes in early EPCs compared to

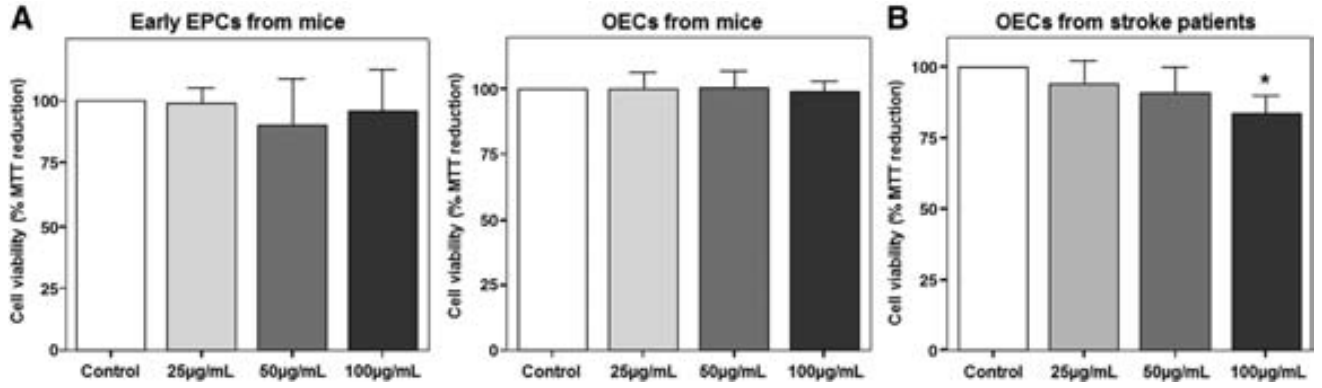

Figure 3. Cell viability determined by MTT assay after SPION-labeled cells. **(A)** Bar graphs represent cell viability for mouse early EPCs (n = 4/7) and mouse OECs (n = 3/10 per treatment). **(B)** Bar graphs represent cell viability for OECs from stroke patients (n = 5/7). Results are expressed as mean ± SD; *P = 0.012.

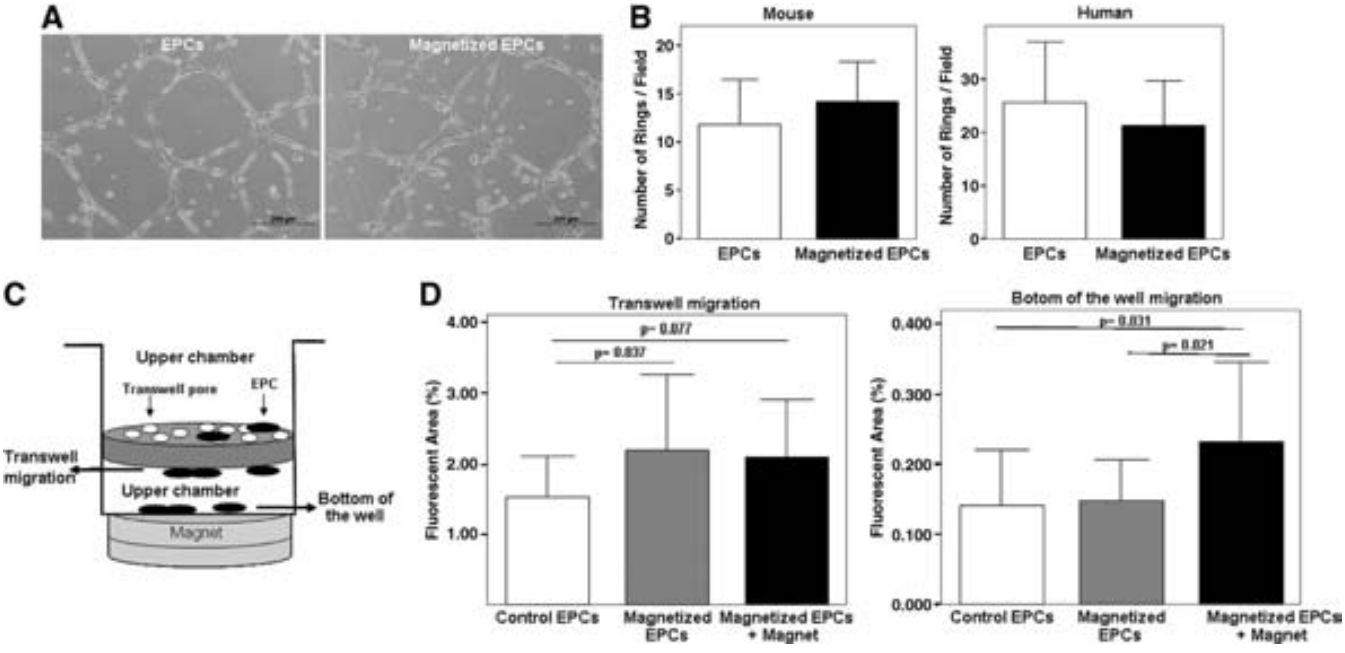

Figure 4. Tubulogenesis and migration of EPCs (OECs). **(A)** Photomicrographs showing tube-like structures shaped by mouse EPCs and magnetized EPCs with 50 µg/mL. **(B)** Bar graphs (mean ± SD) represent the number of rings in mouse (n = 6) and human (n = 4) EPCs in magnetized and non-magnetized cells; differences were not statistically different. **(C)** Schematic cartoon showing the transwell assay and areas of quantification. **(D)** Bar graphs showing percentage of fluorescent cells per field migrated through the transwell membrane (n = 15) or to the bottom of the well (n = 10).

OECs (as shown in Figure 2, *A* and *B*, respectively), which correlated with the results from magnetometry (Supplementary Table 1). In both cell types, diffraction patterns obtained from selected endosomes confirmed the presence of an iron oxide inverse spinel phase (Figure 2, *A* and *B*). Moreover, the cytoplasmic localization of SPIONs was consistent with the iron localization observed by standard Prussian blue staining (Supplementary Figure 1).

EPC viability

MTT assays indicated that co-incubation of SPIONs with mouse early EPCs or OECs did not affect cell viability at any of the tested concentrations (Figure 3, *A*). However, a slight decrease in cell viability was observed for OECs obtained from stroke patients (83.6% ± 6.3%; $P < 0.05$) in comparison to non-treated cells (Figure 3, *B*). Also, treatment with the SPION vehicle solution resulted in reduced viability of OECs from stroke patients (86.6% ± 7.7%; $P < 0.05$). Additional experiments performed to evaluate the safety of the magnetic field indicated that it had no effect on the cell viability of control and magnetized OECs (Supplementary Figure 3).

Magnetized EPCs preserve their tube formation abilities

In vitro angiogenesis assays demonstrated that magnetized EPCs maintained the ability to form tubes (Figure 4, *A*). Indeed, our results indicated that magnetized EPCs isolated from mice (OEC population) formed vessel-like structures similar to control cells in the Matrigel® matrix. In fact, when we quantified tubulogenesis, we found that the number of complete rings (14.1 ± 4.1 vs. 11.8 ± 4.5), number of cell junctions (19.8 ± 5.1

Table 1
Quantification of growth factors' secreted by outgrowth EPCs (OECs).

Growth factor	Mouse		Human	
	Control OECs	Magnetized OECs	Control OECs	Magnetized OECs
FGF basic	17.33 ± 1.87	23.23 ± 12.02	16.26 ± 4.48	25.60 ± 3.6
VEGF	0.27 ± 0.02	3.23 ± 2.34	10.08 ± 5.33	16.30 ± 4.64
HGF	0.50 ± 0.10	0.48 ± 0.19	n.d.	n.d.
PDGF-bb	n.d.	n.d.	n.d.	n.d.

Mouse and human controls, and their corresponding magnetized OECs, were cultured for 24 h to collect conditioned media. A four-plex protein array was used to measure growth factors content of independent experiments (n = 2-3 per group). Values are corrected by the total protein amount (pg of growth factor/μg protein) and expressed as mean ± SD.
PDGF-bb, platelet-derived growth factor; HGF, hepatocyte growth factor; FGF-b, fibroblast growth factor; VEGF, vascular endothelial growth factor; n.d., non-detected.

vs. 16.5 ± 3.6), and vascular perimeters (7 ± 2.5 mm vs. 6.1 ± 2.6 mm) were not significantly different for magnetized EPCs and control EPCs, respectively (Figure 4, *B*). Moreover, human EPCs from stroke patients preserved their tube formation properties after magnetization. Although the assessed parameters were slightly lower for magnetized cells, once again no significant difference was observed (25.5 ± 11.4 vs. 21.2 ± 8.4 for rings, 29.8 ± 11.9 vs. 22.2 ± 5.7 for cell junctions, and 9.3 ± 3.3 mm vs. 7.6 ± 1.8 mm for vascular perimeter; magnetized EPCs and control EPCs, respectively) (Figure 4, *B*).

Increased migration following magnetization is enhanced in the presence of a magnetic field

Transwell migration assays indicated that magnetized EPCs (OEC population) displayed enhanced migration. In fact, at 48 h, the percentage of cells found in the lower part of the transwell insert (Figure 4, *C* shows findings for magnetized cells when a magnet was placed under the plate) was higher for each of the magnetized cell groups compared to control cells (2.19 ± 1.00 and 2.09 ± 0.83 vs. 1.52 ± 0.58; $P = 0.037$ and $P = 0.077$, respectively) (Figure 4, *D*). However, no difference in migration through the membrane was observed between the cell populations in the presence of the magnetic field. In contrast, once cells had crossed the membrane insert, magnetized EPCs migrated more efficiently to the bottom of the well (Figure 4, *C*) in the presence of the magnetic field compared to magnetized cells only or control cells (0.23 ± 0.11 vs. 0.14 ± 0.05 and 0.14 ± 0.07; $P = 0.021$ and $P = 0.031$ respectively) (Figure 4, *D*). Representative images of the data from the transwell migration assay are shown in Supplementary Figure 4A. No difference was observed between the groups at 6 and 24 h (data not shown). Moreover, additional experiments to assess the influence of the magnetic field on control mouse EPCs indicated that migration was unaltered (Supplementary Figure 4B).

Enhanced growth factor secretion following magnetization

As shown in Table 1, magnetized human and mouse EPCs (OECs population) secreted more VEGF and FGF than control cells. Notably, magnetized mouse EPCs displayed up to a 10-fold increase in VEGF secretion. In contrast, similar amounts of HGF were secreted by magnetized and control mouse EPCs, and we were unable to detect PDGF in our assay. Also, we confirmed that magnetized OECs from human subjects secreted increased VEGF and FGF protein using western blotting (Supplementary Figure 5).

ROS levels are increased in magnetized EPCs

Following magnetization of cells with SPIONs, increased cellular ROS was observed (41% increase; $P < 0.001$) in comparison to control cells at 24 h (Supplementary Figure 6). Importantly, this increase in ROS occurred without affecting cell viability (Figure 3, *A*). However, enhanced ROS production in magnetized cells was considered to be moderate because treatment with antimycin, an inhibitor of the electron transport and well-known oxidative stress generator, further increased ROS levels in both control (176% increase; $P < 0.001$) and magnetized cells (223% increase; $P < 0.001$) (Supplementary Figure 6).

Relaxation properties of the SPIONs and magnetized EPCs

Our findings indicated that synthesized SPIONs had excellent T_2 relaxation properties. In this regard, the longitudinal (r1) and transverse (r2) relaxivities at 7 T were found to be 1.6 mM^{-1} s^{-1} and 93 mM^{-1} s^{-1}, respectively, and relaxivity for r2* was found to be 129 mM^{-1} s^{-1}, as obtained from the plots shown in Supplementary Figure 7. Moreover, the T_2 value was reduced in an iron-dependent manner in the agarose phantoms visualized as dark signals in T_2-weighted images (T2W) (Figure 5, *A* and *B*). In addition, cells loaded with SPIONs were visualized in T2W images. Phantoms prepared with suspensions of magnetized EPCs showed a clear signal decrease in a cell-concentration dependent manner, becoming visible (dark signal) at dilutions as low as 1.3×10^4 cells/mL, while remaining invisible with non-magnetized EPCs (Figure 5, *C*). Moreover, T_2 map quantifications showed clear signal decay at increased concentrations of magnetized EPCs compared to non-magnetized cells (see Supplementary Figure 8).

In vivo cell tracking and local guidance

As expected, magnetized EPCs were successfully guided to cortical areas of the brain under the influence of the magnetic gradient created by the implanted magnet (Figure 5, *D*). In fact, T2W images in MRI confirmed the accumulation of hypointense signals in the most external cortical layers close to the magnetic field; however, we did not observe these signals in other brain areas or in the absence of magnet implantation (Figure 5, *E* and *F*). Moreover, we used Prussian blue staining of brain slices to

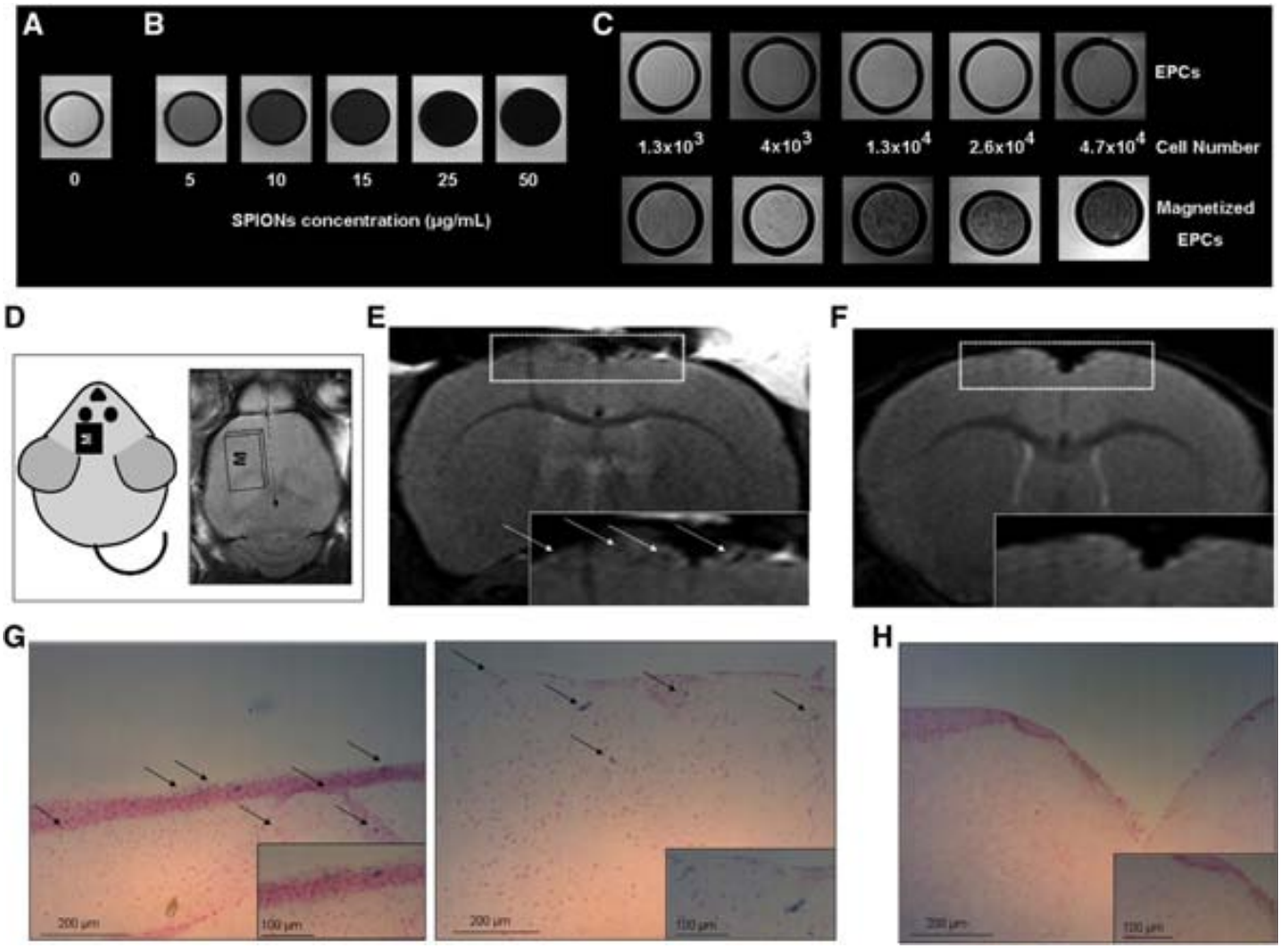

Figure 5. T_2-weighted MR phantom images and in vivo brain cell tracking. **(A)** Agarose control. **(B)** Iron-dependent concentration of SPIONs. **(C)** Phantom images of early mouse EPCs (top) and magnetized EPCs (bottom). Note that magnetized cells can be detected as hypointense signals (dots). **(D)** Schematic cartoon showing the magnet position on a mouse brain and coronal section of a T2W image showing the exact position of magnet implantation. **(E** and **F)** T2W brain images corresponding to mice injected with 3.5×10^4 magnetized early EPCs with **(E)** or without **(F)** magnet implantation. The inserts show areas under the influence of the magnetic field or corresponding area. Prussian Blue staining identified magnetized EPCs in the brain cortex under the influence of the magnetic field **(G)** but not in brains not exposed to the magnetic field **(H)**.

confirm that the hypointense signals observed by MRI indeed corresponded to the presence of the administered EPCs. The presence of blue cells, which were presumed to be our injected EPCs, was confirmed in matching cortical areas (Figure 5, *G*) but was not observed in brains of mice without magnet implantation (Figure 5, *H*). Importantly, magnet implantation at the surface of the skull along with injection of magnetized EPCs seemed to be safe as animals survived throughout the study period (24 h). Additionally, no major sign of tissue injury was observed in vivo by MRI or ex vivo in the brain tissue. The total amount of iron injected with the magnetized cells was approximately 1 μg based on the amount of iron loaded in each early EPC (Supplementary Table 1).

Discussion

In the present study, we demonstrated that the magnetization of EPCs using an aqueous colloidal suspension of SPIONs is safe. In addition, we showed that magnetized OECs from stroke patients retained their ability to form tubes. Strikingly, these SPION-loaded OECs also displayed enhanced migration and secretion of growth factors, such as VEGF and FGF, which was associated with a moderate increase in ROS production. Finally, after intravenous administration of magnetized EPCs, the cells could be tracked in vivo through MRI and safely guided to specific brain areas by applying an external magnetic field. The fact that these findings have been obtained with human cells from stroke patients is of high interest because it suggests that autologous cell transplantation could be possible.

The success of future repair therapies based on the angiovasculogenic potential of EPCs is dependent on the development of methods that allow effective delivery, arrival, engraftment, and trophic support in target tissues. Here, we showed that EPCs could be safely magnetized with SPIONs and that intracellular iron content could be controlled depending on incubation time. Other authors have noted similar changes in iron

load of cord blood derived EPCs when exploring shorter incubation times and similar concentrations of iron.[34] We also observed by TEM that synthesized SPIONs were internalized into the cytoplasm of EPCs within endosomes/lysosomes and were accumulated as nanoparticle clusters, as described elsewhere.[30,35] Interestingly, our study reports for the first time that iron load was larger (about 20-fold) in the early EPC population compared to OECs under the same experimental conditions. These data are particularly relevant for cell magnetic targeting since differences in iron loads can lead to distinct responses when cells are exposed to magnetic fields. Therefore, our data suggest that protocols should be adjusted to achieve efficient magnetic targeting for each cell subtype.

In the field of magnetic cell targeting, other authors have successfully demonstrated that bone marrow stromal cells and $CD133^+$ cells could be guided into specific areas to promote axonal growth in in vivo models of spinal cord injury.[36,37] These studies used an FeNdB magnet to guide magnetically loaded cells to specific sites to enhance spinal cord repair and ultimately improve motor function. In the brain, the use of this technique along with focused ultrasounds has already demonstrated that magnetic targeting synergistically delivers therapeutic nanoparticles across the blood–brain barrier and into specific areas of normal or tumor-containing brains.[38] In fact, Chertok et al[39] have recently demonstrated that intravenously administered magnetic nanoparticles could be guided under the local effect of a magnetic field to brain tumors, inducing changes in the vessel architecture. More recently, neural stem cells were for the first time magnetically targeted into brains in a rat model of cerebral ischemia, and it was shown that ferumoxide-labeled human neural stem cells showed enhanced migration in the presence of a magnetic field.[40] Also, it was reported that under the influence of an external magnetic field, EPCs migrated within subcutaneous implanted Matrigel® plugs.[30] Furthermore, intra-arterial administration of EPCs in the common carotid artery led to a fivefold increase in the number of EPCs in the arterial wall.[29] However, to the best of our knowledge, EPCs have never been magnetically guided into brain tissue. Our results prove that after appropriate magnetization, EPCs can be guided to precise cortical areas of the brain after intravenous administration of relatively low amounts of cells, which could be successfully tracked by MRI. In the context of ischemia, we might expect better engraftment into tissue due to increased blood–brain barrier permeability, although future preclinical studies in animal models of stroke will be needed to determine the efficacy of EPC engraftment in diseased brains. Our results are of enormous importance since they indicate that magnetic targeting of stem cells for enhancing angiogenesis following stroke or traumatic brain injury is possible.

Although further studies are needed to demonstrate that enhanced angiogenesis occurs after EPC engraftment, our results indicated that no animal death or brain hemorrhage occurred following administration of magnetized EPCs. It is important to note that the total amount of cell-loaded iron (1 μg) for the in vivo experiments was about 15 times below the amount of iron typically administered as a contrast agent for MRI studies, which have an advised dose of 0.56 mg/kg for Feridex®.[41] When translating these values to humans, the amount of iron administered to a 70-kg human would be 39 mg, which indicates that 1.4×10^9 cells could be safely injected. Moreover, due to the acidic environment of endosomes, particles should be partially digested inside the cells after a few days. They would be subsequently re-absorbed and mineralized as ferrihydrite, which is stored within ferritin cages. All particles released by the EPCs before completion of this digestion process should be cleared through the liver and kidney in a similar manner to clinically used contrast agents. However, caution must be taken when translating our results to preclinical animal models. In this regard, potential interactions of SPIONs with organ function and systemic iron levels need to be monitored after cell administration.

Importantly, after cell magnetization with SPIONs, EPCs preserve their angiovasculogenic abilities, forming vessel-like structures in vitro. This again indicates the safety of magnetic loading of EPCs. In contrast, migration assays indicate that magnetized EPCs display enhanced endogenous migration capacity compared to control cells. Moreover, in the presence of a magnetic field, they migrated toward areas with larger magnetic field gradients. We believe that migration toward the lower chamber is clearly influenced by cell magnetization and that magnetic forces guide them toward the bottom of the plate.

Considering the in vivo setting, we can hypothesize that circulating magnetized EPCs would be retained in the blood vessel wall near the magnetic forces and then display enhanced migration abilities within the local region. Notably, other authors have reported that loading EPCs with various types of iron oxide nanoparticles does not affect in vitro tube formation of EPCs[30] or proliferation capacity.[42,43] Regarding cell migration, Yang et al.[43] have reported impaired ability of rat and swine EPCs when magnetized with 50 μg/mL of Resovist®, but not at 200 or 400 μg/mL. These results suggest that SPIONs clearly have the potential to modulate the angiogenic responses of EPCs depending on the iron load or nanoparticle type and that these interactions must be carefully studied to evaluate the efficacy of different cell magnetization protocols.

Furthermore, we have demonstrated that the pro-angiogenic paracrine actions of EPCs were enhanced through analysis of their ability to secrete growth factors. We observed that magnetized EPCs not only preserved their paracrine potential but also displayed enhanced secretion of VEGF and FGF. This result is of paramount importance when evaluating this technology for clinical translation. The fact that secretion of other growth factors, such as HGF and PDGF, was not altered suggests that there is preferential activation of specific pathways, which remain to be identified. In this regard, other authors have recently reported that labeling of human mesenchymal stem cells (hMSCs) with ferucarbotran could induce epidermal growth factor receptor (EGFR) overexpression, which contributed to the antitumor capacity of ferucarbotran-labeled hMSCs in a colon cancer model.[44] Additionally, other reports have described that low levels of ROS might function as signaling molecules to modulate angiogenesis.[45] In the present study, we showed that SPIONs induced ROS generation in mouse EPCs without affecting cell viability. Moreover, we found that the production of ROS by the magnetized cells was moderate since antimycin, an oxidative stress inducer, could increase the amount of ROS

produced by magnetized and non-magnetized cells. Consistent with our findings, it has been described that oxidative stress occurs when endothelial cells are exposed to iron oxide nanoparticles[46] and that ROS-dependent up-regulation of VEGF occurs in heart endothelial cells exposed to moderate levels of H_2O_2.[47] Also, it is known that there is a link between VEGF and endothelial cell migration.[48]

In conclusion, our results indicate that EPCs magnetized with SPIONs can enhance angiogenic performance through increased migration and paracrine secretion of growth factors, and that intravenously delivered EPCs can be guided to specific areas of the brain cortex by implanting an external magnet. These results offer exciting new possibilities for numerous cell-based treatments that could potentiate neurorepair in specific brain areas via non-invasive approaches. Future studies should be directed at understanding the paracrine angiogenic balance between promoters and inhibitors after EPC magnetization and determining growth factor secretion patterns according to SPION type, including time–response and dose–response effects. Moreover, our results support the need for further studies in animal models of cerebral ischemia to examine the engraftment potential of magnetized EPCs and whether angiogenesis is enhanced in the target tissue under the influence of the magnetic field in comparison to standard EPCs. Such experiments could confirm if magnetic cell delivery therapies have the potential to improve cell guidance, cell tracking, and pro-angiogenic stimulation.

Appendix A. Supplementary data

Supplementary data to this article can be found online at http://dx.doi.org/10.1016/j.nano.2013.06.005.

References

1. The National Institute of Neurological Disorders and Stroke rt-PA Stroke Study Group. Tissueplasminogen activator for acute ischemic stroke. *N Engl J Med* 1995;**333**:1581-7.
2. Carmichael ST. Themes and strategies for studying the biology of stroke recovery in the poststroke epoch. *Stroke* 2008;**39**:1380-8.
3. Chopp M, Li Y, Zhang J. Plasticity and remodeling of brain. *J Neurol Sci* 2008;**265**:97-101.
4. Ohab JJ, Fleming S, Blesch A, Carmichael ST. A neurovascular niche for neurogenesis after stroke. *J Neurosci* 2006;**26**:13007-16.
5. Ohab JJ, Carmichael ST. Poststroke neurogenesis: emerging principles of migration and localization of immature neurons. *Neuroscientist* 2008;**14**:369-80.
6. Pepper MS. Manipulating angiogenesis. From basic science to the bedside. *Arterioscler Thromb Vasc Biol* 1997;**17**:605-19.
7. Ribatti D, Vacca A, Nico B, Roncali L, Dammacco F. Postnatal vasculogenesis. *Mech Dev* 2001;**100**:157-63.
8. Asahara T, Murohara T, Sullivan A, Silver M, van der Zee R, Li T, et al. Isolation of putative progenitor endothelial cells for angiogenesis. *Science* 1997;**275**:964-7.
9. Urbich C, Dimmeler S. Endothelial progenitor cells functional characterization. *Trends Cardiovasc Med* 2004;**14**:318-22.
10. Hur J, Yoon CH, Kim HS, Choi JH, Kang HJ, Hwang KK, et al. Characterization of two types of endothelial progenitor cells and their different contributions to neovasculogenesis. *Arterioscler Thromb Vasc Biol* 2004;**24**:288-93.
11. Rafii S, Lyden D. Therapeutic stem and progenitor cell transplantation for organ vascularization and regeneration. *Nat Med* 2003;**9**:702-12.
12. Saltzman AJ, Choi SW, Dabreo A, Baur WE, Weiss E, Nguyen K, et al. Endothelial progenitor cells delivered into the pericardial space incorporate into areas of ischemic myocardium. *Cardiovasc Revasc Med* 2010;**11**:241-8.
13. Kalka C, Masuda H, Takahashi T, Kalka-Moll WM, Silver M, Kearney M, et al. Transplantation of ex vivo expanded endothelial progenitor cells for therapeutic neovascularization. *Proc Natl Acad Sci U S A* 2000;**97**:3422-7.
14. Foubert P, Matrone G, Souttou B, Leré-Déan C, Barateau V, Plouët J, et al. Coadministration of endothelial and smooth muscle progenitor cells enhances the efficiency of proangiogenic cell-based therapy. *Circ Res* 2008;**103**:751-60.
15. Taguchi A, Soma T, Tanaka H, Kanda T, Nishimura H, Yoshikawa H, et al. Administration of $CD34^+$ cells after stroke enhances neurogenesis via angiogenesis in a mouse model. *J Clin Invest* 2004;**114**:330-8.
16. Fan Y, Shen F, Frenzel T, Zhu W, Ye J, Liu J, et al. Endothelial progenitor cell transplantation improves long-term stroke outcome in mice. *Ann Neurol* 2010;**67**:488-97.
17. Urbich C, Aicher A, Heeschen C, Dernbach E, Hofmann WK, Zeiher AM, et al. Soluble factors released by endothelial progenitor cells promote migration of endothelial cells and cardiac resident progenitor cells. *J Mol Cell Cardiol* 2005;**39**:733-42.
18. He T, Peterson TE, Katusic ZS. Paracrine mitogenic effect of human endothelial progenitor cells: role of interleukin-8. *Am J Physiol Heart Circ Physiol* 2005;**289**:H968-72.
19. Lee HJ, Kim KS, Park IH, Kim SU. Human neural stem cells over-expressing VEGF provide neuroprotection, angiogenesis and functional recovery in mouse stroke model. *PLoS One* 2007;**2**:e156.
20. Horie N, Pereira MP, Niizuma K, Sun G, Keren-Gill H, Encarnacion A, et al. Transplanted stem cell-secreted vascular endothelial growth factor effects poststroke recovery, inflammation, and vascular repair. *Stem Cells* 2011;**29**:274-85.
21. Andres RH, Horie N, Slikker W, Keren-Gill H, Zhan K, Sun G, et al. Human neural stem cells enhance structural plasticity and axonal transport in the ischaemic brain. *Brain* 2011;**134**:1777-89.
22. Li L, Jiang Q, Ding G, Zhang L, Zhang ZG, Li Q, et al. Effects of administration route on migration and distribution of neural progenitor cells transplanted into rats with focal cerebral ischemia, an MRI study. *J Cereb Blood Flow Metab* 2010;**30**:653-62.
23. Schrepfer S, Deuse T, Reichenspurner H, Fischbein MP, Robbins MC, Pelletier MP. Stem cell transplantation: the lung barrier. *Transplant Proc* 2007;**39**:573-6.
24. Fischer UM, Harting MT, Jimenez F, Monzon-Posadas WO, Xue H, Savitz SI, et al. Pulmonary passage is a major obstacle for intravenous stem cell delivery: the pulmonary first-pass effect. *Stem Cells Dev* 2009;**18**:683-92.
25. Harting MT, Jimenez F, Xue H, Fischer UM, Baumgartner J, Dash PK, et al. Intravenous mesenchymal stem cell therapy for traumatic brain injury. *J Neurosurg* 2009;**110**:1189-97.
26. Billotey C, Wilhelm C, Devaud M, Bacri JC, Bittoun J, Gazeau F. Cell internalization of anionic maghemite nanoparticles: quantitative effect on magnetic resonance imaging. *Magn Reson Med* 2003;**49**:646-54.
27. Syková E, Jendelová P, Herynek V. Magnetic resonance imaging of stem cell migration. *Methods Mol Biol* 2011;**750**:79-90.
28. Nishida K, Tanaka N, Nakanishi K, Kamei N, Hamasaki T, Yanada S, et al. Magnetic targeting of bone marrow stromal cells into spinal cord: through cerebrospinal fluid. *Neuroreport* 2006;**17**:1269-72.
29. Kyrtatos PG, Lehtolainen P, Junemann-Ramirez M, Garcia-Prieto A, Price AN, Martin JF, et al. Magnetic tagging increases delivery of circulating progenitors in vascular injury. *JACC Cardiovasc Interv* 2009;**2**:794-802.
30. Wilhelm C, Bal L, Smirnov P, Galy-Fauroux I, Clément O, Gazeau F, et al. Magnetic control of vascular network formation with magnetically labeled endothelial progenitor cells. *Biomaterials* 2007;**28**:3797-806.

31. Taboada E, Rodríguez E, Roig A, Oró J, Roch A, Muller RN. Relaxometric and magnetic characterization of ultrasmall iron oxide nanoparticles with high magnetization. Evaluation as potential T1 magnetic resonance imaging contrast agents for molecular imaging. *Langmuir* 2007;**23**:4583-8.
32. Rosell A, Arai K, Lok J, He T, Guo S, Navarro M, et al. Interleukin-1beta augments angiogenic responses of murine endothelial progenitor cells in vitro. *J Cereb Blood Flow Metab* 2009;**29**:933-43.
33. Navarro-Sobrino M, Rosell A, Hernández-Guillamon M, Penalba A, Ribó M, Alvarez-Sabín J, et al. Mobilization, endothelial differentiation and functional capacity of endothelial progenitor cells after ischemic stroke. *Microvasc Res* 2010;**80**:317-23.
34. Wilhelm C, Gazeau F. Universal cell labelling with anionic magnetic nanoparticles. *Biomaterials* 2008;**29**:3161-74.
35. Mai XL, Ma ZL, Sun JH, Ju SH, Ma M, Teng GJ. Assessments of proliferation capacity and viability of New Zealand rabbit peripheral blood endothelial progenitor cells labeled with superparamagnetic particles. *Cell Transplant* 2009;**18**:171-81.
36. Sasaki H, Tanaka N, Nakanishi K, Nishida K, Hamasaki T, Yamada K, et al. Therapeutic effects with magnetic targeting of bone marrow stromal cells in a rat spinal cord injury model. *Spine (Phila Pa 1976)* 2011;**36**:933-8.
37. Fujioka Y, Tanaka N, Nakanishi K, Kamei N, Nakamae T, Izumi B, et al. Magnetic field-based delivery of human CD133 positive cells promotes functional recovery following rat spinal cord injury. *Spine (Phila Pa 1976)* 2012;**37**:E768-77.
38. Liu HL, Hua MY, Yang HW, Huang CY, Chu PC, Wu JS, et al. Magnetic resonance monitoring of focused ultrasound/magnetic nanoparticle targeting delivery of therapeutic agents to the brain. *Proc Natl Acad Sci USA* 2010;**107**:15205-10.
39. Chertok B, Moffat BA, David AE, Yu F, Bergemann C, Ross BD, et al. Iron oxide nanoparticles as a drug delivery vehicle for MRI monitored magnetic targeting of brain tumors. *Biomaterials* 2008;**29**:487-96.
40. Song M, Kim YJ, Kim YH, Roh J, Kim SU, Yoon BW. Using a neodymium magnet to target delivery of ferumoxide-labeled human neural stem cells in a rat model of focal cerebral ischemia. *Hum Gene Ther* 2010;**21**:603-10.
41. Runge VM. Safety of approved MR contrast media for intravenous injection. *J Magn Reson Imaging* 2000;**12**(2):205-13.
42. Chen R, Yu H, Jia ZY, Yao QL, Teng GJ. Efficient nano iron particle-labeling and noninvasive MR imaging of mouse bone marrow-derived endothelial progenitor cells. *Int J Nanomedicine* 2011;**6**:511-9.
43. Yang JX, Tang WL, Wang XX. Superparamagnetic iron oxide nanoparticles may affect endothelial progenitor cell migration ability and adhesion capacity. *Cytotherapy* 2010;**12**:251-9.
44. Chung TH, Hsiao JK, Hsu SC, Yao M, Chen YC, Wang SW, et al. Iron oxide nanoparticle-induced epidermal growth factor receptor expression in human stem cells for tumor therapy. *ACS Nano* 2011;**5**:9807-16.
45. Ushio-Fukai M, Alexander RW. Reactive oxygen species as mediators of angiogenesis signaling: role of NAD(P)H oxidase. *Mol Cell Biochem* 2004;**264**:85-97.
46. Zhu MT, Wang Y, Feng WY, Wang B, Wang M, Ouyang H, et al. Oxidative stress and apoptosis induced by iron oxide nanoparticles in cultured human umbilical endothelial cells. *J Nanosci Nanotechnol* 2010;**10**:8584-90.
47. Chua CC, Hamdy RC, Chua BH. Upregulation of vascular endothelial growth factor by H_2O_2 in rat heart endothelial cells. *Free Radic Biol Med* 1998;**25**:891-7.
48. Lamalice L, Le Boeuf F, Huot J. Endothelial cell migration during angiogenesis. *Circ Res* 2007;**100**:782-94.

THE JOURNAL OF PHYSICAL CHEMISTRY C

Article

pubs.acs.org/JPCC

Surface Reactivity of Iron Oxide Nanoparticles by Microwave-Assisted Synthesis; Comparison with the Thermal Decomposition Route

Oana Pascu,[†] Elisa Carenza,[†] Martí Gich,[†] Sònia Estradé,[‡,§] Francesca Peiró,[‡] Gervasi Herranz,[†] and Anna Roig*[,†]

[†]Materials Science Institute of Barcelona (ICMAB-CSIC), Campus UAB, 08193 Bellaterra, Spain

[‡]LENS, MIND-IN2UB, Department of Electronics, University of Barcelona, Martí i Franquès 1, 08028 Barcelona, Spain

[§]TEM-MAT, CCiT, University of Barcelona, Solé i Sabarís 1, 08028 Barcelona, Spain

ABSTRACT: Microwave-assisted chemistry is becoming very attractive in all areas of synthetic chemistry; it is fast, easy to operate, efficient in terms of energy consumption and environmentally friendly. However, a quantitative assessment of this chemical procedure with respect to other widely used chemical routes is lacking. Focusing in the preparation of iron oxide nanoparticles of comparable sizes, we have analyzed the performance of microwave-assisted synthesized nanoparticles compared to those obtained by the widespread thermal decomposition process of metal complexes. On the basis of a multidisciplinary experimental approach, we have unveiled that microwave-synthesized nanoparticles exhibit a surface reactivity significantly smaller than their thermal decomposition counterparts. We ascribe such dissimilarities to the different configurations of crystallographic faceting planes resulting from the particularities of both synthesis routes. We also show that the microwave route allows a direct stabilization of the particles in organic or aqueous media by using either steric or electrostatic stabilizers. A simplified life cycle analysis, as a preliminary framework toward nanoparticles eco-design, shows also a cost-effective positive balance for the microwave synthesis. Our results are of relevance for a broad range of applications including health, information storage, environmental remediation, sensors, or catalysis.

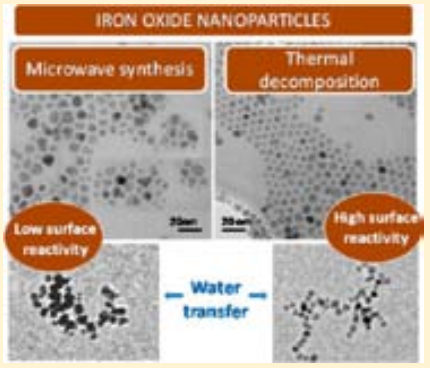

1. INTRODUCTION

Producing functional materials with better or, at least, comparable properties than the existing ones while using cheaper, faster and cleaner synthesis is in high demand.[1] Microwave-assisted chemistry is getting very attractive in all areas of synthetic chemistry because it can boost some competitive advantages over other fabrication methods. It is fast, produces high yields and is easy to operate, being efficient in terms of energy consumption and environmentally friendly. From the mid-1980s, it has been extensively used in organic synthesis.[2−4] During the past decade, the technique has also been widely applied to prepare inorganic nanostructured materials[5−12] with applications in, e.g., electrodes,[13] humidity sensors[14] or catalytic devices.[10] In particular, the versatility of the method for the synthesis of nanoparticles has been reported,[15] and a valuable review on the subject has recently appeared.[16] Lately, we have contributed in this field with the fabrication of 2D and 3D magneto-photonic opals using a microwave nanoparticles deposition approach.[17,18] The resulting magnetic opals exhibit enhanced functionalities. One of the conclusions of the above-mentioned critical review on microwave-assisted synthesis is that claims of the improved physicochemical properties of the nanoparticles prepared by this technique are not always well experimentally supported and a detailed characterization and critical examination of the desired functional properties of nanoparticles prepared by microwave-assisted synthesis vs other conventional preparation methods is needed.[16] Among these, the thermal decomposition of metal complexes carried out in high boiling point organic solvents and in the presence of surfactants is highly relevant. Indeed, the technique is largely recognized to produce excellent quality nanoparticles with small sizes, narrow particle size distributions and high crystallinity, while the resulting nanoparticles are very stable in organic solvents.[19−23] This approach has nevertheless some associated drawbacks, e.g., it requires working under inert atmosphere, at high reaction temperature and it requires long processing times resulting in high energy and time consumption. More recently, thermal decomposition of iron oleate complexes in presence of oleic acid via heat-up processes has been shown as a convenient method for large scale production of nanoparticles.[24,25]

In this context of application-targeted nanoparticles, magnetic nanoparticles have found applicability in many fields such as health, information storage, environmental remediation, sensors, or catalysis.[26−29] Such a wide range of applications has spurred remarkable advances concerning the fabrication of

Received: April 4, 2012
Revised: June 12, 2012
Published: June 20, 2012

magnetic nanoparticles with tailored properties and easy processability. Indeed, controlling the physicochemical characteristics of the particles is crucial to directly in uence on their functional properties and performance. Surface reactivity, in addition to particle size and surface area, will in uence the interaction of the nanoparticle with its surroundings. For example, such different aspects as the photocatalytical activity of a nanoparticle, its interaction with living organisms or their degradation profile will be largely affected by its surface reactivity.[30,31]

Here, we report on the physicochemical properties of iron oxide nanoparticles of comparable sizes fabricated by microwave-assisted synthesis and by the thermal decomposition method. It will be shown that both methods allow us preparing monodisperse crystalline nanoparticles with a superparamagnetic character and a high saturation magnetization value. Remarkably, a relevant difference is the smaller surface reactivity of the nanoparticles resulting from the microwave route. We argue that the difference in surface reactivity results from the lower energy of the crystallographic faceting planes. Such characteristic can be worth to be taken into consideration depending on the final application targeted, for instance in those applications where time aggregation or particle growth is undesirable. It is also shown that microwave synthesis enables a direct stabilization of nanoparticles in aqueous colloidal dispersions at physiological pH, which is an important feature when biomedical applications are envisaged. Finally, a simplified life cycle analysis for the two preparation routes is included as a preliminary framework toward nanoparticles ecodesign: in terms of cost, a positive balance for the microwave synthesis was clearly attained.

2. EXPERIMENTAL SECTION

2.1. Chemicals. The following chemicals were purchased from Sigma-Aldrich and were used without any purification: Iron(III) acetylacetonate ($Fe(acac)_3$, 97%), oleic acid (analytical standard), oleylamine (technical grade, 70%), benzyl alcohol, benzyl ether (98%), 1,2-hexadecandiol (97%), hexane (anhydrous, 95%), ethanol, water solution (25 wt %) of trimethylammonium hydroxide (TMAOH), sodium citrate and deionized water.

2.2. Nanoparticles Synthesis. Synthetic details of the two methods used for the fabrication of iron oxide nanoparticle fabrication, microwave synthesis and thermal decomposition of metal complexes, are detailed below.

A. Microwave-Assisted Synthesis. A nonaqueous sol−gel chemical reaction, similar to the one reported by Niederberger et al.,[6] was used. The most relevant difference in our case is the use of oleic acid or trimethylammonium hydroxide as stabilizers. The microwave experiments were carried out using a CEM Discover reactor (Explorer 12-Hybrid) operating at a frequency of 2.45 GHz and with a maximum power of 300 W. For a typical run, the power was automatically adjusted to heat the sample to the set reaction parameters (temperature and time). During a chemical reaction, the temperature and pressure were monitored by a volume-independent infrared sensor.

Iron oxide nanoparticles (γ-Fe_2O_3/Fe_3O_4) were obtained by mixing $Fe(acac)_3$ (0.35 mmol =123.6 mg) and oleic acid (1.05 mmol = 0.336 mL) in 4.5 mL anhydrous benzyl alcohol at 60 °C for 5 min in the microwave reactor under magnetic stirring for complete dissolution of the precursors. The mixture has a transparent dark-red color. Precursor's solution was further heated in the same microwave reactor to 160 °C (typically using a power of 200 W) and the temperature was kept stable for 5 min. Then, the solution was automatically cooled down to 50 °C by compressed nitrogen in approximately 3 min. The final suspension was black. The nanoparticles were separated by adding ethanol (40 mL), followed by centrifugation at 4000 rpm during 20 min. The supernatant from this first centrifugation was discharged and the precipitate, dispersed in 2 mL hexane with 10 μL oleic acid and it was centrifuged again at 4000 rpm during 20 min. Because no precipitate was separated, the supernatant (nanoparticles in hexane) was centrifuged one more time with ethanol to eliminate the free surfactant. The as-obtained precipitate was redispersed in hexane forming a clear dark brown colloidal dispersion. The nanoparticles were labeled as $\mathbf{(iron\ oxide)_{MW}}$ and used for further analysis. For this batch, using 123.6 mg of Fe precursor, 22 mg of iron oxide nanoparticles were obtained, giving a mass reaction yield of 79%. A second batch labeled as $\mathbf{(iron\ oxide)_{MW\_TMAOH}}$ was prepared using $Fe(acac)_3$ (0.35 mmol =123.6 mg) dissolved in 4.5 mL anhydrous benzyl alcohol but without adding oleic acid in the initial mixture. Instead, at the separation step, 20 μL of TMAOH together with 40 mL of acetone were added and centrifuged at 6000 rpm, 20 min. The supernatant was discharged and the magnetic precipitate, after drying the sample overnight in an oven at 70 °C, was redispersed in 2 mL distillate water containing 10 μL of TMAOH without the need of ligand transfer. The as-prepared dispersion had a pH = 11 that was lowered to 7 using nitric acid.

B. Thermal Decomposition Route. For the synthesis of iron oxide nanoparticles, an adapted procedure of S. Sun et al.[20] was used. $Fe(acac)_3$ (2 mmol), 1,2-hexadecanediol (10 mmol), oleic acid (6 mmol), oleylamine (6 mmol), and benzyl ether (20 mL) were mixed and magnetically stirred under a ow of argon. The mixture was heated to 200 °C for 2 h and then, under argon atmosphere, heated to re ux at 300 °C for 1 h. The black-color mixture was cooled down to room temperature by removing the heat source. Under ambient conditions, ethanol (40 mL) was added to the mixture and a black material was precipitated and separated via centrifugation (4500 rpm, 20 min). The black product was dispersed in hexane in the presence of oleic acid (0.05 mL) and oleylamine (0.05 mL). Centrifugation (4000 rpm, 10 min) was applied to remove any residue. The product was then precipitated with ethanol, centrifuged to remove the solvent (4500 rpm, 20 min), and redispersed in hexane. A further centrifugation (4000 rpm, 30 min) could be made in order to obtain nanoparticles with better monomodal size distribution. Finally, the non dispersible residue was separated and nanoparticles dispersed in hexane, labeled as $\mathbf{(iron\ oxide)_{TD}}$ and used for further analysis. A typical batch using 706.3 mg of Fe precursor produced 131 mg of iron oxide nanoparticles giving then a mass reaction yield of 82%.

2.3. Transfer in Water of the Organically Stabilized Iron Oxide Nanoparticles. The $(iron\ oxide)_{MW}$ and $(iron\ oxide)_{TD}$ systems were subjected to the same ligand transfer procedure.[32] Brie y, mixing an equal volume ratio of NPs dispersed in hexane of known concentration (10 mg/mL) with a TMAOH water solution 0.4 M (pH = 12) two separated phases were formed. The upper one, containing the nanoparticles, was of very dark brown color and the lower one was colorless. The systems were kept for 18 h under magnetic stirring. Next, the dispersion was left to be separated again in

dx.doi.org/10.1021/jp303204d | J. Phys. Chem. C 2012, 116, 15108−15116

two phases; the upper phase had a yellow color and the lower aqueous phase was dark brown, signaling the nanoparticles transfer. The hexane phase was removed carefully and the nanoparticles were precipitated by centrifugation (4500 rpm, 20 min) adding acetone to the water solution. The supernatant was discharged and the precipitate was redispersed by using ultrasounds in a TMAOH water solution. In order to stabilize the nanoparticles in water at pH = 7, nitric acid and a sodium citrate solution (4 mM) in 1:1 volume ratio were added under magnetic stirring. The as-prepared water dispersions were subjected to further analysis. Those systems were labeled as $(\textbf{iron oxide})_{MW\_water}$ and $(\textbf{iron oxide})_{TD\_water}$.

2.4. Chemical Analysis. Elemental microanalysis of the C, H, and N content of the $(\text{iron oxide})_{TD}$ and $(\text{iron oxide})_{MW}$ systems was determined using an Eurovector EA3011 equipment. Dried material was heated at 1200 °C in oxygen atmosphere, and the quantitative determination of elements was given by gas chromatography. Measurements were repeated twice and the results were normalized to the weighted amount of nanoparticles. The final mass percentages obtained were: 17% C, 2.7% H, 0.23% N for $(\text{iron oxide})_{TD}$ and 24% C, 3.7% H, with less than 0.2% N for $(\text{iron oxide})_{MW}$.

2.5. Materials Characterization. Morphological and structural characterization was performed using transmission electron microscopy (TEM and CryoTEM) and X-ray diffraction (XRD). TEM micrographs were obtained with a JEOL JEM-1210 electron microscope, operating at 120 kV. The high resolution TEM images (HRTEM) and selected area diffraction patterns (SADP) were captured using JEOL equipment (JEM-2011 and FEG-2010F, operating at 200 kV). The samples were prepared by depositing a drop of diluted nanoparticles dispersion in hexane onto a carbon grid and letting the solvent to evaporate. The mean diameter and polydispersity of each system were determined by fitting a Gaussian distribution to particle size histograms of over 250−300 measurements of the sizes of different particles from TEM images by using the imageJ software. Cryo-TEM experiments were performed on aqueous suspensions of magnetic nanoparticles at an iron concentration of 10 mM. A drop of suspension was put on Quantifoil grid where a perforated foil is used to bear an ultrathin carbon support foil to minimize the total specimen thickness. The drop was blotted with filter paper and the grid was rapidly quenched into liquid ethane in order to produce "vitreous" ice, without formation of crystals. Then the grid was transferred into the TEM microscope (JEM-2011 operating at 200 kV) where the temperature is kept at −140 °C with liquid nitrogen during the imaging.

Powder X-ray diffraction patterns of the nanoparticles were measured with a Rigaku, "rota ex" RU-200B model using a Cu anode with $\lambda_{K\alpha1}$ = 1.5406 Å and $\lambda_{K\alpha2}$ = 1.5444 Å in the 2θ range of 20−70°. The patterns were analyzed using Rietveld refinement with the Fullprof program,[33] which includes modules to calculate the apparent crystal size and strain. An experimental resolution function was obtained from the refinement of a quartz reference in order to take into account the instrumental broadening.

The weight percentage of surfactant on the nanoparticles surface was determined by thermo gravimetric analysis (TGA). Solid samples (approximately 4 mg) were characterized with a Mettler Toledo TGA/SDRA 851E with the following setup: heating rate 10°/min and temperature range 30−600 °C under a N_2 ux.

The hydrodynamic diameter of the nanoparticles suspended in organic media and water were investigated with a Zetasizer Nano ZS from Malvern Instruments equipped with a He/Ne 633 nm laser. Care was taken that the DLS peak position and width was the same after three consecutive runs of 15 scans each run for all the nanoparticles.

Infrared spectra were acquired using a PerkinElmer FT-IR Spectrum One with U-ATR (universal attenuated total re ectance) accessory having a diamond tip and zinc selenide crystal under the tip. The spectrum, with a 4 cm^{-1} resolution, was recorded between 650 and 4000 cm^{-1} using four scans.

Magnetic characterization was performed with a superconductive quantum interference device (SQUID) magnetometer (Quantum Design MPMS5XL). The sample was prepared using a gelatin capsule filled with compacted cotton impregnated with 200 μL of a hexane dispersion of nanoparticles giving a mass of 2 mg (magnetic material and surfactant). The magnetization values were reported per mass of iron oxide by subtracting the mass of surfactant as measured in TGA experiments.

3. RESULTS AND DISCUSSIONS

Iron oxide nanoparticles were fabricated by microwave heating $(\text{iron oxide})_{MW}$ and thermal decomposition methods $(\text{iron oxide})_{TD}$. Microwave nanoparticles were stabilized using oleic acid while oleic acid and oleylamine at 1:1 molar ratio were used in thermal decomposition. As found by chemical analysis, oleylamine is almost completely eliminated in the cleaning and purification steps. It is noted that oleic acid to iron precursor molar ratio was the same for both systems. Moreover, an electrostatic stabilizer (TMAOH) was also used to directly stabilize in aqueous solution the nanoparticles prepared by microwave heating, $(\text{iron oxide})_{MW\_TMAOH}$. The organically stabilized nanoparticles $(\text{iron oxide})_{MW}$ and $(\text{iron oxide})_{TD}$ were subsequently transferred to water by a ligand exchange procedure, $(\text{iron oxide})_{MW\_water}$ and $(\text{iron oxide})_{TD\_water}$, respectively.

3.1. Structural and Morphological Characterization. Powder X-ray diffraction (XRD) patterns of $(\text{iron oxide})_{MW}$ and $(\text{iron oxide})_{TD}$ are presented in Figure 1. The re ections in the patterns can be indexed with the inverse spinel structures of magnetite or maghemite (ICDD PDF019−0629 and PDF039−1346). The distinction between both phases was not possible due to the closeness of their re ections and the broad re ection

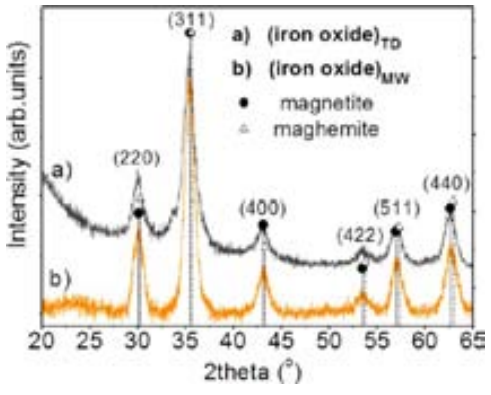

Figure 1. X-ray diffraction patterns corresponding to iron oxide synthesized by thermal decomposition $(\text{iron oxide})_{TD}$ and (b) by microwave heating route $(\text{iron oxide})_{MW}$.

dx.doi.org/10.1021/jp303204d | J. Phys. Chem. C 2012, 116, 15108−15116

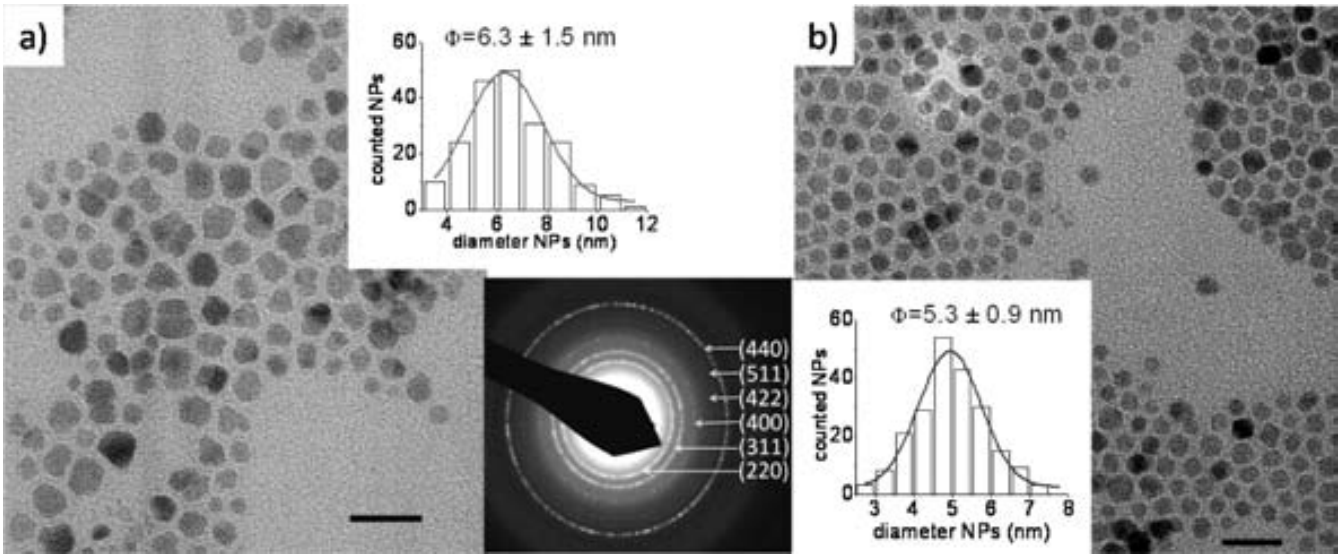

Figure 2. Iron oxide nanoparticles: (a) $(\text{iron oxide})_{MW}$ and (b) $(\text{iron oxide})_{TD}$ (scale bar = 20 nm). Size distributions fitted to a Gaussian function and the selected area electron diffraction (SAED) pattern are included as insets.

Table 1. Mean Size Diameters and Standard Deviations of the Nanoparticles Using Different Techniques and Cluster Sizes of the Water-Stabilized Nanoparticles after Ligand Exchange and after 30 days (Subscript 30d)[a]

	nanoparticles dispersed in organic media				clusters of nanoparticles in water	
	$\langle$ $_{XRD}\rangle$ (nm)	$\langle$ $_{TEM}\rangle$ (nm)	$\langle$ $_{HYD}\rangle$ (nm)	M_S (emu/g)	$\langle$ $_{HYD}\rangle$ (nm)	$\langle$ $_{HYD}\rangle_{30d}$ (nm)
$(\text{iron oxide})_{TD}$	4.60 ± 0.01	5.3 ± 0.9	10.8 ± 1.5	62	28 ± 3	49 ± 3
$(\text{iron oxide})_{MW}$	5.40 ± 0.02	6.3 ± 1.5	12.7 ± 1.5	60	22 ± 0.5	23 ± 1

[a]Saturation magnetization values at room temperature are also included.

peaks observed. The materials will be referred hereafter as iron oxide nanoparticles. The size of the crystalline domains calculated from the peak broadening refinements gave 5.41 ± 0.02 nm for $(\text{iron oxide})_{MW}$ and 4.61 ± 0.03 nm for $(\text{iron oxide})_{TD}$. The apparent maximum strain was about 14.5% for both systems. The two iron oxide nanoparticles are presented by the corresponding TEM micrographs in Figure 2. At first glance only slight differences in the size and shape of nanoparticles, Figure 2, parts a and b, can be observed although a higher polydispersity value is found for the nanoparticles prepared by the microwave route. A possible explanation could be that in the case of microwave synthesis, the effective separation of the nucleation and the growth is not as well-defined as in the case of the thermal decomposition method where two well-separated temperatures differentiate the two processes (200 °C for the nucleation and 300 °C for the particle growth).[34] Table 1 contains the particles sizes obtained by the different techniques.

3.2. Magnetic Characterization. The magnetic properties of $(\text{iron oxide})_{TD}$ and $(\text{iron oxide})_{MW}$ nanoparticles were evaluated by magnetization vs magnetic field measurements at 300 K and by zero-field-cooled (ZFC), field-cooled (FC) temperature dependent magnetization curves using a 50 Oe field. Figure 3 shows typical magnetization loops for superparamagnetic nanoparticles in which neither remnant magnetization nor coercivity at room temperature were observed. The saturation magnetization for both systems is high, with a value of approximately 60 emu/g pointing to the high degree of crystallinity of the nanoparticles. Superparamagnetism is also confirmed by the ZFC-FC magnetization curves, Figure 3 inset. The ZFC magnetization increases with the temperature until

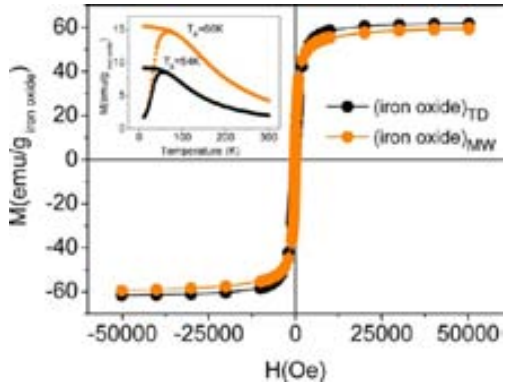

Figure 3. Magnetic characterization of the iron oxide nanoparticles. Comparison of M(H) at 300 K and ZFC-FC with 50 Oe applied field (left inset) between surfactant coated iron oxide nanoparticles synthesized by microwave $(\text{iron oxide})_{MW}$ and thermal decomposition route $(\text{iron oxide})_{TD}$.

reaching a maximum value corresponding to the blocking temperature (T_B) at 54 K for the $(\text{iron oxide})_{TD}$ and 66 K for the $(\text{iron oxide})_{MW}$. Above this temperature, the thermal energy (k_BT) becomes larger than magnetic energy barrier and the nanoparticles enter in the superparamagnetic domain. The temperature dependent magnetic measurements also show that the magnetic susceptibility at low field is about 40% larger for $(\text{iron oxide})_{MW}$ than for $(\text{iron oxide})_{TD}$. It is important to highlight here that from the magnetic point of view, iron oxide nanoparticles prepared by such simple technique as microwave synthesis can be as good as those prepared by more complex and costly thermal decomposition (comparable saturation

dx.doi.org/10.1021/jp303204d | J. Phys. Chem. C 2012, 116, 15108−15116

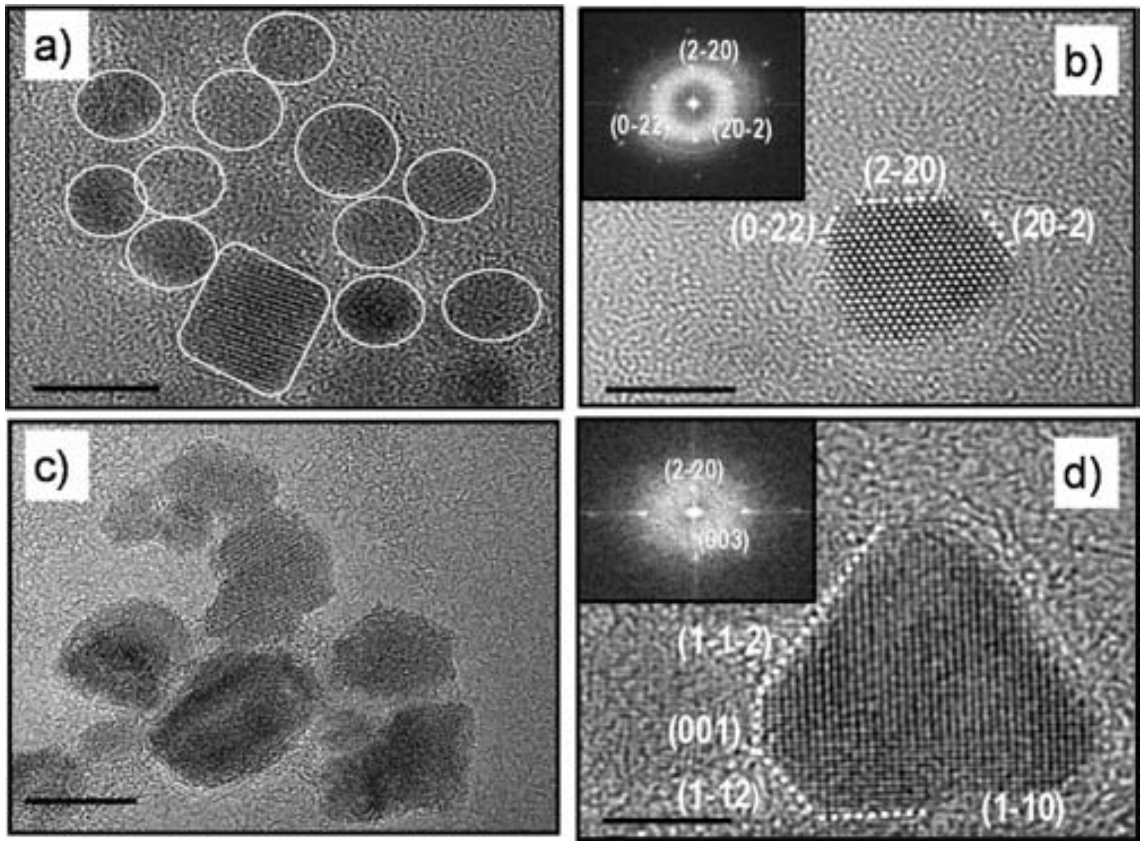

Figure 4. HRTEM images: (a) several (iron oxide)$_{TD}$ nanoparticles where the regular shape is evidenced, (b) a hexagonal (iron oxide)$_{TD}$ nanoparticle in the [111] zone axis condition, faceting planes are indicated (the inset corresponds to the fast Fourier transform (FFT), (c) several (iron oxide)$_{MW}$ nanoparticles where the irregular shape is evidenced, (d) a lobular (iron oxide)$_{MW}$ nanoparticle in the [110] zone axis condition, faceting planes are indicated (the inset corresponds to the FFT) (scale bars =10 nm in parts a and c and =5 nm in parts b and d).

magnetization). In these regards the microwave technique is clearly superior compared to other simple synthetic techniques such as coprecipitation which tend to yield less well crystallized nanoparticles with lower saturation magnetization.[35]

3.3. Surface Chemistry and Reactivity. A more detailed study of the morphology of the nanoparticles showed that in the case of thermal decomposition a large fraction of nanoparticles were monocrystalline and spherical/hexagonal in shape, with only a small number of larger rectangular ones, Figure 4a. High-resolution TEM investigations also revealed that the crystallographic faceting planes of the hexagons presented high Miller indices ((202), (220), and (022)) and thus higher surface energy, Figure 4b. The high-index planes usually have higher surface energy (γ), and for a face-centered-cubic phase the sequence $\gamma(111) < \gamma(100) < \gamma(110) < \gamma(220)$[36,37] can be generated from the distance between those planes and the central Wulff's point.[38] In contrast microwave particles presented a more irregular lobular-like shape, Figure 4c, but still a major fraction of the nanoparticles were monocrystalline. In this case, the crystallographic faceting planes were of low Miller indexes ((110), (001), (112)), Figure 4d, conferring lower surface reactivity to the microwave nanoparticles.

The more reactive surface of the (iron oxide)$_{TD}$ system could be also evidenced by the Cryo-TEM analysis of the nanoparticle clusters formed after their transfer from organic media to water. The images, Figure 5, parts a and b, show that the clusters of (iron oxide)$_{TD\_water}$ formed more dendritic and ramified structures than those of (iron oxide)$_{MW\_water}$ which are more compact and rounded in shape. Second, we have been interested in investigating how such different surface reactivity can be identified or fingerprinted by other techniques. Dynamic light scattering (DLS) measurements, thermo gravimetric analysis (TGA) and infrared spectroscopy (IR) were further used to collect information on the surface chemistry of the nanoparticles. DLS was used to determine the hydrodynamic size and studying the stability of the colloidal dispersion, Figure 6a. The hydrodynamic diameter ($\langle$ $_{HYD}\rangle$), which includes the magnetic core ($\langle$ $_{TEM}\rangle$) and the organic shell (length of the oleic acid 2 nm), is in all cases larger than the diameter determined by TEM. Considering one monolayer of surfactant, the hydrodynamic diameter could be approximated as $\langle$ $_{HYD}\rangle$ = $\langle$ $_{TEM}\rangle$ + 4 nm.[39] DLS gives a $\langle$ $_{HYD}\rangle$ value of 10.8 ± 1.5 nm for (iron oxide)$_{TD}$ which is in good agreement with the one monolayer approximation. In the case of (iron oxide)$_{MW}$ the $\langle$ $_{HYD}\rangle$ value is larger (12.7 ± 1.5 nm) and can be approximated as $\langle$ $_{TEM}\rangle$ + 6 nm pointing out to an interdigitated bilayer surfactant configuration, due to the chemisorbed (covalently binding of carboxylate groups to the surface Fe^{3+}) and physisorbed ligands (oleic acid molecules inserted between adjacent coordinated oleic acid).[40,41]

The hydrodynamic diameter of particle clusters formed in aqueous solutions was measured by DLS at the moment of the solvent exchange and after one month, Figure 6a and Table 1. It was found that the (iron oxide)$_{MW\_water}$ system formed more stable aggregates than the (iron oxide)$_{TD\_water}$ one. Indeed, repeating the measurement after one month, the (iron oxide)$_{TD\_water}$ clusters showed a size increase of about 40%

dx.doi.org/10.1021/jp303204d | J. Phys. Chem. C 2012, 116, 15108−15116

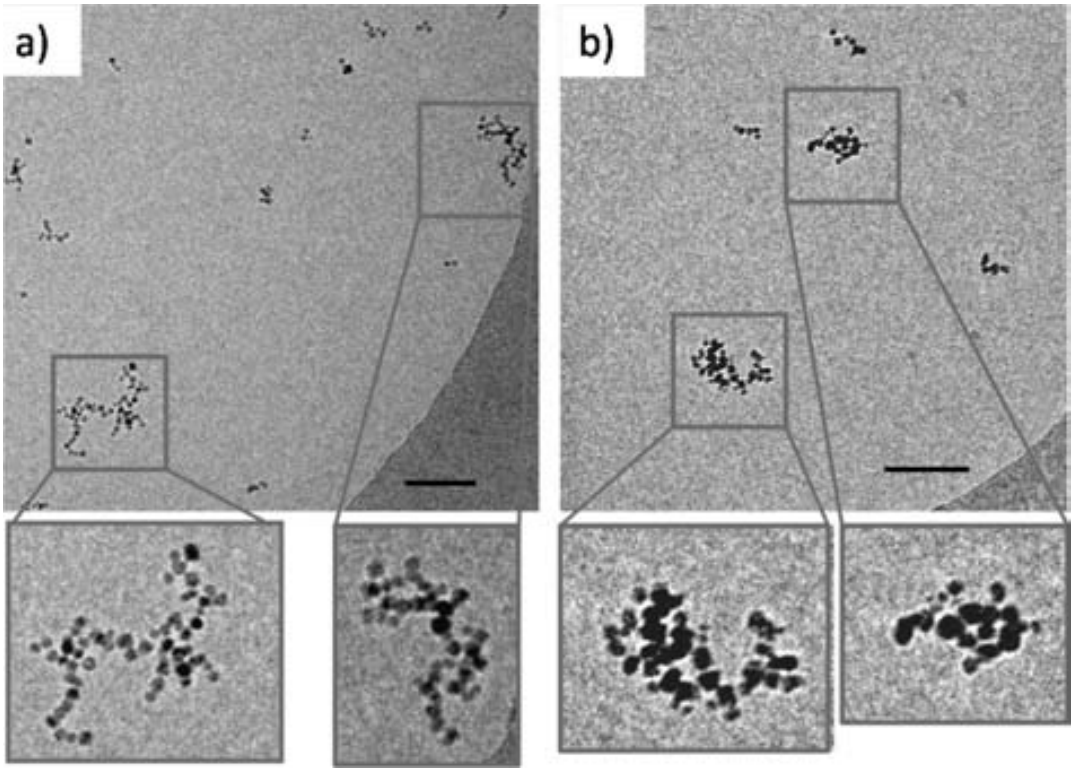

Figure 5. Cryo-TEM micrographs of the clusters formed after solvent exchange from organic to aqueous media: (a) the $(\text{iron oxide})_{TD\_water}$ system forming dendrite shape clusters and (b) the $(\text{iron oxide})_{MW\_water}$ system forming more compacted and rounded clusters (scale bars =100 nm).

while the size for $(\text{iron oxide})_{MW\_water}$ clusters remained constant: the hydrodynamic diameter of $(\text{iron oxide})_{MW\_water}$ clusters was 22 ± 0.5 nm after the solvent exchange and 23 ± 1 nm after 1 month while the hydrodynamic diameter of $(\text{iron oxide})_{TD\_water}$ clusters increased from 28 ± 3 to 49 ± 3 nm after 1 month. Again, this finding re ects the higher reactivity of $(\text{iron oxide})_{TD}$ nanoparticles. To further support the hypothesis of mono or interdigitated layer, thermo gravimetric analysis were performed aiming to qualitatively studying the bonding strength of the surfactant. A strong bond (chemisorption) is associated with weight losses at higher temperature while a weak bond (physisorbed specimens) presents weight losses at lower temperatures.[38] Therefore, one single step of mass loss in the TGA profile is expected when chemisorption is predominant and two or more steps when physisorbed and chemisorbed molecules are present.[40,42,43] The TGA curves are shown in Figure 6b. The 200−500 °C temperature range was chosen as the surfactant desorption zone. Below 200 °C, the slight weight loss is due to the solvent evaporation, and from 200 °C onward the free oleic acid starts to desorb.[44] In the range 200−500 °C only one step was observed for $(\text{iron oxide})_{TD}$, Figure 6b, with a 17% weight loss, associated with chemisorption of oleic acid. In contrast, two steps were observed for $(\text{iron oxide})_{MW}$ suggesting the existence of both chemisorbed and physisorbed molecules. In the 200−300 °C range a first step of 19% weight loss is observed (step I) followed by a second step of 19% between 300−500 °C (step II).

Using those weight loss percentage values, it is possible to quantify the number of surfactant molecules (physisorbed and chemisorbed) per nanoparticle. Among different approximations[41−43] to assess it, the following relation was chosen:[43]

$$\text{weight loss\%} = 100x\frac{m_S}{m_{NP} + m_S} = 100x\frac{\frac{\pi d^2 M_S}{aN_A}}{\frac{1}{6}\pi d^3 \rho_{\text{maghemite}} + \frac{\pi d^2 M_S}{aN_A}} \quad (1)$$

where m_s is the mass of the surfactant and m_{NP} is the mass of the inorganic magnetic core, the weight loss % can be taken from a TGA curves, $\rho_{maghemite}$ = 5.49 g/cm^3, the molecular mass of oleic acid is M_S = 282.5 g/mol and N_A is the Avogadro's number. Considering that the average number of surfactant molecules (n_S) onto the magnetic particle surface is given by $\pi d^2/a$, where $d = \langle\ _{TEM}\rangle$ and a = surface area occupied by one surfactant molecule, substituting n_S in (eq 1) the expression for surfactant coverage can be written as:

$$n_S = \frac{\text{weight loss\%} \times \frac{1}{6}\pi d^3 \rho_{\text{maghemite}} \times 6.023}{M_S\left(1 - \frac{\text{weight loss \%}}{100}\right)} \quad (2)$$

The same equation was used to calculate the average number of surface physisorbed (n_S^{Ph}) and chemisorbed (n_S^{C}) surfactant molecules. Moreover, the surface grafting coefficient (ξ) which gives the density of surfactant molecules per nm^2 and additional information about the arrangement of those molecules can also be calculated.[42] Table 2 gathers the surfactant coverage (n_S^{Ph} and n_S^{C}) and the grafting coefficients (ξ^C and ξ^{Ph}). In the case of $(\text{iron oxide})_{TD}$ the grafting coefficient is 3.6 molecules/nm.^{2} This is close to a theoretical maximum value for a complete monolayer of chemisorbed oleic acid onto a nanoparticle surface[42] and in agreement with the of 3.5 molecules/nm^2 value obtained by Tomoaia-Cotisel et al.[45] For $(\text{iron oxide})_{MW}$ the chemisorbed grafting coefficient is smaller (3.0 molecules/

dx.doi.org/10.1021/jp303204d | J. Phys. Chem. C 2012, 116, 15108−15116

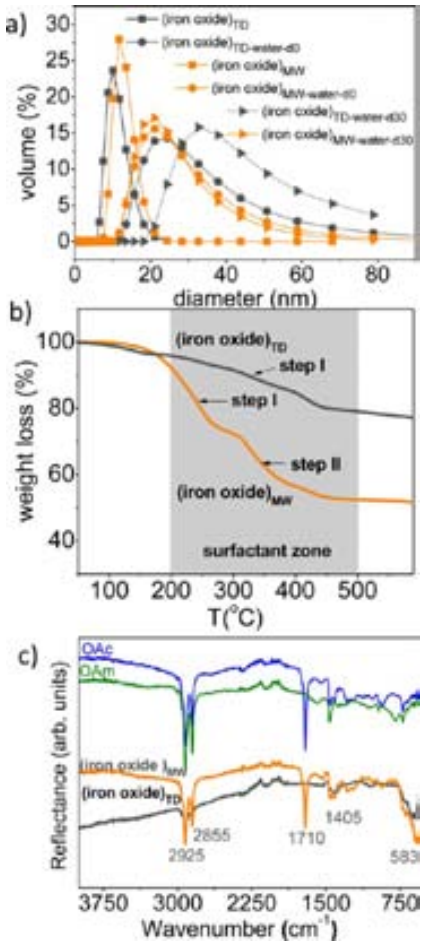

Figure 6. (a) Dynamic light scattering measurements on stable colloidal dispersions of the synthesized nanoparticles. (b) Thermogravimetric analysis. (c) Infrared spectra of the free surfactants and of the iron oxide systems.

nm^2), indicating that the surfaces of these nanoparticles present a lower number of active sites for oleic acid chemisorptions. These results indicate once more that the surface reactivity of $(\text{iron oxide})_{TD}$ is greater than that of $(\text{iron oxide})_{MW}$. Moreover, the physisorbed grafting coefficient obtained for $(\text{iron oxide})_{MW}$ (3.0 molecules/nm^2) is comparable to the corresponding chemisorbed one, as expected for interdigitated structures and in correspondence with the higher carbon content found by chemical analysis. One can expect this physisorbed shell to be stable against cleanings due to the hydrophobic interaction between the carbonyl chains of chemisorbed and physisorbed oleic acid molecules.

These findings are also supported by the infrared spectra (IR) displayed in Figure 6c. When comparing the iron oxide nanoparticles prepared by the two methods, the presence of two sharp bands at 2925 and 2855 cm^{-1} in all four spectra is attributed to the stretching of CH_2 (asymmetric and symmetric) and $-CH_3$ of saturated alkyl chain fragments. The peak at 1710 cm^{-1} found in free oleic acid and also in $(\text{iron oxide})_{MW}$ nanoparticles is due to the free carboxylic group, which in the case of nanoparticles, indicates the presence of oleic acid physisorbed at the surface. The absence of the aforementioned peak in the spectra of $(\text{iron oxide})_{TD}$ shows that in this case there is no free physisorbed surfactant. Instead, the presence of both asymmetric and symmetric carboxylate stretch at 1526 and 1412 cm^{-1} for $(\text{iron oxide})_{MW}$ and at 1543 and 1403 cm^{-1} for $(\text{iron oxide})_{TD}$ indicates that oleic acid is chemisorbed onto the particles surface through a bidentate bond, in agreement with our interpretation of TGA curves. The strong peak at 583 cm^{-1} for both types of nanoparticles is characteristic for the Fe−O bond of the nanoparticle cores.

Finally for microwave synthesis, we have investigated the possibility of adding the surfactant after the reaction was completed and the use of an electrostatic surfactant (TMAOH) to yield the direct stabilization of the nanoparticles in aqueous media $(\text{iron oxide})_{MW\_TMAOH}$. DLS was used to monitor the average size and to confirm the preservation of monodispersity of the nanocrystals, Figure 7. Slightly larger mean size (15.7 nm respect to 12.7 nm) and wider particle size distribution is observed by particles stabilized in water.

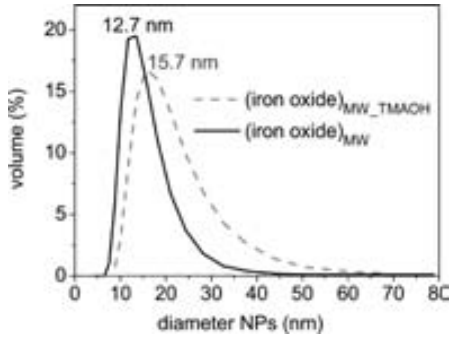

Figure 7. Dynamic light scattering measurements corresponding to the iron oxide nanoparticles by microwaves, $(\text{iron oxide})_{MW}$ corresponds to nanoparticles synthesized in the presence of oleic acid and redispersed in hexane while $(\text{iron oxide})_{MW\_TMAOH}$ corresponds to the nanoparticles prepared in the absence of surfactant and adding an electrostatic surfactant at the end of reaction to subsequently redisperse them in water.

3.4. Life Cycle Analysis. The life cycle analysis (LCA) of a product/material should provide the tools and methodology to assess and quantify the impact of a specific product/material.[46] LCA thus defines the boundaries for the conception of an environmentally benign product/material and it constitutes the

Table 2. Thermogravimetric and Particle Size Values of Iron Oxide Nanoparticles Synthesized by the Two Methods[a]

	$\langle$ TEM$\rangle$ (nm)	A_{NPs}[a] (nm^2)	$\langle$ HYD$\rangle$ (nm)	weight loss (%) step I	weight loss (%) step II	n_S^{Ph} (molecule/NP)	n_S^{C} (molecule/NP)	ξ^{Ph}[a] (molecule/nm^2)	ξ^{C}[a] (molecule/nm^2)
$(\text{iron oxide})_{MW}$	6.3 ± 1.5	125	12.7 ± 1.5	19	19	374	371	3.0	3.0
$(\text{iron oxide})_{TD}$	5.3 ± 0.9	88	10.1 ± 1.8	17	–	–	314		3.6

[a] $A_{NP} = \pi\langle$ TEM$\rangle^2$; $\xi^{Ph} = n_S^{Ph}/A_{NP}$; $\xi^{C} = n_S^{C}/A_{NP}$ [a]Parameters characterizing the nanoparticles surface coverage calculated from these data are included.

dx.doi.org/10.1021/jp303204d | J. Phys. Chem. C 2012, 116, 15108−15116

starting framework for the concept of eco-design. Without having the ambition of performing a LCA for our materials, we have made a comparative study in terms of material yield and resources involved to produce 1 g of iron oxide nanoparticles by microwave and thermal decomposition methods. The results are gathered in Table 3 which contains the energy (computed by the time needed for the chemical reaction to take place at a given temperature) and an estimation of the production cost (in euros). The reaction yield is similar in both cases although a slightly smaller yield was found for the microwave method. It is to note that by increasing the microwave heating temperature, from 160 to 200 °C, the yield increased up to 85%. To produce 1 g of iron oxide by thermal decomposition takes three times longer (a batch of 130 mg takes 160 min) than by microwaves (a batch of 22 mg takes 15 min). Moreover, since the working temperature, heating power and reaction time is much lower in the case of the microwave synthesis; the energy consumption of this technique is reduced by a factor of 10 as compared to thermal decomposition. Regarding the safety of the reagents, benzyl alcohol and benzyl ether are both harmful if inhaled or absorbed through the skin.[47] Benzyl alcohol in small quantities is nonthreatening, but benzyl ether may cause long-term environmental damage. Oleic acid may be harmful in big quantities (>230 mg/kg) and oleylamine is corrosive. The production costs have been estimated considering the prices of reagents and energy. It turns out that the production of 1 g of iron oxide nanoparticles is 40% less costly by microwaves than by the thermal decomposition method. In addition the microwave synthesis does not require working under inert atmosphere and can yield stable dispersions in either polar or nonpolar solvents. Other synthetic methods, namely from oleate complexes also use inexpensive and environmentally friendly compounds to produce nanoparticles of excellent quality.[25]

Table 3. Precursors and Synthetic Parameters to Produce 1 g of Nanoparticles by Microwave and Thermal Decomposition Methods[a]

synthesis information	microwave $(\text{iron oxide})_{MW}$	thermal decomposition $(\text{iron oxide})_{TD}$
iron precursor	$Fe(acac)_3$-5,6 g	$Fe(acac)_3$-5,4 g
solvent	benzyl alcohol (204.5 mL)	benzyl ether (183 mL)
surfactant	oleic acid (15 mL)	oleic acid (15 mL) + oleylamine (15 mL)
reaction yield	79%	82%
time[b]	682 min (11 h)	1756 min (29 h)
maximum temperature	160 °C	300 °C
energy consumption	2.3 kWh	20.5 kWh
price (reagents + energy)	166 €	274 €
working atmosphere	no inert atmosphere	inert atmosphere
colloidal stability	organic/aqueous media	organic media

[a]For the reagents, Sigma-Aldrich prices were used. A 0.0952 €/kWh energy price was assumed according to Europe's energy Portal 2012. [b]Calculated by considering the necessary time used in one batch and adding the required batches to yield 1 g of material.

4. CONCLUSIONS

We have reported that by using a microwave heating route, very moderate temperature (160 °C) and very fast reaction time (5 min) are sufficient to produce iron oxide nanoparticles with small sizes (6 nm), reasonable polydispersity, good degree of crystallinity and excellent magnetic properties although the particles present irregular-lobular shapes. In addition to the stabilization of the nanoparticles in organic solvents, they can be easily dispersible in water without laborious ligand exchange or purification steps. Such characteristics can be consider attractive for scaling-up nanoparticle fabrication.

A significant difference encountered when comparing the nanoparticles synthesized by a microwave-assisted process with those obtained by thermal decomposition of the same size is the smaller surface reactivity of the nanoparticles obtained from the microwave route. We argue that such difference arises from crystallographic faceting planes of low Miller indices in the case of microwaves nanoparticles. This surface characteristic can be particularly relevant depending on the targeted final application and will certainly have an in uence on time aggregation, Oswald ripening processes as well as in their degradation profiles.

In terms of "eco-design" applied to the fabrication of nanoparticles we can conclude that the microwave approach yields an energy consumption reduced by a factor of 10 and 40% lower overall cost.

AUTHOR INFORMATION

Corresponding Author

*Telephone +34 935801853. Fax: +34 935805729. E-mail: roig@icmab.es.

Notes

The authors declare no competing financial interest.

ACKNOWLEDGMENTS

The authors acknowledge the helpful discussion with Dr. J. Faraudo and Dr. S. Marré. A. Emelyanov is acknowledged for his contribution on a sample preparation. The work was partially funded by the Spanish Government (MAT2009-08024, CONSOLIDER-Nanoselect-CSD2007-00041 and RyC contract to M.G.), the Generalitat de Catalunya (2009SGR203 and FI grant to O.P.) and the European Commission (FP7-Marie Curie Actions, PCIG09-GA-2011−294168).

REFERENCES

(1) Biello, D. *Sci. Am.* **2011**, *May*, 25.
(2) Lidstrom, P.; Tierney, J.; Wathey, B.; Westman, J. *Tetrahedron* **2001**, *57*, 9225−9283.
(3) de la Hoz, A.; Diaz-Ortiz, A.; Moreno, A. *Chem. Soc. Rev.* **2005**, *34*, 164−178.
(4) Kappe, C. O. *Angew. Chem., Int. Ed.* **2004**, *43*, 6250−6284.
(5) Peiro, A. M.; Domingo, C.; Peral, J.; Domenech, X.; Vigil, E.; Hernandez-Fenollosa, M. A.; Mollar, M.; Mari, B.; Ayllon, J. A. *Thin Solid Films* **2005**, *483*, 79−83.
(6) Bilecka, I.; Kubli, M.; Amstad, E.; Niederberger, M. *J. Sol-Gel Sci. Technol.* **2011**, *57*, 313−322.
(7) Yin, S.; Luo, Z.; Xia, J.; Li, H. *J. Phys. Chem. Solids* **2010**, *71*, 1785−1788.
(8) Estruga, M.; Domingo, C.; Ayllon, J. A. *Mater. Res. Bull.* **2010**, *45*, 1224−1229.
(9) Abdelsayed, V.; Aljarash, A.; El-Shall, M. S.; Al Othman, Z. A.; Alghamdi, A. H. *Chem. Mater.* **2009**, *21*, 2825−2834.
(10) Park, S.-E. *J. Phys. Chem. Solids* **2008**, *69*, 1501−1504.

(11) Dahl, J. A.; Maddux, B. L. S.; Hutchison, J. E. *Chem. Rev.* **2007**, *107*, 2228−2269.
(12) Bhattacharyya, S.; Gedanken, A. *J. Phys. Chem. C* **2008**, *112*, 659−665.
(13) Saremi-Yarahmadi, S.; Vaidhyanatha, B.; Upul Wijayantha, K. G. *Int. J. Hydrogen Energy* **2010**, *35*, 10155−10165.
(14) Deshmukh, R. G.; Badadhe, S. S.; Mulla, I. S. *Mater. Res. Bull.* **2009**, *44*, 1179−1182.
(15) Bilecka, I.; Niederberger, M. *Nanoscale* **2010**, *2*, 1358−1374.
(16) Baghbanzadeh, M.; Carbone, L.; Cozzoli, P. D.; Kappe, C. O. *Angew. Chem., Int. Ed.* **2011**, *50*, 11312−11359.
(17) Pascu, O.; Gich, M.; Herranz, G.; Roig, A. *Eur. J. Inorg. Chem.* **2012**, 2656−2660.
(18) Pascu, O.; Caicedo, J. M.; Lopez-Garcia, M.; Canalejas, V.; Blanco, A.; Lopez, C.; Arbiol, J.; Fontcuberta, J.; Roig, A.; Herranz, G. *Nanoscale* **2011**, *3*, 4811−4816.
(19) Kang, E.; Park, J.; Hwang, Y.; Kang, M.; Park, J.-G.; Hyeon, T. *J. Phys. Chem. B* **2004**, *108*, 13932−13935.
(20) Sun, S.; Zeng, H.; Robinson, D. B.; Raoux, S.; Rice, P. M.; Wang, S. X.; Li, G. *J. Am. Chem. Soc.* **2004**, *126*, 273−279.
(21) Kwon, S. G.; Hyeon, T. *Acc. Chem. Res.* **2008**, *41*, 1696−1709.
(22) Demortiere, A.; Panissod, P.; Pichon, B. P.; Pourroy, G.; Guillon, D.; Donnio, B.; Begin-Colin, S. *Nanoscale* **2011**, *3*, 225−232.
(23) Park, J.; Joo, J.; Kwon, S. G.; Jang, Y.; Hyeon, T. *Angew. Chem., Int. Ed.* **2007**, *46*, 4630−4660.
(24) Bronstein, L. M.; Huang, X.; Retrum, J.; Schmucker, A.; Pink, M.; Stein, B. D.; Dragnea, B. *Chem. Mater.* **2007**, *19*, 3624−3632.
(25) Park, J.; An, K.; Hwang, Y.; Park, J.-G.; Noh, H.-J.; Kim, J.-Y.; Park, J.-H.; Hwang, N.-M.; Hyeon, T. *Nat. Mater.* **2004**, *3*, 891−895.
(26) Frey, N. A.; Sun, S. In *Inorganic Nanoparticles Synthesis, Applications and Perspectives*; Altavilla, C., Ciliberto, E., Eds.; CRC Press Taylor & Francis Group: Boca Raton, FL, 2011; pp 33−68.
(27) Altavilla, C. In *Inorganic Nanoparticles Synthesis, Applications and Perspectives*; Altavilla, C., Ciliberto, E., Ed.; CRC Press Taylor & Fracis Group: Boca Raton, FL, 2011; pp 313−342.
(28) Schmid, G., Ed.; Wiley-VCH Verlag GmbH & Co. KGaA: Weinheim, Germany, 2004.
(29) Gubin, S. P., Ed.; Wiley-VCH Verlag GmbH & Co. KGaA: Weinheim, 2009.
(30) Auffan, M.; Rose, J.; Chanéac, C.; Jolivet, J.-P.; Masion, A.; Wiesner, M. R.; Bottero, J.-Y.; Houdy, P.; Lahmani, M.; Marano, F., Eds.; Springer: Berlin and Heidelberg, Germany, 2011; pp 264−269.
(31) Ridley, M. K.; Hackley, V. A.; Machesky, M. L. *Langmuir* **2006**, *22*, 10972−10982.
(32) Taboada, E.; Rodriguez, E.; Roig, A.; Oro, J.; Roch, A.; Muller, R. N. *Langmuir* **2007**, *23*, 4583−4588.
(33) Rodriguez-Carvajal, J. *Physica B* **1993**, *192*, 55−69.
(34) Lamer, V. K.; Dinegar, R. H. *J. Am. Chem. Soc.* **1950**, *72*, 4847−4854.
(35) Morales, M. P.; Veintemillas-Verdaguer, S.; Montero, M. I.; Serna, C. J.; Roig, A.; Casas, L.; Martínez, B.; Sandiumenge, F. *Chem. Mater.* **1999**, *11*, 3058−3064.
(36) Su, D.; Horvat, J.; Munroe, P.; Ahn, H.; Ranjbartoreh, A. R.; Wang, G. *Chem.—Eur. J.* **2012**, *18*, 488−497.
(37) Wang, Z. L. *J. Phys. Chem. B* **2000**, *104*, 1153−1175.
(38) Wu, W.; He, Q.; Jiang, C. *Nanoscale Res. Lett.* **2008**, *3*, 397−415.
(39) Zhang, L.; He, R.; Gu, H.-C. *Appl. Surf. Sci.* **2006**, *253*, 2611−2617.
(40) Zboril, R.; Bakandritsos, A.; Mashlan, M.; Tzitzios, V.; Dallas, P.; Trapalis, C.; Petridis, D. *Nanotechnology* **2008**, *19*, 095602−095610.
(41) De Palma, R.; Peeters, S.; Van Bael, M. J.; Van den Rul, H.; Bonroy, K.; Laureyn, W.; Mullens, J.; Borghs, G.; Maes, G. *Chem. Mater.* **2007**, *19*, 1821−1831.
(42) Viali, W. R.; Alcantara, G. B.; Sartoratto, P. P. C.; Soler, M. A. G.; Mosiniewicz-Szablewska, E.; Andrzejewski, B.; Morais, P. C. *J. Phys. Chem. C* **2010**, *114*, 179−188.
(43) Parekh, K.; Upadhyay, R. V.; Belova, L.; Rao, K. V. *Nanotechnology* **2006**, *17*, 5970−5975.
(44) Roca, A. G.; Morales, M. P.; O'Grady, K.; Serna, C. J. *Nanotechnology* **2006**, *17*, 2783−2788.
(45) Tomoaia-Cotisel, M.; Zsako, J.; Mocanu, A.; Lupea, M.; Chifu, E. *J. Colloid Interface Sci.* **1987**, *117*, 464−476.
(46) Khanna, V.; Zhang, Y.; Grubb, G.; Bakshi, B. *R. in Nanoscience and Nanotechnology Environmental and Health Impact*; Grassian, V. H., Ed.; John Wiley & Sons, Inc.: Hoboken, NJ, 2008; p 19.
(47) Nair, B. *Int. J. Toxicol.* **2001**, *20* (Suppl 3), 23−50.

RSC Advances

View Online / Journal Homepage
Dynamic Article Links

Cite this: DOI: 10.1039/c2ra21500d

www.rsc.org/advances

PAPER

Design of biocompatible magnetic pectin aerogel monoliths and microspheres

Carlos A. García-González,*[a] Elisa Carenza,[b] Muling Zeng,[b] Irina Smirnova*[a] and Anna Roig*[b]

Received 19th July 2012, Accepted 22nd August 2012
DOI: 10.1039/c2ra21500d

Novel material formulations for biomedical uses containing magnetic nanoparticles are currently being explored. The synergistic combination of a polymeric matrix and a filler with magnetic properties in hybrid nanoporous materials (aerogels) will confer versatility to the product. In this work, the use of pectin aerogels as a biodegradable matrix containing maghemite nanoparticles (γ-Fe_2O_3 NPs) is studied. The γ-Fe_2O_3 NPs-loaded pectin aerogels are developed in two different morphologies (cylindrical monoliths and microspheres) prepared by a combination of sol–gel and supercritical drying methods. In the case of the aerogel microspheres, the sol–gel method was substituted by the emulsion-gelation procedure. The obtained aerogel-based materials were evaluated regarding their physical appearance and stability and their textural and magnetic properties. The particle size distribution and morphology of the aerogel microspheres were additionally analyzed by laser dispersion spectrometry, static image analysis and scanning electron microscopy. Process parameters influenced the distribution of the γ-Fe_2O_3 NPs within the material. Whereas the γ-Fe_2O_3 NPs were homogeneously distributed throughout the aerogel monoliths, γ-Fe_2O_3 NPs were mostly deposited on the outer surface of the aerogel microspheres. The magnetic properties of maghemite were preserved in the end material after overall processing.

A Introduction

Nowadays, there is a great demand for smart products in the form of nanostructured hybrid organic–inorganic materials. The synergistic characteristics of the different components of these materials provide a broad spectrum of selected properties that meet the requirements of many industrial applications, such as lightweight structural materials, catalysis, electronic or optical devices, medical implants or drug delivery systems.[1]

Maghemite nanoparticles (NPs) under the size of *ca.* 30 nm, have superparamagnetic character at room temperature, high magnetic susceptibility and high saturation magnetization as well as biocompatibility and non-toxicity.[2–4] These properties are already being exploited in several biomedical applications (targeted drug delivery, hyperthermia, contrast agents in magnetic resonance imaging or bioseparation).[5–7] Additionally, iron oxide nanoparticles are the only magnetic nanoparticle approved for clinical use by the US Food and Drug Administration (USFDA).[8] The entrapment of magnetic nanoparticles in polymeric porous matrices will add new functionalities to the polymer and improve the handling of the material. Uses of polysaccharides incorporating iron oxide are being intensively explored because of the non-toxicity and biocompatibility of both materials.[3,9–11] Among the polysaccharide family, pectin is particularly effective as a colonic therapeutic delivery agent because of its resistance to protease and amylase in the upper gastrointestinal tract.[2,12–15]

Supercritical fluid technology, using primarily supercritical carbon dioxide ($scCO_2$), allows the production of nanostructured materials, overcoming some of the limitations of conventional top-down and bottom-up approaches.[16,17] Moreover, the use of $scCO_2$ avoids the post-processing steps of purification generally required by conventional methods to remove organic solvents from the material.[18] In particular, the supercritical drying of gels is a commonly used technology for the production of lightweight (ρ = 0.05–0.50 g cm^{-3}) mesoporous materials, the so called aerogels. The outstanding porosity and textural properties of aerogels are currently being exploited in thermal insulation, catalysis, drug delivery systems and adsorption of pollutants among other applications.[19–21] In addition to these applications, physiologically acceptable microspheres of organic aerogels can be used either for inhalation or oral drug delivery routes and, if composited with a magnetic material, they can be targeted to the appropriate site and tracked by magnetic resonance imaging (MRI).[19,22,23]

The incorporation of magnetic iron oxide NPs in aerogels has already been reported in the form of pure iron oxide aerogels,[24] iron oxide–silica composite aerogels[25–27] and $CoFe_2O_4$–cellulose composite aerogels.[28] In this work, maghemite nanoparticles were incorporated in biocompatible and biodegradable pectin gel matrices in the form of bulk cylinders and microspheres.

[a]*Institute of Thermal Separation Processes, Hamburg University of Technology, Eißendorferstraße 38, D-21073 Hamburg, Germany. E-mail: carlos.garcia@tuhh.de; irina.smirnova@tuhh.de; Fax: 0049 40 42878 4072; Tel: 0049 40 42878 3642*
[b]*Institut de Ciència de Materials de Barcelona (CSIC), Campus de la UAB, E-08193 Bellaterra, Spain. E-mail: roig@icmab.es; Tel: 0034 935801853*

Supercritical drying was then used to obtain magnetic pectin aerogels. The properties of the final materials were examined with regard to their potential application as magnetic targeting drug delivery vehicles.

B Experimental methods

B.1 Reagents

The following chemicals were purchased from Sigma-Aldrich for γ-Fe_2O_3 NPs preparation and were used without any purification: iron(III) acetylacetonate ($Fe(acac)_3$, 97%), oleic acid (analytical standard), benzyl alcohol (98%), hexane (anhydrous, 95%), ethanol, water solution (25 wt%) of trimethylammonium hydroxide (TMAOH), sodium citrate and deionised water.

Two medium-rapid set HM pectin from apple–citrus (WECJ-1, degree of esterification–DE: 66–68%, Pektowin) and citrus (76280, DE: 63–66%, Fluka) peels were used. Ethanol (99.8% purity) and vegetable (canola) oil were obtained from Omnilab and domestic shops, respectively. Deionized water was used in all gelation experiments.

B.2 Processing

B.2.1 Preparation of γ-Fe_2O_3 nanoparticles. A non-aqueous sol–gel microwave-assisted chemical reaction, similar to the one reported by Niederberger *et al.*,[29] was used. The most relevant difference in our case is the addition of oleic acid during the synthesis as a stabilizer.[30] The microwave experiments were carried out using a CEM Discover reactor (Explorer 12-Hybrid) operating at a frequency of 2.45 GHz and with a maximum power of 300 W. For a typical run, the power was automatically adjusted to heat the sample to the set reaction parameters (temperature and time). During a chemical reaction, the temperature and pressure were monitored by a volume-independent infrared sensor. γ-Fe_2O_3 NPs were obtained by dissolving 0.35 mmol $Fe(acac)_3$ and 1.05 mmol oleic acid in 4.5 ml anhydrous benzyl alcohol (with a high dielectric loss tangent value) at 333 K for 5 min in the microwave reactor under magnetic stirring for complete dissolution of the precursors. The precursor solution was further heated in the same microwave reactor to 433 K (typically using 200 W) and the temperature was kept constant for 5 min. Then, the solution was automatically cooled down to 323 K by compressed nitrogen in approximately 3 min. The final suspension was black. The nanoparticles were separated by adding ethanol (40 ml) before centrifuging at 4000 rpm for 20 min. The supernatant from this first centrifugation was decanted and the precipitate was dispersed in 2 ml hexane with 10 μl oleic acid and centrifuged again at 4000 rpm for 20 min. Because no precipitate was removed, the supernatant (nanoparticles in hexane) was centrifuged one more time with ethanol to eliminate the free surfactant. The precipitate was then re-dispersed in hexane, forming a clear dark brown colloidal dispersion. Hexane stabilized iron oxide nanoparticles were transferred to water by a ligand transfer procedure.[31] In brief, two separated phases were formed by mixing an equal volume ratio of NPs dispersed in hexane at a concentration of 10 mg ml^{-1} with a 0.4 M TMAOH–water solution (pH 12). The system was kept under magnetic stirring for 18 h. Next, the dispersion was left to separate again into two phases; the upper phase had a yellow colour and the lower aqueous phase was dark brown, signalling the transfer of the nanoparticles. The hexane phase was carefully removed and the nanoparticles were precipitated by centrifugation (4500 rpm, 20 min), adding acetone to the water solution. The supernatant was decanted and the precipitate was re-dispersed by using ultrasound in a TMAOH–water solution. To stabilize the nanoparticles in water at pH 7, nitric acid and sodium citrate solution (4 mM) in a 1 : 1 volume ratio were added under magnetic stirring. After this step, the water dispersions were ready to be incorporated into the gels.

B.2.2 Preparation of γ-Fe_2O_3-pectin gels. 6% (w/w) pectin aqueous solution was prepared by 24 h mixing with magnetic stirrer (500 rpm). In the cases where the maghemite NPs were incorporated, the maghemite colloidal aqueous dispersion was further diluted in water before the addition of the pectin. 40 g of the pectin solution was heated at 313–333 K with agitation (marine type, d = 40 mm, stirring 500 rpm) for 30 min in an open vessel. Then, a given amount of ethanol was added to this solution (15–25 wt% with respect to the water content), resulting in a very rapid increase in viscosity. The viscous mixture was heated for 5 additional min at 313–333 K. Finally, the mixture was transferred into 5 ml syringes and sealed with Parafilm. After 24 h at room temperature, a two-step (two-fold 99.8% (v/v) EtOH) solvent exchange (SE) at room temperature was performed.

B.2.3 Preparation of γ-Fe_2O_3-pectin gels in the form of microspheres. HM pectin microspheres were prepared *via* the emulsion-gelation method.[22,32] Oil : pectin solution emulsions with 3 : 1 (4 : 1, 5 : 1 and 6 : 1) mass ratios were prepared by mixing (500 rpm) an aqueous phase containing 6% (w/w) of pectin with the corresponding amount of canola oil. For certain 6 : 1 oil-to-pectin solution emulsions, maghemite NPs were dispersed in water before being added to the oil. Ethanol (50 wt% with respect to water content) was then added to the mixture. The resulting emulsion was heated to 313–333 K for 30 min with agitation (marine type, d = 40 mm, stirring 500 rpm). Then, the mixture was placed in an ice bath and continuously stirred at 1400 rpm. Cooling was continued until the oil dispersion containing the weak pectin gel microspheres reached 293 K, after which additional ethanol (to get 100 wt% total ethanol content with respect to water content) was added drop-wise to the liquid mixture. The dispersion was stirred for 2 additional minutes, and then centrifuged (4500 rpm, 5 min). After centrifugation, the pectin microparticles were separated from the oil phase, immersed in 99.8% (v/v) EtOH and stored at room temperature. After 24 h, the gel microspheres were collected and soaked in fresh 99.8% (v/v) EtOH (*i.e.* second solvent exchange).

B.2.4 Supercritical drying of pectin gels. After solvent exchange, the resulting pectin alcogels were dried continuously by supercritical CO_2,[20] using the equipment shown in Fig. 1. In a typical experiment, the alcogels immersed in ethanol were placed into the autoclave (E1 in Fig. 1) and E1 was heated to 313 K by a thin electrical band heater. Once the temperature in the autoclave was constant, CO_2 was fed to E1 by a high-pressure diaphragm compressor (P1, Whitey LC10) until the desired

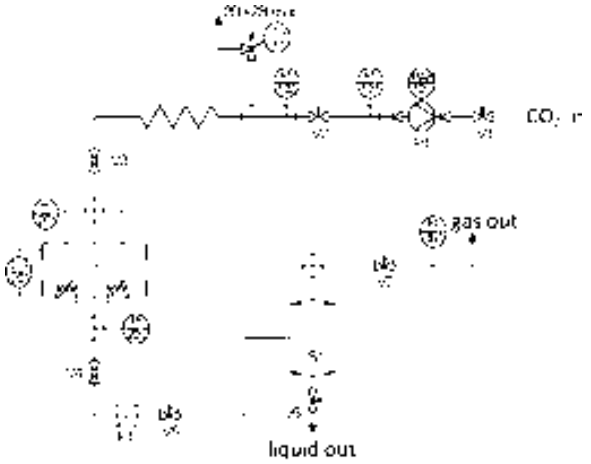

Fig. 1 Process flow diagram of the equipment used for the supercritical drying of pectin aerogels. Tags: V1–V7 = valves; P1 = compressor; E1 = autoclave; S1 = separator; F1 = filter; PAH-101 = high-level pressure alarm; PI-xxx = pressure gauges; PSV-001 = safety valve; TI-201 = thermocouple; LG-201 = sapphire window; FI-301 = flow meter.

working pressure (11.0–12.0 MPa) was reached. The flow of $scCO_2$ from the autoclave was then started by opening valve V4 and the flow rate (2–4 nL min^{-1}) was regulated by the micrometering valve V5. Pectin alcogel monoliths and microspheres were dried in the autoclave for 4 h to assure a complete removal of the solvent. Finally, the pressure was released slowly (depressurization) over 30–60 min at constant temperature (313 K) until atmospheric pressure was reached.

B.3 Physicochemical characterization of the materials

Powder X-ray diffraction patterns of the nanoparticles were measured with a Rigaku, "rotaflex" RU-200B model using a Cu anode with $\lambda_{K\alpha1}$ = 1.5406 Å and $\lambda_{K\alpha2}$ = 1.5444 Å in the 2θ range 20–70°. The diffractogram could be indexed with the maghemite pattern. TEM micrographs for the maghemite nanoparticles were obtained with a JEOL JEM-1210 electron microscope, operating at 120 kV. The samples were prepared by depositing a drop of diluted nanoparticle dispersion in hexane onto a TEM grid and allowing the solvent to evaporate. The mean diameter and polydispersity of each of the nanoparticles were determined by fitting to a Gaussian distribution a particle size histogram of over 200 counts measured from TEM images by the ImageJ software. The hydrodynamic diameters of the maghemite nanoparticles suspended in organic media and water were investigated with a Zetasizer Nano ZS from Malvern Instruments equipped with a He/Ne 633 nm laser. The bulk density (ρ_{bulk}) of the pectin aerogel monoliths was determined by measuring the dimensions and weight of the samples after drying with $scCO_2$. The porosity (ε) of the aerogel can be calculated with the obtained ρ_{bulk} and skeletal density ($\rho_{skeletal}$) by eqn (1):

$$\varepsilon = 1 - \frac{\rho_{bulk}}{\rho_{skeletal}} \quad (1)$$

The textural properties of the aerogels were determined by low-temperature N_2 adsorption–desorption analysis (Nova 3000e). Prior to measurements, the samples were dried under vacuum (<1 mPa) at 333 K for 20 h. The specific surface area (A_{BET}) was determined by the BET (Brunauer–Emmett–Teller) method. The pore volume (V_p) and mean pore diameter (d_p) were estimated using the BJH (Barrett–Joyner–Halenda) method. The iron oxide content in pectin aerogels (6–8 mg) was evaluated thermogravimetrically using a TGA Netzsch TG 209 F1 instrument. Measurements were performed under an oxygen atmosphere with a heating rate of 10 K min^{-1} in the range between room temperature and 1273 K. Micrographs of the pectin aerogel particles were taken in a scanning electron microscope (SEM), and images were acquired using a Quanta FEI 200F microscope in low vacuum mode with a cone LOW kV P.L.A. type with a 500 μm aperture, equipped with a solid-state backscattered probe for energy dispersive X-ray spectrometry (EDS) analysis. Except for maghemite-loaded materials, samples were gold-sputtered (10 nm thickness) prior to imaging in order to minimise charging and improve the image contrast. Particle size distributions of the pectin wet microspheres dispersed in ethanol were measured using a laser dispersion spectrometer (Beckman Coulter LS1332) and with similar obscuration values. The particle size distributions and shapes of dried aerogel microspheres were evaluated by using static image analysis equipment (Morphologi G3) that allows size measurements between 0.5 μm–3000 μm. Magnetic characterization of the maghemite particles and the nanocomposited microspheres were performed with a quantum interference device (SQUID) magnetometer (Quantum Design MPMS5XL).

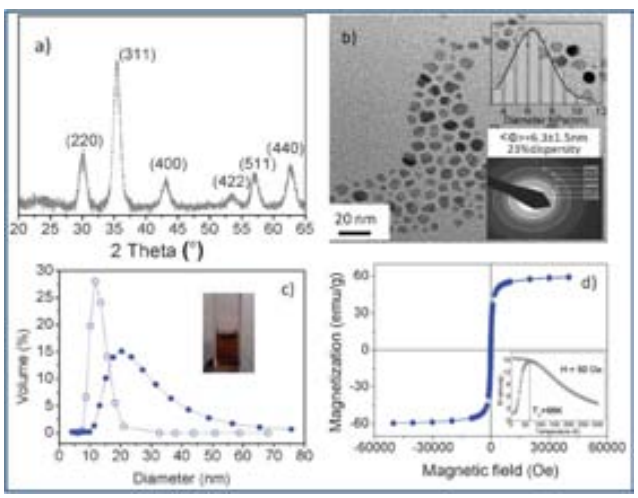

Fig. 2 (a) X-Ray diffraction patterns corresponding to maghemite nanoparticles. (b) TEM image of the nanoparticles. Upper inset includes a size distribution histogram fitted to a Gaussian and the lower inset shows a selected area electron diffraction pattern corresponding to maghemite. (c) Dynamic light scattering histogram of the organic stabilized nanoparticles (empty symbols) and the water stabilized dispersion after ligand exchange (full symbols); a cuvette containing the clear nanoparticle dispersion is shown as an inset. (d) Magnetic characterization of the iron oxide nanoparticles. $M(H)$ at 300 K and $M(T)$, ZFC–FC curves (inset)

C Results and discussion

C.1 Characterization of the γ-Fe_2O_3 nanoparticles

Maghemite nanoparticles were fabricated by microwave-assisted non-hydrolytic sol–gel synthesis. Oleic acid was added to the initial precursor solution to render the nanoparticles stable as colloids in organic solvents. Subsequently, the nanoparticles were transferred to aqueous solutions through a ligand exchange using TMAOH as an electrostatic stabilizer. Powder X-ray diffraction (Fig. 2a) can be indexed to the maghemite, an inverse spinel structure (ICDD PDF039-1346).

Size, polydispersity, shape and structural phase of the nanoparticles were studied by TEM (Fig. 2b). The particles have roughly spherical shapes. The size distribution histogram from a 250 particle count (inset of Fig. 2b) gives an average particle size of 6.3 ± 1.5 nm. Nanoparticles transferred in water at pH 7 formed stable aggregates with a 35 nm mean size (Fig. 2c) and a zeta potential value of −40 mV.

The magnetic properties of the material were evaluated by magnetization *versus* magnetic field at 300 K and zero-field cooled (ZFC)–field cooled (FC) temperature dependent magnetization curves (Fig. 2d). The results at 300 K show a typical magnetization curve of a superparamagnetic system with neither hysteresis nor remanent magnetization. The saturation magnetization is large, 60 emu g^{-1}, pointing to a high crystallinity. Superparamagnetism is also confirmed by the ZFC–FC magnetization curve (inset Fig. 2d). The ZFC magnetization increases with temperature until reaching a maximum, corresponding to the blocking temperature, at 66 K. Above this temperature, the thermal energy becomes larger than the magnetic energy barrier and the nanoparticles enter the superparamagnetic regime.

C.2 γ-Fe_2O_3-pectin aerogels

Aerogel processing starts with the formation of a gel from an aqueous solution, *i.e.* a hydrogel. Then, the water filling the pores of the gel structure is replaced by ethanol, leading to an alcogel, followed by the extraction of the ethanol from the gel by supercritical carbon dioxide ($scCO_2$)-assisted drying. The usual method of pectin gelation by the addition of sucrose[15] to decrease pectin hydration was not suitable to undergo this aerogel processing. During the needed solvent exchange step of the hydrogel to ethanol, the sucrose precipitated and the gel was no longer mechanically stable (Fig. 3, left). Other gelation mechanisms proposed in the literature[33] led to powdery and unstable aerogels by thermal gelation or low textural properties (A_{BET} = 200 m^2 g^{-1}; V_p = 0.38 cm^3 g^{-1}) by acidic gelation. Therefore, a novel processing method for the preparation of pectin aerogels compatible with the intended life science applications was developed in this work. The thermal gelation of HM-pectin (333–353 K, 30 min) with the addition of ethanol (15–25 wt% to water content) produces mechanically stable pectin hydrogels. The addition of ethanol promotes pectin gelation by means of improving the prevalence of pectin–pectin interactions rather than pectin–solvent interactions. Thus, an increase in the viscosity of the pectin solution and the formation of a stable gel is obtained.[34] The use of ethanol as a gelation promoter also effectively reduces the processing time of biocompatible pectin aerogels, either by increasing the solvent exchange rate to ethanol or, if necessary, decreasing the number of solvent exchange steps prior to supercritical drying. Two types of HM-pectin of different origins (citrus and apple–citrus) underwent the same thermal gelation method with equal concentrations of pectin (6 wt% to the water content) followed by direct solvent exchange to ethanol. It was noticed that the immersion of even very soft hydrogel monoliths in EtOH resulted in a rapid increase in hardness after only 1–2 min contact, pointing to a chemical interaction of the pectin with ethanol. Thus, the hydrogels of HM-citrus pectin were generally softer than the gels of apple–citrus pectin but were just as hard after solvent exchange to ethanol. A marked shrinkage in the middle of the gel monolith (Fig. 3, middle) prepared from citrus pectin was observed for different concentrations of pectin, whereas a homogeneous reduction in volume occurred for all samples of apple–citrus pectin (Fig. 3, right). The differences in degree of esterification and molecular structure of pectin depending on the extraction process and the source may lead to the formation of network structures with quite different physical properties.[35,36] The differences in solvent diffusion through the HM-citrus and apple–citrus pectin gel networks may also be related to their different segmental rod-like gel structures.[33,37] Taking these results into consideration, the HM-pectin from apple–citrus was used for further investigation of pectin aerogel processing.

Supercritical CO_2 drying of pectin alcogels (Fig. 4a) over 4 h produced lightweight (ρ = 0.08 g cm^{-3} in Table 1), highly porous (ε = 95%) aerogels (Fig. 4b). Shorter supercritical drying times (1 h) resulted in partial solvent (ethanol) removal, leading to dramatic volume shrinkage and poor physicochemical properties (ρ = 0.32 g cm^{-3}; ε = 77.7%; A_{BET} = 129 m^2 g^{-1}) (not shown). Gel volume shrinkage due to the direct solvent exchange step to ethanol (after SE shrinkage in Table 1) were small in comparison with those obtained after the supercritical drying step (overall shrinkage). Finally, vacuum drying (60 °C, 4 h) was attempted as an alternative drying method but the wet gel structure was not

Fig. 3 Physical appearance of different pectin gel monoliths after solvent exchange to ethanol: HM-pectin from citrus with (left) and without (middle) sucrose addition during gelation, and HM-pectin from apple–citrus without sucrose addition (right).

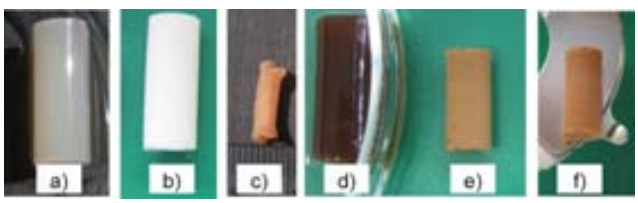

Fig. 4 Drying of (a) pectin hydrogel monoliths by means of (b) supercritical drying, aerogel, and (c) vacuum drying, xerogels. Maghemite nanoparticles can be incorporated in (d) the pectin gel matrix leading to (e) brownish aerogels after supercritical drying. (f) Monolith with 1.5–2.0 wt% in NPs attracted by a magnet.

Table 1 Physicochemical properties of pectin aerogel monoliths with and without addition of maghemite NPs

Fe NP content	Shrinkage (%)		ρ (g cm^{-3})	ε (%)	A_{BET} (m^2 g^{-1})	V_p (cm^3 g^{-1})	d_p (nm)
	After SE	Overall					
None	12 ± 3	48 ± 28	0.08 ± 0.03	95 ± 1	247 ± 12	1.2 ± 0.1	17 ± 1
High	26 ± 3	61 ± 2	0.11 ± 0.01	93 ± 1	284 ± 14	1.5 ± 0.1	22 ± 1

preserved, resulting in a massive volume shrinkage and pore collapse, leading to xerogel type of materials (Fig. 4c) with poor textural properties ($S_{a,BET} < 5$ m^2 g^{-1}).

The influence of the addition of iron oxide nanoparticles onto the pectin gel and aerogel monoliths was examined in this work. Pectin monoliths were prepared by incorporation of the NPs (1.5–2.0 wt% content as a percentage with respect to the pectin content) to the pectin solution. The pectin solutions turned more viscous with the addition of the NPs. Moreover, such addition interfered with the gelation mechanism, leading to an increase in the gelation time. Translucent dark brownish NP-containing pectin hydrogels were thus obtained. No significant leaching of NPs was observed during solvent exchange to ethanol (Fig. 4d). Upon addition of the NPs to the pectin gel formulation, a higher shrinkage is achieved during the solvent exchange and drying processes (Table 1) resulting in opaque, brownish and mechanically stable aerogels (Fig. 4e). The resulting aerogel density increased, due to both the higher shrinkage of the aerogels and the higher skeletal density of maghemite (4.87 g cm^{-3})[2,38] with respect to raw pectin (1.44 g cm^{-3}). However, the addition of NPs enhanced the textural properties of the aerogels (A_{BET}, V_p and d_p in Table 1). Finally, due to the magnetic properties of the maghemite, the pectin aerogel was attracted to a magnet (Fig. 4f).

C.3 Preparation of γ-Fe_2O_3-pectin aerogels in the form of microspheres

The processing method for the preparation of the maghemite NP-loaded pectin aerogel monoliths described in Section 3.2 was adapted for the preparation of aerogel microspheres. The emulsion-gelation method[32,39] was used to produce microspherical gels with the same HM-apple–citrus pectin concentration (6 wt% to the water content) as the monoliths. Previous studies[22,32] have shown that the textural properties of aerogel microspheres are mainly influenced by the gelation parameters (*e.g.* precursor concentration, crosslinking concentration, temperature) and that results obtained for aerogel monoliths can be applied to the development of aerogel microspheres. On the other hand, particle morphology (roundness, mean size, size distribution) is primarily affected by emulsion parameters (*e.g.* oil-to-aqueous phase ratio, surfactant concentration, agitation speed). Moreover, the ability of HM-apple–citrus pectin to provide the phase inversion of the emulsions at certain pectin concentrations was detected. During the cooling and mixing of the emulsion with a 2 : 1 (w/w) oil-to-pectin solution ratio, the phase inversion of the emulsion was observed 2–3 min after addition of ethanol. Therefore, the oil-to-pectin solution ratio was increased to 6 : 1 (w/w) to avoid phase inversion of the emulsion. The increase in the oil-to-pectin solution ratio led to an increase in the mean particle size and a broader particle size distribution (Fig. 5). The formation of larger particles with increasing oil content can be explained by an increase in viscosity

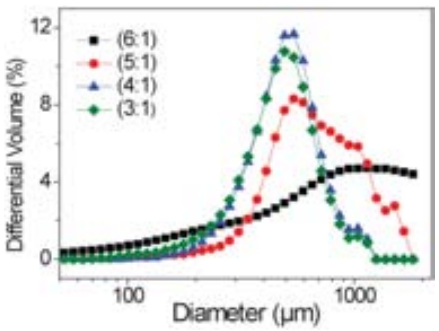

Fig. 5 Particle size distribution of pectin particles at different oil to water ratios from pectin raw material.

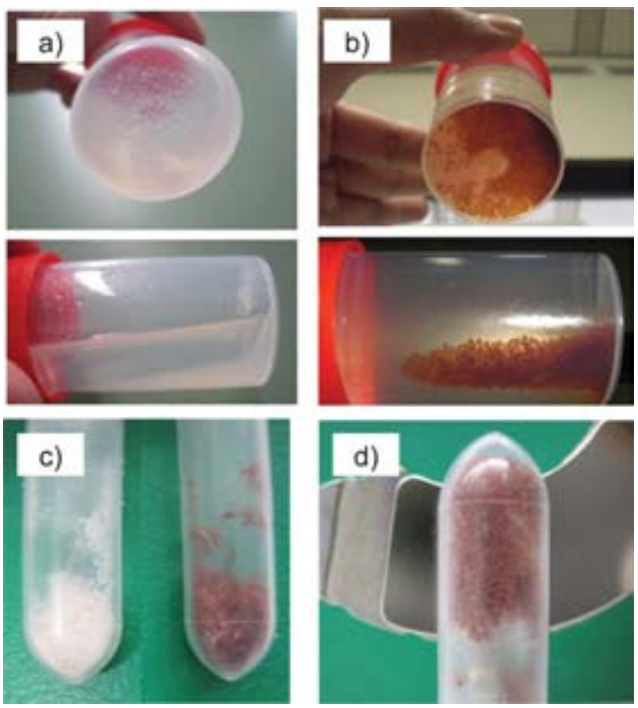

Fig. 6 Pectin alcogel microspheres (a) without and (b) with maghemite NPs were dried by supercritical drying to get nanocomposite aerogels. (c) Maghemite nanoparticle addition led to brown-coloured microspheres (without NPs, left, and with NPs, right). (d) Aerogel microspheres with high NP content (3.7 wt%) were attracted to a magnet.

of the liquid mixture, resulting in an increase in the aqueous droplet size. The use of different oil-to-water ratios did not significantly affect the textural properties of the resulting pectin aerogel microspheres with BET-specific surface areas in the range 440–480 m^2 g^{-1}.

The addition of maghemite NPs to the formulation of pectin gel microspheres led to a change from a light cream colour to

dark brown in both the gel and aerogel microspheres (Fig. 6). No significant leaching of NPs during solvent exchange to ethanol was observed, since the supernatant was colourless and transparent in all cases. The maghemite content of the materials was calculated by TGA as the difference in weight remaining after thermal treatment up to 1263 K of the nanocomposite material (7.6 wt%, Fig. 6c right) compared to the weight loss observed in the pectin aerogel (3.9 wt%, Fig. 6c left). A maghemite content in the aerogel microspheres of 3.7 wt% was obtained. Moreover, the incorporation of the iron oxide-NPs within the pectin aerogel network improved the end textural properties of the microspheres (with 3.7 wt% NPs content: A_{BET} = 501 ± 25 m^2 g^{-1}, V_p = 2.8 ± 0.2 cm^3 g^{-1} and d_p = 17 ± 1 nm; without NPs: A_{BET} = 442 ± 22 m^2 g^{-1}, V_p = 2.4 ± 0.1 cm^3 g^{-1} and d_p = 31 ± 2 nm).

The particle size distribution of wet alcogels and dried aerogels were studied by laser dispersion spectrometry (Fig. 7) and by static image analysis (Fig. 8a), respectively.

Shrinkage of the particle size of pectin microspheres can be observed after supercritical drying when comparing the median particle diameters (d_{50}) of the wet gels and aerogels (insets in Fig. 7 and Fig. 8a). This trend agrees with the volume shrinkage observed for the pectin aerogel monoliths (Section 3.2). High sphericity of the aerogel particles was obtained with circularity values greater than 0.95 (Fig. 8b,c). However, the presence of few aggregates was noticed for the aerogel microspheres without γ-Fe_2O_3 NPs (Fig. 8c). A shift towards lower particle sizes and coarser particle size distribution was observed when maghemite NPs were incorporated in both the wet and the dry forms.

The SEM pictures of pectin aerogels (Fig. 9a,b) show spherical particles with a porous microstructure formed by a rod-like network. A similar appearance was observed for the maghemite NP-loaded pectin aerogels (Fig. 9c,d). Lighter areas, corresponding to NP addition, were observed in Fig. 9d. SEM pictures of the NP loaded-aerogels without gold sputtering improved the contrast between the iron NPs (conductive) and the pectin matrix (low conductivity) (Fig. 10). It was then observed that the iron NPs formed a layer on the surface of the pectin aerogel microspheres (Fig. 10a). However, the NPs in the aerogel particle were not homogeneously distributed upon the surface

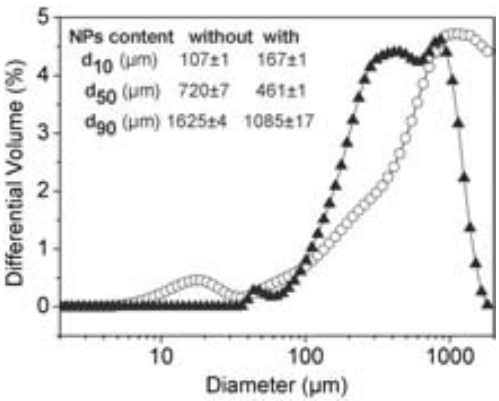

Fig. 7 Particle size distribution by laser dispersion spectrometry of pectin gel microspheres with (triangles) and without (circles) maghemite NPs. Inset: percentiles 10 (d_{10}), 50 (d_{50}) and 90 (d_{90}) of the particle size distribution for both samples.

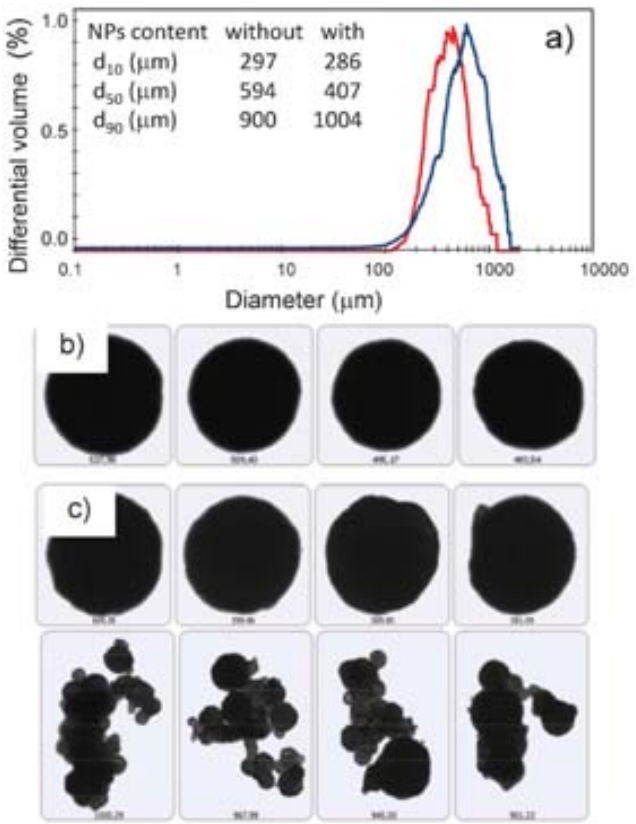

Fig. 8 Static image analysis of pectin aerogel microspheres with (red) and without (blue) maghemite NPs: (a) particle size distribution; intake: percentiles 10 (d_{10}), 50 (d_{50}) and 90 (d_{90}) of the particle size distribution for both samples. Microspheres with high sphericity were obtained in both cases (b,c), although the presence of some agglomerates was observed in the case of aerogels without γ-Fe_2O_3 NPs (c).

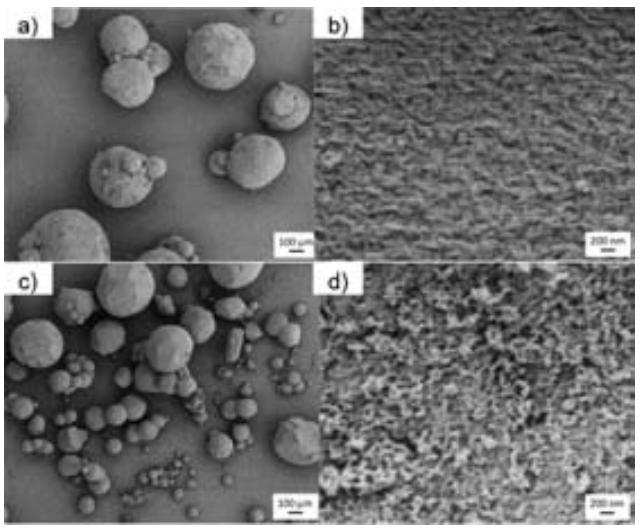

Fig. 9 SEM pictures of pectin aerogel microspheres without (top) and with the addition of γ-Fe_2O_3 NPs (bottom).

but formed islands of a few monolayers thick, which were easily seen when using the electron retrodispersion mode of the SEM (Fig. 10a,b). The maghemite origin of the islands was confirmed by iron content detection with EDS analysis (Fig. 10c).

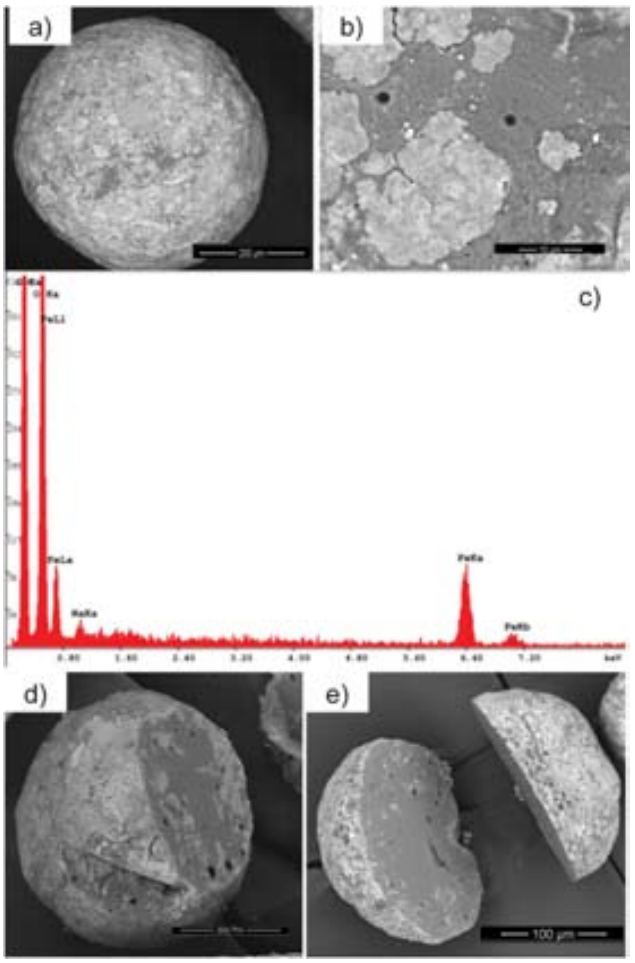

Fig. 10 Distribution of γ-Fe_2O_3 NP loading in pectin aerogel microspheres: (a) γ-Fe_2O_3 NPs were observed in the outer surface of the aerogel microspheres (b) forming islands. (c) EDS analysis confirmed the γ-Fe_2O_3 NPs origin of the islands. (d,e) SEM pictures of cut microspheres reveal that γ-Fe_2O_3 NPs are mainly present in the outer shell of the aerogel microsphere.

The chemical interaction *via* hydrogen bonding of the hydroxyl groups of the maghemite NPs and the carbonyl groups of the pectin matrix is regarded as a plausible reason for the adsorption of NPs in the aerogel. This NP–pectin interaction also explains the insignificant loss of NPs upon aerogel processing during the removal of the oil phase or the solvent exchange steps to ethanol. Similar chemical interactions between other carbonyl group-containing compounds and inorganic oxides have been previously reported in the literature.[40]

Cutting of the pectin aerogel microspheres, using a scalpel, revealed that the γ-Fe_2O_3 NPs were predominantly located on the surface (Fig. 10d,e). The origin of this NP layer on the surface of the pectin aerogel microspheres is thought to arise from the spontaneous location of the NPs in the water–oil interface of the emulsion prior to the gelation of the disperse phase (pectin aqueous solution). This effect was related to the reduction of the surface charge of the NPs due to the competitive adsorption on the NPs of the ethanol added to the system to promote gelation.[41] Moreover, the change in surface charge of the NPs is also promoted by the lowering of the pH value in the aqueous solution (γ-Fe_2O_3 NPs initially stabilized at pH 7 were put in contact with pectin solutions at pH 3.3).[42] The reduction of the water–oil interfacial energy by means of the adsorption of the NPs on this region is regarded as the driving force behind this local and spontaneous assembly of the maghemite particles at the interface. Hydrodynamic forces in the emulsion due to the density difference between the NPs and the aqueous solution (*e.g.* biased Brownian motion of the NPs in a centrifugal force field within the aqueous solution droplets) may also favor the location of the NPs in the water–oil interface.

Moreover, the prevention of droplets from flocculation and coalescence due to the binding of the NPs to the surface of the water droplets (oil/water interphase) in a Pickering-like emulsion might cause the emulsion to be more stable (*i.e.* fewer aggregates)[43] and may explain the reduction in aerogel particle size after the addition of NPs previously observed in Fig. 8.

Finally, the magnetic properties of the microspheres were evaluated by magnetization *versus* magnetic field at 300 K (Fig. 11). The results show a typical magnetization curve of a superparamagnetic system with neither hysteresis nor remanent magnetization, as was also the case of the original maghemite nanoparticles (Fig. 2). This result indicates that the incorporation of maghemite nanoparticles in the pectin aerogel microspheres does not modify the properties of the initial nanoparticles, even though they formed aggregates. The inset of Fig. 11 contains a zero field cooled–field cooled magnetization curve as a function of temperature. The ZFC curve displays a clear maximum, signaling a blocking temperature at around 40 K, as expected for a superparamagnetic system.

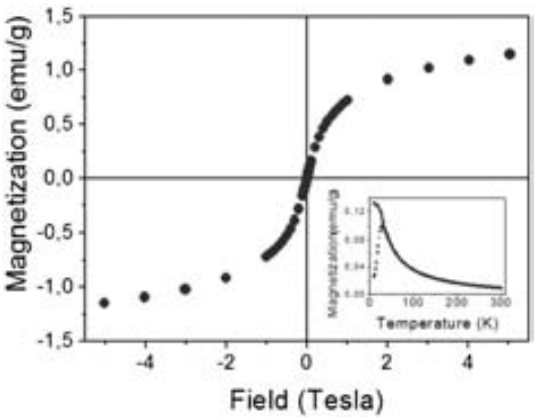

Fig. 11 Magnetization *versus* magnetic field of the maghemite loaded microspheres at 300 K. $M(T)$, ZFC–FC curves are depicted in the inset.

Conclusions

High methoxyl apple–citrus pectin aerogels containing maghemite nanoparticles were produced in the form of cylinders and microspheres. The addition of iron oxide nanoparticles to the aerogel monolith formulation gave the aerogels magnetic properties, changed their color from white to dark brown, and increased the aerogel density (*ca.* 38% higher) and the specific surface area (*ca.* 15%). The addition of iron oxide nanoparticles in the emulsion formulation of the same origin resulted in a more

viscous solution and prevented the droplets of the dispersed phase of the emulsion from flocculation and coalescence. Maghemite nanoparticles were preferentially adsorbed on the outer surface of the aerogel microspheres in the form of islands, but their magnetic properties were unchanged after being incorporated into the microspherical aerogel matrix. The obtained magnetic nanoporous materials set the basis for a future study regarding their application in targeted delivery and magnetic resonance imaging tracking.

Acknowledgements

C.A. García-González acknowledges the Spanish Ministry of Education for the financial support through a postdoctoral fellowship in the frame of the National Program for Staff Mobility from the R&D&i National Plan 2008–2011. M. Zeng acknowledges the CSC scholarship number 2011703001. Authors are grateful to Frank Rimoschat (research group of Prof. Heinrich, Institute of Solids Process Engineering and Particle Technology, Hamburg University of Technology) for his technical support with the measurements of particle size distribution by laser dispersion. The authors want to acknowledge Pektowin company for the supply of the citrus–apple HM-pectin. The work was partially funded by the Spanish Government (MAT2009-08024, CONSOLIDER-Nanoselect-CSD2007-00041) and the Generalitat de Catalunya (2009SGR203). Authors are grateful to Ryan Vargas and Dr Oana Pascu for the synthesis and characterization of some of the nanoparticles. The contributions of Aleksej Vdovin, Jerico J. Uy and Ho Ka Carol Chan in the development of the pectin aerogels are gratefully acknowledged.

References

1 C. Burda, X. Chen, R. Narayanan and M. A. El-Sayed, *Chem. Rev.*, 2005, **105**, 1025–1102.
2 S. Sahu and R. K. Dutta, *J. Magn. Magn. Mater.*, 2011, **323**, 980–987.
3 A. L. Daniel-da-Silva, T. Trindade, B. J. Goodfellow, B. F. O. Costa, R. N. Correia and A. M. Gil, *Biomacromolecules*, 2007, **8**, 2350–2357.
4 B. H. Kenzaoui, M. R. Vilà, J. M. Miquel, F. Cengelli and L. Juillerat-Jeanneret, *Nanomedicine*, 2012, **7**, 1275–1286.
5 E. Taboada, R. Solanas, E. Rodríguez, R. Weissleder and A. Roig, *Adv. Funct. Mater.*, 2009, **19**, 2319–2324.
6 U. Jeong, X. Teng, Y. Wang, H. Yang and Y. Xia, *Adv. Mater.*, 2007, **19**, 33–60.
7 R. D. Halpert, *Gastrointestinal Imaging: The Requisites*, Mosby Elsevier, Philadelphia (PA, USA), 2006.
8 T. Neuberger, B. Schöpf, H. Hofmann, M. Hofmann and B. von Rechenberg, *J. Magn. Magn. Mater.*, 2005, **293**, 483–496.
9 F. Llanes, C. Diaz, H. Ryan and R. H. Marchessault, *International Journal of Polymeric Materials*, 2002, **51**, 537–545.
10 F. Jones, H. Cölfen and M. Antonietti, *Colloid Polym. Sci.*, 2000, **278**, 491–501.
11 S. Dumitriu, *Polysaccharides: structural diversity and functional versatility*, Marcel Dekker, New York (US), 2005.
12 W. G. T. Willats, J. P. Knox and J. D. Mikkelsen, *Trends Food Sci. Technol.*, 2006, **17**, 97–104.
13 H. N. Englyst, S. Hay and G. T. Macfarlane, *FEMS Microbiol. Lett.*, 1987, **45**, 163–171.
14 P. Sriamornsak, *Silpakorn University International Journal*, 2003, **3**, 206–227.
15 S. M. Brejnholt, in *Food Stabilisers, Thickeners and Gelling Agents*, ed. A. Imeson, Blackwell Publishing Ltd, Singapore, 2010.
16 S. Bozbag, D. Sanli and C. Erkey, *J. Mater. Sci.*, 2012, **47**, 3469–3492.
17 D. Sanli, S. Bozbag and C. Erkey, *J. Mater. Sci.*, 2012, **47**, 2995–3025.
18 Y.-P. Sun, *Supercritical Fluid Technology in Materials Science and Engineering. Syntheses, Properties and Applications*, Marcel Dekker, New York, NY, USA, 2002.
19 C. A. García-González, M. Alnaief and I. Smirnova, *Carbohydr. Polym.*, 2011, **86**, 1425–1438.
20 C. A. García-González, M. C. Camino-Rey, M. Alnaief, C. Zetzl and I. Smirnova, *J. Supercrit. Fluids*, 2012, **66**, 297–306.
21 I. Smirnova, S. Suttiruengwong and W. Arlt, *J. Non-Cryst. Solids*, 2004, **350**, 54–60.
22 C. A. García-González, J. J. Uy, M. Alnaief and I. Smirnova, *Carbohydr. Polym.*, 2012, **88**, 1378–1386.
23 A. Berg, M. W. Droege, J. D. Fellmann, J. Klaveness and P. Rongved, *EP*, 0707474B1, 1994.
24 J. W. Long, M. S. Logan, C. P. Rhodes, E. E. Carpenter, R. M. Stroud and D. R. Rolison, *J. Am. Chem. Soc.*, 2004, **126**, 16879–16889.
25 E. Taboada, R. P. del Real, M. Gich, A. Roig and E. Molins, *J. Magn. Magn. Mater.*, 2006, **301**, 175–180.
26 L. Casas, A. Roig, E. Molins, J. M. Grenèche, J. Asenjo and J. Tejada, *Appl. Phys. A: Mater. Sci. Process.*, 2002, **74**, 591–597.
27 M. Popovici, M. Gich, A. Roig, L. Casas, E. Molins, C. Savii, D. Becherescu, J. Sort, S. Suriñach, J. S. Muñoz, M. D. Baró and J. Nogués, *Langmuir*, 2004, **20**, 1425–1429.
28 R. T. Olsson, M. A. S. Azizi Samir, G. Salazar Alvarez, L. Belova, V. Strom, L. A. Berglund, O. Ikkala, J. Nogués and U. W. Gedde, *Nat. Nanotechnol.*, 2010, **5**, 584–588.
29 I. Bilecka, M. Kubli, E. Amstad and M. Niederberger, *J. Sol-Gel Sci. Technol.*, 2011, **57**, 313–322.
30 O. Pascu, E. Carenza, M. Gich, S. Estradé, F. Peiró, G. Herranz and A. Roig, *J. Phys. Chem. C*, 2012, **116**, 15108–15116.
31 E. Taboada, E. Rodríguez, A. Roig, J. Oró, A. Roch and R. N. Muller, *Langmuir*, 2007, **23**, 4583–4588.
32 M. Alnaief, M. A. Alzaitoun, C. A. García-González and I. Smirnova, *Carbohydr. Polym.*, 2011, **84**, 1011–1018.
33 R. J. White, V. L. Budarin and J. H. Clark, *Chem.–Eur. J.*, 2010, **16**, 1326–1335.
34 D. Oakenfull and A. Scott, *J. Food Sci.*, 1984, **49**, 1093–1098.
35 P. Sriamornsak, N. Wattanakorn and H. Takeuchi, *Carbohydr. Polym.*, 2010, **79**, 54–59.
36 B. R. Sharma, L. Naresh, N. C. Dhuldhoya, S. U. Merchant and U. C. Merchant, *Times Food Processing Journal*, 2006, **6**, 44–51.
37 M. L. Fishman, P. H. Cooke and D. R. Coffin, *Biomacromolecules*, 2004, **5**, 334–341.
38 U. Schwertmann and R. M. Cornell, *Iron Oxides in the Laboratory: Preparation and Characterization*, Wiley-VCH Verlag GmbH, Weinheim (Germany), 2000.
39 M. Alnaief and I. Smirnova, *J. Supercrit. Fluids*, 2011, **55**, 1118–1123.
40 B. P. Binks and C. P. Whitby, *Colloids Surf., A*, 2005, **253**, 105–115.
41 F. Reincke, S. G. Hickey, W. K. Kegel and D. Vanmaekelbergh, *Angew. Chem., Int. Ed.*, 2004, **43**, 458–462.
42 I. T. Lucas, S. Durand-Vidal, E. Dubois, J. Chevalet and P. Turq, *J. Phys. Chem. C*, 2007, **111**, 18568–18576.
43 E. Dickinson, *Curr. Opin. Colloid Interface Sci.*, 2010, **15**, 40–49.